ULTRASONIC PULSE SCATTERING BY FISH MUSCLE WITH APPLICATIONS TO QUALITY INSPECTION

by

MANFRED FREESE

A THESIS

SUBMITTED TO THE FACULTY OF GRADUATE STUDIES

IN PARTIAL FULFILMENT OF THE REQUIREMENTS FOR THE DEGREE

OF DOCTOR OF PHILOSOPHY IN ELECTRICAL ENGINEERING

DEPARTMENT OF ELECTRICAL ENGINEERING

UNIVERSITY OF MANITOBA

WINNIPEG, MANITOBA

CANADA

OCTOBER 1974

ULTRASONIC PULSE SCATTERING BY FISH MUSCLE WITH APPLICATIONS TO QUALITY INSPECTION

by

MANFRED FREESE

A dissertation submitted to the Faculty of Graduate Studies of the University of Manitoba in partial fulfillment of the requirements of the degree of

DOCTOR OF PHILOSOPHY

It may be a weed instead of a fish that,
after all my labour, I may at last pull up.

Michael Faraday

ACKNOWLEDGEMENTS

The author would like to thank Dr. M. A. K. Hamid, Dr. E. G. Bligh and Dr. W. E. Johnson for their encouragement and support during the course of this work. For Dr. Hamid's assistance in the reviewing and editing of the text, the author is particularly grateful.

The assistance provided by H. Ballon in performing many of the measurements is greatly appreciated, as is the co-operation of members of the analytical chemistry group of the Freshwater Institute in performing biochemical analyses, and Dr. D. P. Scott and B. Hobden in advising and assisting in the histological aspects of the work.

The author wishes to express his deep appreciation to his wife, Barbara, for her patience and forbearance, and for the typing of a rather difficult manuscript.

Finally, the author would like to thank the Fisheries Research Board of Canada for granting him a leave of absence and supporting the research project.

ABSTRACT

This dissertation presents the results of an investigation of the origin and characteristics of ultrasonic volume backscatter in the 1 to 5 MHz frequency range from fish muscle tissue as a function of the tissue composition and condition. Scattering by the tissue structural components is analyzed with particular emphasis on scattering by rough interfaces and thin membranes. A fairly detailed physical optics treatment for scattering by a rough surface of low reflectance is presented in this connection. In the context of this work the problem of in situ diagnostic pulse backscatter measurements for soft animal tissues is examined both theoretically and experimentally. Various aspects, including the effects of absorption, pulse bandwidth and scatterer response, are discussed and analyzed. The problem of calibration, the derivation of a backscatter coefficient and the use of broadband beam near-field measurements are also examined.

The tissue measurements are restricted principally to the lateral myomere of lake whitefish (Coregonus clupeaformis), a fatty species, and pickerel (Stizostedion vitreum), a lean species. However, additional measurements on model media of air and oil bubble suspensions, tissue structural components and bovine muscle are included for comparison.

It is found that the backscatter from whitefish muscle (transverse incidence with respect to the muscle fibers) in the frequency range of 2.3 to 4.8 MHz generally varies as $\lambda^{-2.4}$, where λ is the wavelength, compared to $\lambda^{-1.3}$ for pickerel and $\lambda^{-2.4}$ for a sample of bovine

skeletal muscle. The results are interpreted with the aid of theoretical calculations based on a first order statistical scattering model of the fish tissue, histological observations and measurements of the model media. The $\lambda^{-1.3}$ dependence for pickerel appears to be due primarily to scattering by the muscle fibers and the myosepta.

It is shown that, if the tissues are free of gas bubbles, lipid inclusions are usually the dominant scatterers in whitefish; for total lipid contents up to 6%, a roughly linear relationship between the backscatter intensity and the lipid content is observed. However, it is also shown that, as a result of decompression, gas bubbles are almost invariably present in whitefish, in which case these tend to be the predominant scatterers.

In addition to the system modelling of the composite tissue scattering process and the ultrasonic characterization of fish tissue, the results are of significance towards the development of practical ultrasonic inspection and/or quality control techniques in the fishing industry, as well as other segments of the food processing industry. The results may also be valuable for the development of ultrasonic diagnostic techniques in the biomedical field.

TABLE OF CONTENTS

Chapter Page

Chapter Page

Chapter Page

LIST OF FIGURES

Figure | Page

LIST OF TABLES

CHAPTER 1

INTRODUCTION

The need for better methods of objective evaluation and inspection of quality in the processing and marketing of fish is widely recognized [Stevenson & Kellogg, Ltd. (1970)]. Although much progress has been made in identifying and isolating the factors affecting quality [FAO (1964), (1969)], adequate means of grading and inspection are still lacking in many important areas, particularly where rapid, non-destructive testing applicable in situ is a key consideration. One such area is that of inspection for parasites. The occurrence of these intramuscular parasites in many economically important species (e.g. whitefish and cod) constitutes a grave problem in the industry [McIvor (1965); Stevenson & Kellogg, Ltd. (1970); FAO (1969)]. Work on the detection of these parasites by means of ultrasound [Freese (1969)], particularly Triaenophorus crassus in whitefish, showed that a pulse-echo technique was feasible but was hampered by tissue scattering. Preliminary work on the ultrasonic properties of tissue [Freese and Makow (1968.a.b)] suggested that ultrasonic techniques might also be exploited for quality control and inspection purposes in other areas, for example, to distinguish fresh and frozen-thawed tissue and to determine the fat content of round fish.

For the development of such methods and optimization of the parasite detection process, a knowledge of the tissue backscatter characteristics under all possible conditions is required. Although considerable experimental data on the ultrasonic propagation parameters for biological

media is available [El'piner (1964); Dunn et al. (1969)], including fish tissue [Haslett (1962); Freese and Makow (1968.b); Matsui and Shibata (1971)], it was found that quantitative data on the scattering properties of fish, as well as of soft animal tissues generally, is presently lacking. In respect to human tissue, for example, Hill (1972), in a recent paper given at the Workshop Conference on the Interaction of Ultrasound and Biological Tissues, observed

> "....very little indeed is known in quantitative terms about the backscattering properties of human tissues, and virtually nothing about their frequency dependence."

Until recently [Aldridge and Tattersall (1971); Szilard and Scruton (1973)], there has been little apparent effort made in exploiting ultrasonic diffuse scattering for industrial, non-destructive testing applications. Although ultrasound is widely used, with few exceptions the methods rely on specular pulse reflection, absorption and velocity. Similarly in the biomedical field, where ultrasound is widely used for visualization purposes, few attempts have been made to investigate and measure scattering by different biological tissues in a quantitative sense until recently [Senapati et al. (1972); Waag and Lerner (1973)], although its potential for characterizing the structure of tissues has certainly been recognized [e.g. Wild and Reid (1953); Reid and Sikov (1972)].

The lack of progress in the development of scattering methods is not hard to explain. In the case of many industrial applications, where the sample to be tested is readily accessible and has a well-defined geometry, absorption and velocity can generally be determined more easily and accurately than the scattering properties. In addition, the development of satisfactory diagnostic scattering procedures in both the

industrial and biomedical sectors has generally been deterred by obstacles such as lack of accuracy, ambiguities in the results, high reverberation levels due to intervening interfaces (as, for example, in echoencephalography), the presence of moderate to high attenuation in the tissues and theoretical and experimental difficulties due to the complex nature of the scattering media.

To obtain a proper perspective of these obstacles and to furnish a realistic model for the development of fish inspection techniques and hardware, a detailed analysis of the tissue backscatter problem is necessary.

In this dissertation we present the results of an investigation of volume backscatter from fish tissues in the 1 to 5 MHz range, and we consider the problem of pulse backscattering by soft tissues for in situ applications. The origin and characteristics of the backscatter are examined theoretically and experimentally, and are correlated with the overall composition and condition of the tissues. Although the measurements are restricted principally to the lateral myomere of lake whitefish (Coregonus clupeaformis) and pickerel, also known as walleye (Stizostedion vitreum), some measurements on model media and bovine muscle are included for purposes of comparison.

The theoretical work falls broadly into two categories. The first is concerned with the analysis of the different scatterers found in fish tissues, and also to some extent in other animal tissues. The objective may be summed up as an attempt to estimate the magnitude and wavelength dependence of the backscatter by the various tissue inhomogeneities. In spite of the fact that we have specifically referred to

volume scattering, a significant portion of the scattering in both mammalian and fish tissues may be from thin membranes and organ interfaces intersecting the insonified volume. In the case of fish muscle, a regular series of involuted thin membranes bind the muscle segments that give fish muscle its distinctive chevron-shaped appearance. These membranes or tissue sheets are usually far from smooth at millimeter wavelengths and may have characteristic impedances significantly different from those of the surrounding tissues. Scattering from rough surfaces and thin membranes is thus given major emphasis and a fairly comprehensive first order treatment is presented.

The other part of the theoretical work is concerned with the analysis of the actual measurement problem. A phenomenological view of the stochastic scattering process due to Faure (1964), Ol'shevskii (1967) and Middleton (1967), (1972) is adopted and a model of the tissue scattering process is derived. The resultant model greatly facilitates the analysis of the scattering process by illustrating in a straightforward manner the influence of the various scattering medium parameters and those of the measurement setup. It is thus valuable in the design and optimization of new diagnostic systems. Various aspects of the scattering process, including the statistical properties, the effects of absorption, the signal pulse characteristics and measurements in the transition region between the near and far fields, are analyzed and compared with the results of experiments.

1.1 Background and Approach

Of the two fundamental roles of scattering mentioned in the introduction, the inverse scattering problem represents by far the more difficult problem. As in the case of the forward (input-output) problem,[1] two basic techniques are commonly employed in the solution of the inverse problem. The first of these attempts to directly invert the problem, while the second approach employs a comparison method and might therefore be more properly termed pseudo-inverse. Frequently these two methods are combined. We shall employ the latter method which in its essential features is similar to regression analysis. Unfortunately, as in the case of regression analysis, or to use the analogy of a black box from circuit theory, two boxes may be equivalent at particular frequencies but the contents are not necessarily identical. This lack of uniqueness underlines the fact that, although in principle scattering measurements can reveal a great deal about the structure of a medium, in practice additional information derived from other sources is required if the analysis of the scattering is to yield useful results.

1.1.1 Scattering Techniques

In applications where anisotropy and geometry are not a problem, some of the bistatic scattering techniques used in optical and microwave studies [Van De Hulst (1957); Kerker (1969); Wheelon (1959); Beckmann and Spizzichino (1963)] may be employed to advantage. Thus, Senapati et al. (1972) examined rough surface scattering as a function

---

[1] Rigorous solution of the relevant statistical wave or diffusion equation versus Monte Carlo methods.

of frequency and angle from frog muscle and liver tissues. However, in general bistatic measurements are difficult to perform in the case of scattering from tissue volumes or embedded surfaces because of interference by strong reflections from the outer surface. For inspection applications of deep-lying tissues in situ only monostatic volume scattering measurements can normally be considered. This entails some loss of information but it should be remembered that due to the absence of polarization effects, bistatic acoustic compressional wave scattering measurements yield comparatively less information than do analogous electromagnetic and optical measurements [Van De Hulst (1957)]. Nonetheless, it is clear that this aggravates the problem of measurement ambiguities further. Depending on the nature of the application and of the ambiguities, be it number, size and shape distribution and/or composition of the scatterers, the backscatter measurements may have to be supplemented by additional information regarding the medium.

In some cases it may be possible to obtain this information by other ultrasonic measurements, for example, absorption and velocity, but just as often this proves impractical and some other means have to be found.

1.1.2 Scattering by Random Media

Two principal lines of attack towards the solution of random scattering problems are evident. The first of these is via the wave equation for inhomogeneous media or the equivalent integral equation. The inhomogeneous wave equation has the form

$$\nabla^2\Psi(\vec{r}) + k^2\Psi(\vec{r}) = q(\vec{r}) \qquad (1.1.1)$$

where $\Psi(\vec{r})$ is the velocity potential and $q(\vec{r})$ represents the sources. In regions of variable compressibility and/or density which constitute the inhomogeneites (bulk scatterers) in the medium, $q(\vec{r})$ will differ from zero giving rise to scattering of the incident waves.

Foreign bodies which scatter the sound (surface scatterers) are usually more easily treated in terms of an integral equation equivalent to (1.1.1). For an incident plane wave $\Psi_i(\vec{r}) = e^{jk\vec{r}-j\omega t}$, one obtains [Morse and Ingard (1968)]

$$\Psi(\vec{r}) = \Psi_i(\vec{r}) + \sum_j \iiint_{V_j} G(\vec{r}|\vec{r}_o)\, \chi(\vec{r}_o)\, \Psi(\vec{r}_o)\, dv_o + \sum_\ell \iint_{S_\ell} \left[\Psi(\vec{r}_o)_s \frac{\partial G(\vec{r}|\vec{r}_o)}{\partial n_o} - G(\vec{r}|\vec{r}_o) \frac{\partial \Psi(\vec{r}_o)}{\partial n_o}\right] ds_o \tag{1.1.2}$$

where $G(\vec{r}|\vec{r}_o)$ is the Green's function, $\chi(\vec{r}_o)$ is the strength of the local inhomogeneity, $\Psi(\vec{r}_o)$ is the local velocity potential and $\vec{n}_o$ is the local surface normal.

Several approximation techniques (ibid.) have been developed for evaluating either (1.1.1) or (1.1.2). Among the best known is the Born approximation technique obtained by substituting $\Psi_i(\vec{r}_o)$ for $\Psi(\vec{r}_o)$ in (1.1.2) and then iterating to obtain the n-tuply scattered waves ($n > 1$).

The first order Born approximation will be valid only to the extent to which interaction of the scatterers including 'self-interaction' via the scattered field may be neglected. This implies that the scattered field be much smaller than $\Psi_i(\vec{r})$.

The statistical properties of the scattering may be found by solving (1.1.1) or (1.1.2) for specified space-time statistics of the

scattering inhomogeneities. However, evaluation beyond the first Born approximation is generally difficult, even in those few cases where simple analytical statistical parameter distributions such as the Gaussian distribution may be applicable. We shall use the Born approximation to evaluate scattering by a rough sheet in Chapter 2.

The alternate approach assumes that the scattering results from equivalent discrete scatterers (in effect point-scatterers or scattering centers) located randomly throughout the volume (or on the surface) of the insonified medium. The scattering centers are essentially mathematical fictions but take on a certain physical reality when the impedance discontinuities are sufficiently sharply defined. Thus, air bubbles with dimensions less than the ultrasonic wavelength are rather well approximated by discrete scatterers. Larger scatterers may sometimes be represented by an aggregate of scattering centers physically identifiable as the specular flare points, diffracting edges and points of the scattering obstacle. The point-scatterer approach is thus conceptually closest to the geometrical theory of diffraction of Keller (1953).

The stochastic nature of the scatterers may be taken into account by direct averaging over the scatterer statistical parameters or by an equivalent very general procedure of averaging over the random configurations of the scatterers consistent with the statistical information available. This method of statistical averaging was introduced by Foldy (1945) to treat n^{th}-order multiple scattering from random scatterers. When used in conjunction with the wave equation

approach, this technique leads to the stochastic forms of the wave equation (1.1.1) and (1.1.2).[1]

The point-scatterer theory has been greatly developed in the field of underwater acoustics within recent years by Faure (1964), Ol'shevskii (1967) and Middleton (1967). The latter author, in particular, has applied this method to some very complex reverberation problems [Middleton (1972)].

What makes the point-scatterer approach so attractive is the ease with which various characteristics of the medium and the measurement system can be introduced. Thus, even if the impulse responses of the point-scatterers are not initially specified making it impossible to calculate the actual backscatter level, the scatterer model can still be used to analyze the influence of the measurement system and medium parameters on the statistical parameters that characterize the resultant scattering. With the impulse response specified, the point-scatterer theory becomes a convenient vehicle for implementing the analysis of the pseudo-inverse scattering problem. We shall make use of the point-scatterer theory in both of these contexts.

1.2 Résumé

A brief review of the structure and composition of skeletal muscle tissue outlining the similarities and differences of mammalian

---

[1] Details of this procedure and conditions for the validity of the method, including an examination of the fundamental problem of n^{th}-order random multiple scattering--the lack of completeness, may be found in a paper by Waterman and Truell (1961); see also various papers by Twersky (1962, 1963).

and fish muscle is given at the beginning of Chapter 2. The chapter, however, is devoted mainly to a theoretical analysis of the scattering cross-sections of the various fish tissue inhomogeneities, although some experimental data is introduced to delimit and simplify the analysis. A major part of the chapter deals with scattering by rough surfaces and thin membranes. Scattering by rough interfaces of low reflectivity (normalized characteristic admittance near unity) is analyzed using a slightly modified form of the physical optics solution due to Beckmann and Spizzichino (1963). The results are then applied to a heuristic treatment of scattering by a rough thin sheet and generalized for narrow-beamwidth and short pulse incidence. At the end of the chapter a working definition for the pulse backscatter coefficient is given which serves as the principal basis for reporting of the experimental scattering results.

A composite model of the tissue volume backscatter process based on the Middleton-Ol'shevskii point-scatterer theory is developed in Chapter 3. Elementary statistical and signal processing concepts are reviewed and expressions for the first and second moments are derived, together with suitable first order corrections for the effects of absorption and finite bandwidth.

The significance of the pulse bandwidth in terms of the transmitter-receiver bandwidth, the effects of absorption, and the resultant modifications in the scattering and near-field distributions are examined in some detail. The latter is illustrated by a number of comparisons of experimental near-field and transition region pulse measurements with theoretical CW and wideband data. The use of these

measurements in the case of in situ measurements is then considered from a practical standpoint and various advantages and disadvantages of such measurements are outlined.

Chapter 4 describes the experimental methods and instrumentation used in the measurements. Important data is given on the beam and pulse parameters, the reference calibrations and the various transducer and instrument characteristics. The determination of the near- and far-field equivalent insonified volumes is discussed and the results are compared with theory. Also described in this chapter are the different techniques employed to measure ultrasonic absorption and velocity and the methods used to determine the various other tissue properties of interest.

In Chapter 5 the results of backscatter measurements are presented. The first section of the chapter is devoted to an investigation of the backscatter from a model medium of gelatin containing air bubbles for the purpose of verifying the basic experimental approach and the calibration of the setup. The results are compared with first order scattering theory. The volume backscatter as a function of frequency from the lateral muscles of whitefish and pickerel is then analyzed and interpreted in terms of the characteristics of the known inhomogeneities considered in Chapter 2. Further evidence in the form of experimental measurements on model media of gelatin and oil bubbles and measurements from excised pinbones and myosepta is given and compared with the results of theoretical calculations.

The dependence of backscattering on the tissue composition, the measurement conditions and the nature of the fish is investigated. Other aspects examined are the problem of gas bubbles in the tissues

and the stability of the resultant backscatter. Lastly, some results of backscatter measurements on other species of fish and mammalian (bovine) muscle are presented to round out the experimental investigation.

Chapter 6 summarizes the principal findings and conclusions. A number of potential applications and possible extensions of the work are outlined.

The appendices, with the exception of Appendix C, contain material strictly of a review nature on reverberation process statistics and statistical functions. Appendix C contains a detailed treatment of the scattering of rectangular- and cosine-shaped pulses from a rough surface for the case of a Gaussian beam.

1.3 Mathematical Conventions

At the outset there always seems to arise the question as to which units and sign conventions to adopt. Unless the conventions are clearly stated, the results can be very confusing because of the mixture of standard mathematical, electrical and mechanical symbols and quantities commonly employed in the field of acoustics. Throughout this thesis we will employ the following conventions and definitions:

(a) The pressure of an outward travelling wave is given by

$$p(\vec{r},t) = \frac{P_o}{r} e^{j(\vec{k}\cdot\vec{r}-\omega t)} \qquad (1.3.1)$$

where the time dependence $e^{-j\omega t}$ will often be suppressed.

(b) The positive frequency phasor is negative and thus opposite to accepted engineering usage. As a result, the mechanical reactances have signs opposite to the analogous electrical reactances.

(c) Analytic or quasi-analytic signals will be expressed in the form $V(t) = V_o(t)e^{-j\omega_c t}$. If the Fourier transform pairs are defined by the equations

$$S(\omega) = F[s(t)] = \int_{-\infty}^{\infty} s(t)e^{j\omega t}\, dt$$

$$s(t) = F^{-1}[S(\omega)] = \frac{1}{2\pi}\int_{-\infty}^{\infty} S(\omega)e^{-j\omega t}\, d\omega \qquad (1.3.2)$$

the transform of the analytic signal $s(t) = s_o(t)e^{-j\omega_c t}$ becomes

$$F[s(t)] = S_o(\omega - \omega_c) \qquad (1.3.3)$$

The transform of the derivative is given by

$$F[\dot{s}(t)] = -j\omega S_o(\omega - \omega_c) \qquad (1.3.4)$$

where the dot indicates differentiation with respect to time. Alternatively, (1.3.4) may be expressed in the inverse form as

$$F^{-1}[-j\omega S(\omega)] = -j\omega_c s(t) + \dot{s}_o(t)e^{-j\omega_c t} \qquad (1.3.5)$$

CHAPTER 2

SCATTERING FROM FISH TISSUE INHOMOGENEITIES

In order to be able to extract the maximum amount of useful information from scattering data, it is important that one knows as much as possible about the nature of the scatterers and the medium. We will examine in this chapter the composition and structure of fish muscle tissue and consider in some detail scattering by the different tissue inhomogeneities. In the case of the latter, we will concentrate on obtaining basic estimates of the backscatter magnitudes from the scatterers, that is to say, free of any encumbrances resulting from absorption by the tissues, non-ideal incident field characteristics and various limitations and constraints associated with the experimental setup. These latter aspects will be considered in Chapters 3 and 4. With the exception of scattering from certain membranes (myosepta) occurring in fish muscle, the analysis of the scatterers is relatively straightforward.

Unlike most of the other tissue scatterers, the myosepta extend over the entire width of the incident ultrasonic beam and thus require a more rigorous analysis. By treating the myosepta as rough thin sheets, comparatively simple heuristic expressions for their CW reflectivities are derived in Section 2.3. Using Fourier transform methods these expressions are then generalized in Section 2.4 for finite

Gaussian beam and short pulse incidence. The discrete impulse scatterer interpretation of the resultant pulse backscatter expressions leads to a natural definition of the scattering strength in terms of the incident pulse energy that is compatible with the use of short pulses. The backscatter strength so defined is used as the principal basis of reporting the experimental results.

We begin our analysis of fish tissue volume scattering with a brief review of the nature of fish myomere.

2.1 The Structure and Composition of Fish Muscle[1]

The great majority of North American freshwater fishes can be classified as either soft-rayed or spiny-rayed types. The two species considered in this thesis are examples of these two types. Whitefish (Coregonus clupeaformis) is a herring-like, soft-rayed species while pickerel (Stizostedion vitreum vitreum) is representative of the spiny-rayed type. Although there are obvious external and internal differences, fundamentally the anatomies of both types are the same. The most significant difference from our point of view lies in their composition, specifically the fat content described in Section 2.1.3. The effects of this on the volume scattering of ultrasound prove to be highly significant.

---

[1]Much of the descriptive material in this section was taken from Vol. IIA by Harder in Handbuch der Binnenfischerei Mitteleuropas, edited by Demoll, Maier and Wundsch(1964), and Fish as Food, Vol. I, edited by Borgstrom (1961). Specific data for whitefish and pickerel, except for the data on lipid composition by Awad (1967), were obtained from measurements performed by the author.

2.1.1 Arrangement of the Myomere

Perhaps the most striking feature of fish skeletal muscle is the segmentation of the muscles into layers, Fig. 2.1. The chevron-like involution of the muscle layers or myomere, Fig. 2.2, gives layers a cone-shaped appearance in three dimension. A cross-section of the body of a whitefish (Coregonus clupeaformis) in the region between the dorsal fin and the head is shown in Fig. 2.3. The distinctive patterns of the myomere in a cross-section of fish (patterns vary in different parts of the body) are characteristic of a species. Identical patterns may be found in other species, particularly members of the same family. The individual myomere are bounded by thin membranes called myosepta. The thickness of the myomere and myosepta varies depending on the species of fish, location within the body and age of the fish. The location of a series of fine bones (pinbones) in the epaxial muscles shown in Fig. 2.3 should be noted.

The actual skeletal muscle consists of thread-like fibers or muscle cells typically 75 to 200 μm in diameter. (When only a single cell nucleus is present one speaks of a muscle cell in contrast to the muscle fiber or myofiber which has many nuclei.) Except in the belly region of the body, these cells run parallel to the body axis. The length of an individual fiber is thus greater than the thickness of the myomere segment. The myofibers are held in a matrix of collagenous components and elastin fibril called myocommata; the connective tissue coalesces to form the myosepta, described in detail in Section 5.2.

2.1.2 Comparison of Mammalian and Fish Myomere

The differences between fish myomere and mammalian myomere are apparent in the aggregation of the myofibers. In mammalian muscle,

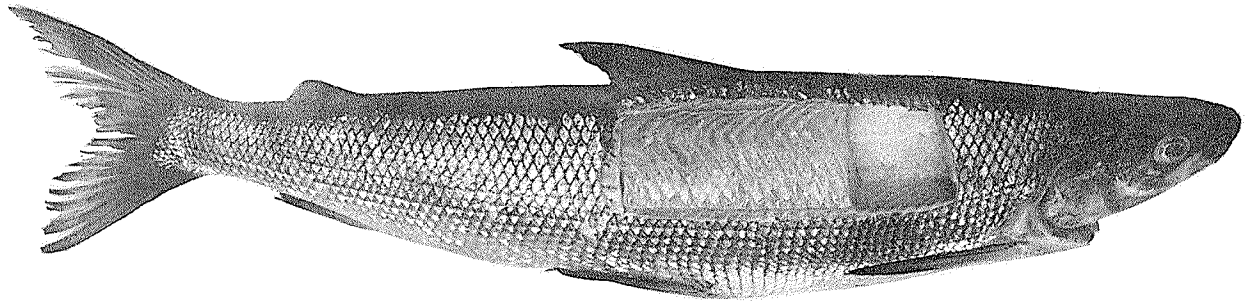

Fig. 2.1(a) Exposed myomere in whitefish

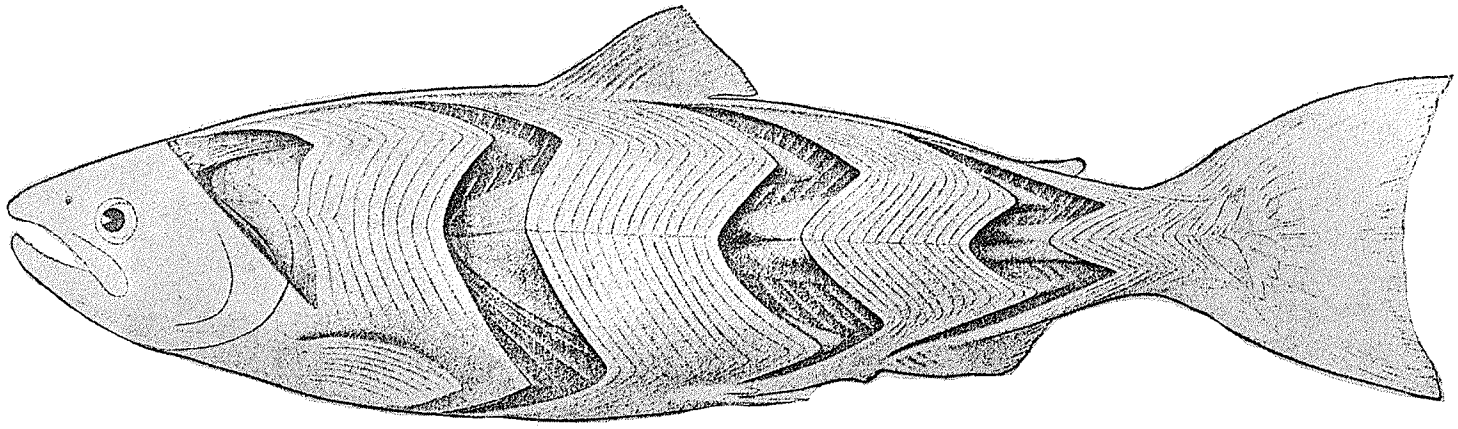

Fig. 2.1(b) Musculature of salmon [reproduced from Greene (1913)]

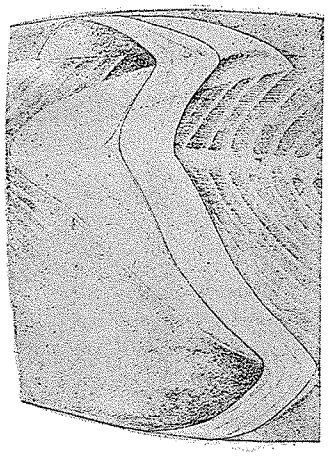

Fig. 2.2 View of individual myotomes in salmon [reproduced from Greene (1913)]

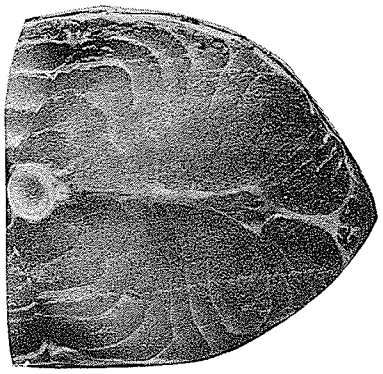

Fig. 2.3 Whitefish cross-section showing position of pinbones

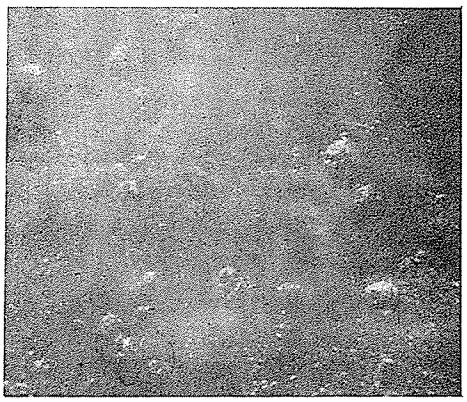

Fig. 2.4 Whitefish myoseptum section showing presence of air bubbles; magnification 25x

myofibers are joined together by connective tissue cells to form bundles, which in turn form still bigger bundles making up a given muscle. Thus, the aggregate muscle fibers in mammalian myomere are longer than in the case of fish. In mammalian myomere, the connective tissue corresponding to the myocommata is called the endomysium. The connective tissue surrounding a primary bundle, which consists of perhaps 40 fibers, is referred to as the perimysium. The primary bundles which may be combined into secondary and tertiary bundles are surrounded by a thick sheath of connective tissue, the epimysium. The mammalian myomere contain a proportionately greater amount of connective tissue (stroma). As a result, one might expect that mammalian myomere at mm wavelengths would appear less homogeneous than fish myomere assuming that corresponding tissue components have similar acoustic impedances.

For comparison the breakdown of the various protein fractions in beef and fish muscle is roughly as follows [Dyer and Dingle (1961)]:

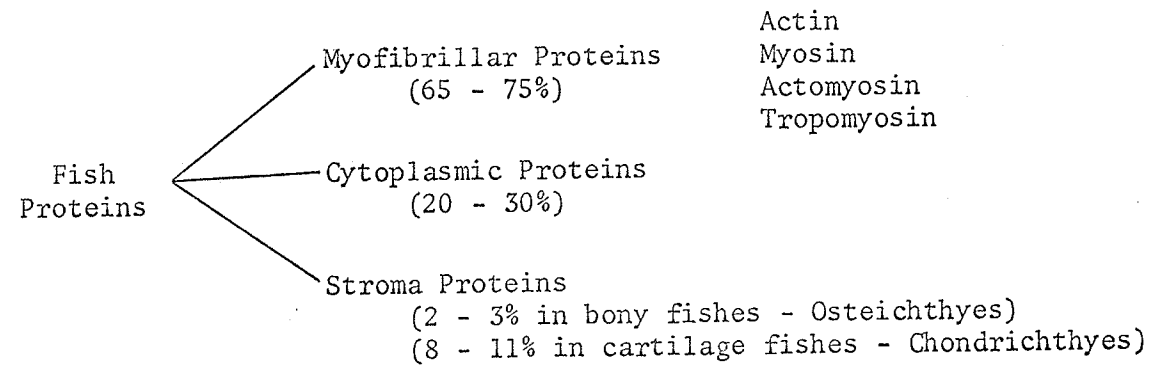

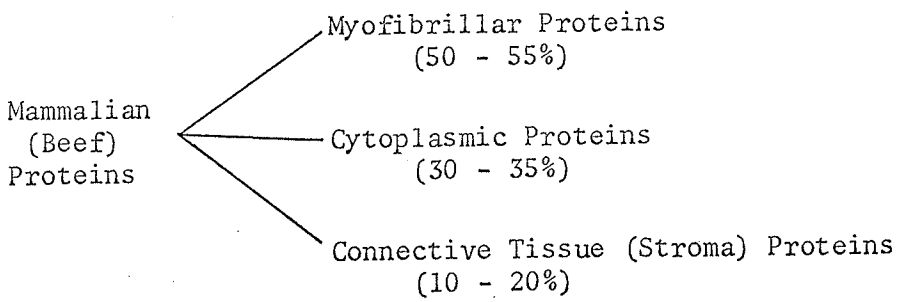

2.1.3 Fat Content and Distribution

The amount of fat in the tissues varies greatly depending on the species, the particular tissues and sites considered, available nutrients, whether the fish migrates for spawning, seasonal and other environmental parameters [Jacquot (1961)]. In general, the soft-rayed species exhibit a higher fat content than most spiny-rayed fish. It should be cautioned, however, that the range of fat content in the soft-rayed species can and does vary from negligible fat, i.e. <0.5%, to a rather remarkable 60% in siscowets (Cristivomer namaycush siscowet), a sub-species of lake trout; variations of 15% within the same species are not uncommon. Some typical values for whitefish and pickerel are given in Table 2.1.

TABLE 2.1

COMPOSITION OF FISH MUSCLE

Fish	Water %	Protein %	Lipid %	Carbohydrates and Ash[a] %
Whitefish (Fat >5.0%)[b]	75.5	15.7	7.6[d]	
Whitefish (Med. 1.5-5.0%)	77.7	17.9	3.3	1.2
Whitefish (Lean <1.5%)	81.1	16.6	1.1	
Pickerel (<0.7%)	81.0	16.8	0.6	
Fat Fish[c]	68.6	20	10	1.4
Medium Fat Fish	77.2	19	2.5	1.3
Lean Fish	81.8	16.4	0.5	1.3

(a) Glycogen may range up to 0.85%

(b) Average values observed in our experiments, see Sec. 4.6

(c) Jacquot (1961)

(d) Two samples only (six replicates)

Awad (1967) found that in fresh whitefish myomere containing 3.8% lipid, 21% was in the form of phospholipid, 73% was triglycerides and the remainder was in the form of free fatty acids (4.6%) and cholesterol (1.4%). Most of the phospholipid would normally be located intracellularly in the form of liposomes in the fibers. Depending on species, migration period, etc., a small proportion of the other lipids may also be found intracellularly dispersed [Greene (1913)]. In lean and medium-fat fish the liposomes are seldom more than 2 μm in diameter.

Our interest will be centered on the great trunk or lateral muscle of the fish, Fig. 2.1. The trunk muscle contains two distinct types of muscle, a superficial thinner portion of red muscle and a larger deeper mass of white muscle separated by connective tissue containing much adipose tissue. The thin red muscle layer, which normally contains a very great amount of fat in fatty species, is visible in the whitefish cross-section shown in Fig. 2.3. The white muscle making up the bulk of the lateral muscle is normally not nearly as fat; values of 2 - 6% are typical of the white muscle in whitefish, although values in excess of 10% are occasionally encountered. Greene (1913), in describing the storage of fat in the muscular tissue of King salmon (Oncorhynchus tschawytscha), a soft-rayed species like whitefish, stated:

> The fats of the pink (lateral) muscle are distributed in the connective tissue between the muscle fibers--i.e. they are intermuscular. The pink muscle carries a relatively large amount of connective tissue which supports the muscle fibers and the blood vessels, and this connective tissue has a high percentage of adipose tissue. In it are found enormous numbers of fat droplets, which vary within a wide range of size. The smallest droplets are often not more than 1 or 2 μm in diameter, but there are numerous fat globules of this region that are as much as 100 μm in diameter.

The above salmon myomere described by Greene contained 10.5% lipid. Our own observations suggest that a similar description is applicable to the whitefish lateral muscle, although on the average the diameters of the droplets are smaller reflecting the lower fat content.

2.2 Scattering Cross-sections of Tissue Inhomogeneities

Although the muscle cells will not give rise to large discrete echoes [scattering from them may contribute significantly to the total absorption, Pauly and Schwan (1971)], there are several other larger inhomogeneities that on occasion may give rise to observable echoes. In estimating the relative importance of each of these, we have to examine their structures and ultrasonic properties in more detail.

The objective of this and the next section is to derive theoretical estimates of the relative and absolute scattering strengths of the different tissue inhomogeneities likely to be found in myomere. The emphasis will be on whitefish muscle.

Initially, we shall employ the backscatter cross-section (BCS) defined as [Crispin and Siegel (1968)]

$$\sigma = \lim_{r \to \infty} 4\pi r^2 \left| \frac{\Phi_s}{\Phi_i} \right|^2 \qquad (2.2.1)$$

where r is the distance from the point of observation to the origin of a coordinate system centered at the scattering body, $|\Phi_i|$ is the velocity potential (or pressure) magnitude of the incident monochromatic (CW) plane wave, and $|\Phi_s|$ is the magnitude of the scattered wave velocity potential (pressure). This definition will be extended in Section 2.4 to cover the case of an incident pulse.

2.2.1 Pinbone Backscatter Cross-section

A series of fine bones known as pinbones are found in the epaxial muscles of many species. In pickerel or walleye these bones lie almost in the median plane of the fish and they can generally be avoided. On the other hand, in whitefish the pinbones project upwards and outwards making it difficult to avoid interception by the ultrasonic beam. The bones will thus give rise to a small amount of backscatter that may be significant at lower frequencies.

Long Wavelength BCS Approximation

At longer wavelengths the pinbones can be represented as segments of thin truncated cylinders with their effective lengths determined by the incident beamwidth, pulse length and incidence angle. The pinbone curvature over this length may be neglected and the geometrical cross-section may be approximated by a circular area of radius $a = \sqrt{a'b'}$, where a' and b' are the major and minor dimensions of the area, respectively. With these approximations introduced, an acoustic BCS may be simply derived by analogy with Chu's formula for the thin conducting wire [Crispin and Maffett (1968)], i.e.

$$\sigma = \pi L^2 (k_1 a)^4 \sin^6\theta_1 \times \left| \frac{(q_a - 1)}{2q_a + (k_1 a \sin\theta_1)^2 \left[\ell n(\tfrac{1}{2}\gamma k_1 a \sin\theta_1) - j\pi/2\right]} + \frac{\rho_2 - \rho_1}{\rho_2 + \rho_1} \right|^2 \times \left[\frac{\sin(k_1 L \cos\theta_1)}{k_1 L \cos\theta_1} \right]^2 , \quad L >> \lambda \qquad (2.2.2)$$

where $$q_a = \frac{\rho_2 c_2^2}{\rho_1 c_1^2} \frac{\sin^2\theta_1}{\sin^2\theta_2}$$

θ_1 is the angle between the bone and the direction of incidence, a is the equivalent radius, $\gamma = 1.781$ is the Euler constant, $k = 2\pi/\lambda$, ρ is the density, c is the velocity and ρc^2 is the reciprocal of the compressibility. The subscripts 1 and 2 denote the medium and bone parameters, respectively. For ρ_2, $\rho_2 c_2^2 = 0$, (2.2.2) becomes identical to Chu's formula with the incident E-field directed along the wire.

Short Wavelength BCS Approximation

At short wavelengths the physical optics solution for the finite elliptic cylinder is useful. The solution for the elliptic cylinder [Crispin and Siegel (1968)] is

$$\sigma = \frac{ka^2b^2L^2 \sin\theta \, |R|^2}{[(a\cos\phi)^2 + (b\sin\phi)^2]^{3/2}} \left[\frac{\sin(kL\cos\theta)}{kL\cos\theta}\right]^2 ;$$

$$kb \gg 1 \quad , \quad a \geq b \qquad (2.2.3)$$

where 2a and 2b are the respective major and minor axes, ϕ is the azimuthal angle and the other parameters are as before. Eq. (2.2.3) is not applicable if the curvature of the pinbones is such that the relative phase shift over the effective length L at normal incidence exceeds $\pi/4$. This requirement may be expressed in terms of the radius of curvature (R_c) as $L < \sqrt{R_c \lambda}$.

Since the bones are not completely rigid but are essentially opaque, (2.2.3) is multiplied by a factor $|R|^2$, the square of the (absolute) reflection coefficient given by

$$R = \frac{\sin\theta - \beta}{\sin\theta + \beta} \qquad (2.2.4)$$

where β is the normalized admittance $\rho_1 c_1 / \rho_2 c_2$.

2.2.2 Gas Bubble and Liquid Inclusion Cross-sections

Depending on the species, condition and handling of a fish, various other types of bounded scattering inhomogeneities (and combinations of them) may be present; they include gas bubbles, oil globules and tissue fluid inclusions.

Long Wavelength BCS Approximations

Treating these inhomogeneities as small spherical scatterers, a formula for the backscatter cross-section may be derived from a series development of the exact solution for the non-rigid sphere. The resultant formula differs slightly from the one based on the Rayleigh approximation [Rayleigh (1896)]. The first order approximation of the solution is

$$\Phi_s \simeq -A(k_1a)^3 \left[\frac{\rho_2 c_2^2 - \rho_1 c_1^2}{3\rho_2 c_2^2 - \rho_1 c_1^2 (k_1a)^2 (1 + jk_1a)} + \frac{\rho_2 - \rho_1}{2\rho_2 + \rho_1} \cos\theta \left[1 - \frac{1}{jk_1r} \right] \right] \frac{e^{jk_1r}}{k_1r} \quad ; \quad \begin{matrix} k_1a << 1 \\ k_1r >> 1 \end{matrix} \tag{2.2.5}$$

where A is the incident wave amplitude, Φ_s is the scattered wave velocity potential, a is the sphere radius, θ is the scattered wave direction with respect to the positive z-axis and the media parameters are as before in (2.2.2).

Using (2.2.5) and (2.2.1) the BCS ($\theta = 0$) for the sphere becomes

$$\sigma = 4\pi a^2 (k_1 a)^4 \left| \frac{\rho_2 c_2^2 - \rho_1 c_1^2}{3\rho_2 c_2^2 - \rho_1 c_1^2 (k_1 a)^2 (1 + jk_1 a)} + \frac{\rho_2 - \rho_1}{2\rho_2 + \rho_1} \right|^2 ; \qquad ka < 1 \tag{2.2.6}$$

In the case of an air bubble $\rho_1 c_1^2 >> \rho_2 c_2^2$. If, moreover, $\rho_1 c_1^2 (ka)^2 >> 3\rho_2 c_2^2$, (2.2.6) reduces to

$$\sigma \simeq \frac{4\pi a^2}{1 + (ka)^2} ; \qquad ka << 1 \tag{2.2.7}$$

Values of (2.2.7) together with the exact CW values for a pressure release (Dirichlet) sphere taken from Hickling's (1962) paper are plotted in Fig. 2.5. In comparison with the rigid sphere the resonance region contains very little ripple thus indicating strong attenuation of the creeping waves--a well-known fact.

The simpler Rayleigh BCS formula which neglects the factor $\rho_1 c_1^2 (1 + jk_1 a) (k_1 a)^2$ in (2.2.6) may be employed for fluid (water) inclusions ($ka << 1$). For lipid globules, however, depending on the value of ka, the full expression (2.2.6) must generally be used as $\rho_2 c_2^2 \leq \rho_1 c_1^2$. The computed BCS values for lipid bubbles are shown in Fig. 2.5 and are seen to be several orders of magnitude smaller than for air bubbles of comparable size.

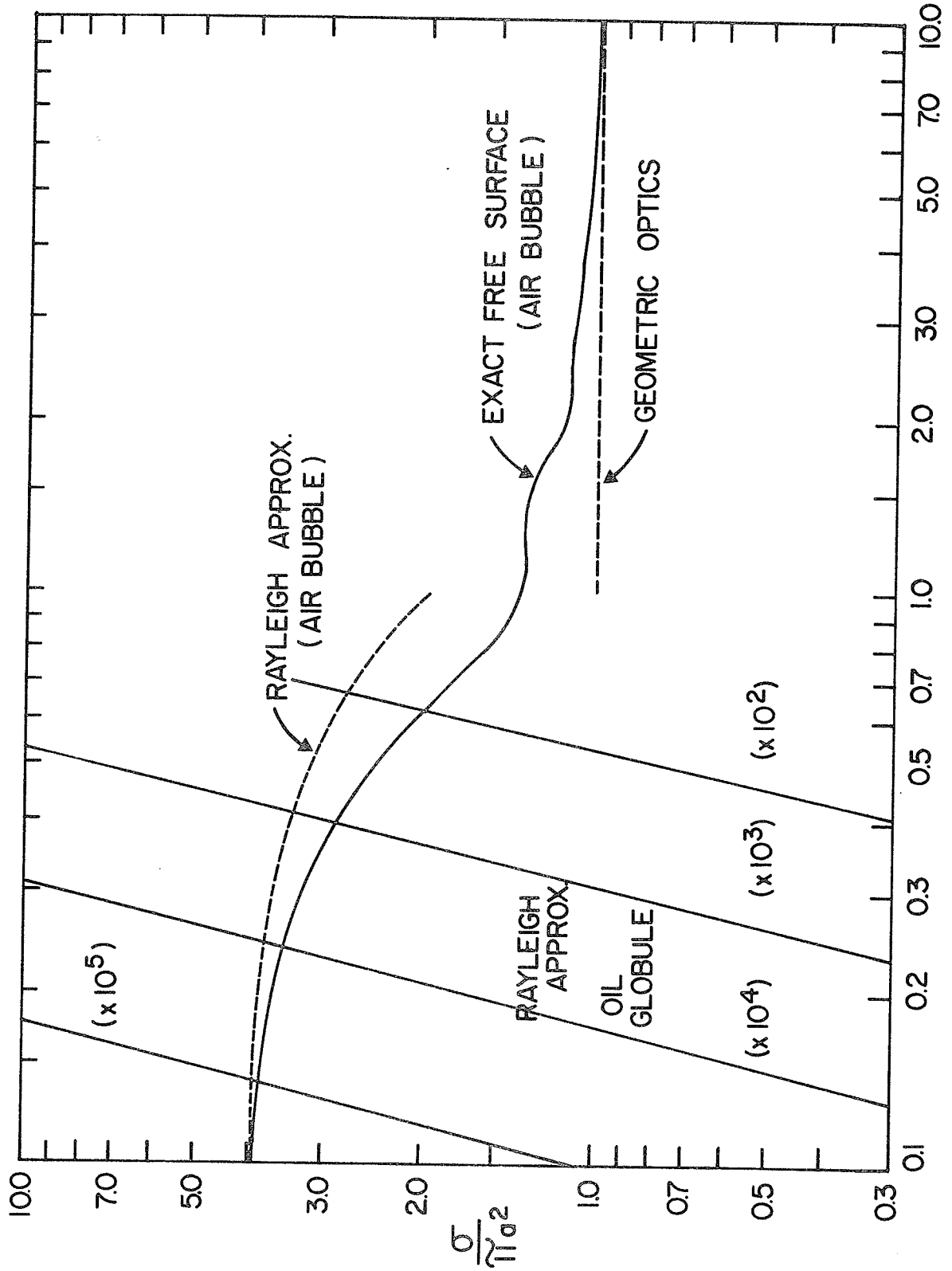

Fig. 2.5 Backscatter cross-sections of pressure release sphere and Rayleigh oil droplet.

Resonant Gas Bubbles

For the denominator of the first (monopole) term in (2.2.5) to tend to zero requires that $(ka)^2 \simeq 3\rho_2 c_2^2/\rho_1 c_1^2$ or, alternatively, $\omega_o = \frac{c_2}{a}\left(\frac{3\rho_2}{\rho_1}\right)^{\frac{1}{2}}$ which is known as the gas bubble resonance condition. The scattered wave causes damping of the resonance as is indicated by (2.2.5). In practice there are also viscosity and other losses. For this reason, it is normally necessary to replace the jka term in the denominator of (2.2.5) by a more general damping factor, $-j\delta(\omega)$. The scattered wave potential (2.2.5) may be rewritten in the useful form [Morse and Feshbach (1953), Chapter 11]

$$\Phi_s \simeq \frac{a\,A}{(\omega_o/\omega)^2 - 1 - j\delta(\omega)}\left(\frac{e^{jkr}}{r}\right) \qquad (2.2.8)$$

The BCS corresponding to (2.2.8) is given by

$$\sigma = \frac{4\pi a^2}{[1 - (\omega_o/\omega)^2]^2 + \delta^2(\omega)} \qquad (2.2.9)$$

which at resonance takes on the maximum value of $\sigma = \lambda^2/\pi$ if the only loss is due to radiation, i.e. $\delta = ka$.

For very small bubbles the resonance condition must be modified to take the effects of surface tension into account. The excess pressure due to surface tension is given by $P_{ST} = 2T/a$, where T is the surface tension. The resonance condition for an air bubble in the fish tissue is modified to

$$\omega_o \simeq \frac{1}{a}\left(\frac{3\gamma P_o \tau}{\rho}\right)^{\frac{1}{2}} \qquad (2.2.10)$$

where γ is the ratio of the specific heats of the gas, P_o is the atmospheric pressure and $\tau = 1 + (2T/aP_o)$ is a function of the bubble radius. The effective surface tension in the tissue may differ somewhat from the value in water which is 73 dynes/cm.

A general formula which also incorporates thermal conductivity correction is given by Dunn and Fry (1961). They give the corresponding total cross-section defined later in (5.1.4) as

$$Q_B = \frac{bc_1}{2} \left| \frac{\frac{3\gamma P_o}{a^2} + \omega^2 \rho_1}{\left\{ \frac{1}{4\pi a} \left[\omega^2 \rho_1 - \frac{3g\gamma P_o}{\varepsilon a^2} \right] \right\}^2 + b^2 \omega^2} \right| \qquad (2.2.11)$$

where $b = b_t + b_r + b_v$ is the total loss factor with

b_t = thermal dissipation parameter--generally negligible

b_r = radiation damping parameter = $\frac{\rho_1 \omega^2}{4\pi c_1} = \frac{\pi \rho_1 c_1}{\lambda^2}$

b_v = viscous dissipation parameter = $\eta/\pi a^3$

$g = 1 + \frac{2T}{aP_o}\left(1 - \frac{1}{3h}\right)$

$\varepsilon = [1 + d\ (1 + d)]$, with $d = \frac{3(\gamma - 1)}{2sa}$

$s = \left[\frac{\omega_o \rho_2 C_p}{2K}\right]^{\frac{1}{2}}$

K = thermal conductivity

$h = \gamma/\varepsilon$; $1 < h < \gamma$

C_p = heat capacity at constant pressure

T = surface tension

η = viscosity of the tissue medium

Comparing the dissipation parameters b_r and b_v for small bubble radii in a moderately viscous fluid, we note that the viscous loss will

become dominant as the frequency is decreased. Eq. (2.2.11) is valid for $ka \ll 1$, but is not valid for $ka > 1$ due to the appearance of higher order radiation modes. Solving (2.2.10) yields a resonant bubble radius of 3.2 μm at 1.1 MHz ($\rho = 1.05$ gm/cm^3 and $ka = 1.4 \times 10^{-2}$). Assuming viscosities in the range of $10 - 10^2$ poise for the tissue and 0.5 poise for the lipid, the viscous damping at 1.1 MHz would be much too large to give rise to any appreciable resonance scattering from bubbles suspended in these media. For a resonant gas bubble suspended in a larger fluid (water) bubble, e.g. in thawed fish, η is $O(10^{-2})$. Using (2.2.9) and (2.2.11) with $4\eta/(\rho_1 \omega a^2) \simeq 0.06$ and taking the combined damping constant as $\delta = 0.1$, the BCS of the resonant gas bubble (σ_{res}) is $2 \times 10^{-2} \lambda^2/\pi$ or 1.3×10^{-2} mm^2. The additional viscous damping thus reduces σ_{res} by a factor of 50 from the maximum value ($\eta = 0$).

The resonance Q ($=\frac{2\pi \text{ bandwidth}}{\omega_o}$) for $\delta = 0.1$ is approximately 10, which at 1.1 MHz is equivalent to a bandwidth of 110 KHz. Since the bandwidth of the incident 1.1 MHz pulse is 290 KHz, it should be possible to detect the presence of resonance scattering by the resultant narrowing of the scattered pulse spectrum.

The stability of bubbles of this size is somewhat problematical. Even if the tissues of the fish are saturated with gas, the bubbles would probably shrink fairly quickly by gas diffusion across the bubble wall due to their excess pressure. However, unlike the situation in pure water, the bubbles are surrounded by a more complex medium, and as a result some of the bubbles, e.g. those lying next to myosepta, might have longer life spans. The nature of the bubble skin and that of the surrounding medium will, of course, affect the resonance frequency.

Short Wavelength BCS Approximations

It is more difficult to establish the exact shapes of the large bubbles in situ. Although it may be an artefact, there appears to be a tendency for the air bubbles in fresh fish to form on and within the myosepta. As a result the majority of these bubbles appear ellipsoidal in shape with one axis much smaller than the other two (Fig. 2.4). Since in most cases the other two axes are equal or nearly equal, the bubbles can be approximated by oblate spheroids. In the case of the intermuscular lipid globules, however, the fiber connective tissue constraints may force the larger droplets to assume prolate spheroidal rather than oblate spheroidal shapes.

Physical optics cross-sections have been derived for the various quadric surfaces. However, in general, we will require the average BCS ($\langle\sigma\rangle$)[1] as the scatterers are randomly oriented, with the possible exception of the air bubbles. Although $\langle\sigma\rangle$ is often simpler in form than the original aspect dependent BCS, obtaining a rigorous average can be a formidable task. On the other hand, the average of the frequency independent geometrical cross-section (which constitutes the leading term of the physical optics solution when expressed in terms of an asymptotic power series) can be readily obtained with the help of the following theorem: The average geometrical cross-section of a large impenetrable, convex body with random orientation is one fourth of its surface area. A simple proof of this well-known theorem is given by Van De Hulst (1957).

---

[1]See definition in (2.2.15)

Ideally, for the geometrical BCS to provide a reasonably accurate measure of the actual BCS, the ratio D/λ (largest dimension of the body in wavelengths) should be at least three and preferably much greater. Nonetheless, if creeping waves are not dominant, the average geometrical BCS $\langle\sigma_g\rangle$ will often yield a fairly accurate estimate of the actual average value for D/λ as low as 0.3. The reason for this is that the higher order terms in the expression for the physical optics cross-section will be largely averaged out as a result of averaging over the aspect angle and the size distribution of the scatterers in the medium [Van De Hulst (1957), Chapter 11; also Kerker (1969), Chapter 7]. This averaging occurs in addition to the inherent averaging in the specular pulse return stemming from the finite pulse bandwidth.

The geometrical BCS of an ellipsoid defined by the equation $\left(\frac{x}{a}\right)^2 + \left(\frac{y}{b}\right)^2 + \left(\frac{z}{c}\right)^2 = 1$ is [Crispin and Siegel (1968)]

$$\sigma_g = \frac{\pi a^2 b^2 c^2}{[a^2\sin^2\theta\cos^2\phi + b^2\sin^2\theta\sin^2\phi + c^2\cos^2\theta]^2} \qquad (2.2.12)$$

where θ and ϕ are the coordinate angles in the standard spherical coordinate system and $a > b > c$. The oblate spheroid is defined by setting $a = b$, while for the prolate spheroid it is desirable to redefine the major axis as c (to maintain the z-axis as the symmetry axis) and set $a = b < c$.

Using the relation $\langle\sigma_g\rangle = 1/4\ S$, where S is the surface area of the convex scatterer, we obtain for the oblate spheroid

$$\langle \sigma_g \rangle = 1/2 \left[\pi a^2 + \pi ac \frac{\sin^{-1} e}{e} \right] \qquad (2.2.13)$$

where $e = (a^2 - c^2)^{1/2}/a$. [With the major axis redefined as the c-axis (2.2.13) is also applicable to the prolate spheroid.] For $e = 0$, (2.2.13) reduces to the BCS of the sphere. For $e = 1$, the case of a disc of radius a, (2.2.13) cannot be expected to hold as the theorem is inapplicable. Nevertheless, (2.2.13) does yield the correct cross-section in the limit as $\lambda \to 0$.

The BCS of the perfectly reflecting disc is given by

$$\sigma = \pi a^2 (ka)^2 \cos^2\delta \left[\frac{2J_1(u)}{u} \right]^2 \qquad (2.2.14)$$

where $u = 2ka \sin\delta$ and δ is the angle of incidence with respect to the disc normal.

The average cross-section $\langle \sigma \rangle$ is defined as

$$\langle \sigma \rangle = \frac{1}{4\pi} \int_{\Omega} \sigma(\Omega) \, d\Omega \qquad (2.2.15)$$

where Ω is the solid angle. Evaluating the integral to obtain $\langle \sigma_g \rangle$ for the disc, we find

$$\langle \sigma_g \rangle \simeq \frac{\pi a^2}{2} \left[1 - \frac{2J_1(4ka)}{4ka} \right] \qquad (2.2.16)$$

the effect of the $\cos^2\delta$ factor in (2.2.14) being negligible for large ka. In the limit as $ka \to \infty$, (2.2.16) becomes identical to (2.2.13) since $c = 0$.

2.3 Scattering from the Myosepta

The aim of this section will be to derive an estimate of the nature and magnitude of the backscatter from the myosepta. The thickness of the membranes being quite small, we will employ the Born approximation to obtain a first order approximation of the solution by superposing the fields from the two sides of the membrane. For this purpose we will utilize a physical optics solution for a rough surface of non-uniform admittance that we will derive based in part on the formulation of the rough surface problem by Beckmann and Spizzichino (1963). We will begin our analysis by considering geometrical reflection from a smooth transparent thin sheet. This will provide us with a basis for superposing the physical optics solutions.

2.3.1 Specular Reflection by a Transparent Smooth Thin Sheet

A schematic representation of reflection and transmission by a transparent smooth thin sheet is sketched in Fig. 2.6. An incident plane wave of unit amplitude will give rise to a reflected wave (R), a transmitted wave (T_1) and various higher order reflected and transmitted waves which may be simply expressed as

$$T_n = (1 - R^2)\,(-R)^{n-1}, \qquad n = 1, 2, 3... \tag{2.3.1}$$

For $|R| \ll 1$, we have from (2.3.1)

$$T_n \simeq (-1)^{n-1}\,|R|^{n-1} \tag{2.3.2}$$

Assuming a plane wave of pressure $p_1(\vec{r}) = P_o e^{j\vec{k}_i \cdot \vec{r}}$ is incident at an angle δ_i with respect to the z-axis (Fig. 2.6) on an infinite plane

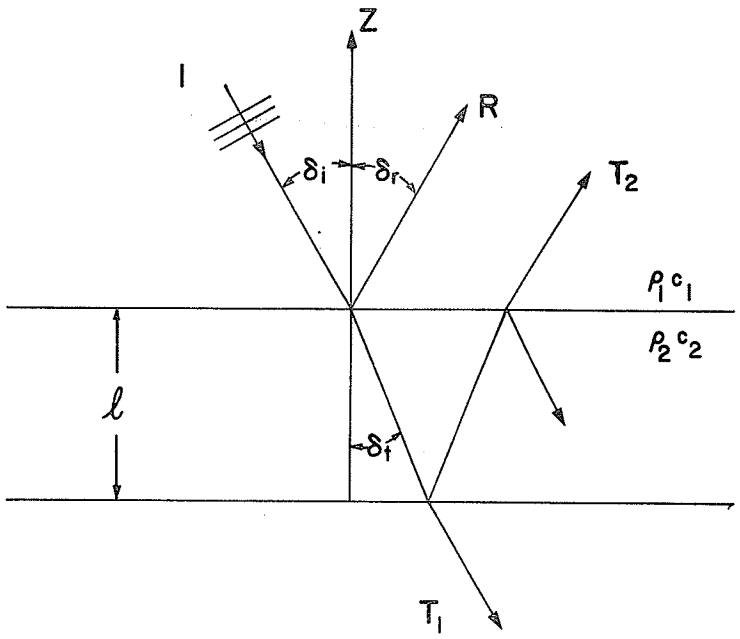

Fig. 2.6 Reflections from a thin transparent sheet.

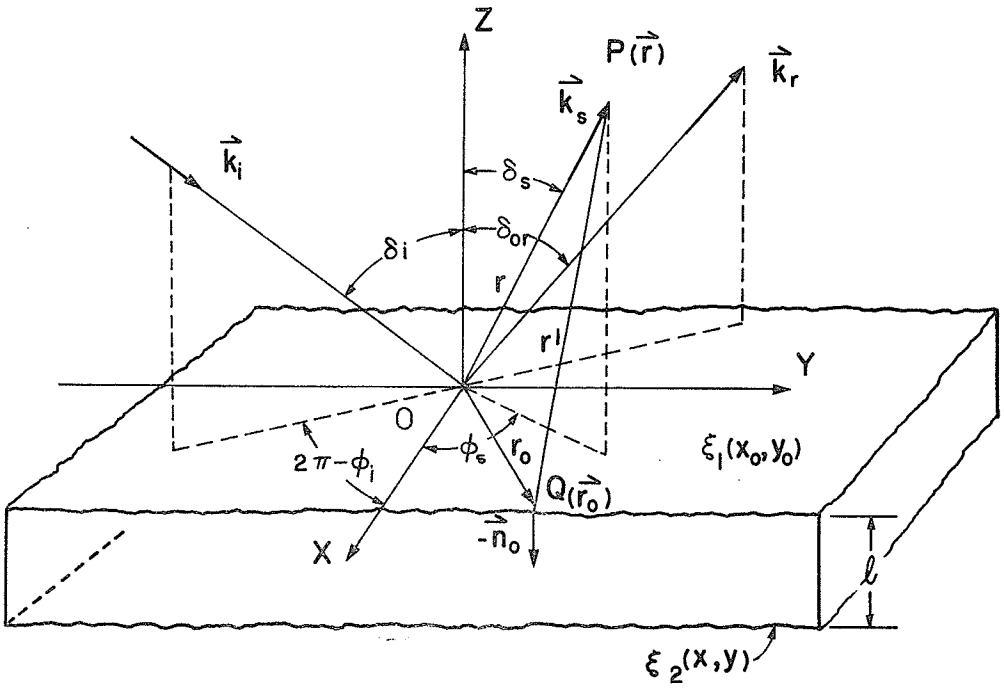

Fig. 2.7 Coordinate system for scattering from a rough thin sheet.

surface of admittance $\beta_o = \rho_1 c_1/\rho_2 c_2$, the reflection coefficient R becomes

$$R = \frac{\cos\delta_r - \beta_o \cos\delta_t}{\cos\delta_i + \beta_o \cos\delta_t} \tag{2.3.3}$$

or alternatively

$$R = \frac{\cos\delta_i - \beta_o \left[1 - (c_2/c_1)^2 \sin^2\delta_i\right]^{\frac{1}{2}}}{\cos\delta_i + \beta_o \left[1 - (c_2/c_1)^2 \sin^2\delta_i\right]^{\frac{1}{2}}} \tag{2.3.4}$$

where δ_t is the transmission angle as shown in Fig. 2.6 and where we will assume that $(c_1/c_2) > |\sin\delta_i|$. Eq. (2.3.4) is the acoustic analogue of the well-known Fresnel relations of electromagnetic theory.

For a plane sheet of average thickness ℓ the reflection coefficient R_1 from the upper surface z = 0 is given by (2.3.3). Similarly the reflection coefficient at the lower plane $z = -\ell$ is given by

$$R_2 = \frac{\beta_o \cos\delta_t - \cos\delta_i}{\beta_o \cos\delta_t + \cos\delta_i} \tag{2.3.5}$$

If we consider only the incident plane wave and the two first order reflected waves (Fig. 2.6), the field at the upper surface becomes

$$p \simeq P_o \left(1 + R_1 + R_2 e^{j2\alpha_2\ell}\right) \tag{2.3.6}$$

In essence this is equivalent to the Born approximation which is hence used indirectly. The phase Φ of the reflected wave from the lower surface relative to the incident wave is given by

$$j\Phi = j2\alpha_2\ell$$

$$= j2k_2\ell \cos\delta \qquad (2.3.7)$$

Digressing for a moment we see that

$$R_\ell \simeq R_1 + R_2 e^{j2\alpha_2\ell} = -j2 \left[\frac{1-m}{1+m}\right] (\sin\alpha_2\ell)\, e^{j\alpha_2\ell} \qquad (2.3.8)$$

where $m = \dfrac{\beta_o \cos\delta_t}{\cos\delta_i}$.

Summing the higher order reflections (transmission factors $\simeq 1$)

$$e^{j\alpha_2\ell} [1 - e^{j2\alpha_2\ell} + e^{j4\alpha_2\ell} \ldots] = \frac{1}{2\cos\alpha_2\ell} \qquad (2.3.9)$$

When the higher order terms are included the reflection coefficient for a plane (fluid) layer of thickness ℓ becomes

$$R_\ell \doteq -j \left[\frac{1-m}{1+m}\right] \tan\alpha_2\ell \qquad (2.3.10.a)$$

and for $m = 1 - \varepsilon$, $|\varepsilon| \ll 1$

$$R_\ell \simeq -j\tfrac{1}{2}\varepsilon\tan\alpha_2\ell \qquad (2.3.10.b)$$

The exact solution of the layer boundary value problem [Brekhovskikh (1960)] is

$$R = \frac{\cos\delta_i - \beta_o \cos\delta_t}{\cos\delta_i + \beta_o \cos\delta_t + j2 \cot\alpha_2\ell} \qquad (2.3.11)$$

We obtain for $m = 1 - \varepsilon$, $|\varepsilon| \ll 1$ and $\alpha_2\ell < \pi/4$

$$R_\ell \simeq -j\tfrac{1}{2}\varepsilon\tan\alpha_2\ell$$

which is the previous result in (2.3.10.a). We note that under these conditions the layer behaves like a short-circuited transmission line.

For the scattered intensity where we are interested in $|R|^2$, we obtain either from (2.3.11) or from the first order result (2.3.8)

$$|R_\ell|^2 \simeq \varepsilon^2 \sin^2\alpha_2\ell \quad , \qquad |\varepsilon| << 1 \tag{2.3.12}$$

Our simple model would thus seem to provide a satisfactory approximation for $|\varepsilon| << 1$, $(\alpha_2\ell) < \pi/4$ and $(c_1/c_2) > |\sin\delta_i|$.

2.3.2 Kirchoff Solution for a Rough Surface of Non-uniform Admittance

The Kirchoff solution for a plane wave incident on a perfectly reflecting rough surface is derived in detail by Beckmann and Spizzichino (1963). Proceeding from Beckmann's initial formulation of the problem we will generalize the analysis to include the case of finite non-uniform surface admittance.

We represent the myosepta membranes as a thin plane sheet of average normalized admittance $\beta = \rho_1 c_1/z_2$ where z_2 is the specific acoustic impedance of the myosepta. The sheet is rough on both sides and is oriented with respect to the coordinate system in the manner shown in Fig. 2.7. The actual reflecting surfaces S_1 and S_2 are described by the functions $z = \xi_1(x,y)$ and $z = \xi_2(x,y)-\ell$, where ξ_1 and ξ_2 are random variables with zero means. Initially we consider scattering only by the top surface, i.e. we let $\ell \to -\infty$.

Referring to Fig. 2.7, let us assume a monochromatic spherical wave given by

$$p_i(\vec{r},\omega) = P_o\psi(\theta)\,\frac{e^{j\vec{k}_i\cdot\vec{r}_i}}{r_i} \tag{2.3.13}$$

is incident on the surface; P_o denotes the amplitude, $\psi(\theta)$ is a far-field beam function and r_i is the distance from the source to a point Q on S.[1] The scattered field $p_s(\vec{r},\omega)$ at a point P may be obtained by evaluating the Helmholtz integral [Baker and Copson (1950)] over the surface S given for $e^{-j\omega t}$ time dependence by

$$p_s(\vec{r},\omega) = -\iint_S \left[G \frac{\partial p}{\partial n_o} - p \frac{\partial G}{\partial n_o} \right] ds \qquad (2.3.14)$$

where $p = p(\vec{r}_o,\omega)$ is the pressure at point Q on the surface, $\vec{n}_o$ is the local normal on S pointing in the positive direction and $G = G_\omega(\vec{r}|\vec{r}_o)$ is the Green's function

$$G_\omega(\vec{r}|\vec{r}_o) = \frac{e^{jkr}}{4\pi r} \qquad (2.3.15)$$

where r is the distance of the observation point P from the point Q. Assuming that $|\vec{r}_i|$ and $|\vec{r}| >> |\vec{r}_o|_{max}$, the Fraunhofer or far-field approximations may be introduced

$$p_i(\vec{r}_i,\omega) \simeq P_o\psi(\theta) \frac{e^{jkr_{io}}}{r_{io}} e^{j\vec{k}_i\cdot\vec{r}_o} \quad , \quad r_{io} >> r_o \qquad (2.3.16)$$

and

$$G_\omega(\vec{r}|\vec{r}_o) \simeq \frac{e^{jkr_{so}}}{4\pi r_{so}} e^{-j\vec{k}_s\cdot\vec{r}_o} \quad , \quad r_{so} >> r_o \qquad (2.3.17)$$

where r_{io} and r_{so} are the respective distances of the source and observation point from the origin; $\vec{k}_i$, $\vec{k}_s$ are the wave vectors of the incident and scattered waves, respectively, and $|\vec{k}_i| = |\vec{k}_s| = 2\pi/\lambda$.

---

[1] Beckmann (ibid.) assumes homogeneous plane wave incidence.

Next it is assumed that the values of p and $\partial p/\partial n_o$ at any point on the surface may be represented by the field that would be present on the tangent plane at that point, provided the local radius of curvature is not too small in comparison with the wavelength. This key assumption is usually referred to as the physical optics approximation. The boundary conditions may then be expressed as

$$p\big|_s = (1 + R)\, p_i \tag{2.3.18}$$

$$\left.\frac{\partial p}{\partial n_o}\right|_s = n_o \cdot \nabla p = p_i (1 - R)\, \vec{k}_i \cdot \vec{n}_o \tag{2.3.19}$$

where R is the reflection coefficient.

Substituting (2.3.16-19) into (2.3.14) one obtains

$$p_s(\vec{r},\omega) \simeq j \frac{p_o\, e^{jk(r_{io}+r_{so})}}{4\pi\, r_{io} r_{so}} \iint_S \psi(\vec{r}_o)\, (R\vec{\mu} - \vec{\nu}) \cdot \vec{n}_o\, e^{j\vec{\mu}\cdot\vec{r}_o}\, ds \tag{2.3.20}$$

where $\vec{r}_o = x_o \vec{a}_x + y_o \vec{a}_y + \xi(x_o,y_o)\, \vec{a}_z$ and $\vec{a}$ is the unit vector along $\vec{r}_o$; $\vec{\mu} = \vec{k}_i - \vec{k}_s$ is the recoil vector with components

$$\begin{aligned} \mu_x &= k\,(\sin\delta_i \cos\phi_i - \sin\delta_s \cos\phi_s) \\ \mu_y &= k\,(\sin\delta_i \sin\phi_i - \sin\delta_s \sin\phi_s) \\ \mu_z &= -k\,(\cos\delta_i + \cos\delta_s) \end{aligned} \tag{2.3.21}$$

and hence

$$k^2\gamma^2 = \mu_x^2 + \mu_y^2 = k^2[\sin^2\delta_i + \sin^2\delta_s - 2 \sin\delta_i \sin\delta_s \cos(\phi_s - \phi_i)] \tag{2.3.22}$$

and

$$\vec{\nu} = \vec{k}_i + \vec{k}_s \tag{2.3.23}$$

The decreasing value of $\psi(\vec{r}_o)$ away from the origin will assure convergence of the integral by effectively limiting the insonified surface area. In the limit of homogeneous plane wave incidence [$\psi(\vec{r}_o) \equiv 1$ with $(P_o r_{io}^{-1})$ remaining constant as $r_{io} \to \infty$], apart from the use of slightly different symbols, (2.3.20) becomes identical to Eq. (18a), Sec. 3.1, Beckmann and Spizzichino (1963).

Partly to sidestep the difficulties introduced by assuming plane wave incidence, Beckmann normalizes his solution with respect to the specularly reflected wave from a perfectly reflecting smooth plane of the same dimensions, for the same angle of incidence and distance. He defines the resultant quantity as the scattering coefficient ρ. Analogously, we will define an acoustic scattering coefficient Γ as

$$\Gamma = \frac{p_s(\vec{r},\omega)}{-p_r} \tag{2.3.24}$$

where p_r is the specularly reflected wave from the equivalent perfectly smooth pressure release plane.

Except for the case of a smooth surface and/or perfect reflectance, the integral (2.3.20) is difficult to evaluate in most cases because of the dependence of R on δ_i. However, if R can be rendered effectively constant, e.g. by ensemble averaging, the integration may be performed. Provided certain conditions are met (Chapters 4.4 and 5.4, ibid.) such a procedure is justified, and the resultant ensemble averaged coefficient can then be expressed as

$$\langle\Gamma\rangle_f \simeq \langle R\rangle \langle\Gamma\rangle \tag{2.3.25}$$

and the intensity scattering coefficient $\langle \Gamma\Gamma^* \rangle_f$ as

$$\langle \Gamma\Gamma^* \rangle_f \simeq \langle RR^* \rangle \langle \Gamma\Gamma^* \rangle \tag{2.3.26}$$

where $\langle R \rangle \simeq R(\delta_i)$, $\langle RR^* \rangle = |R(\delta_i)|^2$ and the subscript f denotes the finite non-zero admittance of the surface. A more rigorous treatment leading to essentially the same results is given in a paper by Kuo (1964).

The angle of incidence δ_i should be near normal if (2.3.25) and (2.3.26) are to be valid for $\beta_o \simeq O(1)$. In the case of the myosepta this condition is not met; hence, fluctuations in admittance either intrinsically or due to variations in the local angle of incidence may affect the character of the scattering. We will generalize our analysis to take this into account.

The problem of scattering by a surface of non-uniform impedance was treated theoretically by Heaps (1956), while the problem of admittance variations due to the local angle of incidence was considered by Parkins (1967). Parkins' evaluation, however, is restricted to the case of $\mu_z^2 \langle \xi^2 \rangle >> 1$. A number of essentially exact solutions have also been obtained for certain specialized surface geometries, e.g. Twersky (1950, 1951).

Although intrinsic admittance fluctuations are not likely to be encountered in the case of the myosepta, for the sake of generality we will initially assume that, in addition to roughness, the surface has a finite, non-zero, non-uniform admittance β. We will assume that the following conditions apply to the intrinsic variations in β:

i) β does not vary significantly over a distance less than a wavelength[1]

ii) $|\Delta\beta| << |\cos\delta_i + \beta|$.

Subject to these constraints the tangent plane approximation and the boundary conditions on p_i given by (2.3.18) and (2.3.19) may be retained.

Assuming that $\psi(\vec{r}_o)$ is slowly varying compared to the phase, we may move it outside the integral of (2.3.20), i.e.

$$p_s(\vec{r},\omega) \simeq j\, P_s \iint_S (R\vec{\mu} - \vec{\nu})\cdot \vec{n}_o\, e^{j\vec{\mu}\cdot\vec{r}_o}\, ds \tag{2.3.27}$$

where

$$P_s = \frac{P_o\, \psi(\delta_i,\phi_i,\theta)\, e^{jk(r_{io}+r_{so})}}{4\pi r_{io} r_{so}} \tag{2.3.28}$$

The normal $\vec{n}_o$ is given by

$$\vec{n}_o = \frac{\nabla(z-\xi)}{|\nabla(z-\xi)|} = \frac{\vec{a}_z - \left(\frac{\partial\xi}{\partial x_o}\right)\vec{a}_x - \left(\frac{\partial\xi}{\partial y_o}\right)\vec{a}_y}{\left[1 + \left(\frac{\partial\xi}{\partial x_o}\right)^2 + \left(\frac{\partial\xi}{\partial y_o}\right)^2\right]^{\frac{1}{2}}} \tag{2.3.29}$$

and hence

$$\vec{n}_o\, ds = \vec{n}'\, dA \tag{2.3.30}$$

where $\vec{n}' = \nabla(z-\xi)$ and $dA = dx_o dy_o$.

It will be convenient to express R in terms of the parameter m; from (2.3.4) we have

$$R_{i\ell} = \frac{1 - m_{i\ell}}{1 + m_{i\ell}} \tag{2.3.31}$$

---

[1] We will show that, if the correlation distance of the admittance fluctuations is much smaller than the wavelength, the resultant Rayleigh scattering will be negligible in comparison to the overall tissue volume scattering.

where

$$m_{i\ell} = \beta(\sec^2\delta_{i\ell} - (c_2/c_1)^2 \tan^2\delta_{i\ell})^{\frac{1}{2}} \tag{2.3.32}$$

R_i, m_i and δ_i are given the subscript ℓ to emphasize their local dependence. Setting $m_{i\ell} = m_i + \Delta m_{i\ell}$, we obtain after some manipulations of (2.3.31) and neglecting second order quantities

$$R_{i\ell} \simeq R_i - \frac{2\Delta m_{i\ell}}{(1 + m_i)^2} + \frac{(\Delta m_{i\ell})^2}{(1 + m_i)^2}$$

$$\simeq R_i - (1 + R_i)^2 \frac{\Delta m_{i\ell}}{2} \quad , \quad \Delta m_{i\ell} << (1 + m_i) \tag{2.3.33}$$

where $R_i = \dfrac{1 - m_i}{1 + m_i}$. By one of those fortunate coincidences, (2.3.32) turns out to have a relatively simple derivative--namely with

$\beta = \beta_o + \Delta\beta = \beta_o - (\beta_o/\rho_2\ \Delta\rho_2 + \beta_o/c_2\ \Delta c_2)$

$$\Delta m_{i\ell} = -m_i \frac{\Delta\rho_2}{\rho_2} - \left[m_i + \left(\frac{c_2}{c_1}\right)^2 \frac{\beta_o^2}{m_i} \tan^2\delta_i\right] \frac{\Delta c_2}{c_2} - \left[1 - \left(\frac{c_2}{c_1}\right)^2\right] \frac{\beta_o^2}{m_i} \frac{\sin\delta_i}{\cos^3\delta_i}\ \Delta(\delta_i)_\ell \tag{2.3.34}$$

For convenience we will assume that c_2 is constant so that the intrinsic variation in β is due solely to fluctuations of ρ_2. With this simplification (2.3.34) reduces to

$$\Delta m_{i\ell} \simeq \Delta\beta_i + \frac{q_c\beta_o^2}{m_i \cos^2\delta_i} \frac{\vec{n}'_{xy} \cdot \vec{k}_{ixy}}{(-k_{iz})} \tag{2.3.35}$$

where $\vec{n}'_{xy} = \vec{n}' - \vec{a}_z$, $\vec{k}_{ixy} = \vec{k}_i - (k_{iz}\vec{a}_z)$; $q_c = 1 - \left(\dfrac{c_2}{c_1}\right)^2$ and $\Delta\beta_i = \Delta\beta_o\ m_i/\beta_o$. Substituting (2.3.29), (2.3.30), (2.3.33) and (2.3.35) into (2.3.27) we get

$$p_s(\vec{r},\omega) = p_s^{(I)}(\vec{r},\omega) + p_s^{(II)}(\vec{r},\omega) + p_s^{(III)}(\vec{r},\omega)$$

where

$$p_s^{(I)}(\vec{r},\omega) = jP_s \iint_A (R_i\vec{\mu}-\vec{\nu})\cdot\vec{n}'\, e^{j\vec{\mu}\cdot\vec{r}_o}\, dA$$

$$p_s^{(II)}(\vec{r},\omega) = -j\tfrac{1}{2}(1+R_i)^2 P_s \iint_A [\Delta\beta_i\mu_z+\Delta\beta_i\vec{\mu}_{xy}\cdot\vec{n}'_{xy}]\, e^{j\vec{\mu}\cdot\vec{r}_o}\, dA$$

$$p_s^{(III)}(\vec{r},\omega) = -jq_c \frac{(1+R_i)^2}{2k} \frac{\beta_o^2}{m_i} \frac{P_s}{\cos^3\delta_i} \iint_A \vec{n}'_{xy}\cdot\vec{k}_{ixy}(\mu_z+\vec{\mu}_{xy}\cdot\vec{n}'_{xy})\, e^{j\vec{\mu}\cdot\vec{r}_o}\, dA \qquad (2.3.36)$$

with $\vec{\mu}_{xy} = \vec{\mu} - \mu_z\vec{a}_z$; $\vec{\nu}_{xy}$ and $\vec{r}_{oxy}$ will be similarly defined. $p_s^{(I)}(\vec{r},\omega)$ includes the specularly reflected wave and essentially corresponds to Beckmann's solution subject to the approximation of $\langle R\rangle$ by R_i.

The first term of $p_s^{(II)}(\vec{r},\omega)$ represents scattering resulting primarily from intrinsic admittance variations, although the roughness factor $e^{j\mu_z\xi}$ does appear in the integrand. If we were to set $\xi \equiv 0$, the first term becomes virtually identical to the result obtained by Heaps (1956) for the Fraunhofer approximation (Eq. 22 in his paper); the two coincide in the backscatter direction.

Unlike Heaps' solution, the first term of $p_s^{(II)}(\vec{r},\omega)$ is not reciprocal in δ_i and δ_s. Although only the complete solution as represented by (2.3.27) is required to be reciprocal, there would appear to be the same difficulty in that (2.3.27) is reciprocal only to the extent that R_i is symmetrical or constant. This shortcoming is a consequence of the tangent plane approximation. However, in the case of the myosepta where both β_o and c_2/c_1 are near unity, R_i will be relatively small and roughly constant over a significant range of δ_i. In practice, therefore, differences in the results for $\delta_s \neq \delta_i$ will be quite small.

The second term of $p_s^{(II)}(\vec{r},\omega)$ represents an interaction correction resulting from the intrinsic fluctuations in β and the roughness. The third component $p_s^{(III)}(\vec{r},\omega)$ arises from the fluctuations of the admittance due to variations in the local angle of incidence.

Coherent Scattering

We will assume that ξ and the surface autocorrelation functions $C(\vec{d})$ are Gaussian. If ξ has a variance h^2 and $\langle\xi\rangle = 0$, the first and second order characteristic functions are given by [Parzen (1960), Beckmann and Spizzichino (1963)]

$$F_1(\mu_z) = \left\langle e^{j\mu_z\xi} \right\rangle = e^{-\frac{1}{2}h^2\mu_z^2} \tag{2.3.37}$$

and

$$F_2(\mu_z, -\mu_z) = \left\langle e^{j\mu_z(\xi_1-\xi_2)} \right\rangle = e^{-h^2\mu_z^2[1-C(d)]} \tag{2.3.38}$$

where

$$C(d) = h^{-2} \left\langle \xi_1\xi_2 \right\rangle = e^{-d^2/T_\xi^2} \tag{2.3.39}$$

and $d = |\vec{d}|$ is the distance between any two points $(x_{o1}, y_{o1}; x_{o2}, y_{o2})$ on the surface.

The assumption of Gaussian surface-height distribution and autocorrelation is obviously suspect in many instances. The main justification for its use is that the resultant mathematical convenience and simplicity more than offset the loss of accuracy in the results since in most cases an exact analytical expression for the correlation function is unavailable. Of course, if the approximation is to possess

any physical validity the surface must be free of any hidden periodicities that might affect the scattered field, while the Gaussian distribution should be at least representative of the surface distribution within a unit variance of the origin.

An inherent advantage of using a Gaussian correlation function is that the surface-slope probability distribution $P(\xi')$ is also Gaussian, i.e. [Beckmann and Spizzichino (1963), Appendix D]

$$P\{\xi'\} = \frac{T_\xi}{2h\sqrt{\pi}} \exp\left[-\frac{(\xi')^2 T_\xi^2}{4h^2}\right] \tag{2.3.40}$$

Since ξ, $\partial\xi/\partial x_o$ and $\partial\xi/\partial y_o$ are uncorrelated (ξ being a stationary random process), ensemble averaging these stochastic variables and the random variable $\Delta\beta_i$ in (2.3.36) yields

$$\begin{aligned}\left\langle p_s(\vec{r},\omega)\right\rangle &= \left\langle p_s^{(I)}(\vec{r},\omega)\right\rangle + \left\langle p_s^{(II)}(\vec{r},\omega)\right\rangle + \left\langle p_s^{(III)}(\vec{r},\omega)\right\rangle \\ &\simeq \left\langle p_r(\vec{r},\omega)\right\rangle + \left\langle p_s^{(1)}(\vec{r},\omega)\right\rangle \end{aligned} \tag{2.3.41}$$

where substituting (2.3.37) and denoting $\partial\xi/\partial\alpha$ by ξ'_α with $\alpha = x_o$ or y_o

$$\begin{aligned}\left\langle p_r(\vec{r},\omega)\right\rangle &= j\left\langle e^{j\mu_z\xi}\right\rangle P_s \iint_A (R_i\mu_z - \nu_z)\, e^{j\vec{\mu}_{xy}\cdot\vec{r}_{oxy}}\, dA \\ &\simeq j\mu_z R_i\, e^{-\frac{1}{2}\mu_z^2 h^2} P_s \iint_A e^{j\vec{\mu}_{xy}\cdot\vec{r}_{oxy}}\, dA \end{aligned} \tag{2.3.42}$$

and

$$\begin{aligned}\left\langle p_s^{(1)}(\vec{r},\omega)\right\rangle &= -j\,\tfrac{1}{2}q_c(1+R_i)^2 \frac{\beta_o^2 P_s \left\langle e^{j\mu_z\xi}\right\rangle}{m_i k\cos^3\delta_i} \\ &\quad \times \left[k_{ix}\mu_x\left\langle \xi_x'^2\right\rangle + k_{iy}\mu_y\left\langle \xi_y'^2\right\rangle\right] \iint_A e^{j\vec{\mu}_{xy}\cdot\vec{r}_{oxy}}\, dA \end{aligned} \tag{2.3.43}$$

For an isotropic Gaussian surface, $\left\langle p_s^{(1)}(\vec{r},\omega)\right\rangle$ reduces to

$$\left\langle p_s^{(1)}(\vec{r},\omega)\right\rangle = \frac{jq_c(1+R_i)^2 P_s \beta_o^2 h^2 e^{-\frac{1}{2}\mu_z^2 h^2}}{m_i T_\xi^2 \cos^2\delta_i} \frac{(\vec{k}_{ixy}\cdot\vec{\mu}_{xy})}{k_{iz}} \iint_A e^{j\vec{\mu}_{xy}\cdot\vec{r}_{oxy}}\, dA$$

The integrals in (2.3.42-43) representing the well-known Fraunhofer scattering pattern will have an increasingly narrow peak centered at $\delta_s = \delta_i$ as the area of the surface is increased. $\left\langle p_r(\vec{r},\omega)\right\rangle$ thus corresponds to the specularly reflected wave. Hence, denoting the scattering coefficient for an equivalent perfectly reflecting smooth plane by Γ_o, we have the 'zero' order result

$$\left\langle \Gamma_f^{(0)}\right\rangle = R_i \left\langle e^{j\mu_z\xi}\right\rangle \Gamma_o = R_i\, e^{-\frac{1}{2}\mu_z^2 h^2}\, \Gamma_o \quad \text{(Gaussian surface)} \tag{2.3.44}$$

with

$$\Gamma_o = \operatorname{sinc}(\mu_x L)\, \operatorname{sinc}(\mu_y L)$$

which is similar to (2.3.25). $\left\langle p_s^{(1)}(\vec{r},\omega)\right\rangle$ also contributes to the coherent wave. However, since $\mu_{xy} = [0,0]$ in the specular direction, $\left\langle p_s^{(1)}(\vec{r},\omega)\right\rangle$ will be relatively small in all directions. Combining the coherent contributions, we obtain the following first order approximation of $\langle\Gamma\rangle_f$

$$\langle\Gamma\rangle_f = \left[R_i + \tfrac{1}{4}q_c \frac{\beta_o^2 (k_{ix}\mu_x \left\langle \xi_x'^2\right\rangle + k_{iy}\mu_y \left\langle \xi_y'^2\right\rangle)(1+R_i)^2}{m_i k^2 \cos^4\delta_i}\right] \left\langle e^{j\mu_z\xi}\right\rangle \Gamma_o \tag{2.3.45}$$

and for the Gaussian surface

$$\langle\Gamma\rangle_f = \left[R_i + \frac{q_c \beta_o^2 \vec{k}_{ixy}\cdot\vec{\mu}_{xy} h^2 (1+R_i)^2}{m_i k_{iz}^2 T_\xi^2 2 \cos^2\delta_i}\right] e^{-\frac{1}{2}\mu_z^2 h^2}\, \Gamma_o \tag{2.3.46}$$

The Scattered Field Intensity

The average intensity $\langle I_s \rangle$ for monochromatic plane waves may be defined as $\langle I_s \rangle = \frac{1}{2}\langle p_s p_s^* \rangle / \rho_1 c_1$ where p_s^* is the complex conjugate of p_s. Suppressing the constant $\frac{1}{2}(\rho_1 c_1)^{-1}$ and using (2.3.36)

$$\left\langle p_s p_s^* \right\rangle = \sum_{n=I}^{III} \left\langle p_s^{(n)} p_s^{(n)*} \right\rangle + \sum_{\substack{n,m=I \\ n \neq m}}^{III} \left\langle p_s^{(n)} p_s^{(m)*} \right\rangle \qquad (2.3.47)$$

In order to evaluate (2.3.47) we require the auto-covariance function for the stochastic variable $\Delta\beta_i$. We will assume a normal function--namely

$$\left\langle \Delta\beta_i(\vec{r}_{o1})\ \Delta\beta_i(\vec{r}_{o1} + \vec{d}) \right\rangle = \varepsilon_i^2\ e^{-d^2/T_\beta^2} \qquad (2.3.48)$$

where $\varepsilon_i^2 = \left\langle \Delta\beta_i^2 \right\rangle$ is the variance, $\left\langle \Delta\beta_i \right\rangle = 0$. The evaluation of (2.3.47) is then relatively straightforward for the stationary processes we have postulated.

The procedure we adopted to evaluate (2.3.36) was somewhat different from the one used by Beckmann (integration by parts, loc. cit.) in that we relied on a knowledge of the first moment of the slope distribution. However, by first integrating by parts before ensemble averaging, it would appear that explicit knowledge of the slope moments is not required for the evaluation of $\left\langle p_s^{(I)}(\vec{r},\omega) \right\rangle$. This is correct to first order, since for constant R the slopes do not affect the coherent component in the specular direction ($\mu_{xy} = 0,0$). For the diffuse scatter which is of concern mostly in directions other than the specular direction, the slope effects are still not very significant if $\mu_z^2 h^2 << 1$ and $R_i >> 0$, but they become an essential factor when $R_i \approx 0$. We then find that if we are to avoid obtaining non-physical

results the slope effects cannot be treated in the manner that neglects the so-called edge effects. To make the matter a little clearer, we will obtain the specular scattering $\langle p_r \rangle$ by means of partial integration and ensemble averaging but without neglecting the edge effects. Under these conditions we should obtain the identical result to (2.3.42). We had

$$p_s^{(I)}(\vec{r},\omega) \simeq j\, R_i\, P_s \iint_A [\mu_z - \xi'_x\mu_x - \xi'_y\mu_y]\, e^{j\vec{\mu}\cdot\vec{r}_o}\, dA \qquad (2.3.49)$$

Integrating by parts yields for an area $A = 4L^2$

$$p_s^{(I)}(\vec{r},\omega) = jR_iP_s \left\{\mu_z \int_{-L}^{L}\int e^{j\vec{\mu}\cdot\vec{r}_o}\, dx_o dy_o - \frac{2\mu_x^2 L}{\mu_z}\left(\frac{\sin\mu_x L}{\mu_x L}\right)\int_{-L}^{L} e^{j\mu_z\xi}\Big|_{x_o=-L}^{L} e^{j\mu_y y_o}\, dy_o \right.$$
$$\left. - \frac{2\mu_y^2}{\mu_z}\left(\frac{\sin\mu_y L}{\mu_y L}\right)\int_{-L}^{L} e^{j\mu_z\xi}\Big|_{x_o=-L}^{L} e^{j\mu_x x_o}\, dx_o + \frac{\mu_x^2+\mu_y^2}{\mu_z}\int_{-L}^{L}\int e^{j\vec{\mu}\cdot\vec{r}_o}\, dx_o dy_o\right\} \qquad (2.3.50)$$

Since the process is stationary and uniform, the expectation values along any line located on the surface must be the same. Therefore, ensemble averaging and completing the integrations results in

$$\left\langle p_s^{(I)}(\vec{r},\omega)\right\rangle = j\left[\frac{\mu^2-(k\gamma)^2}{\mu_z}\right] e^{-\frac{1}{2}\mu_z^2h^2}\, 4L^2(\mathrm{sinc}\mu_x L\ \mathrm{sinc}\mu_y L)\, R_iP_s$$
$$= j\,\mu_z\, e^{-\frac{1}{2}\mu_z^2h^2}\, (\mathrm{sinc}\mu_x L)(\mathrm{sinc}\mu_y L)\, 4L^2\, R_iP_s \qquad (2.3.51)$$

which is identical to (2.3.42). What is interesting is that the edge effect contribution appears to cancel the net slope-term contribution since we could have obtained the above result without resorting to ensemble averaging of the slopes simply by neglecting the slope contribution in (2.3.49) in the first place. By neglecting the line integrals in (2.3.49) the resultant solution will contain the extra contribution $(k\gamma)^2 = \mu_x^2 + \mu_y^2$.

The first and last integrals of (2.3.50) may be combined; Beckmann defines for this purpose the geometric factor L given by

$$L = -\frac{1}{2k\cos\delta_i}\,\frac{\vec{\mu}\cdot\vec{\mu}}{\mu_z} \tag{2.3.52}$$

The error in the diffusely scattered field intensity due to neglect of the edge effect is therefore proportional to

$$\frac{(\vec{\mu}\cdot\vec{\mu})^2}{\mu_z^2} - \mu_z^2 = (2k\cos\delta_i L)^2 - \mu_z^2$$

Clearly the error will be small in most applications for all angles not near grazing incidence, and will be zero in the specular direction. However, since the correction term $p_s^{(III)}(\vec{r},\omega)$ depends expressly on the slopes, it becomes essential that this dependence be carefully approximated when $R_i \approx 0$ and $\Delta\beta_i = 0$.

Although fundamentally it makes no difference which technique is used to evaluate (2.3.36) and (2.3.47), it would appear to be easiest to employ direct ensemble averaging of the slopes. To save on notation we will let $q = [1-(c_2/c_1)^2][\beta_o^2/m_i][1/\cos^2\delta_i]$ and we will also use the parameter g defined as (ibid.)

$$g = \mu_z^2 h^2 = [kh(\cos\delta_i + \cos\delta_s)]^2 \tag{2.3.53}$$

$\sqrt{g}$ is the generalized Rayleigh criterion of the surface roughness. Its physical meaning is clear when it is compared to (2.3.7).

Ensemble averaging (2.3.47), we find that interaction terms of the form

$$\iiiint \left\langle \xi_r \xi_s^i \, e^{j\mu_z(\xi_r-\xi_s)} \right\rangle \, e^{j\vec{\mu}_{xy}\cdot\vec{d}_{oxy}} \, dA_1 dA_2 \quad ,$$

$$\iiiint \left\langle \xi'_r \xi'_s \right\rangle \left\langle e^{j\mu_z(\xi_r - \xi_s)} \right\rangle \; e^{j\vec{\mu}_{xy}\cdot\vec{d}_{oxy}} \; dA_1 dA_2$$

(where r,s = 1,2, r ≠ s, and i = 0 or 2) do not contribute real power for symmetrical probability distributions of ξ and ξ'. Renumbering the terms of (2.3.47) from one to eight, we obtain for the average scattered field intensity $\left\langle I_s(\vec{r},\omega) \right\rangle$

$$\left\langle I_s(\vec{r},\omega) \right\rangle = \sum_{n=1}^{8} \left\langle I_s^{(n)}(\vec{r},\omega) \right\rangle \tag{2.3.54}$$

where

$$\left\langle I_s^{(1)} \right\rangle = |R_i P_s|^2 \; \mu_z^2 \iiiint \left\langle e^{j\mu_z(\xi_1 - \xi_2)} \right\rangle \; e^{j\phi_d} \; dA_1 dA_2$$

$$\left\langle I_s^{(2)} \right\rangle = |R_i P_s|^2 \iiiint [\mu_x^2 \left\langle \xi'_{1x}\xi'_{2x} e^{j\mu_z(\xi_1 - \xi_2)} \right\rangle + \mu_y^2 \left\langle \xi'_{1y}\xi'_{2y} e^{j\mu_z(\xi_1 - \xi_2)} \right\rangle \; e^{j\phi_d} \; dA_1 dA_2$$

$$\left\langle I_s^{(3)} \right\rangle = \tfrac{1}{4}|(1+R_i)^2 P_s|^2 \; \mu_z^2 \iiiint \left\langle (\Delta\beta_i)_1 (\Delta\beta_i)_2 \right\rangle \left\langle e^{j\mu_z(\xi_1 - \xi_2)} \right\rangle e^{j\phi_d} \; dA_1 dA_2$$

$$\left\langle I_s^{(4)} \right\rangle = \tfrac{1}{4}|(1+R_i)^2 P_s|^2 \iiiint \left\langle (\Delta\beta_i)_1 (\Delta\beta_i)_2 \right\rangle [\mu_x^2 \left\langle \xi'_{1x}\xi'_{2x} \; e^{j\mu_z(\xi_1 - \xi_2)} \right\rangle + \mu_y^2 \left\langle \xi'_{1y}\xi'_{2y} \; e^{j\mu_z(\xi_1 - \xi_2)} \right\rangle] \; e^{j\phi_d} \; dA_1 dA_2$$

$$\left\langle I_s^{(5)} \right\rangle = \frac{q^2 |(1+R_i)^2 P_s|^2 \mu_z^2}{4k^2 \cos^2\delta_i} \iiiint \left\langle [k_{ix}^2 \xi'_{1x}\xi'_{2x} + k_{iy}^2 \xi'_{1y}\xi'_{2y}] \; e^{j\mu_z(\xi_1 - \xi_2)} \right\rangle \; e^{j\phi_d} \; dA_1 dA_2$$

$$\left\langle I_s^{(6)} \right\rangle = \frac{q^2 |(1+R_i)^2 P_s|^2}{4k^2 \cos^2\delta_i} \iiiint \Big\langle [k_{ix}^2 \mu_x^2 \xi_{1x}^2 \xi_{2x}^2 + k_{iy} k_{ix} \mu_x \mu_y \xi'^2_{1y} \xi'^2_{2x} + (k_{iy}\mu_x + k_{ix}\mu_y)^2 \xi'_{1x}\xi'_{2x}\xi'_{1y}\xi'_{2y} + k_{iy} k_{ix} \mu_x \mu_y \xi'^2_{1x} \xi'^2_{2y} + k_{iy}^2 \mu_y^2 \xi'^2_{1y} \xi'^2_{2y}] \; e^{j\mu_z(\xi_1 - \xi_2)} \Big\rangle \; e^{j\phi_d} \; dA_1 dA_2$$

$$\left\langle I_s^{(7)} \right\rangle = \frac{\mu_z q |R_i(1+R_i)^2||P_s|^2}{k \cos\delta_i} \iiiint \left\langle (k_{ix}\mu_x \xi'_{1x}\xi'_{2x} + k_{iy}\mu_y \xi'_{1y}\xi'_{2y}) \cos\mu_z(\xi_1-\xi_2) \right\rangle e^{j\phi_d}\, dA_1 dA_2$$

$$\left\langle I_s^{(8)} \right\rangle = \frac{\mu_z q |R_i(1+R_i)^2||P_s|^2}{k \cos\delta_i} \iiiint \left\langle (k_{ix}\mu_x \xi_x'^2 + k_{iy}\mu_y \xi_y'^2) \cos\mu_z(\xi_1-\xi_2) \right\rangle e^{j\phi_d}\, dA_1 dA_2$$

By using the following relation derived by interchanging the order of differentiation and ensemble averaging[1]

$$\left\langle \xi'_{i\alpha}\xi'_{j\beta}\, e^{-j\mu_z(\xi_1-\xi_2)} \right\rangle = h^2 \left[\frac{\partial^2 C}{\partial_i\alpha \partial_j\beta} + g \frac{\partial C}{\partial_i\alpha} \frac{\partial C}{\partial_j\beta} \right] e^{-g(1-C)} \quad (2.3.55)$$

where $i,j = 1,2$, and $\alpha,\beta = x,y$, we obtain

$$\left\langle \xi'_{1\alpha}\xi'_{2\beta}\, e^{j\mu_z(\xi_1-\xi_2)} \right\rangle = \frac{2h^2}{T_\xi^2} e^{-d^2/T_\xi^2} e^{-g(1-C)} \left[1 - \frac{2(\alpha_1-\alpha_2)}{T_\xi^2}(1 + ge^{-d^2/T_\xi^2} \right]$$

$$\simeq \frac{2h^2}{T_\xi^2} e^{-d^2/T_\xi^2} e^{-g(1-C)} \quad (2.3.56)$$

The contribution of the second term will be small in comparison to the first term [when e^{-d^2/T_ξ^2} is large, $(\alpha_1-\alpha_2)^2/T_\xi^2$ is small and vice versa].

For $g \ll 1$, we approximate e^{gC} by $1 + gC$. The evaluation of the resultant integrals can then be further expedited if it is assumed that the surface area diameters are much greater than the largest correlation distance for any of the stochastic variables. For a circular

---

[1] This is permissible since the postulated Gaussian process is stationary, see Parkins (1967).

area $A = \pi a^2$ we obtain with the help of the Fourier-Bessel transform relation

$$1/2\pi A \iiiint_A e^{-md^2/T^2}\, e^{j\phi_d}\, dA_1 dA_2 = \int_0^a J_o(k\gamma u)\, e^{-mu^2/T^2}\, udu$$

$$\text{(Limit)}\ a \to \infty = (T^2/2m)\, e^{-(k\gamma T)^2/4m} \qquad (2.3.57)$$

and (2.3.56)

$$\langle I_s^{(1)} \rangle \simeq \langle p_r \rangle \langle p_r \rangle^* + |R_i P_s|^2\, \pi a^2 \pi g \mu_z^2 T_\xi^2\, e^{-g-(\frac{1}{2}k\gamma T_\xi)^2} \qquad (2.3.58.a)$$

and

$$\langle I_s^{(2)} \rangle \simeq |R_i P_s|^2\, \pi a^2 2\pi k^2 \gamma^2 h^2\, [1 + \tfrac{1}{2} g\, e^{-(\frac{1}{2}k\gamma T_\xi)^2}]\, e^{-g-(\frac{1}{2}k\gamma T_\xi)^2} \qquad (2.3.58.b)$$

Except for μ_z^2 replacing $(2k \cos\delta_i)^2 L^2 = (\vec{\mu}\cdot\vec{\mu}/\mu_z)^2$, $\langle I_s^{(1)} \rangle$ is identical to Beckmann's result.

Similarly, after substituting (2.3.48) into (2.3.54) we obtain

$$\langle I_s^{(3)} \rangle \simeq \tfrac{1}{4} |(1+R_i)^2 P_s|^2\, \varepsilon_i^2 (\pi a)^2\, \mu_z^2\, e^{-g}\, [T_\beta^2\, e^{-(\frac{1}{2}k\gamma T_\beta)^2} + g T_c^2\, e^{-(\frac{1}{2}k\gamma T_c)^2}] \qquad (2.3.59.a)$$

and

$$\langle I_s^{(4)} \rangle \simeq |(1+R_i)^2 P_s|^2\, \varepsilon_i^2 (\pi a)^2 (k\gamma)^2\, 2h^2/T_\xi^2\, [T_\beta^2\, e^{-(\frac{1}{2}k\gamma T_\beta)^2} + g T_c^2\, e^{-(\frac{1}{2}k\gamma T_c)^2}] \qquad (2.3.59.b)$$

where $T_c^{-2} = T_\beta^{-2} + T_\xi^{-2}$. As in the case of $\langle I_s^{(2)} \rangle$, $\langle I_s^{(4)} \rangle$ which is proportional to the slope variance may be neglected. We note that the leading terms vary as λ^{-2} for $(k\gamma T_\beta) \ll 1$.

For $I_s^{(5)}$ we obtain

$$\langle I_s^{(5)} \rangle \simeq \tfrac{1}{4} |(1+R_i)^2 P_s|^2 (\pi a)^2 2q^2 g\, \frac{(\vec{k}_{ixy}\cdot\vec{k}_{ixy})}{(k_{iz})^2}\, [1 + e^{-(\frac{1}{2}k\gamma T_\xi)^2}]\, e^{-g-(\frac{1}{2}k\gamma T_\xi)^2} \qquad (2.3.60)$$

which vanishes as $h^2 \to 0$. Had we used the partial integration and the approximation discussed earlier, we would have obtained

$$\left\langle I_s^{(5)} \right\rangle_b \simeq \tfrac{1}{4} \left| (1+R_i)^2 P_s \right|^2 \frac{(\vec{k}_{ixy} \cdot \vec{\mu}_{xy})^2}{(k_{iz})^2} q^2 (\pi a)^2 \left[a^2 \Gamma_o^2 + g T_\xi^2 \, e^{-(\frac{1}{2} k\gamma T_\xi)^2} \right] e^{-g}$$

which would seem to be incorrect since the leading term does not vanish as $h \to 0$.

The evaluation of $\left\langle I_s^{(6)} \right\rangle$ is more involved and requires the fourth order moments. Alternatively, one can derive additional relations of the type (2.3.55-56). However, as $\left\langle I_s^{(6)} \right\rangle$ has a maximum possible magnitude of $4 \left\langle p_s^{(1)}(\vec{r},\omega) \right\rangle^2$ [see (2.3.43-44)], its contribution will be negligible for $g \ll 1$.

Finally, combining the interaction terms $\left\langle I_s^{(7)} \right\rangle$ and $\left\langle I_s^{(8)} \right\rangle$ we get for $g \ll 1$

$$\left\langle I_s^{(7)} \right\rangle + \left\langle I_s^{(8)} \right\rangle \simeq \left| R_i (1+R_i)^2 \right| \left| P_s \right|^2 (\pi a)^2 \, q \mu_z \frac{(\vec{k}_{ixy} \cdot \vec{\mu}_{xy})}{(-k_{iz})} \, 2h^2/T_\xi^2 \, e^{-g}$$

$$\times \left[a^2 \Gamma_o^2 + T_\xi^2 (1+g) \, e^{-(\frac{1}{2} k\gamma T_\xi)^2} + \tfrac{1}{2} T_\xi^2 \, g \, e^{-(k\gamma T_\xi)^2/8} \right] \qquad (2.3.61)$$

where $\Gamma_o = 2(k\gamma a)^{-1} J_1(k\gamma a)$. Since $\vec{\mu}_{xy} = [0,0]$ in the specular direction, the first term will be small everywhere, and as a result the second term is likely to be more significant. We note that both $\left\langle I_s^{(5)} \right\rangle$ and $\left(\left\langle I_s^{(7)} \right\rangle + \left\langle I_s^{(8)} \right\rangle \right)$ exhibit a λ^{-2} dependence for $k\gamma T_\xi \ll 1$ similar to $\left\langle I_s^{(3)} \right\rangle$ and $\left\langle I_s^{(4)} \right\rangle$. This seems to be characteristic of surface admittance variations in the long wavelength approximation.

This completes the evaluation of (2.3.54) for $g \ll 1$. As g becomes larger it will be necessary to retain an increasing number of

higher order terms, while for g >> 1, the integrals of (2.3.54) may be evaluated asymptotically.

Beckmann (loc. cit.) evaluates the integral

$$\int_0^\infty J_0(k\gamma u)\ e^{-g(1-C)}\ u\,du$$

by taking $[e^{-g(1-C)}]$ as the fast varying function with the stationary point at u = 0 and $|C''(0)| = 2/T^2$ where C''(0) is the second derivative of C(u) evaluated at the origin. This results in an intensity scattering coefficient $\langle \Gamma\Gamma^* \rangle_f$ corresponding to $\langle I_s^{(1)} \rangle$ given by

$$\langle \Gamma\Gamma^* \rangle_f \simeq R_i R_i^* (\pi L^2/A)\ [(T_\xi^2/g) e^{-k^2\gamma^2 T^2/4g}] \qquad (2.3.62)$$

where now the expression in the square brackets of (2.3.62) becomes the slope distribution (2.3.40) in the geometric optics limit, i.e.

$$P(s) = (1/2\pi\Delta^2) e^{-s^2/2\Delta^2} = (\mu_z^2/4\pi)(T^2/g) e^{-k^2\gamma^2 T^2/4g}$$

where $\Delta^2 = h^2|C''(0)|$, and $s^2 = (\mu_x^2+\mu_y^2)/\mu_z^2$. [A more general proof for arbitrary slope distributions was given recently by Barrick (1968)]. Thus, with $|\mu_z|$ replacing $(2k \cos\delta_i)L$, we have for g >> 1

$$\langle I_s^{(1)} \rangle \simeq |R_i P_s|^2 (\pi a)^2 \mu_z^2 T_\xi^2 g^{-1} e^{-(k\gamma T_\xi)^2/4g} \qquad (2.3.63)$$

The remaining integrals may be evaluated in the same manner.

A number of comparisons of Beckmann's theory with experimental backscatter data from surfaces with known approximate Gaussian surface-height distributions and Gaussian correlation functions has revealed significant discrepancies under certain conditions. The nature of these discrepancies and shortcomings of the theory have been extensively

discussed in the literature and various modifications and improvements have been suggested, e.g. Clay and Medwin (1964); Horton et al. (1967); Fung and Leovaris (1969); and Melton and Horton (1970).

Fung and Leovaris (1969), noting that (2.3.62) only fitted data from surfaces with gentle slopes, observed that Backmann's asymptotic evaluation had neglected the effect of the weighting factor u in the integrand. By expanding C(u) about the correct stationary point u_o and setting

$$C(u_o) + |C'(u_o)|u_o \simeq 1 \quad , \quad g >> 1 \tag{2.3.64}$$

where the prime indicates the derivative, and using the equation

$$\int_o^\infty J_o(k\gamma u)\ e^{-mu/T}\ udu = \frac{T^2}{m^2[1+(k\gamma T/m)^2]^{3/2}} \tag{2.3.65}$$

they obtained

$$\langle \Gamma\Gamma^* \rangle \simeq \frac{2\pi L^2}{A} \int_o^\infty J_o(k\gamma u)\ e^{-gC'(u_o)u}\ udu$$

$$\simeq \frac{2\pi L^2}{A} \frac{gC'(u_o)}{[(gC'(u_o))^2 + (k\gamma)^2]^{3/2}}$$

$$\simeq \left(\frac{2\pi L^2}{A}\right) \left(\frac{\cos^2\theta}{2k^2}\right) \frac{B}{[\cos^4\theta + B\sin^2\theta]^{3/2}} \tag{2.3.66}$$

where $B = [2kh^2C'(u_o)]^{-2}$. As $u_o \to 0$, Eq. (2.3.66) $\to$ (2.3.62). As Fung and Leovaris point out in their paper, this result has the advantage of incorporating the true correlation function and appears to yield significantly better agreement at both low and high grazing angles. At the same time it may explain why workers had obtained consistently better agreement with the Kirchoff theory using an empirical exponential correlation for surfaces that were Gaussian with Gaussian correlation functions.

We shall now limit our discussion to the problem at hand and set $\Delta\beta_i = 0$ as intrinsic admittance variations do not appear to be significant in the case of the myosepta. This eliminates $\langle I_s^{(3)} \rangle$ and $\langle I_s^{(4)} \rangle$ leaving in most cases $\langle I_s^{(1)} \rangle$ as the dominant term for $g << 1$ and $R_i \neq 0$.

2.3.3 First Order Scattering from a Rough Thin Sheet

The orientation of the rough sheet with respect to the coordinate system was given in Fig. 2.7. We will assume that reflection coefficients of the upper and lower surfaces are both small, i.e. $|R_i| < 0.3$, and that the sheet's average thickness ℓ is a fraction of a wavelength. On the basis of (2.3.8), the layer scattering coefficient may then be approximated to first order by

$$\Gamma_{f\ layer} \simeq \Gamma_{f1} + \Gamma_{f2}\, e^{j2\alpha_2 \ell} \tag{2.3.67}$$

We will represent the scattering coefficient for a particular member of the ensemble of surfaces under consideration as

$$\Gamma_f = \langle \Gamma \rangle_f + \Delta\Gamma_f \tag{2.3.68}$$

where $\Delta\Gamma_f$ is the fluctuating part having a zero mean.

We can obtain a very good insight into the layer scattering characteristics simply by considering the degree of correlation of the scattered waves from the upper and lower surfaces expressed in terms of the scattering coefficients. The advantage is that we need not specify the actual surface probability distributions.

Using (2.3.68) and (2.3.67) the ensemble averaged intensity scattering coefficient becomes

$$\langle \Gamma\Gamma^* \rangle_{f\ layer} = \langle \Gamma \rangle_{f1} \langle \Gamma \rangle_{f1}^* + \langle \Gamma \rangle_{f2} \langle \Gamma \rangle_{f2}^* + \langle \Delta\Gamma_{f1} \Delta\Gamma_{f1}^* \rangle + \langle \Delta\Gamma_{f2} \Delta\Gamma_{f2}^* \rangle$$
$$+ \left(\langle \Gamma \rangle_{f1} \langle \Gamma \rangle_{f2}^* + \langle \Delta\Gamma_{f1} \Delta\Gamma_{f2} \rangle^* \right) e^{-j2\alpha_2 \ell}$$
$$+ \left(\langle \Gamma \rangle_{f1}^* \langle \Gamma \rangle_{f2} + \langle \Delta\Gamma_{f1}^* \Delta\Gamma_{f2} \rangle \right) e^{j2\alpha_2 \ell} \qquad (2.3.69)$$

where we neglect the interaction of the lower surface roughness with the upper surface roughness on the specular power since it is a second order effect. Otherwise (2.3.69) is quite general and includes the case of a lossy layer ($\alpha_2 = \alpha_2' - j\alpha_2''$), different roughnesses of the two sides and different reflection coefficients.

In the case of the myosepta, $\alpha_2'' \ell$ will be negligible. For the simplest case of $\lambda_1 \approx \lambda_2$ (within the layer), $R_{i1} = -R_{i2}$, and symmetrical probability distributions of ξ_1 and ξ_2 with $g_1 = g_2$, and $T_{\xi 1} = T_{\xi 2}$ we have

$$\langle \Gamma \rangle_{f1} = -\langle \Gamma \rangle_{f2} \qquad (2.3.70)$$

$$\langle \Delta\Gamma_{fi} \Delta\Gamma_{fj}^* \rangle = \langle \Delta\Gamma_{fj} \Delta\Gamma_{fi}^* \rangle \qquad (2.3.71)$$

where $i,j = 1,2$ and

$$\langle \Delta\Gamma_{fi} \Delta\Gamma_{fj} \rangle = \mathcal{T} \langle \Delta\Gamma_{fi} \Delta\Gamma_{fi}^* \rangle^{\frac{1}{2}} \langle \Delta\Gamma_{fj} \Delta\Gamma_{fj} \rangle^{\frac{1}{2}} \quad , i \neq j \qquad (2.3.72)$$

$\mathcal{T}$ is the cross-correlation coefficient of the ensemble of surface reflectivities for the upper and lower surfaces of the layer. Substituting (2.3.70-72) into (2.3.69), (2.3.69) becomes

$$\langle \Gamma\Gamma^* \rangle_{f\ layer} = 4 \sin^2 \alpha_2 \ell \left(\langle \Gamma \rangle_f \langle \Gamma \rangle_f^* + \langle \Delta\Gamma_f \Delta\Gamma_f^* \rangle \right)$$
$$+ 2(1-\mathcal{T})(1-2 \sin^2 \alpha_2 \ell) \langle \Delta\Gamma_f \Delta\Gamma_f^* \rangle \qquad (2.3.73)$$

where in view of (2.3.71) we have dropped the subscripts 1 and 2.

The principal result we observe is that the specular term $4\sin^2\alpha_2 \ell \langle\Gamma\rangle_f \langle\Gamma\rangle_f^*$ is unaffected by the values of τ; only the diffuse scattering is affected. Before considering the effect of different values of τ on $\langle\Delta\Gamma\Delta\Gamma^*\rangle_{layer}$, however, we will examine how τ is related to the actual statistical parameters of the surfaces.

The individual terms of (2.3.69) are evaluated as in the previous section, i.e. $\langle\Gamma_{f1}\Gamma_{f1}^*\rangle$ and $\langle\Gamma_{f2}\Gamma_{f2}^*\rangle$ are integrated over S1 and S2, respectively. For the interaction terms the integrations are performed over both S1 and S2; we will illustrate this for the special case of identical Gaussian surface statistics for S1 and S2.

Referring to (2.3.36), (2.3.54) and (2.3.58.a), we have

$$\langle p_{s1}^I p_{s2}^{I*}\rangle = -|R_i|^2|P_s|^2 \mu_{z1}\mu_{z2} \left\langle \iint_{A1} e^{j\vec{\mu}\cdot\vec{r}_{o1}}\, dA_1 \iint e^{j\vec{\mu}\cdot\vec{r}_{o2}}\, dA_2 \right\rangle$$

and with $\mu_z = \mu_{z1} = \mu_{z2}$

$$\langle \Delta\Gamma_{f1}\Delta\Gamma_{f2}^*\rangle = -|R_i|^2 \mu_z^2 \iint_{A1}\iint_{A2} \left\langle e^{j\mu_z(\xi_1-\xi_2)} \right\rangle e^{j\vec{\mu}_{xy}\cdot\vec{d}}\, dA_1 dA_2 - \langle\Gamma_{f1}\rangle \langle\Gamma_{f2}\rangle^*$$

(Although it is a convenient way of analyzing the problem, it is not essential to split Γ_f into steady and fluctuating parts.) We define the cross-correlation at d = 0 by

$$\langle \xi_1\xi_2\rangle_{d=0} = \langle\xi_1^2\rangle^{\frac{1}{2}} \langle\xi_2^2\rangle^{\frac{1}{2}} K_{cc}$$

where $|K_{cc}| \leq 1$. Since the statistical parameters of the two surfaces including the autocorrelation functions (2.3.48) are the same, we have

$$\left\langle \xi_1(\vec{r}_{oxy})\ \xi_2(\vec{r}_{oxy}+\vec{d})\right\rangle \ = \ h^2\ K_{cc}\ C(d)$$

Retaining only the first two terms of the series for $e^{gK_{cc}C(u)} \equiv e^{KgC}$

$$\left\langle \Delta\Gamma_{f1}\Delta\Gamma^*_{f2}\right\rangle \ = -2\pi(\pi a^2)\,|R_i|^2\mu_z^2\int_o^a e^{-g(1-K_{cc}C(u))}\,J_o(k\gamma u)\,u\,du \ + \ |R_i|^2\langle\Gamma\rangle\langle\Gamma\rangle^*$$

Comparing the above result with (2.3.72) shows that for $K_{cc} \geq 0$, $K_{cc} \equiv T$. For $-1 \leq K_{cc} < 0$ the above result appears to be approximate in that we are considering only the first order term m = 1 of the diffuse scatter. The coefficients of the higher order terms of the e^{KgC} series alternate between $\cos^2(\alpha_2\ell)$ for m odd, and $\sin^2(\alpha_2\ell)$ for m even.

Three interesting cases, illustrated in Fig. 2.8, correspond to T = +1, 0 and -1. If the two surfaces are perfectly positively correlated, i.e. $\xi_1(\vec{r}_{oxy}) = \xi_2(\vec{r}_{oxy})$, then

$$\left\langle|\Gamma|^2\right\rangle_{f\ layer} \ = \ 4\ \sin^2(\alpha_2\ell)\ \left[\left|\left\langle\Gamma\right\rangle_f\right|^2 + \ \left\langle|\Delta\Gamma|_f^2\right\rangle\right] \ , \quad T = 1 \tag{2.3.74}$$

This result is the same as would have been obtained by multiplying the scattered field intensity from the single surface S1 by the effective reflection coefficient of the membrane (2.3.11). If the two surfaces are entirely uncorrelated, then

$$\left\langle|\Gamma|^2\right\rangle_{f\ layer} \ = \ 4\ \sin^2(\alpha_2\ell)\ \left|\langle\Gamma\rangle_f\right|^2 + 2\left\langle|\Delta\Gamma|_f^2\right\rangle \ , \quad T = 0 \tag{2.3.75}$$

Finally, for the case of perfect negative correlation $\xi_1(\vec{r}_{oxy}) = -\xi_2(\vec{r}_{oxy})$, we have from (2.3.58.a)

$$\left\langle|\Gamma|^2\right\rangle_{f\ layer} = 4\ \sin^2(\alpha_2\ell)\left|\langle\Gamma\rangle_f\right|^2 + 4\ \cos^2(\alpha_2\ell)\left\langle|\Delta\Gamma|_f^2\right\rangle \ , \quad T = -1 \tag{2.3.76}$$

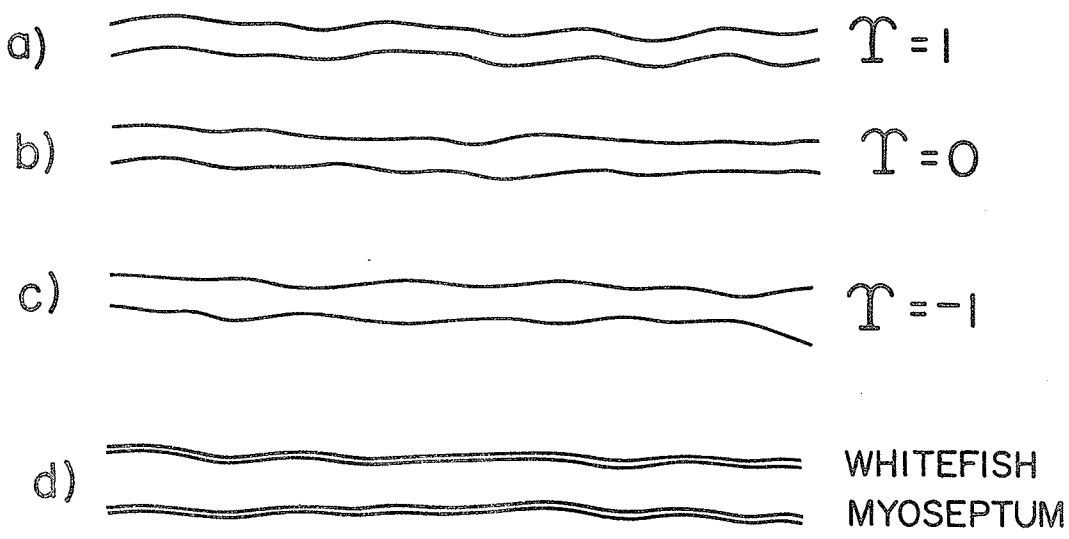

Fig. 2.8 Examples of thin rough layer cross-sections
(a) surfaces correlated, T = 1
(b) surfaces uncorrelated, T = 0
(c) surfaces negatively correlated, T = -1
(d) composite surface myoseptum model.

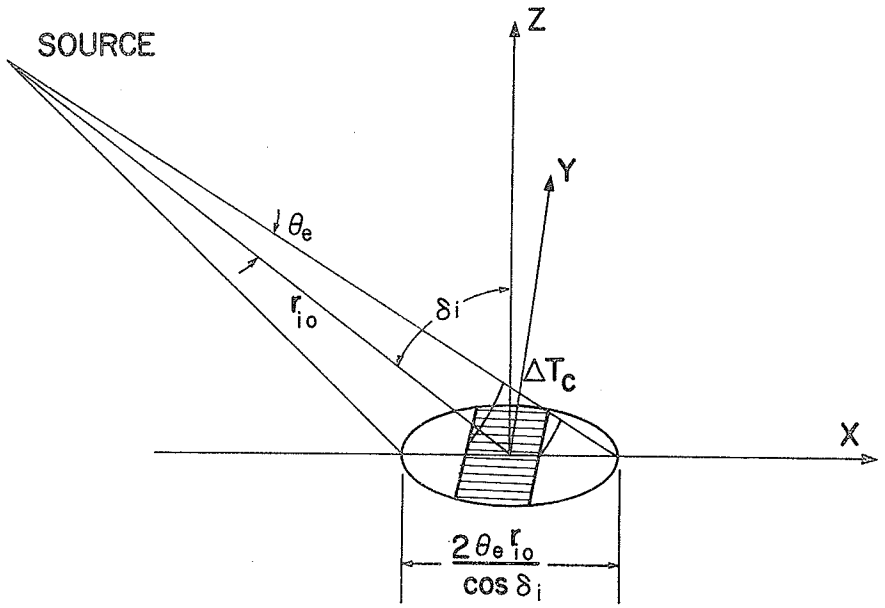

Fig. 2.9 Geometry of a pulsed beam incident on a planar surface.

The diffuse scattering term m = 1 in (2.3.58.a) vanishes in those directions where

$$\alpha_2 \ell = 2\pi\ell/\lambda\ (\cos\delta_i + \cos\delta_s) = \tfrac{1}{2}(4n + 1)\pi \quad , \quad n = 0,1,2...$$

This does not mean, however, that there is no scattering, only that the scattering is greatly reduced in these directions.

Comparing (2.3.74-76), the specular terms are seen to be unchanged while the diffuse scattering terms have different coefficients. For thin layers ($\alpha_2 \ell << \pi/2$), the diffusely scattered intensity is increased by a factor of $(2 \sin^2 \alpha_2 \ell)^{-1}$ as Υ decreases from +1 to 0.

Interestingly, for $\Upsilon = 0$ the angular pattern of the diffusely scattered intensity, apart from a factor of two, is indistinguishable from that of a single surface with the same surface characteristics. If the lower surface of the layer were to be plane, the equivalence of the diffuse scattering would be complete. This finding is confirmed by recent experimental results obtained by Leovaris and Fung (1973) working with thin layers of the type above.

The case of $\Upsilon = -1$ is perhaps a little unrealistic in practice. However, if higher order terms of the series for e^{KgC} can be neglected and $\cos\alpha_2 \ell \simeq 1$, the diffusely scattered power will be doubled compared to the uncorrelated layer and this would seem to be in accord with the physical picture of the surface in Fig. 2.8(c).

Based on our histological examinations, the whitefish myosepta membranes in situ appear to have a sandwich structure of the type shown in Fig. 2.8(d). The outer layers consist primarily of adipose tissue while the inner layer is composed mostly of much tougher connective tissue.

The extension of (2.3.67) and (2.3.69) to additional layer interfaces is clear. The only difference is that the scattered waves (subject to the Born approximation) from a particular interface must now be delayed by the total delay incurred in passing through the various layers. [The problem of n planar layers is considered in many texts, e.g. Schoch (1950); Brekhovskikh (1960).]

Effects of Curvature

In the region that is insonified the myosepta have only a slight curvature over the beam diameter, see Figs. 2.2 and 4.2. (The beams were actually incident at a somewhat lower level than is indicated in Fig. 4.2.) It can be shown that for the specular (coherent) scattering coefficient the effects of this curvature may be approximated by multiplying $\langle \Gamma \rangle$ by a divergence factor derived from geometrical optics considerations, see Chapter 11 of Beckmann and Spizzichino (1963).

In comparison to the effects of curvature on the coherent scattering, its effects on the diffuse scatter are much less significant. Qualitatively, we can see that the two main effects are a very slight reduction in the effective correlation length (thereby broadening the angular distribution of the scattering) and a small increase in the range of the angle of incidence. Since the beamwidths used in the measurements are relatively small compared to the curvature, it would appear that the effects of curvature on the backscatter from an individual myoseptum can be neglected, and only the change in the average angle of incidence for the myosepta lying at different tissue depths need be taken into account.

2.4 Effects of Beamwidth and Pulses on Rough Surface Scattering

The effect of beamwidth was touched on in the previous section. In essence, if the beam does not vary appreciably over a distance equal to several times the correlation lengths of the various stochastic processes, the beam function may be moved outside the Helmholtz integral, see (2.3.20). Hence, under these conditions the effects on $\langle\Gamma\rangle$ and $\langle|\Gamma|^2\rangle$ are negligible and the beam only limits the extent of the surface insonified all of which lies in the first Fresnel zone as is implied by the far-field approximation.

With the exception of a few measurements at 7 MHz, the beamwidths used in the measurements are considerably greater than the T_ξ's of the myosepta.

2.4.1 Review of the Effect of Narrow Beamwidth

The effect of a narrow Gaussian beamwidth was considered by Horton and Muir (1967) using Eckart's theory (1953) for the case of low-frequency scattering. The same approach may be employed to illustrate the effect of beamwidth in Beckmann's theory.

We will assume that the incident beam amplitude variation on the surface is given by

$$\psi(\vec{r}_o) = \exp\left[-\frac{|r_{oxy}|^2}{r_{io}^2\,\theta_e^2}\left[1 - \sin^2\delta_i\cos^2(\phi-\phi_i)\right]\right] \qquad (2.4.1)$$

where the equivalent beamwidth is defined as $2r_{io}\theta_e$ and r_{io} is the distance of the source from the origin. Using Horton and Muir's approach, it is convenient to rotate the coordinate system into azimuthal alignment with the incident beam and rewrite (2.4.1) as

$$\psi(x_o,y_o,\omega) = \exp\left[-\frac{x_o^2}{a^2} - \frac{y_o^2}{b^2}\right] \tag{2.4.2}$$

where $a = r_{io}\theta_e/\cos\delta_i$ and $b = r_{io}\theta_e$. Substituting (2.4.2) into (2.3.20) we can show that

$$\left\langle p_s^{(I)}(\vec{r},\omega)\right\rangle_{fb} \simeq j\mu_z R_i P_{io}\, e^{jk(r_{io}+r_{so})}(\pi ab)\exp\left[-\frac{\mu_x^2a^2}{4} - \frac{\mu_y^2b^2}{4} - \frac{g}{2}\right] \tag{2.4.3}$$

where $P_{io} = P_o/4\pi r_{io}r_{so}$. Comparing (2.4.3) with the homogeneous plane wave result (2.3.42), the factor $\exp\left[-(\tfrac{1}{2}\mu_x a)^2 - (\tfrac{1}{2}\mu_y b)^2\right]$ is seen to take the place of the Fraunhofer pattern coefficient Γ_o. Hence, it follows that

$$\langle\Gamma\rangle_{fb} = R_i \exp\left[-\frac{\mu_x^2a^2}{4} - \frac{\mu_y^2b^2}{4} - \frac{g}{2}\right]$$

The derivation of the scattered field intensity is slightly more complex. Expressing the surface height correlation function in rectangular coordinates as

$$C(\zeta,\eta) = \exp\left[-\tfrac{1}{2}\left(\frac{\zeta^2}{T_x^2} + \frac{\eta^2}{T_y^2}\right)\right] \tag{2.4.4}$$

we can show that for $g \ll 1$

$$\left\langle I_s^{(1)}\right\rangle_{fb} \simeq \left\langle p_s^{(I)}\right\rangle_{fb}\left\langle p_s^{(I)}\right\rangle^*_{fb} + |R_i|^2 I_{io}A\mu_z^2 g\pi mn \exp\left[-\frac{\mu_x^2m^2}{2} - \frac{\mu_y^2n^2}{2} - g\right] \tag{2.4.5}$$

where $A = \pi ab$, $I_{io} = |P_{io}|^2$ and $m^{-2} = a^{-2} + T_x^{-2}$, $n^{-2} = b^{-2} + T_y^{-2}$. The second (diffuse scattering) term, apart from the factor e^{-g}, is the exact equivalent of Eq. 51 in Horton and Muir's paper (loc. cit.).

Similarly, for $g \gg 1$ we obtain

$$\left\langle I_s^{(1)}\right\rangle_{fb} \simeq |R_i|^2 I_{io}A\mu_z^2\pi wv \exp\left[-\frac{\mu_x^2w^2}{2} - \frac{\mu_y^2v^2}{2}\right] \tag{2.4.6}$$

where $w^{-2} = a^{-2} + gT_x^{-2}$, $v^{-2} = b^{-2} + gT_y^{-2}$. The subscripts fb denote the finite beamwidth.

In summary, we note that the implicit factor of one-half in (2.4.5-6) represents the effect of the beam amplitude taper. Otherwise, when we set $T_x^2 = T_y^2 = \frac{1}{2}T^2$ and assume $a^{-2}, b^{-2} << \frac{1}{2}T^{-2}$, (2.4.5) and (2.4.6) become the same as the homogeneous plane wave results.

2.4.2 Effect of Pulses

The effect of using a pulsed beam on the reflectivity can be more easily appreciated by referring to Fig. 2.9. The effective insonified area for the CW beam is given by

$$A_{CW} = \frac{\pi r_{io}^2 \theta_e^2}{\cos\delta_i} \tag{2.4.7}$$

For a pulse s(t), $2\Delta T$ in duration, the maximum return will originate from this equivalent area provided $2r_{io}\theta_e \tan\delta_i < c\Delta T$. For smaller grazing angles the area reduces to

$$A_p \simeq b(c\Delta T)\ \mathrm{cosec}\delta_i \tag{2.4.8}$$

where b is the range element width which on the average equals $4/3\ r_{io}\theta_e$. The effective insonified area at any given moment is thus variable. Assuming that $c\Delta T$ is sufficiently long so that pulse transient effects on $\langle \Gamma\Gamma^* \rangle$ may be neglected, the instantaneous coefficient $\langle \Gamma\Gamma^* \rangle$ will still vary depending on the ratios of $b^2/4T_y^2$ and $(c\Delta T\ \mathrm{cosec}\delta_i)^2/T_x^2$. Fortunately, in the case of the myosepta both the average instantaneous effective beamwidth and the spatial pulse duration will be considerably greater than the correlation lengths. Hence, except in the region of

the nearest and farthest intercept points when strong transient conditions prevail, the backscatter return will be approximately

$$\left\langle p_s^{(I)}(\vec{r},\omega)\right\rangle \simeq j\mu_z R_i P_{io}\, e^{jk(r_{io}+r_{so})}\int_A S(\omega)\, e^{-(y^2/b^2+x^2/a^2+g/2)} \times e^{j\vec{\mu}_{xy}\cdot\vec{r}_{oxy}}\, dA \qquad (2.4.9)$$

where by the definition (1.3.2), $S(\omega) = (P_o/r_{io})^{-1} F[p_i(\vec{r},t)]$ and $p_i(\vec{r},t) = P_o/r_{io}\, s(t)$ is the incident wave.

Assuming a narrowband pulse of the form

$$\begin{aligned} s(t) &= s_o(t)\, e^{-j(\omega_c t_{ro}-\phi_c)} && |t_{ro}| \le \Delta T \\ &= 0 \quad , && |t_{ro}| > \Delta T \end{aligned} \qquad (2.4.10)$$

with the retarded time given by $t_{ro} = t - (r_{io}+r_{so})/c$, we obtain after multiplication of (2.4.9) by $e^{-j\omega t_{ro}}$ and integrating,

$$\left\langle p_s(\vec{r},t)\right\rangle = \frac{-F(\delta_i,\delta_s)R_i P_{io} A}{c}\int_{-\infty}^{\infty} j\omega\, S(\omega)\, e^{-\gamma_1^2\omega^2 - j\omega t_{ro}}\, d\omega \qquad (2.4.11)$$

where $\gamma_1^2\omega^2 = \frac{\mu_x^2 a^2}{4} + \frac{\mu_y^2 b^2}{4} + \frac{g}{2}$, $F(\delta_i,\delta_s) = (\cos\delta_i + \cos\delta_s)$ and $c = \omega/k$ is the velocity. Using (1.3.4) and the convolution theorem we find

$$\left\langle p_s(\vec{r},t)\right\rangle = \frac{j\mu_{zc} R_i P_{io} A}{2\gamma_1\sqrt{\pi}}\int_{t_{ro}+\Delta T}^{t_{ro}-\Delta T} [s_o(t_{ro}-u) + j/\omega_c\, \dot{s}_o(t_{ro}-u)] \times e^{-u^2/4\gamma_1^2 - j\omega_c(t_{ro}-u)+j\phi_c}\, du \qquad (2.4.12)$$

where $\mu_{zc} = \mu_z|_{k=\omega_c/c}$. Unless the rise time is comparable to the inverse carrier frequency (i.e. the pulse is no longer narrowband but is broadband) the second term of (2.4.12) may be neglected. For convenience we will usually advance the phase of the incident pulse carrier by $\pi/2$,

i.e. we set $\phi_c = \pi/2$. Eq. (2.4.12) is evaluated for cosine and rectangular (incident) pulses in Appendix C.

Scattered Pulse Energy

To obtain the scattered pulse energy we make use of the Wiener-Khintchine theorem. The ensemble averaged autocorrelation function $\langle E(\tau)\rangle$ of $p_s(\vec{r},t)$ may be expressed as

$$\langle E(\tau_r)\rangle = \frac{1}{2\pi}\int_{-\infty}^{\infty} \langle p_s(\vec{r},\omega)p_s(\vec{r},\omega)^*\rangle\ e^{-j\omega\tau_r}\ d\omega \qquad (2.4.13)$$

The scattered pulse energy is then obtained by setting $\tau_r = 0$ and multiplying $\langle E(t_{ro1})\rangle$ by $(2\rho c)^{-1}$.

Assuming the surface correlation functions, elevations and beamwidth are Gaussian as before, we obtain the following result corresponding to $\langle I_s^{(1)}\rangle$

$$\langle E^{(1)}(\tau_r)\rangle = \frac{|R_i|^2|P_{io}|^2}{4}\int_{-\infty}^{\infty}\iint_A ab\ e^{-\frac{1}{2}(\zeta^2/a^2+\eta^2/b^2)}\ \mathrm{erfc}\left(\frac{\zeta}{\sqrt{2}a}\right)\ \mathrm{erfc}\left(\frac{\eta}{\sqrt{2}b}\right)$$
$$\times\ e^{-g[1-C(\zeta,\eta)]\mu_z^2|S(\omega)|^2}\ e^{j(\mu_x\zeta+\mu_y\eta)}\ d\zeta d\eta\ e^{-j\omega\tau_r}\ d\omega \qquad (2.4.14)$$

where $t_{ro2} = t_{ro1} - \tau_r$,

$$\mathrm{erfc}(x) = 1 - \mathrm{erf}(x) = 1 - 2/\sqrt{\pi}\int_0^x e^{-u^2}\ du$$

and $C(\zeta,\eta)$ is defined by (2.4.4).

For $g \ll 1$ we may show (Appendix C)

$$\langle E^{(1)}(\tau_r)\rangle \simeq \frac{F(\delta_i,\delta_s)^2|R_i|^2|P_{io}|^2}{c^2}\left\{\frac{(\pi ab)^2}{2\pi}\int_{-\infty}^{\infty}\omega^2\ e^{-2\gamma_1^2\omega^2}\ |S(\omega)|^2\ e^{-j\omega\tau_r}\ d\omega\right.$$
$$\left. + \frac{g_o(\pi ab)(\pi mn)}{2\pi}\int_{-\infty}^{\infty}\omega^4\ e^{-2\gamma_2^2\omega^2}\ |S(\omega)|^2\ e^{-j\omega\tau_r}\ d\omega\right\} \qquad (2.4.15)$$

where $\gamma_1^2\omega^2 = (\tfrac{1}{2}\mu_x a)^2 + (\tfrac{1}{2}\mu_y b)^2 + \tfrac{1}{2}g_o\omega^2$, $\gamma_2^2\omega^2 = (\tfrac{1}{2}\mu_x m)^2 + (\tfrac{1}{2}\mu_y n)^2 + \tfrac{1}{2}g_o\omega^2$ and $g = g_o\omega^2 = c^{-2}h^2(\cos\delta_i + \cos\delta_s)^2\omega^2$.

For $g >> 1$ we may show that

$$\left\langle E^{(1)}(\tau_r)\right\rangle \simeq \frac{F(\delta_i,\delta_s)^2|R_i|^2|P_{io}|^2}{c^2}\ \frac{(\pi ab)}{2}\int_{-\infty}^{\infty} wv\omega^2\ e^{-2\gamma_o^2}\ |S(\omega)|^2\ e^{-j\omega\tau_r}\ d\omega \tag{2.4.16}$$

where $\gamma_o^2 = (\tfrac{1}{2}\mu_x w)^2 + (\tfrac{1}{2}\mu_y v)^2$.

In the case of the myosepta, $a >> T_x$ and $b >> T_y$, so that to a very good approximation $\mu_x^2w^2 \simeq \mu_x^2T_x^2/g$ and $\mu_y^2v^2 \simeq \mu_y^2T_y^2/g$. As a result, γ_o and $(wv\omega^2)$ are to all intents independent of wavelength and may be moved outside the integral of (2.4.16), yielding for $g_c >> 1$

$$\left\langle E^{(1)}(\tau_r)\right\rangle \simeq F(\delta_i,\delta_s)^2|R_i|^2|P_{io}|^2\ e^{-2\gamma_o^2}\ (\pi ab)\ \frac{(\pi T_xT_y)}{g_oc^2}\ \frac{1}{2\pi}\int_{-\infty}^{\infty}|S(\omega)|^2\ e^{-j\omega\tau_r}\ d\omega \tag{2.4.17}$$

By the autocorrelation theorem we then have the following equivalent forms

$$\begin{aligned}\left\langle E^{(1)}(\tau_r)\right\rangle &= E_o\pi T_xT_y\ e^{-2\gamma_o^2}\ (g_oc^2)^{-1}\ T_{ef}\ K_o(\tau_r)\ \cos\omega_c\tau_r \\ &= E_o\pi T_xT_y\ e^{-2\gamma_o^2}\ (g_oc^2)^{-1}\ \cos\omega_c\tau_r\int_{-\infty}^{\infty} s_o^*(u)s_o(u+\tau_r)\ du\ ,\quad g_c >> 1\end{aligned} \tag{2.4.18}$$

where $E_o = F(\delta_i,\delta_s)^2|R_i|^2|P_{io}|^2(\pi ab)$ and $K_o(\tau_r)$ is the pulse envelope correlation coefficient defined as (see Appendix B)

$$K_o(\tau_r) = 1/T_{ef}\int_{-\infty}^{\infty} s_o^*(u)\ s_o(u+\tau_r)\ du \tag{2.4.19}$$

The integrals of (2.4.15) may be evaluated with the aid of the convolution theorem

$$\frac{1}{2\pi}\int_{-\infty}^{\infty} \omega^{2n}\, e^{-2\gamma^2\omega^2}\, |S(\omega)|^2\, e^{-j\omega\tau_r}\, d\omega$$

$$= \frac{T_{ef}}{2\gamma\sqrt{2\pi}} \int_{-\tau_r+2\Delta T}^{\tau_r-2\Delta T} e^{-u^2/8\gamma^2}\, (-1)^n\, \frac{\partial^{2n}}{\partial\tau_r^{2n}}\, [K_o(\tau_r-u)\cos\omega_c(\tau_r-u)]\, du \tag{2.4.20}$$

If we now assume that the incident pulse is narrowband, i.e. the pulse bandwidth BW $<<$ ω_c, we may write $\omega = \omega_c + \omega_d$ and ignore all terms of the order of ω_d/ω_c or higher. From (2.4.20) it can be seen that this is equivalent to neglecting the derivatives of $K_o(\tau_r - u)$. Hence,

$$\left\langle E^{(1)}(\tau_r)\right\rangle \simeq \frac{E_o k_c^2 \pi ab T_{ef}}{2\gamma_1\sqrt{2\pi}} \int_{-\tau_r+2\Delta T}^{\tau_r-2\Delta T} e^{-u^2/8\gamma_2^2}\, K_o(\tau_r-u)\, \cos\omega_c(\tau_r-u)\, du$$

$$+ \frac{E_o k_c^2 g_c \pi mn T_{ef}}{2\gamma_2\sqrt{2\pi}} \int_{-\tau_r+2\Delta T}^{\tau_r-2\Delta T} e^{-u^2/8\gamma_2^2}\, K_o(\tau_r-u)\, \cos\omega_c(\tau_r-u)\, du \quad ,$$

$$g_c << 1 \tag{2.4.21}$$

Finally, if $2\gamma_1^2\omega_c BW << 1$, the exponentials in (2.4.15) may be expanded about the carrier frequency ω_c yielding

$$\left\langle E^{(1)}(\tau)\right\rangle \simeq E_o k_c^2\, [\pi ab\, e^{-2\gamma_1^2\omega_c^2} + g_c \pi mn\, e^{-2\gamma_2^2\omega_c^2}]\, T_{ef} K_o(\tau_r)\, \cos\omega_c\tau_r \tag{2.4.22}$$

This confirms, as might be expected from the form of (2.4.10), that for a sufficiently narrowband incident pulse the zero-order approximation of the scattered pulse covariance may be obtained simply by multiplying the CW intensity expressions by the incident pulse shape covariance $[T_{ef}K_o(\tau_r)\, \cos\omega_c\tau_r]$. Of course, this approximation is far better for $g_c >> 1$ than for the case of $g_c << 1$ since in the former case $\left\langle I_s^{(1)}\right\rangle$

is essentially independent of wavelength while for $g_c << 1$, $(\langle I_s^{(1)} \rangle - \langle p_r \rangle \langle p_r \rangle^*)$ varies as λ^{-4}. Thus, unless the pulse is narrowband and/or the angle of incidence δ_i is near zero, for Rayleigh scattering it will generally be necessary to employ either (2.4.15) or (2.4.21) depending on $2\gamma_1^2 \omega_c BW \lesssim 1$. The resultant average pulse distortion is considered in general in connection with the effects of absorption in Chapter 3, while the particular cases of cosine and rectangular pulse distortion are examined in Appendix C.

Analogously to the backscatter cross-section (2.2.1), we may now define a backscatter strength in terms of the ratio of the scattered pulse energy to the incident pulse energy. When using short pulses such a definition is in some ways more appropriate, and corresponds directly to the elementary signal description of the scattering process which is employed in Chapter 3.

2.4.3 Definition of the Backscatter Coefficient

Strictly speaking, the scattering cross-section of a scatterer is not defined when the incident wave has a significant bandwidth. However, the attractions of characterizing the scattering by a single parameter are considerable. Thus, on the basis of the results of the preceeding subsection we define the backscatter strength σ_s as

$$\sigma_s = \underset{R \to \infty}{\text{Limit}} \; 4\pi R^2 \frac{\int_{t_1}^{t_2} |U_s(t)|^2 \, dt}{\int_{t}^{t+\Delta t} |s_r(t)|^2 \, dt} \tag{2.4.23}$$

where Δt is the reference (incident) pulse length, and

where $s_r(t)$ is the instantaneous reference pulse, $U_s(t)$ is the backscattered signal and $t_2 - t_1 = T_\ell$ is the duration of the backscattered signal.[1] The time averaged backscatter coefficient (Ω) is then obtained by normalizing σ_s with respect to the effective insonified volume $V_\ell = V(T_\ell)$. The reference pulse may be obtained using a frequency invariant scatterer or a suitable approximation thereof, see Section 4.2.

Unless $U_s(t)$ and $s_r(t)$ are the actual propagating plane waves--they are not necessarily so restricted--the backscatter strength defined by (2.4.23) and the BCS defined by (2.2.1) are entirely different. Unlike the BCS which for a given frequency and orientation is an invariant of the scatterer, σ_s will normally depend on the transmitter and receiver characteristics through $s_r(t)$ and $U_s(t)$ and, of course, on the incident pulse bandwidth. σ_s is thus a less universal parameter than the BCS. The reason for adopting such a broad definition is that in practice the measured scattering will be dependent upon the nature of the source and receiver. However, it should be noted that if the scatterers are frequency invariant over the bandwidth of the incident pulse, the backscatter strength as defined will be independent of the source-receiver characteristics provided the phase and amplitude variations of the incident beam over the spatial coherence limits of the scatterer are negligible.

It has been the practice in underwater acoustics to define, in analogy to the BCS definition, a backscatter coefficient in terms of

---

[1] Since the signal envelope squared is proportional to the signal magnitude squared, $s_r(t)$ and $U_s(t)$ in (2.4.23) may be replaced by their corresponding envelopes $E_r(t)$ and $E_s(t)$.

the ratio of the far-field scattered power per unit volume to the incident power [Ol'shevskii (1967)]. By extending this definition to a band of frequencies and including the effects of the source and receiver, an average backscatter coefficient (averaged over the band of frequencies) may be defined if the spectral characteristics of the source and receiver are known, e.g. Mohammed (1967). By means of the Parseval theorem it can be shown that the backscatter coefficient defined in this manner and our definition (2.4.23) are equivalent.

Parseval's theorem requires that

$$\int_{-\infty}^{\infty} |E(t)|^2 \, dt = \int_{-\infty}^{\infty} |G(f)|^2 \, df = 2\int_{0}^{\infty} |G(f)|^2 \, df \qquad (2.4.24)$$

where G(f) is the Fourier transform of $E(t)$. By setting $E(t) = 0$ outside the interval T_ℓ we may extend the limits of the integral to $+\infty$ and $-\infty$. The equivalent expression to (2.4.23) in the frequency domain is obtained by applying the Parseval theorem to the numerator and denominator of (2.4.23). This is permissible since (2.4.23) is defined as the ratio of separately measurable energies. Thus we have

$$\sigma_s = \underset{R \to \infty}{\text{Limit}} \; 4\pi R^2 \frac{\int_0^{\infty} |G_s(f)|^2 \, df}{\int_0^{\infty} |G_r(f)|^2 \, df} \qquad (2.4.25)$$

The close connection of (2.4.25) to the backscatter cross-section as conventionally defined in (2.2.1) is evident. For CW incidence $|G_s(f)|^2 \to |F(f)|^2 |H(f)|^2 I(f)\delta(f)$, where I(f) is the incident intensity, H(f) is the scatterer transfer function, F(f) is the equivalent receiver-source transfer function and $\delta(f)$ is the delta-function. Hence $|F(f)|^2$ cancels and (2.4.25) reduces to the conventional BCS definition.

With $\Omega = \sigma_s/V_\ell$, where σ_s is defined by (2.4.23) or (2.4.25), we are now in a position to estimate the contribution of the myosepta to the tissue volume backscatter.

CHAPTER 3

FIRST ORDER APPROXIMATION OF PULSE SCATTERING IN A RANDOM ABSORBING MEDIUM

In the case of in situ measurements, it is in practice difficult to approximate the rather idealized conditions postulated in the previous chapter. Thus, in the case of tissues, absorption, anisotropy, complex geometries and the effect of non-ideal incident fields must be taken into account. To this must be added considerations of pulse shape and bandwidth, various experimental and instrumental limitations and, of course, the statistical properties of the scatterers and the medium. For the analysis of such an array of parameters, the point-scatterer theory developed and refined by Ol'shevskii (1966) and Middleton (1951, 1966, 1972) is probably the best approach, at least if the problem is to remain at all tractable.

In the first three sections we will review the essential features of the Middleton-Ol'shevskii theory for the case of static reverberation and proceed to adapt the theory to the problem at hand. Apart from the derivation of some simple first order corrections for the effects of absorption and finite bandwidth, the adaptation is straightforward. In subsequent sections we will consider in greater detail the effects of absorption on the pulses and the measurement accuracy, the relationship of the received signal to the actual ultrasonic pulse, and the subject of near-field pulse backscatter measurements.

3.1 Introductory Remarks

The key assumptions made in the Middleton-Ol'shevskii statistical model of volume reverberation are:

a) the scattering inhomogeneities may be represented by equivalent point-scatterers;

b) in any sufficiently small portion of the insonified volume the point-scatterers are randomly, uniformly and independently distributed, thus defining the reverberation process as a Poisson process (Appendix A).

Further it is assumed that:

c) the scatterers reradiate independently;

d) multiple scattering is negligible.

Under these conditions the resultant reverberation process may be represented as the superposition of M random events given by

$$X(t) = \sum_{m=1}^{M} U_m(t,\vec{r}_m,\vec{q}_m) \qquad (3.1.1)$$

where $U_m(t,\vec{r}_m,\vec{q}_m)$ is the elementary signal or event associated with the m^{th} point-scatterer, $\vec{q}_m$ denotes the other stochastic properties of the point-scatterer and M is a random variable with the Poisson probability distribution given by (A.1.5).

Clearly, scattering by the myosepta would appear to violate condition a) and most likely also b). For this reason it will be necessary to exclude it initially and treat scattering by the myosepta separately as a component process of the overall composite process.

3.2 Phenomenological Model of Tissue Volume Scattering

In addition to the basic restrictions on the scatterers given in the previous section, we will assume the following conditions:

1) the tissue is anisotropic in only two dimensions with the symbols ($||$) and ($\perp$) denoting the directions parallel and perpendicular to the muscle fibers, respectively. The tissue is characterized by velocities $c_{2||}$, $c_{2\perp}$, absorptions $\alpha_{||}$, $\alpha_{\perp}$, and density ρ_2;
2) the tissue scatterers are static over the pulse repetition interval;
3) monostatic operation;
4) the tissues are oriented with the muscle fibers perpendicular to the beam axis;
5) the incident beam is sufficiently narrow so that the beam may be considered perpendicularly incident;
6) far-field conditions prevail;
7) the pulse bandwidth and spatial distances are such that the effects of velocity dispersion are completely negligible in comparison to the effects of absorption;
8) the transducer is located in a non-dissipative medium of impedance $\rho_1 c_1$ (water) adjoining the tissues;
9) the velocities c_1 and c_2 are nearly equal ($c_1/c_2 < 1.05$), hence refraction of the incident beam at the water-tissue interface is negligible.

With the possible exception of 5), none of these conditions should prove too unrealistic or impractical. To meet 5), however,

the far-field condition 6) may be overly restrictive for in situ measurements (Sections 3.3 and 3.6).

The geometry of the experimental set-up is depicted in Fig. 3.1. The distance along the transducer axis to the surface of the fish is r_o. The interval (t_2-t_1) over which the backscatter is to be analyzed is delayed by (t_o-t_1) in order to avoid reflections from the surface. If the scales are removed from the fish, the two-way ultrasonic transmission loss at the interface is negligible. However, for the sake of generality, we will assume a two-way transmission coefficient $T_c = (1 - |R_{12}|^2)$ where R_{12} is the reflectivity of the surface.

The elemental signal U_m received from the m^{th} scatterer located at a distance $|\vec{r}_m| = r_o + c_2\tau_m$ from the origin may be expressed as

$$U_m(\omega,\vec{r}_m,\vec{q}_m) \simeq \frac{T_c e^{j2k(r_o+c_2\tau_m)}}{4\pi(r_o+c_2\tau_m)^2}\left[e^{-2\alpha(\omega)c_2\tau_m}\,\Phi_m(\omega,\theta_a,\phi_a)\right.$$

$$\left.\times\,\Psi^2(\omega,\theta,\phi)\;S(\omega)\right] \qquad (3.2.1)$$

where $S(\omega)$ = driving signal[1]

$\Psi(\omega,\theta,\phi)$ = equivalent beam transfer function (see Section 3.4)

$\Phi_m(\omega,\theta_a,\phi_a)$ = far-field scattering pattern of the point-scatterer

where $\theta_a = \theta_o-\theta$, $\phi_a = \phi_o-\phi$ and θ_o,ϕ_o are the equivalent random orientation angles of the scatterer

$\alpha(\omega)$ = absorption of the medium (transverse direction)

τ_m = local fixed time with respect to the shifted coordinate system centered at the interface ($\tau = 0$).

---

[1]The relationship of the ultrasonic pulse to the applied electrical signal and the actual received pulse is examined in detail in Section 3.4.

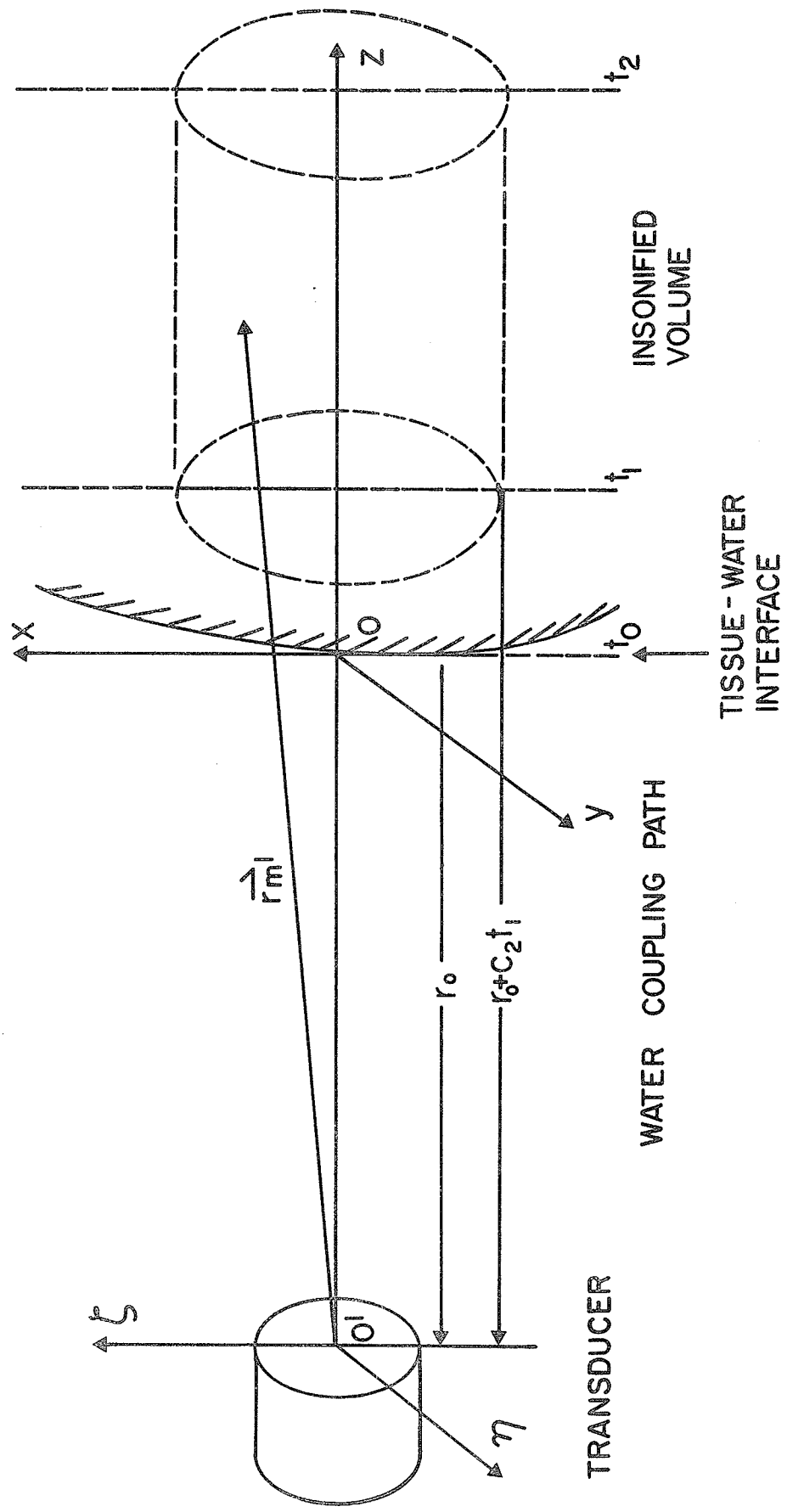

Fig. 3.1 Geometry of the tissue scattering experiments.

When the absorption cannot be neglected, the Fourier transform should be replaced by the Laplace transform, Middleton (1972), Pt. III. However, as it was assumed that the medium is absorptive but non-dispersive,[1] we may retain the Fourier transform formalism if we define the absorption coefficient α as $\alpha = \alpha(|\omega|)$ where α is positive real. Thus the received signal pulse in the time domain becomes by (1.4.2)

$$U_m(t,\vec{r}_m,\vec{q}_m) = \frac{T_c}{8\pi^2 r_m^2}\int_{-\infty}^{\infty} \Phi_m(\omega,\theta_a,\phi_a)\Psi^2(\omega,\theta,\phi)S(\omega)e^{-2\alpha(|\omega|)c_2\tau_m - j\omega t_m}\,d\omega \quad ,$$

$$\tau_m > 0 \qquad (3.2.2)$$

where $t_m = t - 2r_o/c_1 - 2\tau_m$ is the retarded time.

The determination of $U_m(t,\vec{r}_m,\vec{q}_m)$ is greatly simplified if $\Psi^2(\omega,\theta,\phi)$ can be moved outside the integral. Assuming a small increase in error can be tolerated, we will factor $\Psi^2(\omega,\theta,\phi)$ from under the integral in (3.2.2) and replace it by the two-way beam pattern $\overline{\Psi^2(\omega_c,\theta,\phi)}$ averaged as a function of frequency over the bandwidth of $S(\omega)$ and referred to the center frequency. Essentially, $\overline{\Psi^2(\omega_c,\theta,\phi)}$ is the beam pattern measured in the experiments when using pulses.

It will be useful to expand the scatterer function $\Phi(\omega,\theta_a,\phi_a)$ about the center frequency $\omega_c/2\pi$. A similar representation for $\alpha(|\omega|)$ would be desirable but is not possible because we are taking the absolute value of ω. However, if α varies only slightly over the bandwidth β of the pulse $S_o(\omega_d)$, i.e.

$$2\left.\frac{\partial\alpha}{\partial\omega}\right|_{|\omega_c|}\beta c_2\,\tau_{max} \ll 1 \quad , \qquad \omega > 0$$

---

[1] This assumption, although a good approximation, is in fact non-physical for in a real (causal) physical system the absorption and dispersion are Hilbert transforms of each other; see, for example, MacDonald and Brachman (1956).

then for all τ_m over the bandwidth β, we may put to a good approximation

$$e^{-2\alpha(|\omega|)c_2\tau_m} = e^{-2\alpha(|\omega_c|)c_2\tau_m}\left[1 - 2\left.\frac{\partial\alpha}{\partial\omega}\right|_{|\omega_c|}\omega_d c_2\tau_m + \ldots\right] \qquad (3.2.3)$$

where $\omega_d = \omega - \omega_c$ and $k_d = \omega_d/c = k - k_c$ as before, and ω_d takes on both positive and negative values. However, the spectra of the signal pulse $S_o(\omega)$ will generally taper off faster than ω^{-1} so that no convergence problems will be encountered. In fish myomere the absorption in the range 1 - 10 MHz is roughly linear [Freese and Makow (1968b)] and we may therefore replace $(\partial\alpha/\partial\omega|_{|\omega_c|})$ by $\alpha_c/|\omega_c|$. Substituting (3.2.3) into (3.2.2) we obtain the first order result valid for $\left|\frac{1}{\Phi}\frac{\partial^n\Phi}{\partial k_c^n}\left(\frac{\beta}{c}\right)^n\right| << 1$

$$U_m(t,\vec{r}_m,\vec{q}_m) \simeq \frac{T_c\,\Phi(k_c,\theta_a,\phi_a)}{4\pi r_m^2}\,\overline{\Psi^2(\omega_c,\theta_m,\phi_m)}\;e^{-2\alpha(|\omega_c|)c_2\tau_m}\,e^{-j\omega_c t_m}\,I(t_m,\vec{r}_m,\vec{q}_m) \qquad (3.2.4)$$

where

$$I(t_m,\vec{r}_m,\vec{q}_m) = \frac{1}{2\pi}\int_{-\infty}^{\infty}\left[1 + \left(\frac{1}{\Phi}\frac{\partial\Phi}{\partial k}\right)_{k_c}\frac{\omega_d}{c_2}\right]\left[1 - 2\left.\frac{\partial\alpha}{\partial\omega}\right|_{\omega_c}\omega_d c_2\tau_m\right]S_o(\omega_d)e^{-j\omega_d t_m}\,d\omega_d$$

Eq. (3.2.4) is rather interesting. For example, it shows that the distorting effect of a scatterer having a rising frequency response may in fact be partially offset by the absorption of the medium. For a constant cross-section ($\partial\Phi/\partial k_c = 0$), $\Phi = \Phi(\theta_a,\phi_a)$ is dependent only on the scatterer orientation. If the absorption is zero, (3.2.4) reduces to the simplest possible result where the backscattered pulse is a time-delayed, amplitude-scaled copy of the incident pulse.

Approximating the transmitted pulse s(t) by a narrowband pulse of the form

$$s(t) = s_o(t)\,e^{-j\omega_c t}, \quad |t| \le \Delta T$$
$$= 0, \quad |t| > \Delta T$$

where $2\Delta T$ is the pulse length, and employing the transform relation

$$F[\dot{s}_o(t)] = -j\omega_d S_o(\omega_d) \quad ,$$

we obtain

$$I(t_m) = s_o(t_m) + jB_m \dot{s}_o(t_m) \tag{3.2.5}$$

where $B_m = \left[\left(\frac{1}{\Phi}\frac{\partial\Phi}{\partial k}\right)_{k_c} \frac{1}{c_2} - 2\left.\frac{\partial\alpha}{\partial\omega}\right|_{\omega_c} c_2\tau_m\right]$.

Thus to first order, the backscattered pulse in an absorbing medium consists of a copy of the incident pulse plus a quadrature component proportional to the pulse envelope derivative. This means that the backscattered pulse exhibits phase modulation with the amplitude of the quadrature component depending on the location of the point-scatterer in the tissue. The nature of the pulse distortion will be examined further by means of exact solutions for specific examples in Section 3.5.

The next step consists of obtaining the moments of (3.1.1). In principle one can obtain all the moments of the scattered field by direct ensemble averaging but the amount of algebra required for moments higher than the second moment becomes prohibitive. The higher moments may be more easily obtained via the characteristic function derived in Appendix A.

Inserting (3.2.4) and (3.2.5) into (A.1.10), the first moment becomes

$$\langle X(t_1)\rangle = \frac{T_c}{4\pi}\int_{V_\ell} \langle n(\vec{r})\rangle \overline{\Psi^2(\omega_c,\theta,\phi)}\; L(\vec{r})\; \langle \Phi(k_c,\vec{q},\vec{r}) I(t_r,\vec{r},\vec{q})\rangle_{\vec{q}}\; e^{-j\omega_c t_r}\, dv \tag{3.2.6}$$

where

$$L(\vec{r}) = \frac{e^{-2\alpha(|\omega_c|)c_2\tau}}{|\vec{r}|^2} \quad , \quad |\vec{r}| = r_o + c_2\tau \quad ,$$

$$I(t_r,\vec{r},\vec{q}) = s_o(t_r) + jB\,\dot{s}_o(t_r) \quad ,$$

$$B(\vec{r},\vec{q}) = \left[\left(\frac{1}{\Phi}\frac{\partial\Phi}{\partial k}\right)_{k_c}\frac{1}{c_2} - 2\frac{\alpha_c}{|\omega_c|}c_2\tau\right] \quad ,$$

$$t_r = t_1 - \frac{2r_o}{c_1} - 2\tau \quad ,$$

$n(\vec{r})$ = point-scatterer density .

The ensemble average $\langle \Phi(k_c,\vec{r},\vec{q})I(t_r,\vec{r},\vec{q})\rangle$ contains three terms

$$\langle \Phi(k_c,\vec{r},\vec{q})I(t_r,\vec{r},\vec{q})\rangle = \langle \Phi(k_c,\vec{r},\vec{q})\rangle\, s_o(t_r) + j/c_2 \left\langle \frac{\partial\Phi}{\partial k_c}\right\rangle \dot{s}_o(t_r)$$

$$- j\,2\,\frac{\alpha_c}{|\omega_c|}c_2\tau \left\langle \Phi(k_c,\vec{r},\vec{q})\right\rangle \dot{s}_o(t_r)$$

Depending on the circumstance, one or both of the latter terms may not be needed.

The second moment from (A.1.11) is given by

$$\langle X(t_1)X(t_2)\rangle = \frac{T_c^2}{(4\pi)^2}\int_{V_\ell}\langle n(\vec{r})\rangle\,\overline{[\Psi^2(\omega_c,\theta,\phi)]}^2\,L^2(\vec{r})\,\langle \Phi^2 I(t_{r1})I(t_{r2})\rangle_{\vec{q}}$$

$$e^{-j\omega_c(t_{r1}+t_{r2})}dv + \langle X(t_1)\rangle\,\langle X(t_2)\rangle \qquad (3.2.7)$$

Eq. (3.2.6) and (3.2.7) now express the moments in terms of the scatterer response, the point-scatterer density, the transducer beam functions, the absorption and velocity of the tissue, the interface transmission coefficient and the incident signal.

3.3 Backscatter Statistical Properties

The zero-order absorption is common to the individual processes and varies only slightly over the pulse length. Therefore, it may be factored (see Section 3.3.5) and the resultant process compensated if the absorption coefficient is known. Assuming this is the case, we will then have $\overline{\Psi^2(\omega_c,\theta,\phi)}L(\vec{r})\ \exp\left[2\frac{\alpha}{|\omega_c|}c_2\tau\right]$. It will be convenient to replace these functions by a more general gain function $\overline{G^2(\omega_c,\vec{r})}$ which is independent of absorption.

3.3.1 Mean and Variance of the Backscatter

Substituting $\overline{G^2(\omega_c,\vec{r})}$ and effecting a change of variable

$$dv = \tfrac{1}{2}c_2\ dA\ dt_r \tag{3.3.1}$$

where $t_r = t - (2r_o/c_1 + 2\tau)$, and since $I(t_r,\vec{q})$ of (3.2.6) is non-zero only in the interval $(t_r-\Delta T, t_r+\Delta T)$, the mean for the partially compensated process $Z_a(t)$ may be written as

$$\left\langle Z_a(t)\right\rangle = \frac{-T_c c_2}{8\pi}\int_{-\Delta T}^{\Delta T}\left\langle n(t-t_r)\right\rangle\int_{A(t_r)}\overline{G^2(\omega_c,\theta,\phi,t-t_r)}\left\langle\Phi(k_c,\vec{q})I(t_r,\vec{q})\right\rangle_{\vec{q}} \times e^{-j\omega_c t_r}\ dA\ dt_r \tag{3.3.2}$$

The variance and covariance may be obtained similarly.

We now define the effective beam cross-section in the insonified volume V_ℓ as

$$\Lambda^{(1)}(t) = \int_{A(t)}\overline{G^2(\omega_c,\theta,\phi,t)}\ dA = \int_0^{\theta(r)}\int_0^{2\pi}\overline{\Psi^2(\omega_c,\theta,\phi,t)}L(\vec{r})\ \exp\left[2\frac{\alpha}{|\omega_c|}c_2\tau\right]\ r^2\sin\theta\ d\phi d\theta \tag{3.3.3}$$

In order to avoid non-physical results, the retarded time t_r may be modified by redefining the pulse interval for $s(t)$ as

$$s(t_r) = s_o(t_r-\Delta T)\ e^{-j\omega_c(t_r-\Delta T)} \quad , \qquad |t_r-\Delta T| \leq \Delta T$$

$$= 0 \quad , \qquad |t_r-\Delta T| > \Delta T$$

In an arbitrary interval $(t_{r1}t_{r2})$, scatterers outside $(t_{r1}t_{r2})$ provide contributions to the process near the ends of the interval. This problem is avoided by shifting the reference origin by ΔT as above, but in order not to lose symmetry in the limits we define a new variable $t_r' = t_r-\Delta T$.

If $\langle n(t)\rangle$, $\Lambda^{(1)}(t)$ and $\frac{\alpha}{|\omega_c|}\ c_2\tau$ vary only negligibly over the instantaneous effective scattering volume, i.e. $\langle n(t-t_r)\rangle \simeq \langle n(t)\rangle$, etc., the mean (3.3.2) becomes

$$\langle Z_a(t)\rangle \simeq \frac{-\frac{1}{2}c_2T_c}{4\pi}\langle n(t)\rangle\ \Lambda^{(1)}(t)\ \langle\Phi(k_c,\vec{q})\rangle_{\vec{q}} \int_{-\Delta T}^{\Delta T} S_{od}(t_r')\ e^{-j\omega_c t_r'}\ dt_r' \tag{3.3.4}$$

where $\quad s_{od}(t_r') = s_o(t_r') + jB\ \dot{s}_o(t_r')$

$$B = \left[\frac{1}{\langle\Phi\rangle}\left\langle\frac{\partial\Phi}{\partial k_c}\right\rangle\frac{1}{c_2} - 2c_2\left.\frac{\partial\alpha}{\partial\omega}\right|_{|\omega_c|}\tau\right]$$

and $\quad 2\tau = (t - t_r' - \frac{2r_o}{c_1} - \Delta T) \simeq t - \frac{2r_o}{c_1} - \Delta T$

With $B = 0$, (3.3.4) reduces to the standard form which for volume backscatter in the far field is independent of the distance, see Middleton (1967), Pt. 1.

The phase angle $\omega_c t'_r = \omega_c(t-2/c_1-2\tau-\Delta T)$ referred to the reception point is randomized due to the random distribution of the point scatterers. In the general case the carrier may undergo a further phase shift ϕ_m as a result of the scattering. These two (spatial and temporal) phase shifts are additive and uniformly distributed over the common interval 0 to 2π [Beckmann and Spizzichino (1963), Ch. 7]. For a quasi-harmonic signal such as $s(t'_r) = s_o(t'_r)e^{-j\omega_c t'_r}$, $\langle Z_a(t)\rangle$ will be equal to zero as will all of the odd-order moments if the process is strictly stationary (see Section 3.3.5).

The variance of the process $Z_a(t)$ may be obtained from (3.2.7). The real part is given by

$$\text{Var.}[\text{Re } Z_a(t)] = \tfrac{1}{2}[\langle Z_a(t)Z_a^*(t)\rangle - \langle Z_a(t)\rangle\langle Z_a^*(t)\rangle]$$

$$\simeq -\tfrac{1}{4}\frac{T_c^2 c_2}{(4\pi)^3}\langle n(t)\rangle\,\Lambda^{(2)}(t)\left\langle\sigma(k_c,\vec{q})\right\rangle_{\vec{q}}\int_{-\Delta T}^{\Delta T}\left\langle s_{od}^2(t'_r)\right\rangle_{\vec{q}}\,dt'_r \tag{3.3.5}$$

where

$$\left\langle s_{od}^2(t'_r)\right\rangle_q = s_o^2(t'_r) + \left(\frac{4\pi}{\langle\sigma\rangle_{\vec{q}}}\right)\left\langle\left(\frac{\partial\Phi}{\partial k_c}\right)^2\right\rangle_q\frac{1}{c_2^2}\dot{s}_o^2(t'_r)$$

$$+ 4\left(\frac{\partial\alpha}{\partial|\omega_c|}\right)^2 c_2^2\,\dot{s}_o^2(t'_r)\tau^2 + \frac{8\pi}{\langle\sigma\rangle_{\vec{q}}}\left[\left\langle\left(\Phi\,\frac{\partial\Phi}{\partial k_c}\right)\right\rangle_q\frac{1}{c_2}s_o(t'_r)\,\dot{s}_o(t'_r)\right.$$

$$\left. - 2c_2\langle\Phi\rangle_q\frac{\partial\alpha}{\partial|\omega_c|}s_o(t'_r)\,\dot{s}_o(t'_r)\tau - 2\left\langle\frac{\partial\Phi}{\partial k_c}\right\rangle_q\frac{\partial\alpha}{\partial|\omega_c|}\tau\,\dot{s}_o^2(t'_r)\right]$$

and

$$\Lambda^{(2)}(t) = \int_{A(t)}\overline{G^2(\omega_c,\theta,\phi,t)}^2\,dA$$

For symmetrical signals the terms containing $s_o(t')\dot{s}_o(t')$ will drop out simplifying the equation to

$$\text{Var.}[\text{Re } Z_a(t)] = -\tfrac{1}{4}\frac{T_c^2 c_2}{(4\pi)^2}\left\langle n(t)\right\rangle \Lambda^{(2)}(t)\left\{\frac{\langle\sigma(k_c,\vec{q})\rangle_q}{4\pi}\int_{-\Delta T}^{\Delta T} s_o^2(t_r')\,dt_r'\right.$$

$$+\left[\frac{1}{c_2^2}\left\langle\left(\frac{\partial\Phi}{\partial k_c}\right)^2\right\rangle_{\vec{q}}+\frac{\langle\sigma\rangle_{\vec{q}}}{\pi}\left(\frac{\alpha}{|\omega_c|}\right)^2 c_2^2\,\tau^2\right.$$

$$\left.\left.-4\left\langle\frac{\partial\Phi}{\partial k_c}\right\rangle_{\vec{q}}\frac{\alpha}{|\omega_c|}\,\tau\right]\int_{-\Delta T}^{\Delta T}\dot{s}_o^2(t_r')\,dt_r'\right\} \qquad (3.3.6)$$

Eq. (3.3.6) contains only second order correction terms. It will be shown in Section 3.5 that for moderate absorptions and sufficiently short delay and measurement intervals these correction terms may be ignored. Eq. (3.3.6) then reduces to the classical result for the instantaneous (diffusely) scattered power

$$\text{Var.}[\text{Re } Z_a(t)] = \tfrac{1}{4}\frac{T_c^2 c_2}{(4\pi)^3}\langle n(t)\rangle \Lambda^{(2)}(t)\langle\sigma(k_c,\vec{q})\rangle_{\vec{q}}\int_{-\Delta T}^{\Delta T} s_o^2(t_r')\,dt_r' \qquad (3.3.6.a)$$

Integrating (3.3.6.a) over the interval $T_\ell = t_2 - t_1$ yields the total diffusely scattered energy from the equivalent insonified volume $V_\ell^{(2)}$. The latter equivalent volume is given by

$$V_\ell^{(2)} = \int_{z_1}^{z_2} \Lambda_n^{(2)}(z)\,dz \qquad (3.3.7)$$

where $\Lambda_n^{(2)}(z)$ is the normalized effective beam cross-section defined in (3.3.5) and $z = \tfrac{1}{2}c_2 t$. The effective insonified volume $V_\ell^{(1)}$ may be defined in the same manner for the coherent scattering.

It should be noted that in the far field $\Lambda^{(2)}(t)$ varies as r^{-2} in contrast to $[\Lambda^{(1)}(t)]^2$ for the deterministic component which is independent of r.[1]

3.3.2 Probability Distribution of the Backscatter

The key role in determining the character of the backscatter is played by the process density parameter s_ρ which may be defined as

$$s_\rho = \langle N \rangle \tau_{ef} \tag{3.3.8}$$

where $\langle N \rangle$ is the average number of elementary scattered signals received [$\simeq \langle n(t) \rangle \Lambda^{(1)}(t)$] and τ_{ef} is the equivalent signal duration. The latter may be conveniently defined in terms of either the signal amplitude or the signal energy integral. With

$$T_{ef} = \int_{-\infty}^{\infty} s_o^2(t)\, dt \tag{3.3.9}$$

$$\tau_{ef} = \int_{-\infty}^{\infty} s_o(t)\, dt \tag{3.3.10}$$

and the envelope $s_o(t)$ normalized to unity, it may be easily shown [Ol'shevskii (1967)] that these definitions are related by

$$T_{ef} = \Delta_{ef} \tau_{ef}^2 = \Delta_{ef}/\beta^2 \tag{3.3.11}$$

where Δ_{ef} is the equivalent width of the pulse power spectrum and β is the equivalent width of the amplitude spectrum (Appendix B).

---

[1] Despite our initial assumption of random scatterers, the existence of a very small deterministic component in the total scattered power $\langle Z_a(t) Z_a^*(t) \rangle$ is not ruled out, see Middleton (1967), Pt. 1.

At low densities [0(< 10)] there will be finite gaps of zero amplitude in the reverberation envelope resulting in a δ-function at the origin of the corresponding amplitude probability density distribution function [Middleton (1960), Ch. 11]. As $s_\rho \to \infty$, the probability of zero amplitude will decrease to zero and the distribution of the backscatter will tend toward a Gaussian probability distribution as required by the central limit theorem [Parzen (1960); Middleton (1960)]. For intermediate densities, a number of series representations have been derived such as the Gram-Charlier series, see Marcum (1948); Ol'shevskii (1967).

In order for the process Z(t) to tend towards a Gaussian process, one of the conditions to be fulfilled is that none of the elementary signals predominates over the others to the extent of yielding a significant contribution to the sum process. In general, it is preferable to treat these echoes separately. The probability distribution of the sum process W[V(t)] can then be obtained via the characteristic functions of the separate independent component processes.

3.3.3 Envelope Statistics

So far we have only considered the full signal. Due to the nature of the processing chosen, namely, full-wave rectification of the signal, the phase is eliminated and only the envelope of the received signals will be available.[1]

---

[1] Strictly speaking this is not correct. If we assume the original signal is bandlimited to some arbitrary upper frequency, the rectified signal's derivatives being discontinuous, it will contain frequencies to infinity and thus in principle the phase can be recovered within an integer multiple of π.

Expressing the backscatter signal as an approximately analytic signal [Rice (1945)]

$$X(t) = E(t)\, e^{-j[\omega_c t - \Theta(t)]} \tag{3.3.12}$$

$$\text{Re } X(t) = [X_{cos}^2 + X_{sin}^2]^{\frac{1}{2}} \cos\left[\omega_c t + \tan^{-1}\left(\frac{X_{sin}}{X_{cos}}\right)\right] \tag{3.3.13}$$

where $X_{cos} = E(t)\cos\theta(t)$, $X_{sin} = E(t)\sin\theta(t)$ and $E(t), \theta(t)$ are the envelope and phase of the signal $X(t)$, respectively. Conventionally, the components X_{cos} and X_{sin} are demodulated using quadrature detection. In contrast to $E(t)$ they may bear little or no resemblance to the original signal. However, the choice of $E(t)$ complicates the evaluation of the probability distribution. The reason for this is that the rectification process is non-linear. It can be shown (ibid.) that when $X(t)$ is Gaussian with zero mean, the envelope is described by the Rayleigh distribution given by

$$W(E) = \frac{E}{\sigma_x^2} \exp\left[- \frac{E^2}{2\,\sigma_x^2} \right] \tag{3.3.14}$$

where σ_x^2 is the variance of the Gaussian process. The corresponding distribution of the envelope intensity $I = E^2$ will be exponential (χ^2 distribution with parameters $n = 2$ and σ_x)

$$W(I) \simeq \frac{1}{\langle I \rangle} \exp\left[- \frac{I}{\langle I \rangle} \right] \tag{3.3.15}$$

where $\langle I \rangle = \langle E^2 \rangle = 2\sigma_x^2$.

Important parameters of the Rayleigh distribution that we will require are:

mean amplitude $\langle E \rangle = \sqrt{\pi/2}\ \sigma_x$ (3.3.16.a)

mean intensity $\langle E^2 \rangle = 2\sigma_x^2$ (3.3.16.b)

fluctuation variance $\sigma_e^2 = \frac{1}{2}(4 - \pi)\sigma_x^2 \simeq 0.43\sigma_x^2$ (3.3.16.c)

coefficient of variation $\gamma_v = \frac{\left[\langle E^2 \rangle - \langle E \rangle^2\right]^{\frac{1}{2}}}{\langle E \rangle} = \frac{\sigma_e}{\langle E \rangle} \simeq 0.52$ (3.3.16.d)

The envelope distributions of a number of known composite processes have been derived. The Rice distribution for the sum of a normal process and a constant (sinusoidal) signal is perhaps best known and is applicable when the scattering process contains a coherent (deterministic) component.

The envelope distribution in this case is given by (ibid.)

$$W(E_1) = \frac{E_1}{\sigma_x^2} \exp\left[-\frac{(E_1^2 + b_o^2)}{2\sigma_x^2}\right] I_o\left(\frac{E_1 b_o}{\sigma_x^2}\right) \qquad (3.3.17)$$

where E_1 is the envelope of the composite process

$$V(t) = X(t) + b_o\, e^{-j\omega_c t}$$

b_o is the constant signal amplitude and $I_o(\ )$ is the zero-order modified Bessel function of the first kind.

The determination of the envelope distribution for arbitrary distributions of the reverberation is a much more difficult undertaking, particularly if the process density s_ρ is low [Mullen and Middleton (1958)].

The correlation coefficients and power spectra of the backscatter and of the backscatter envelope fluctuations are briefly reviewed in Appendix B.

3.3.4 Composite Scattering Process

The total scatter process will be represented as the sum of four independent Poisson processes plus a non-Poisson essentially deterministic process Y(t).

$$V(t) = \sum_{i=1}^{4} X_i(t) + Y(t) \qquad (3.3.18)$$

where each of the $X_i(t)$ has the form

$$X_i(t) = \sum_{m=1}^{M} U_{im}(t, r_m, q_m)$$

In particular, if we assign the processes as follows:

$X_1(t)$ - scattering from lipid globules (Rayleigh region)

$X_2(t)$ - scattering from lipid globules (geometric optics region)

$X_3(t)$ - scattering from air bubbles

$X_4(t)$ - scattering from other tissue components (background scattering from myosepta, muscle fibers, myocommata, i.e. connective and adipose tissues not constituting part of the myosepta, and blood vessels)

$Y(t)$ - 'leakage' of surface interface and midline reverberation and possibly scattering from pinbones.

One or two of the component processes will be dominant in most cases. To the extent that Y(t) can be neglected and $X_4(t)$ approximates a Poisson process, the composite process will be Poisson. Accordingly, a single process density could be defined if so desired; details may be found in the papers by Middleton (1967), Pt. 1, and Faure (1964).

The moments in which we will be primarily interested are given by

$$\langle V(t) \rangle = \sum_{i=1}^{4} \langle X_i(t) \rangle + \langle Y(t) \rangle \tag{3.3.19}$$

$$\langle V^2(t) \rangle = \sum_{i=1}^{4} \langle X_i^2(t) \rangle + \langle Y^2(t) \rangle \tag{3.3.20}$$

$$\text{Var. } [V(t)] = \langle V^2(t) \rangle - \langle V(t) \rangle^2 \tag{3.3.21}$$

If, in addition to being independent, the component process averages are zero, the composite process covariance reduces to the sum of the individual process covariances, i.e.

$$\langle V(t_1)V(t_2) \rangle = \sum_{i=1}^{4} \langle X_i(t_1)X_i(t_2) \rangle + \langle Y_i(t_1)Y(t_2) \rangle \tag{3.3.22}$$

3.3.5 Averaging and Stationarization

The methods of sampling and averaging the data are to a large extent determined by the nature of the stochastic process, the parameter or distribution being measured and the intended application. However, in most cases some form of time averaging is sought in addition to ensemble averaging in order to reduce the number of sample runs required. The most stringent condition for the time averaging and ensemble averaging operations to be completely interchangeable, subject only to the constraint of independent samples, is that the stochastic process be strictly stationary--a process being defined as strictly stationary

if its statistical properties remain invariant under a shift of the time axis [Ol'shevskii (1967)]. Depending on the previously mentioned factors, the statistical properties may need to be determined at every point of the random medium or an average measure over a given region may suffice. While in the former case the process should be ideally strictly stationary (for time averaging), the requirements in the latter case are much less stringent. Thus, in the present study we will generally limit the investigation to obtaining estimates of the backscatter statistics averaged over a specified tissue depth interval. However, before this can be done the process data must normally be free of any dominant deterministic trends.

If a particular process X(t) can be expressed in the form

$$X(t) \simeq f(t)\, Z(t) \quad , \quad t = 2r/c \tag{3.3.23}$$

where f(t) is a deterministic function and Z(t) is a stationary stochastic process, the process may be stationarized by multiplying X(t) by $[f(t)]^{-1}$. In general, the resultant process will not be stationary in the strict sense; however, depending on the statistic, it may now be possible to utilize time averaging over some finite interval. The scattering process was compensated for zero-order absorption in the above manner but could not be stationarized because of the possible presence of components having different range dependences.[1]

---

[1] A number of ways, other than using ensemble averaging exclusively, have been employed to circumvent this problem. Simplest and most common perhaps is to neglect differences in range dependence over the measurement interval by using a sufficiently great distance between the source and insonified volume. Another method is to range gate the composite process into shorter segments and, assuming that the component processes do not overlap in the selected intervals, use varying compensation in the different segments.

It was recognized that essentially range independent and stationary conditions could be realized over short intervals in the transducer near field, particularly in the region centered on the axis about a_T^2/λ from the transducer. The field structure in this region is rather similar to that of a focussed transducer and for this reason is exploited in many diagnostic applications. It turns out, as will be shown in Section 3.6, that the response from both coherent and diffuse scatterers in this region is almost constant. Since the beam cross-section and therefore the number of insonified scatterers is also nearly constant, the process after compensation for absorption (neglecting differential absorption over the pulse BW) will be approximately stationary if the scatterer distribution is homogeneous. Actual experiments with unbounded model random media showed this to be the case, the backscatter level remaining essentially constant in the near field.

A combination of time averaging and ensemble averaging was employed. For each specimen the experimental moment averages and the coefficient of variation γ_V were calculated according to the following formats:

$$\left\langle \overline{F(V)} \right\rangle = \frac{1}{MT_\ell} \sum_{i=1}^{M} \int_0^{T_\ell} F_i[V(t)]\, dt \qquad (3.3.24)$$

and

$$\left\langle \gamma_V \right\rangle = \frac{1}{M} \sum_{i=1}^{M} \frac{\left[\overline{E^2} - (\overline{E})^2 \right]_i^{\frac{1}{2}}}{\overline{E}_i} \qquad (3.3.25)$$

where M is the number of aggregate members and the bars denote time averaging over the interval T_ℓ.

Independence of the ensemble aggregate members was assured by displacing the transducer laterally at least one beam diameter from one backscatter record to the next. This also had the effect of randomizing the coherent echoes from the pinbones (in whitefish) and the myosepta. In general, however, the inclination of the myosepta with respect to the incident beam axis was sufficient for scattering from adjacent myosepta to overlap within a given backscatter record.

3.4 Relationship of the Received Pulse to the Ultrasonic Pulse

The received pulse differs significantly from the actual transmitted acoustic pulse. Representing the electrical driving pulse $s(t)$ by its Fourier transform $S(\omega)$ and neglecting any interaction effects, the received pulse $S_{rec}(\omega)$ may be represented as

$$S_{rec}(\omega) \simeq [H_{et}(\omega)H_{er}(\omega)]\ [H_{tt}(\omega)H_{tr}(\omega)]$$

$$\times D_t(\omega,\vec{r},\vec{k}_i)D_r(\omega,\vec{r},\vec{k}_s) \times H_s(\omega,\vec{r},\vec{k}_i,\vec{k}_s)\ \frac{1}{r^2}\ e^{j2\vec{k}\cdot\vec{r}}\ S(\omega) \tag{3.4.1}$$

where $H_{et}(\omega)$ - transmitter electrical network transfer function

$H_{er}(\omega)$ - receiver electrical network transfer function

$H_{tt}(\omega)$ - transducer aperture transfer function (transmitting)

$H_{tr}(\omega)$ - transducer aperture transfer function (receiving)

$D_t(\omega,\vec{r})$ - beam diffraction pattern transfer function (transmitting)

$D_r(\omega,\vec{r})$ - beam diffraction pattern transfer function (receiving)

$\frac{1}{r}\ e^{j\vec{k}\cdot\vec{r}}$ - propagation path transfer function

$H_s(\omega,\vec{r},\vec{k}_i,\vec{k}_s)$ - scatterer transfer function

In general, the propagation vector $\vec{k}$ is complex. D_r and D_t are integral operators transforming the respective aperture transfer functions. When employing the same transducer to transmit and receive, the radiator and receiver transfer functions are given by

$$H_{tt}(\omega) = \frac{Z_r(\omega)}{Z_1(\omega) + Z_r(\omega)} \qquad (3.4.2.a)$$

$$H_{tr}(\omega) = \frac{Z_2(\omega)}{Z_2(\omega) + Z_r(\omega)} \qquad (3.4.2.b)$$

where $Z_1(\omega)$ and $Z_2(\omega)$ are the electro-mechanical impedances of the transducer element and $Z_r(\omega)$ is the mechanical radiation impedance of the acoustic medium into which the transducer is radiating. It is customary to normalize the radiation impedance with respect to the characteristic impedance of the medium so that for $ka_T > 5$ the normalized radiation impedance is essentially unity. In general, the impedances characterizing the transducer will be approximately the same whether transmitting or receiving so that we may put $Z_1(\omega) = Z_2(\omega)$ and thereby assure reciprocity at the transducer inputs since $D_t(\omega,\vec{r}) = D_r(\omega,\vec{r})$.

The matching electrical networks are not necessarily the same for transmitting and receiving although in our case they were. Hence, if only monostatic far-field operation is considered, the transducer aperture and beam diffraction pattern transfer functions may be combined into equivalent beam transfer functions $\Psi_t(\omega) = \Psi_r(\omega)$ as in Section 3.2. With these simplifications, (3.4.1) becomes

$$S_{rec}(\omega) \simeq KH_s(\omega,\vec{k}_i,-\vec{k}_i)\ \Psi^2(\omega)\ H_e^2(\omega)\ e^{2\gamma r}\ S(\omega) \qquad (3.4.3)$$

and for a non-dissipative medium, by (1.3.2)

$$s_{rec}(t) \simeq \frac{K}{2\pi} \int_{-\infty}^{\infty} H_s(\omega,\vec{k}_i,-\vec{k}_i)\ \Psi^2(\omega)\ H_e^2(\omega)\ S(\omega)\ e^{-j\omega(t-2r/c)}\ d\omega \tag{3.4.4}$$

where K is a scale factor. If the scatterer is relatively frequency insensitive in the frequency region where $\Psi^2(\omega)$ and $H_e^2(\omega)$ are of significant amplitude [or alternately, H_s oscillates about some mean value much more rapidly than $\Psi^2(\omega)\ H_e^2(\omega)$], $H_s(\omega,\vec{k}_i,-\vec{k}_i)$ may be equated to a constant and moved outside the integral.

Finally, if $S(\omega) = 1$ corresponding to the spectrum of a δ-function impulse at time $t = 0$, then it is clear from (3.4.3) that the magnitude spectrum of the received pulse $S_{rec}(\omega)$ is proportional to the power spectrum of the actual ultrasonic pulse.

From the forms of the received pulse and the input pulse, the network response and therefore the acoustic pulse can be evaluated, although in practice this may have to be done numerically. Referring to Table 4.1, the -6 dB bandwidth of the magnitude spectrum $|S_{rec}(\omega)|$ of the received 3.5 MHz pulse is 1.3 MHz. This indicates that the 3 dB bandwidth of the ultrasonic pulse is about 1.3 MHz. The percentage bandwidth ($\equiv$ 100%/Q) of the ultrasonic pulse is therefore 36%. However, as the same transducer is being used to transmit and receive, the received pulse 3 dB bandwidth is more appropriate and will be employed here.

3.5 Effect of Absorption on the Pulses

In Section 3.2 a first order correction for the absorption by the medium was obtained by suitably redefining the absorption coefficient

so as to permit the use of Fourier transforms. This same technique may be used to obtain 'exact' solutions. Comparing (3.2.2) and (2.4.11) or (C.1.1), the forms of the integrals are seen to be similar. Thus with appropriate changes in the interpretation of the parameters, (2.4.11) can also represent a pulse propagating in a non-dispersive square-law medium. To illustrate this for a rectangular video pulse, we set $\alpha = \gamma^2$ and $[\langle R \rangle |A_c| L\pi \text{ ab } k_c] = 1$. Then, letting $\omega_c \to 0$, (C.1.5) reduces to

$$s_r(t_r) = \frac{1}{2} \text{erf} \left(\frac{t_r - \Delta T}{2\sqrt{\alpha}} \right) - \frac{1}{2} \text{erf} \left(\frac{t_r + \Delta T}{2\sqrt{\alpha}} \right) \tag{3.5.1}$$

which is identical to the solution obtained by Gorshkov (1957) for a rectangular video pulse propagating in a square-law absorbing medium. With the above changes (C.1.3) and (C.1.5) represent the general solutions for a cosine and a rectangular RF pulse propagating in a square-law medium, respectively.

Using the same stratagem Gorshkov also derived the solution for a rectangular video pulse propagating in a linear absorbing medium. For a linear absorbing medium we require transforms of exponential integrals of the type

$$\int_{-\infty}^{\infty} e^{-\gamma|\omega|} \, S(\omega) \, e^{-j\omega t_r} \, d\omega$$

where $\gamma = 2\alpha c_2 \tau$. By the methods employed in Section 2.4, the solution may be readily obtained becoming for the rectangular video pulse of width $2\Delta T$

$$s_r(t_r) = \frac{1}{\pi} \tan^{-1} \left(\frac{t_r - \Delta T}{\gamma} \right) - \frac{1}{\pi} \tan^{-1} \left(\frac{t_r + \Delta T}{\gamma} \right) \tag{3.5.2}$$

However, the RF pulse expressions are somewhat more complicated than in the case of the square-law medium. For the unit amplitude cosine pulse of width $2\Delta T$ we obtain

$$s_r(t_r) = \text{Re}\ [F(\omega_c) + \tfrac{1}{2}F(\omega_1) + \tfrac{1}{2}F(\omega_2)] \qquad (3.5.3)$$

where

$$F(\omega) = \frac{j\, e^{-j\omega t_{ro}}}{2\pi}\ [e^{-\gamma\omega}\ E_1(-\gamma\omega - j\omega u) - e^{\gamma\omega}\ E_1(\gamma\omega - j\omega u)] \Bigg|_{u = t_{ro} + \Delta T}^{u = t_{ro} - \Delta T}$$

and $\omega_1 = \omega_c - \omega_o$, $\omega_2 = \omega_c + \omega_o$ and $\omega_o = \pi/\Delta T$; $E_1(z)$ is the complex exponential integral defined as [Abramowitz and Stegun (1965)]

$$E_1(z) = \int_z^\infty \frac{e^{-\lambda}}{\lambda}\, d\lambda \qquad (|\arg z| < \pi)$$

As before, the solution for the rectangular pulse is simply $F(\omega_c)$ which reduces to (3.5.2) as $\omega_c \to 0$.

In contrast to the incident pulses, the scattered pulses appear increasingly smeared out as $(\alpha c_2 \tau)$ increases. The greatest distortion of the pulse will occur near $t_r = \pm\Delta T/2$. This is to be expected since the lower and higher sideband frequencies are associated with the portions of the pulse varying most rapidly. The pulse distortion is proportional to the pulse bandwidth. At the center of the pulse $s(t_r)$, the frequency is approximately equal to $\omega_c/2\pi$ and the total attenuation is represented by $\exp(-2\alpha_c c_2 \tau)$. This can be seen more clearly by considering the derivative (C.1.6) or the envelope derivative factor $B\, \dot{s}_o(t_r)$ in (3.2.5). For the cosine pulse and $\frac{\partial \Phi}{\partial k_c} = 0$, $B\, \dot{s}_o(t_r)$ becomes

$$B\,\dot{s}_o(t_r) = -2\,\frac{\alpha_c}{|\omega_c|}\,c_2\tau\,\dot{s}_o(t_r)$$

$$= -\alpha_c\,\frac{\omega_o}{|\omega_c|}\,(c_2\tau)\,\sin\omega_o t_r \qquad (3.5.4)$$

where $\alpha = \alpha_c \left|\frac{\omega}{\omega_c}\right|$, $\omega_o = \pi/\Delta T$ and $t_r = t - 2r_o/c_1 - 2\tau$.

Effects of Differential Absorption on the Measurements

At 5.0 MHz the absorption in fatty whitefish is about 3 dB/cm or $\alpha/f = 6.9 \times 10^{-8}\,cm^{-1}$. Thus, for a sample thickness of 1.17 cm the return (two-way) loss is 7 dB at ω_c. For a bandwidth of 1.2 MHz, $|B_{max}| = 9.7 \times 10^{-2}$ or less than 10% distortion. The normalized signal return $s_r(t_r)$ from an impulse scatterer in the absorbing medium after compensation at the center frequency may be expressed as

$$s_r(t_r) = A(t_r)\,e^{-j\delta(t_r)} = \tfrac{1}{2}\,[(1 + \cos\phi_r) - jB\,\sin\phi_r] \qquad (3.5.5)$$

where $\phi_r = \omega_o t_r$. The effect of the absorbing medium can then be seen by integrating the modulus squared of (3.5.5) from $-\pi$ to π, or

$$\int_{-\Delta T}^{\Delta T} |A(t_r)|^2\,dt_r = (3/4 + B^2/4)\,\Delta T \qquad (3.5.6)$$

Eq. (3.5.6) shows that to first order the apparent pulse intensity at the integrator output is too large by $\varepsilon_I = B^2/3$. For the example we gave above, the maximum relative error in the measured pulse energy is $< 3.3 \times 10^{-3}$. It should be noted that this error is inversely proportional to the pulse width squared since

$$\frac{1}{3} B^2 = \frac{1}{12} \left(\frac{\alpha_c}{f_c}\right)^2 \frac{(c_2\tau)2}{\Delta T^2} \qquad (3.5.7)$$

Finally, if the backscatter is integrated over an interval $L = \frac{1}{2}c_2 T_\ell$

$$\bar{\varepsilon}_I \simeq \frac{1}{12} \left(\frac{\alpha_c}{f_c}\right)^2 \left(\frac{1}{\Delta T}\right)^2 \frac{1}{L} \int_0^L r^2 \, dr = \frac{1}{36} \left(\frac{\alpha_c L}{f_c \Delta T}\right)^2 \qquad (3.5.8)$$

the average error for L = 1.17 cm is reduced to $\bar{\varepsilon}_I = 2.7 \times 10^{-4}$.

It is slightly more difficult to compute the error for the pulse magnitude. Expanding the integrand corresponding to (3.5.6) for $|B_{max}| << 1$, the correction becomes $\varepsilon_M \simeq B^2/2$ or 50% greater than ε_I. The average error will be $\bar{\varepsilon}_M \simeq \frac{3}{2} \bar{\varepsilon}_I$.

In view of the magnitude of the other sources of error, see Chapter 4, we may thus neglect the effects of the differential absorption in the analysis of our experimental data.

3.6 Near-field Backscatter Measurements

It was indicated that by performing the backscatter measurements in the radiating near field at a distance a_T^2/λ from the transducer a number of practical advantages could be gained. Before discussing these advantages it will be useful to briefly describe the beam structure and point out the major differences between wideband and CW beams.

3.6.1 Ultrasonic Beam Characteristics

The most drastic changes in switching from CW to pulsed operation are observed in the near-field structure and to a lesser extent

in the side-lobe structure of the far field. The sharp nulls and extreme amplitude fluctuations characteristic of the CW near field are greatly smoothed with increasing bandwidth.

The well-known approximate solution for the circular aperture due to Lommel (1885) yields an axial intensity of the form

$$I(z) \simeq \left(\frac{P_o}{f'}\right)^2 \left(\frac{\pi a_T^2}{z\lambda}\right)^2 \left(\frac{\sin \frac{1}{4}y}{\frac{1}{4}y}\right)^2 \tag{3.6.1}$$

with

$$y = \frac{2\pi}{\lambda}\left(\frac{1}{f'} + \frac{1}{z}\right) a_T^2 \tag{3.6.2}$$

where f' is the point source distance (positive or negative) to the aperture and a_T is the aperture radius. The nulls occur at integer multiples of π, i.e. $\frac{1}{4}y = m\pi$. For a plane wave, f' is equal to ∞ and $m\pi = 2\pi(a_T^2/\lambda)/z$ is the path difference of the rays from the rim and center of the aperture to the axial point z. Many writers therefore normalize the path lengths with respect to a_T^2/λ, i.e. $s = z\lambda/a_T^2$.

Papadakis and Fowler (1971) investigated the effects of increasing the bandwidth on the beam structure. In their paper they present the results of numerical computations based on the CW solution for the circular aperture using empirically determined Fourier coefficients. Their results show that the near-field structure is free of sharp nulls if the bandwidth is wide enough and this is also confirmed by our measurements, see Fig. 3.2(a).

Adopting the convention of referring to the diffraction maxima and minima on the acoustic axis as $Y_n^{(+)}$ and $Y_n^{(-)}$, respectively, with $Y_o^{(+)}$ the maximum at s = 1.0, the axial intensity variation in Fig. 3.2(b)

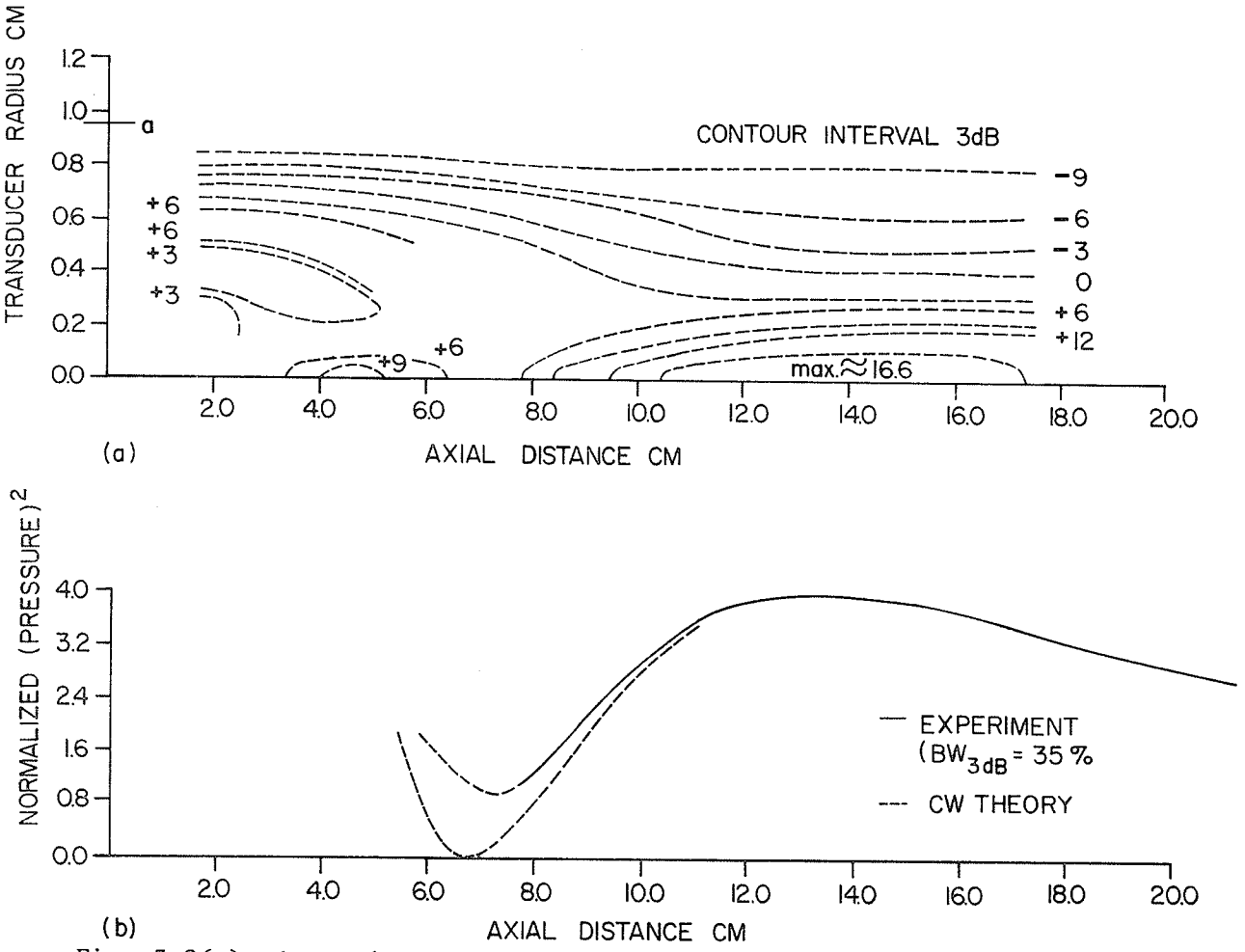

Fig. 3.2(a) Approximate sound intensity contours for a circular transducer aperture; f_c = 2.3 MHz, a = 0.95 cm, a^2/λ = 13.5 cm, target - 0.318 cm ϕ ball-bearing.

(b) Axial sound intensity variation.

indicates a pressure ratio $Y_o^{(+)}$: $Y_1^{(-)}$ of approximately 1.9 in contrast to a ratio of ∞ predicted for the CW case. (The ordinates and contours in Figs. 3.2 to 3.4 are normalized two-way received signal peak amplitudes.) Along the axis in the interval s = 0.9 to 1.1, in what we will call the transition region, the $Y_o^{(+)}$ maximum appears almost level and slightly broader than the CW beam. The beam profile at the $Y_o^{(+)}$ maximum for the 2.25 MHz transducer is shown in Fig. 3.3(a). For radial distances less than ¼ a_T, the measured and theoretical CW values are in close agreement. At larger off-axis distances, however, side-lobe fluctuations in the wideband beam are virtually absent.

3.6.2 Near-field Measurement Considerations

Although the use of transition region measurements has inherent disadvantages, it has some important practical advantages for in situ determinations of tissue backscatter. Using a conventional far-field criterion of $4a_T^2/\lambda$, for a 2 cm diameter aperture the minimum range at 5 MHz is 120 cm. The -3 dB beam diameter at this distance is 2 cm which is far too large for in situ measurements. Placing the specimen in the transition region, on the other hand, provides a narrow beam and, in view of the beam structure [see Fig. 3.2(a)], will yield approximate stationarity of the diffuse scattering.[1] Thirdly, the absorption loss

---

[1] An alternative is to use a focussed beam. It can be shown [Lommel (1885); Cf. Born and Wolf (1964)] that the field distribution in the plane of the geometrical focus is the same as in the far field, see Fig. 3.3(b). The important thing to remember, however, is that plane-wave conditions are only realized if the scatterer is located entirely within the main lobe of the beam and vice versa. Another aspect of the use of focussed transducers is the application of variable focussing as a sensing tool [Ishimaru (1969)]. It is clear from our discussion in Section 2.4 that a finely focussed beam could be used to determine the surface relief spatial correlation interval.

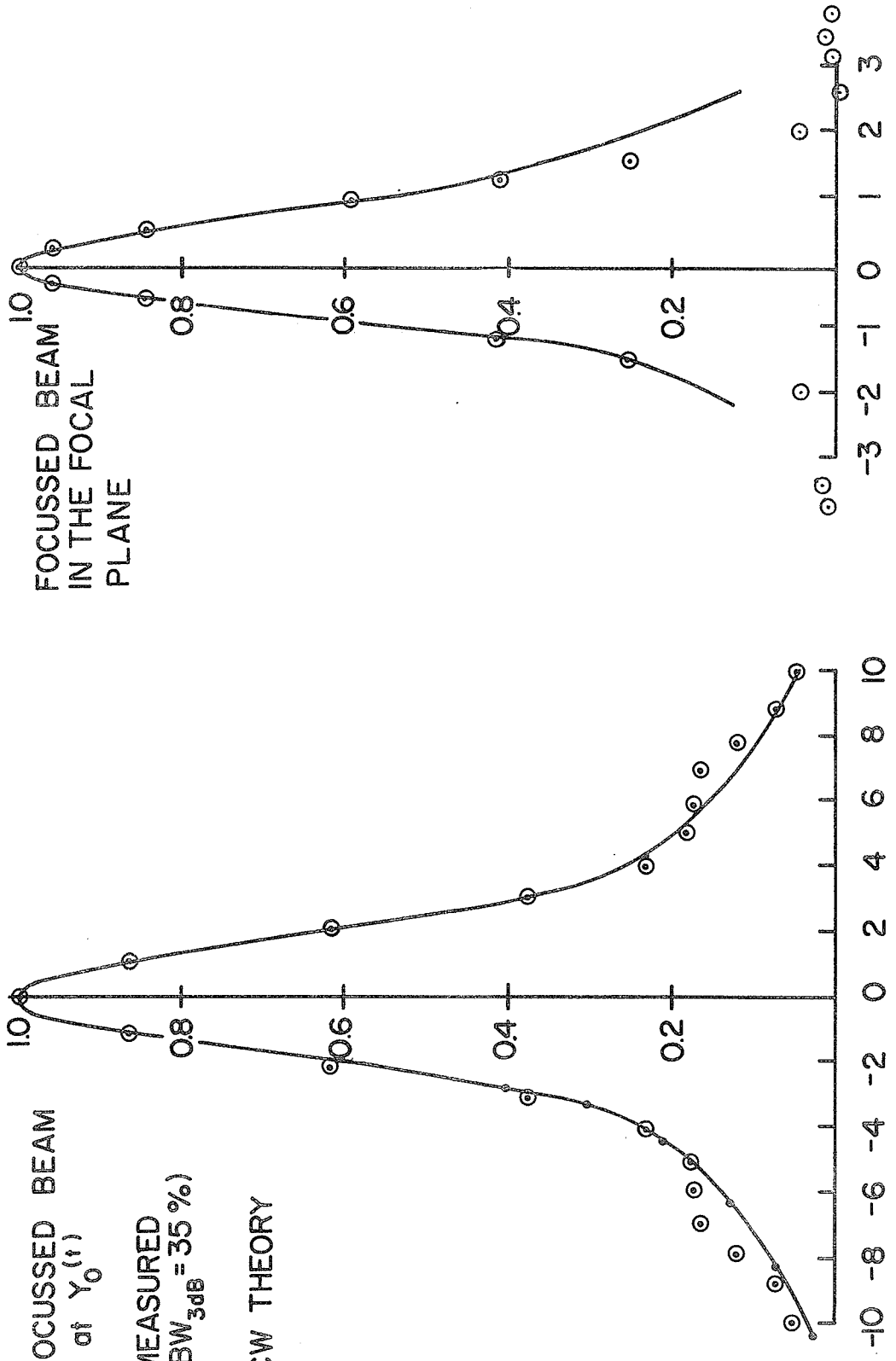

Fig. 3.3 Normalized two-way beam cross-sections: (a) unfocussed transducer; f_c = 2.3 MHz, a = 0.95 cm; (b) focussed transducer; f_c = 7.0 MHz, a = 0.975 cm, focus = 19 cm.

in a water column of 120 cm is about 14 dB at 5 MHz. Utilizing the transition region, the transducer-target separation is decreased by a factor of four and the absorption is reduced 11 dB thereby improving the signal to noise ratio by 23 dB--an important advantage considering the low level of the backscatter signals.

The disadvantages of this approach are the sacrifice of the relatively simple far-field conditions and the lack of validity of some of the theoretical results based on the Fraunhofer approximation. However, this can be rather misleading. It is not difficult to show [see Melton and Horton (1970)] that under normal conditions, short of zero beamwidth incidence, the transducer will be in the Fresnel field of the surface when it extends across the entire beam; this is sometimes overlooked. For a point source the criterion for validity of the Fraunhofer assumption may be expressed approximately as (ibid.)

$$r_{io} \sin^{-2}\theta_o < \lambda/8 \qquad (3.6.3)$$

where θ_o is the half-angle beamwidth of the source. Restating this condition for a surface located in the transition region, i.e. with $r_{io} = a_T^2/\lambda$ and $\sin\theta_o \simeq a_T/4r_{io}$, we see that the criterion is met for a point receiver on the axis but not over the finite aperture of the actual transducer. If we utilize the Fraunhofer far-field expressions we should therefore expect some significant errors in the case of coherent scattering from structures extending across the beam.

The error incurred may be estimated by comparing the measured and theoretically predicted reflection from a reflector situated in the near field of the transducer. The average received CW signal has been

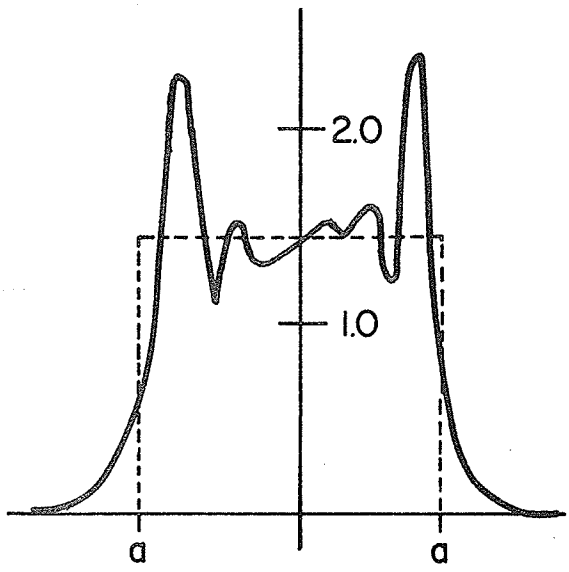

Fig. 3.4 Near-field pattern 2 cm from aperture at 2.3 MHz, a = 0.95 cm.

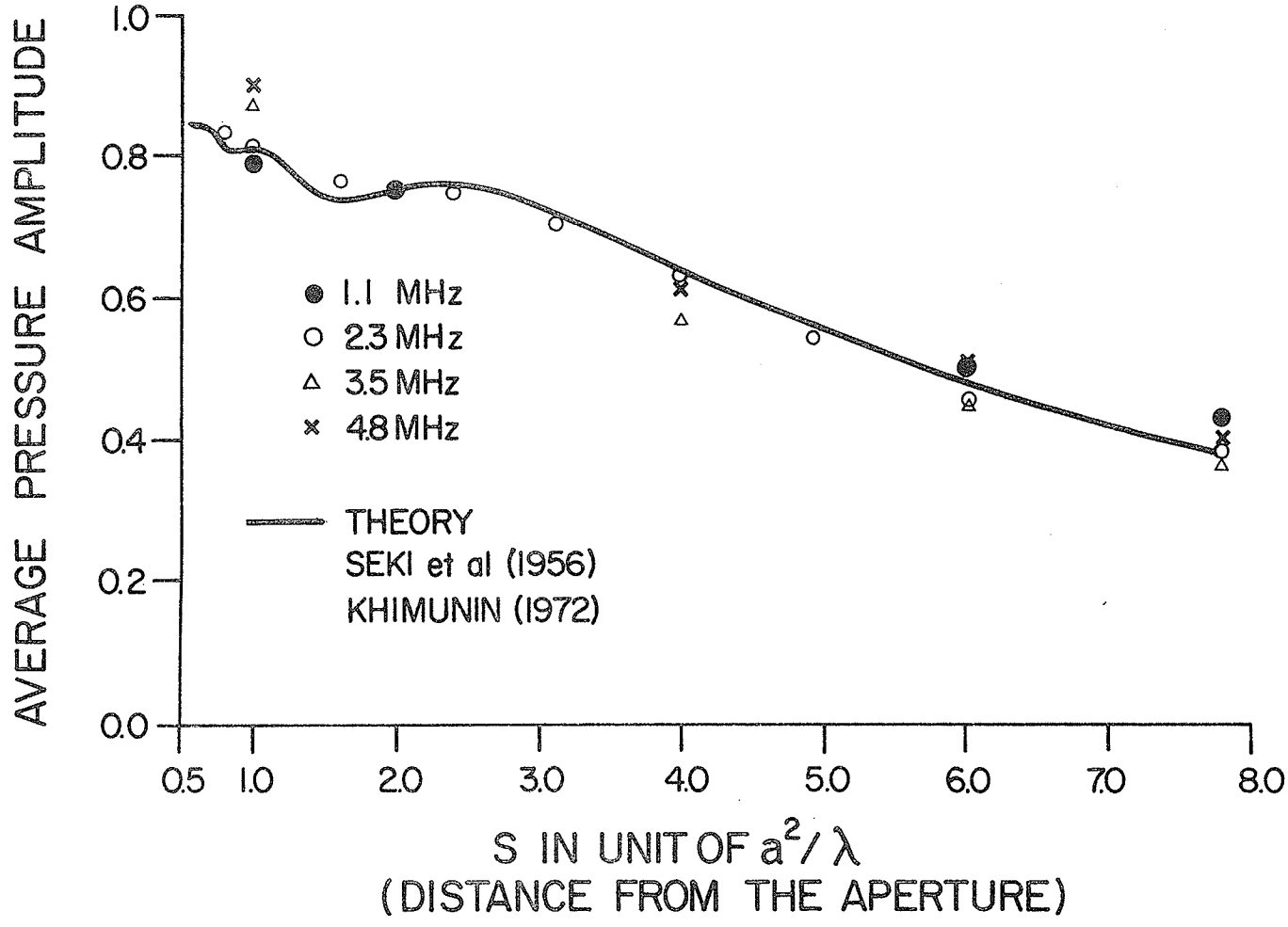

Fig. 3.5 Average normalized pressure amplitude over the receiving transducer aperture as a function of transducer separation in units of a_T^2/λ.

computed for the equivalent problem of two identical pistons by Seki et al. (1956) and more recently by Khimunin (1972). The theoretical values show that the reflection is essentially independent of ka_T (within 0.3%) for $ka_T > 50$ and $s > 1.0$ (reflector at $s > 0.5$) and this is also approximately confirmed by experiments. The theoretical and experimental values of the received signal amplitude (proportional to the average pressure amplitude over the receiving aperture) are plotted in Fig. 3.5. The experimental values were obtained using the pulses described in Chapter 4; the diameters of the transducer crystals and the reflector were 19 mm and 50 mm, respectively. The latter therefore did not intercept the entire beam at the farthest position ($s = 3.9$). Nonetheless, the experimental results (compensated for the absorption by the water column) are in substantial agreement with the theoretical CW values. Using the radius $r_{eq}^{(1)}$ of the effective beam cross-section $\Lambda^{(1)}(s)$ given in Table 4.3 as the radius of the equivalent disc, the discrepancy between the theoretical cross-section (2.2.14) and the measured value was on the average -4.6 dB.

It should be noted that the graph in Fig. 3.5 exhibits a point of inflection at $s \simeq 2.0$ (reflector at $s \simeq 1$) and a response that is practically constant over the range from $s = 1.3$ to $s = 2.8$. Hence, for the coherent planar scatterer extending normally across the beam, the response will also be approximately constant as in the case of the random point-scatterers.

In many applications it is desirable to perform the measurements with the transducer either close to or in contact with the medium. An exact evaluation of the resultant near-field problem is out of the question.

However, by treating the incident field as a pseudo-random distribution, the problem can be treated in an approximate manner. Such an approach has been used by the author [Freese (1973)] and others, and is justified by the fact that the equivalent point-scatterers are randomly distributed with respect to the incident field. It follows from an application of the principle of conservation of beam intensity that in the absence of coherent components, the backscatter level for $s < 1.0$ will remain nearly constant.

3.6.3 Pulse Distortion in the Beam

When using short pulses some distortion of the pulses is unavoidable even in the far field. This is due to the pulse bandwidth and the dependence of the beam on wavelength. As was indicated earlier, factoring the beam function $\Psi(\omega,\theta,\phi)$ from under the integral, e.g. in (3.2.2), implies a constant beam pattern over the bandwidth of the incident signal $S(\omega)$. For this to be the case, the percent change in the signal envelope must be only a small fraction of the time required for this change to propagate across the transducer aperture. In other words, we require that $\Delta t = 2a_T/c$ be much smaller than the pulse rise time ΔT_r, where a_T is the aperture radius and c is the velocity. Making use of the bandwidth rise time relationship for an RF pulse $\Delta T_r \simeq 0.7/BW$, this condition may be expressed as

$$BW << \frac{0.35c}{a_T}$$

For an aperture 2 cm in diameter, the bandwidth would have to be less than 50 KHz. In contrast, the ultrasonic pulses used in the experiments

have bandwidths considerably in excess of 50 KHz (Table 4.1). The effect of this is a smoothing of the beam pattern in the near field as was shown and also a certain amount of distortion at the beam periphery and in the near field. However, provided the pulse duration is at least several cycles in length (> 4) at the center frequency and there are no large coherent scatterers at the beam periphery, the error resulting from this distortion will normally be quite small when performing measurements either in the far field or in the transition region. The reason for this is that the maximum contribution to the scattering will be from an annular region centered at an angle $\theta \approx \sin^{-1}(1.4/ka_T)$ off axis, while the distortion does not become significant until $\theta \approx \sin^{-1}(\pi/ka_T)$ at $s = 1.0$. Another factor tending to reduce the effects of distortion is the intrinsic averaging of the process. This becomes important in the case of near-field measurements of diffuse scattering at ranges less than $s = 0.75$.

CHAPTER 4

EXPERIMENTAL METHODS

In this chapter the principal methods and means employed for the experimental measurements are described. The instrumentation and techniques used for the measurement of ultrasonic backscatter, velocity and absorption are discussed in the first four sections. These sections also contain important calibration data, including the equivalent volumes, the beam and pulse characteristics and various transducer and instrument parameters that are required for the measurements reported in Chapter 5. The last two sections describe the chemical and histological methods that were used to determine the composition and physical properties of the different media investigated.

4.1 Backscatter Measurements

This section provides details of the operating characteristics, calibration and accuracy of the electronic instrumentation developed for the backscatter measurements. Certain data on the characteristics of the pulses employed in the experiments, including an examination of the pulse distortion due to shortcomings in the frequency response of the instrumentation, is also given.

4.1.1 Instrumentation: Backscatter Analyzer Operation

A block diagram of an analyzer which was designed for processing of the backscatter signals is shown in Fig. 4.1. In essence, the analyzer is a high-frequency version of the familiar echo integrator employed in studies of fish abundance estimation and underwater sound scattering. It has, however, a number of additional features not normally found in sonar equipment of this type.

An early version of the analyzer was described by DeGroot (M.S., 1970). For this reason, since the instrument is not of primary interest here, the circuit details will not be discussed except in a few instances where subsequent modifications significantly altered the instrument characteristics.

When operating monostatically, a single transducer acts as both transmitter and receiver. Different pulse carrier frequencies (1 - 10 MHz) may be selected by changing transducers and switching in appropriate matching networks (Fig. 4.1). The matching networks greatly improve the S/N by both matching and bandlimiting the input and by further shaping the RF pulse to approximate a cosine pulse of the form

$$\begin{aligned} s(t) &= \tfrac{1}{2}\left(1 + \cos\frac{\pi t}{\Delta T}\right)\cos\left(\omega_c t + \phi\right) && |t| \le \Delta T \\ &= 0 && |t| > \Delta T \end{aligned} \qquad (4.1.1)$$

After pre-amplification of the RF signal, the signal is passed through a time varied gain (TVG) amplifier.

The main function of the TVG is to compensate the backscatter for attenuation rather than $1/r^2$ spreading. This is required to approximately stationarize the backscatter as was discussed in Chapter 3.

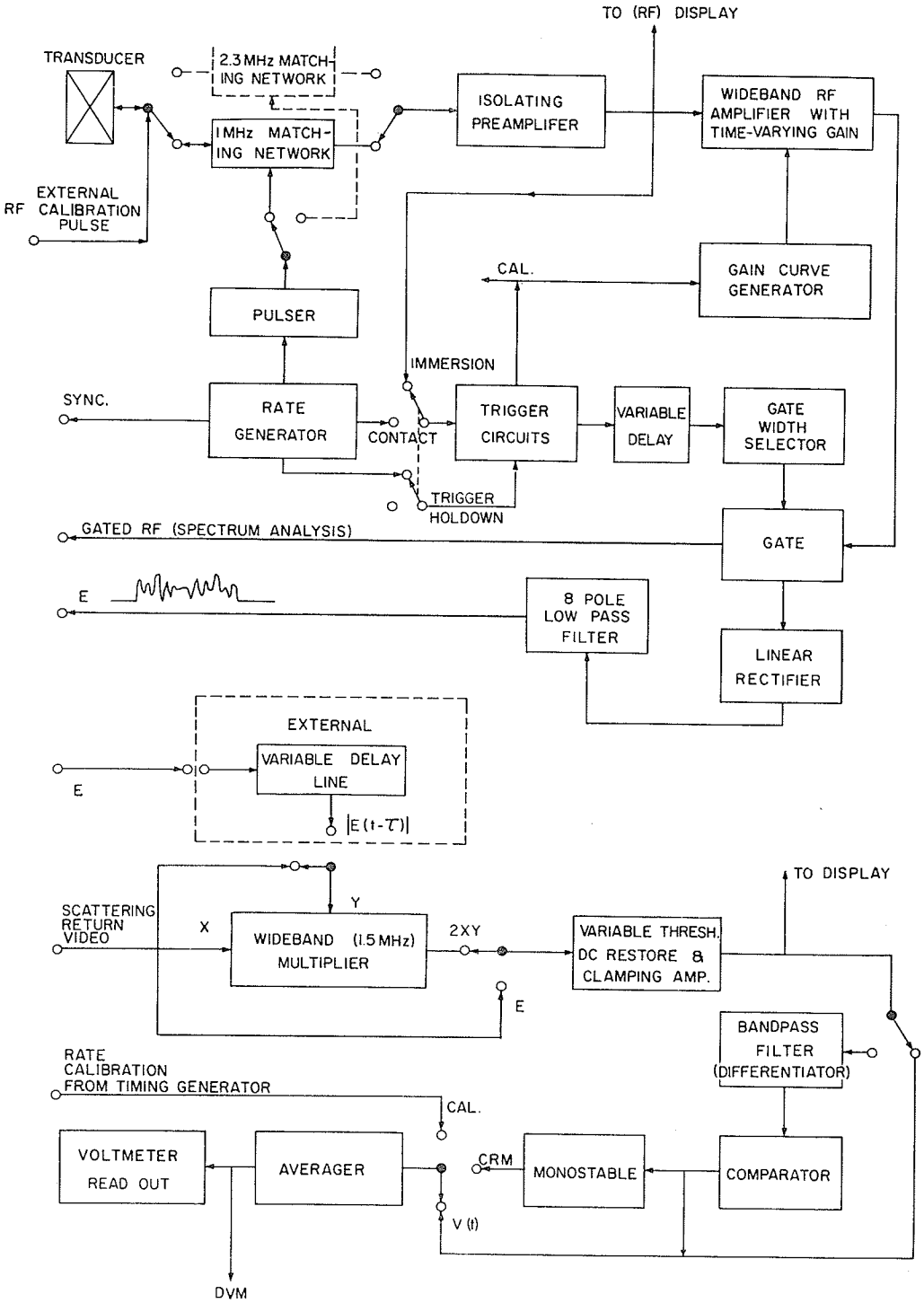

Fig. 4.1 Block diagram of the analyzer.

The TVG amplifier consists of a voltage controlled wideband IC amplifier; the gain varies exponentially with applied control voltage. The TVG amplifier is triggered either by the transmitted pulse when operating in the contact mode or the first echo return from the surface of the tissue when using the immersion mode as illustrated in Fig. 4.2. Multiple and false triggering, e.g. on air bubbles in the water delay path, are prevented by a lock-out circuit.

Following stationarization, the signal is gated. The depth and width of the gate are variable but typical values used for most of the measurements are 7.5 μsec and 15 μsec, corresponding to 5.8 mm and 11.6 mm, respectively. The initial depth interval of about 6 mm is normally sufficient to prevent the front surface echoes from contaminating the backscatter from the myomere. By using a sufficiently narrow gate width, the envelope amplitude as a function of time (depth) may be obtained.

After full-wave rectification, the gated signal is filtered to remove the higher order sidebands which arise as a result of the rectification process. This is necessary to insure a uniform response at each processing stage over the range of input frequencies (1 - 10 MHz) and to prevent the slope detector circuit from responding to the higher band signals (centered about even multiples of the carrier frequency).

The averager integrates the signal V(t) over the gate interval T_ℓ forming the average

$$I[V(t)] = K' \int_{-\infty}^{t} V(u)\, e^{-\frac{(t-u)}{RC}}\, du$$

$$\simeq K \int_{0}^{T_\ell} V(u)\, du \qquad (4.1.2)$$

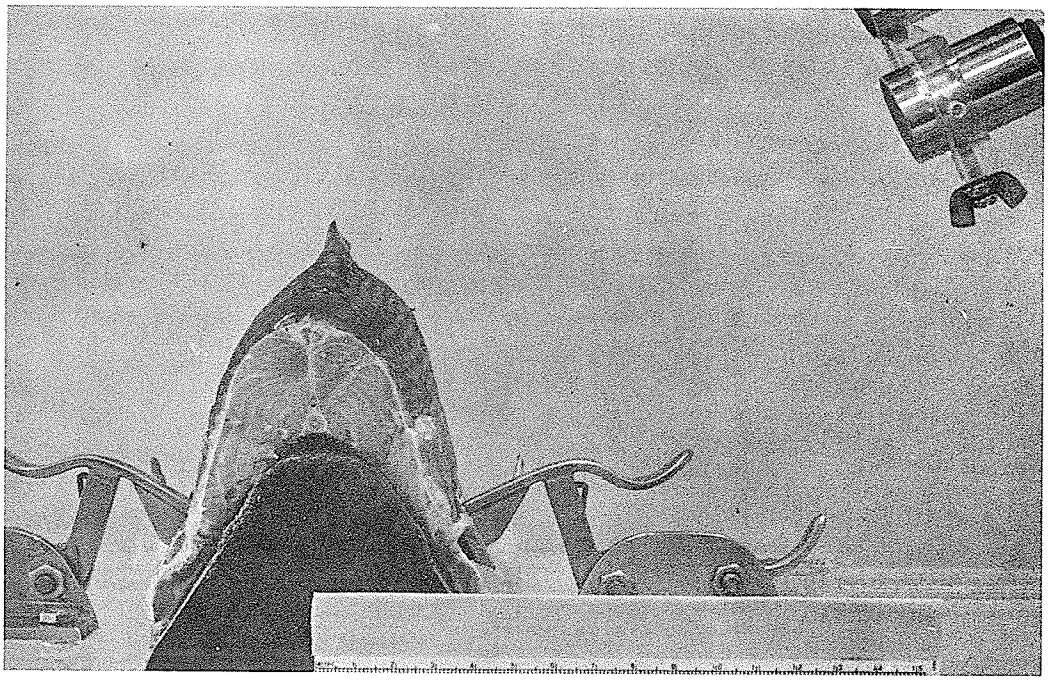

Fig. 4.2 Immersion operation

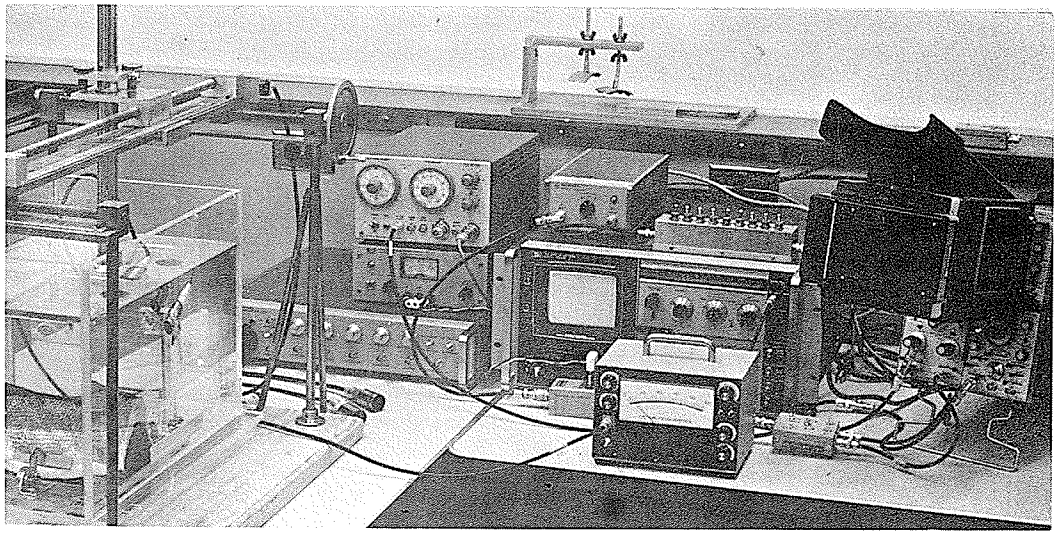

Fig. 4.3 Test facility

where K is a constant and RC is the time constant of the integrator. The result is displayed on a panel meter (Fig. 4.3) or on a DVM.

The signal V(t) is determined according to the processing mode selected:

i) the integral of the envelope is obtained by selecting V(t) = E(t);

ii) applying E(t) to both the X and Y inputs of the IC multiplier yields $E(t)^2$, see Fig. 4.4;

iii) delaying the Y input by τ μsec by means of an external delay line permits the point by point measurement of the autocovariance function of the envelope

$$I[E(t)\ E(t-\tau)] = K \int_0^{t-\tau} E(u)\ E(u+\tau)\ du \qquad (4.1.3)$$

The integrator is preceded by a variable threshold (discriminator) and clamping operational amplifier. The purpose of the clamp is to restore the DC signal.

The variable threshold has several functions. The cumulant distribution of the envelope (or envelope squared) of a member aggregate may be obtained by varying the threshold which is calibrated to read directly the equivalent signal amplitude. The density distribution may then be easily obtained from the cumulant distribution. The threshold is also used to insure that the signal amplitudes do not exceed the dynamic range of the instrument.

The instrument becomes a combined pulse height analyzer and counting rate meter (CRM) when the constant amplitude output from the comparator is applied by way of a one shot to the averager. This mode is

also used to check the gate triggering when the immersion mode is employed and an oscilloscope is not available.

The repetition frequency may be varied but normally a fixed frequency of 1 KHz was selected. The frequency is verified by switching the analyzer to the CAL. position.

The principal signal waveforms may be accessed for monitoring the operation of the analyzer and further processing, e.g. spectrum analysis of the gated backscatter.

4.1.2 Analyzer Calibration

The attenuators in the instrument were calibrated against a precision reference attenuator to an accuracy of 0.2 dB. The gain of the analyzer electronic circuitry was checked by the insertion of a 3-cycle boxcar RF burst (usually 2.25 MHz) at the analyzer transducer input. Overall calibration of the backscatter analyzer was verified prior to each series of backscatter measurements by determining the pulse return from a stainless steel ball-bearing reference target placed at the $Y_o^{(+)}$ maximum of the transducer. The short term stability of the analyzer under normal daytime operating conditions using the immersion mode was better than ±0.2 dB/hr.

Multiplier Response

The multiplier response was measured over a 20 dB range of the input signal for frequencies between 60 KHz and 1.5 MHz. The exponent (squaring mode) decreased from the correct value of 2.0 at 0.5 MHz to 1.96 at 0.9 MHz. Otherwise, the response was essentially constant over a 20 dB dynamic range of the input signals. A table of correction factors

for the different signal pulses was established experimentally (Table 4.1) by means of point by point numerical evaluation. The maximum error in the multiplier response at the shortest pulse lengths employed is about 8%.

TABLE 4.1

PULSE CHARACTERISTICS AND MULTIPLIER RESPONSE

Carrier Frequency MHz	RF Pulse Width (FWHM) μsec	Video Pulse 3 dB Bandwidth MHz ×0.58	Approximate Filtered Video Pulse 3 dB Bandwidth MHz ×0.58	Multiplier Correction Constant (Experimental)
1.09	2.06	0.17	0.17	1.06
2.25	1.10	0.32	0.32	1.00
3.45	0.80	0.44	0.44	1.00
4.80	0.54	0.65	0.58	1.04
7.00	0.37	0.95	0.70	1.08

The integral of the ideal cosine pulse amplitude (4.1.1) is given by $I(E) = KA_o\Delta T$ where A_o is the peak envelope amplitude and $2\Delta T$ is the pulse width. The integral corresponding to the pulse energy is thus $I(E^2) = 3/4\ KA_o^2\Delta T$. The performance of the instrument and the deviation of the actual pulse from the postulated pulse were compared at the different frequencies; the results are given in Table 4.2. The experimental and calculated values are in generally good agreement.

The measured values of $K\Delta T$ correspond to the filtered video pulse full width half maximum (FWHM) times the constant K; the filtered

TABLE 4.2

ANALYZER PERFORMANCE AND PULSE DISTORTION

Carrier Freq. MHz	I(E) Meas.	A_o † Meas. Volts	$K\Delta T$*† Meas. (FWHM)	$K\Delta T$ Calc. (FWHM)	A_o^2 † Meas.	A_o^2 Calc.	I(E^2) Meas.	I(E^2)** Calc.	I(E^2) Calibration Std. Error %	Backscatter Strength Std. Error %
1.09	14.5	0.82	17.8	17.7	0.65	0.67	17.5	17.7	6.7	9.1
2.25	5.8	0.60	9.3	9.67	0.37	0.36	5.0	5.24	6.3	8.9
3.45	4.6	0.72	6.4	6.39	0.51	0.52	5.1	5.00	6.5	9.0
4.80	3.3	0.66	5.1	5.00	0.40	0.43	3.2	3.30	7.8	9.1
7.00	4.1	0.79	4.25	5.20	0.63	0.62	4.9	4.87	9.7	10.3

(*) Instrument constant K = 8.5

(**) Multiplier functional relationship $V(t) = 2E(t)^2$

(†) Measured with HP 180 oscilloscope

pulse bandwidths were given in Table 4.1. The measurement accuracy of the 3.5 - 7.0 MHz values is about ±5%. Bearing this in mind, a value of $K\Delta T$ less than the measured value indicates a narrower pulse than the ideal cosine shape and vice versa. Thus, the 7.0 MHz result indicates significant stretching of the pulse (with about 10% overshoot) by the filter network and consequently a considerable divergence of the actual pulse from the cosine pulse (4.1.1). The fact that the measured value of A_o^2 at 7.0 MHz does not show any significant fall-off is likely due to overshoot.

TVG Amplifier Response

The response of the IC amplifier was true exponential as a function of applied bias voltage to within ±4% over a 20 dB dynamic range at 3.0 MHz. To improve the S/N of this stage only 13.5 dB of this range was utilized, thus limiting the TVG to a maximum of 8 dB/cm for a 7.5 μsec gate delay and 15 μsec gate width. The linearity of the ramp voltage (generated by an op-amp integrator) in the range of interest was approximately ±2% (0 - 6 dB/cm ramp) yielding a minimum TVG accuracy of about ±6%. The linearity of the ramp, and thus the performance of the TVG amplifier, could certainly be improved further. The problem, of course, is to determine the magnitude of the TVG, since even with a TVG of 4 dB/cm a 50% error is possible if the absorption is unknown. The effect of this is shown in Fig. 4.5. Since the absorption increases with frequency, the maximum possible error in Ω rises exponentially with frequency, and as a result the measurement accuracy deteriorates rapidly at high frequencies.

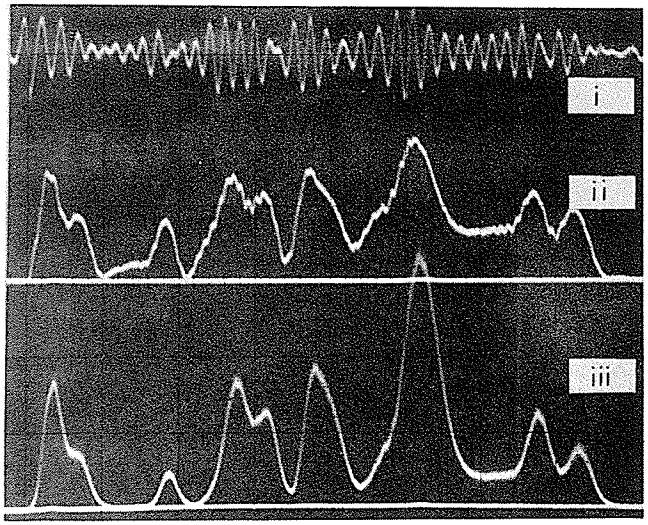

Fig. 4.4 Typical 2.3 MHz back-scattered signal from whitefish muscle

i) RF signal; sweep = 2 μsec/div
ii) Gated envelope; TVG 3 dB/cm
iii) Square of envelope; $y = 2x^2$

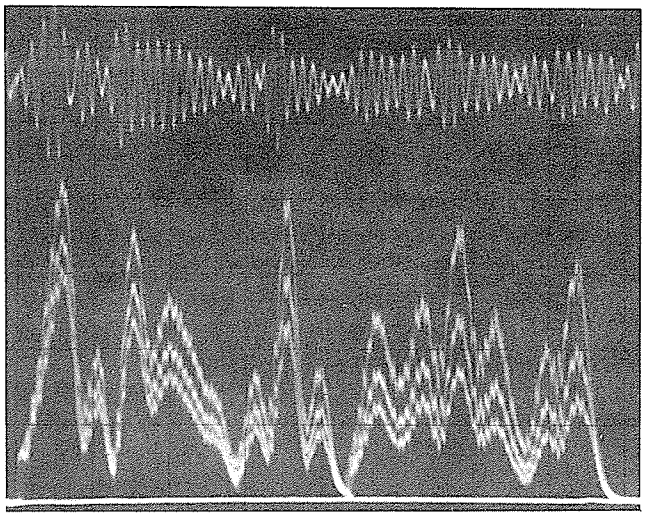

Fig. 4.5(a) Effect of TVG on the signal envelope

TVG; 0 - 2.25 - 4.5 dB/cm
Center freq. = 3.45 MHz
Sweep = 2 μsec/div

Fig. 4.5(b) Effect of TVG error on Ω

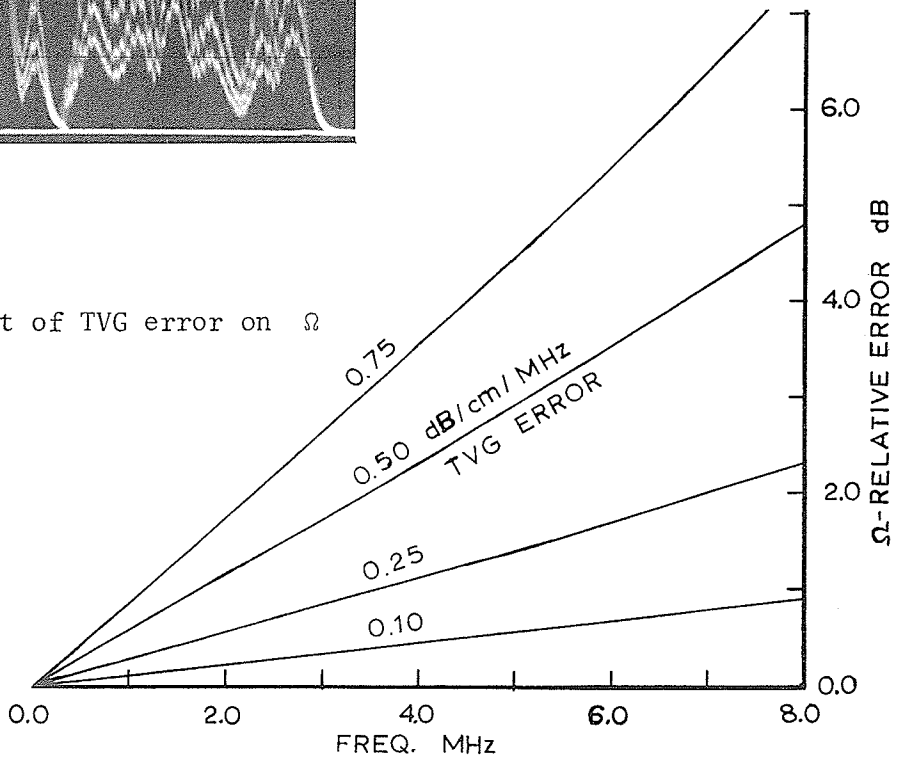

Rectifier Response

The offset in the rectifier stage was significantly improved by employing Schottky Hot Carrier diodes. The remaining offset error was further compensated by a counter offset of 2.5% (full scale) in the integrator in the linear operating mode and 1.2% in the squaring mode. Except at low signal levels below about 0.1 V of the 0 to 1.1 V dynamic range, the linearity of the rectifier was better than ±3% over the range of input frequencies.

Measurement Accuracy

The standard errors of the $I(E^2)$ calibration values used to normalize the backscattered pulse energy (backscatter strength) and the standard errors of individual determinations of the backscatter strength σ_s are tabulated in Table 4.2. The error in σ_s in this case does not include possible errors in the TVG magnitude nor possible errors associated with the experimental subject medium, e.g. interference from surface reverberation. These are considered separately.

The standard errors of the magnitude measurements $I(E)$ were slightly lower than in the case of the $I(E^2)$ measurements. At 2.3 MHz and 4.8 MHz the standard errors of the normalized backscatter magnitudes were 8.2% and 8.4%, respectively.

4.2 Reference Target Calibration

The problem of realizing a suitable target of known cross-section for the purpose of short pulse calibration is considered in this section.

The backscatter cross-section of a rigid sphere as a function of incident wavelength is known to fluctuate appreciably for $2\pi a < 20\lambda$ [Rayleigh (1896); Stenzel (1938)]. Moreover, it has been shown [Hickling (1962)] that for an elastic solid sphere the fluctuations can be even more extreme, nor are they, in general, attenuated with increasing frequency. Aside from simple weight considerations, this is the chief reason why a Dirichlet type target is normally employed in sonar calibration. The absence of oscillations in the cross-section of the Dirichlet or 'pressure release' sphere, Fig. 2.5, beyond about $ka = 5$ is explained by the fact that the circumferential or creeping waves are more rapidly attenuated than in the case of the rigid sphere. However, if the bandwidth of the incident pulse is sufficiently wide, then as Hickling's results show, these variations are smoothed out and the specular pulse return may be used for calibration purposes; only a small correction is necessary to compensate for the finite impedance of the sphere. The specular return, it should be noted, is not contaminated by any creeping wave contribution. Rheinstein (1968) investigated the composition of the backscattered pulses from a sphere by means of Fourier analysis of their time domain components. He showed that the specular cross-section of the sphere varies smoothly as a function of ka. Thus, for values of $ka < 40$ this should be borne in mind.

The reason for preferring a rigid sphere for calibration is the availability, low cost and high precision of stainless steel ball bearings. In contrast, an accurate and reproducible Dirichlet spherical target with a small cross-section is difficult to realize at high frequencies. One would be more or less forced to use a planar reflector

which has the disadvantages of being aspect dependent and causing pulse distortion because of the gain dependence on wavelength.

The minimum reference sphere diameter employed was ka = 14.6 at 1.1 MHz. The corresponding effective echoing area diameter ($\sqrt{2a\lambda/\pi}$) of 1.66 mm was still small in comparison to the beam diameter of 9.5 mm at the $Y_o^{(+)}$ diffraction focus (see Table 4.3).

The effect of halving and doubling the diameters of the ball bearings was investigated at the various wavelengths employed. The measured changes were generally within ±0.5 dB of the predicted change of 6 dB.

4.3 Transducer Parameters

Experimental values of the beam parameters of the various transducers employed in the experiments, specifically the carrier frequencies, the actual $Y_o^{(+)}$ distances, the beamwidths and the equivalent insonified volumes are given in this section. These values are compared to theoretical results (some of which were referred to earlier in Section 3.6) and published experimental CW data for both near- and far-field conditions.

The 1.1, 2.3, 3.5 and 5.0 MHz transducers were nominally 3/4 in. diameter immersion style supplied without tuning coils by Aerotech Laboratories. The transducer crystals were lead metaniobate composition ceramics and were sealed with flat epoxy matching layers. The Q's of the received pulses (Table 4.1) varied between 3.2 and 4.3.

Using a 1/8 in. ball bearing target, the near-field patterns of the transducers were mapped to determine the degree of field symmetry.

The near-field pattern at a distance of 20 mm from the 2.3 MHz transducer is shown in Fig. 3.4.

The axial magnitudes were similarly obtained (Figs. 3.2 and 3.3) and the measured positions of the $Y_o^{(+)}$ maxima were compared with the calculated values $z = a^2/\lambda_c$. The results are given in Table 4.3 and agree more closely than might be expected in view of the pulse bandwidths and uncertainties in the effective crystal diameters. Some measurements at 7.0 MHz were made using a focussed transducer. The transducer, having a nominal diameter of 20 mm (the plated electrode diameter of an identical transducer measured 19.5 mm), exhibited a maximum at 19 cm from the aperture. In comparison, the $Y_o^{(+)}$ maximum of a similar but unfocussed transducer would have been at 44.3 cm from the aperture.

The average -6 dB beamwidth at the $Y_o^{(+)}$ maxima of the 3.5 MHz and 4.8 MHz transducers as measured by the above method was 5.45 mm which agrees well with the CW theoretical predictions that the -3 dB beamwidth at the $Y_o^{(+)}$ maximum is approximately one quarter the transducer diameter [Zemanek (1971)]. The 1.1 MHz beamwidth was 6.4 mm or 1.18 times wider than the mean value above. An increase in beamwidth, however, is also indicated as a/λ takes on values < 10 (ibid.); at 1.1 MHz $a/\lambda = 6.9$.

In order to compare measurements in the far field with measurements made in the transition region, $s = 1.0$, the beam characteristics were also determined at $s = z\lambda/a^2 = 3.9$. Values of the -6 dB beamwidths are given in Table 4.4. CW theory (ibid.) predicts a beamwidth equal to the piston (crystal) diameter at $s = 3.89$.

TABLE 4.3

BEAM CHARACTERISTICS AT $s = 1.0$ $[Y_o^{(+)}]$

f_c [(a)] MHz	Z Measured cm	$Z=a^2/\lambda$ [(b)] Calc. cm	-6 dB Beam Diameter [(c)] mm	$r_{eq}^{(1)}$ mm	$r_{eq}^{(2)}$ mm	$V_\ell^{(1)}=\int\Lambda_n^{(1)}(z)dz$ [(d)] cm^3 (±16%) [(f)]	$V_\ell^{(2)}=\int\Lambda_n^{(2)}(z)dz$ [(d)] cm^3 (±10%)
1.09	6.5	6.56	6.4	5.1	3.1	0.92	0.35
2.25	13.5	13.7	4.9	4.6	2.6	0.74	0.23
3.45	21.0	20.8	5.5	5.0	2.9	0.89	0.30
4.8	29.5	28.9	5.3	4.9	2.7	0.86	0.27
7.0 [(e)]	19.0	44.3	2.0	1.65	1.05	0.09 [(g)]	0.04 [(g)]

(a) Spectrum analyzer determination

(b) a = 9.5 mm

(c) ±0.5 mm accuracy

(d) $V_\ell = \frac{1}{2}\pi r_{eq}^2 cT_\ell$; T_ℓ=15 μsec; $c=1.491\times10^6$ mm/sec

(e) Focussed transducer

(f) Estimated maximum error

(g) Estimated maximum error 34% and 20%, respectively

TABLE 4.4

BEAM CHARACTERISTICS AT $s = 3.9$

f_c MHz	-6 dB Beamwidth mm	$r_{eq}^{(1)}$ mm	$r_{eq}^{(2)}$ mm	$V_\ell^{(1)}$ cm^3	$V_\ell^{(2)}$ cm^3	$\frac{V_\ell^{(1)}(3.9)}{V_\ell^{(1)}(1.0)}$	$\frac{I(s=1.0)}{I(s=3.9)}$ [a]
1.09	19.3	12.4	8.6	5.4	2.6	5.9	5.7
2.25	18.7	11.9	8.3	4.9	2.4	6.6	5.9 [b]
3.45	19.6	12.6	8.7	5.6	2.6	6.3	5.9
4.8	19.8	13.3	9.1	6.3	2.9	7.3	6.0
7.0 [c]	10.7	7.25	5.05	1.8	0.9	19.0	18.0

(a) Corrected for absorption in water; $\alpha = \alpha_o f^2$ where $\alpha_o \approx 1.0 \times 10^{-15}$ at 20^oC

(b) Indirectly determined

(c) Focussed transducer

The measured values are seen to be only slightly greater on the average than the nominal 19 mm crystal diameters.

To determine the effect of the ball bearing diameter, the measurements at 3.5 MHz and 4.8 MHz were repeated using balls 1/16 in. in diameter. The smaller targets increased the resolution of the side-lobes but had negligible effect on the resultant beamwidths. The equivalent volumes at s = 1.0 were generally 5 to 10% greater. However, as the possibility of errors due to interference effects is increased, particularly at 3.5 MHz, it was decided to average the two sets of measurements (Table 4.3). The measurements at 1.1 MHz were obtained with 1/4 in. and 1/8 in. ball bearing targets.

The equivalent volumes $V_{\ell}^{(1)}$ and $V_{\ell}^{(2)}$ were calculated from the beam pattern profiles. Values of $V_{\ell}^{(1)}$ and $V_{\ell}^{(2)}$ and the corresponding equivalent beam radii are given in Tables 4.3 and 4.4. To a good approximation, the equivalent radius, $r_{eq}^{(2)}$, at s = 1.0 may be taken as one half of the -6 dB (two-way) beamwidth, for $\left\langle r_{eq}^{(2)}/(\text{-6 dB beamwidth})\right\rangle_{s=1.0} = 0.525$.

A comparison of the axial intensity ratios [I(s=1.0)/I(s=3.9)] and the corresponding volume ratios is useful. Values are given in Table 4.4. The intensity ratio values are subject to considerable error due to uncertainty in the absorption over the acoustical path. Nonetheless, with the exception of the 4.8 MHz value, the ratios are close to the theoretical CW value of 6.35 [Papadakis and Fowler (1970)]. Comparing the various values for the 4.8 MHz transducer in Tables 4.3 and 4.4 suggests that $V_{\ell}^{(1)}(s=3.9)$ may be too large by 0.5 cm^3.

The volume and intensity ratios for the focussed transducer are roughly three times greater than for the planar apertures. From the diffraction formulae for the circular aperture [Lommel (1885)], it may be shown that the ratio of the axial beam intensities and the focus at the $Y_o^{(+)}$ maximum of a focussed and an unfocussed aperture of the same diameter and source strength is given by

$$\frac{I_f(f)}{I_{unf}(a^2/\lambda)} = \frac{\pi^2 a^4}{4f^2 \lambda^2} \qquad (4.3.1)$$

where f is the focal distance and a is the aperture radius. Using the argument of conservation of beam energy and taking into account the 0.0125 cm difference in the transducer radii, the equivalent beam area cross-section ratio (and the equivalent volume ratio) is 13.4. The measured value (Table 4.3) is 9.2. Integration of the patterns $[2J_1(u)/u]^2$ and $[2J_1(u)/u]^4$ yields a value for the ratio $[V_\ell^{(1)}/V_\ell^{(2)}]$ of approximately 2.0 compared to an experimental value of 2.3.

The main problems associated with the use of the focussed transducer are that the equivalent beamwidth at the focus may be too small and that the beam pattern differs from that of a planar aperture.

As was shown in Chapter 2, the effect of the finite beamwidth on the reflectivity for beamwidths less than the correlation distance of the scattering surface (volume) is essentially the same as that of the correlation distance. Therefore, under these conditions the beamwidth, like the pulse length, becomes one of the parameters determining the backscatter strength per unit volume, Ω. However, even if the beamwidth

exceeds the correlation distance, the field distribution at the focal plane of the focussed transducer is given to a first approximation by the Fraunhofer pattern and thus differs significantly from the distribution in the $Y_o^{(+)}$ plane of the unfocussed transducers. As a result, the Ω values are still not exactly comparable. The change in distribution may be inferred from the results given in Tables 4.3 and 4.4. Thus, at s = 1.0, $\langle V_\ell^{(1)}/V_\ell^{(2)} \rangle_{s=1.0} \simeq 3.0$, while at s = 3.9, $\langle V_\ell^{(1)}/V_\ell^{(2)} \rangle_{s=3.9} \simeq 2.1$; this indicates a significant change in the beam patterns. The latter, it should be noted, is in agreement with the theoretical value ($\simeq 2.0$) based on the Fraunhofer pattern.

Having discussed the backscatter measurement system characteristics and its calibration, we now turn in the next few sections to briefly describe the principal methods used to determine the velocity and absorption, and various chemical and histological properties of the tissues employed in the experiments.

4.4 Velocity and Absorption Measurements

Several different techniques were used to determine the ultrasonic velocity and absorption of the various media investigated. Generally, the methods were of the substitution type, involving distilled water as the reference medium.

4.4.1 Velocity Determinations

By measuring the change in time delay of an echo from a suitable reflector, first without the sample and then with the sample in place between the transducer and reflector, the velocity in the sample may be

obtained from the relation

$$\frac{1}{v_2} = \frac{1}{v_1} + \frac{t_2 - t_1}{2S} \qquad (4.4.1)$$

where v_2 - sample velocity

v_1 - velocity in water

S - sample thickness

$t_2 - t_1$ - delay time difference

The velocity of pure water, obtained from published data [Konenenko and Yakovlev (1969)] and checked by direct measurement, served as the reference. The thicknesses of the tissue samples were gauged ultrasonically and verified by means of caliper measurements.

The maximum error for a single measurement of velocity using samples at least 1.5 cm thick is about 1%. The relative accuracies of the velocity determinations obtained by means of a least squares fit of four or five different sample thicknesses (from the same fish) are estimated at 0.3%.

4.4.2 Absorption Measurements

The methods employed in earlier measurements of velocity and absorption in whitefish were described by Freese and Makow (1968.b). For frequencies up to 3 MHz a buffer rod technique was employed while at higher frequencies a contact reflector method was used. Diffraction and matching corrections were obtained by substituting distilled water as the absorbing medium. The samples were compressed by 5 to 10% in the

measurement cavity which may have caused some twisting in orientation and separation of the tissues. This in turn may have given rise to large errors in measurements parallel to the muscle fibers. For this reason it was decided to use ultrasonic gauging and a non-contact, reflector method of the substitution type for subsequent velocity and absorption measurements on muscles.

Using a narrow beam with the sample placed at the $Y_o^{(+)}$ diffraction focus, the thickness of the sample can be gauged ultrasonically to within 5% with negligible loss of accuracy in the final result. In this way compression of the samples can be entirely avoided. [Of course, the use of a narrow beam reduces the inherent averaging over the sample and increases the sensitivity to tissue inhomogeneities, hence resulting in a greater variation in the individual measured values. However, provided the beam was not less than about 5 mm in width (3 dB), this did not present a problem.]

The maximum error in single transverse and parallel absorption measurements (3.5 to 5.0 MHz) for a sample are estimated at 19% and 40%, respectively. A minimum sample thickness of 1.5 cm and an anisotropy ratio of 1:4 are assumed. The much larger error in absorption measurements parallel to the fiber direction is the result of the effect of alignment error.

In the case of the gelatin model media (Section 5.1), the experimental values of absorption were obtained from observations of the reverberation (backscatter) decay rates, suitably corrected for beam divergence. The reason for using this method was to avoid disturbing what was essentially a fluid medium. Employing a minimum path length

of 4.5 cm, the probable error at the lowest bubble concentration measured was estimated at ±0.069 cm^{-1} or ±0.6 dB/cm.

For the measurements of the absorption in water, echoes from a flat, polished quartz reflector and a ball bearing were compared over path lengths ranging from 59 to 230 cm. Applying appropriate diffraction corrections [Seki et al. (1956); Khimunin (1972); Gitis and Khimunin (1968)], a value of $\alpha_w/f^2 = 2.9 \times 10^{-4} cm^{-1} MHz^{-2}$ was obtained which is in fair agreement with the published CW values.

4.4.3 Pulse Absorption Spectroscopy

The method basically consists of performing a power spectrum analysis of extremely wideband pulses before and after passage through the absorbing medium. Subtracting the resultant spectra then yields the absorption spectrum of the medium.

The method was implemented by using a highly damped, focussed, lithium sulphate, 3/4 in. diameter, immersion style transducer (made by Krautkrämer) to generate a nearly single cycle 12 MHz center frequency pulse. Hence, the RF pulse spectrum was more than 20 MHz in width. The transducer was focussed on a 1/8 in. stainless steel ball reflector at a distance of 12 cm (geometrical focus) in distilled water. The reflected pulses (first without the sample, i.e. in distilled water, and then with the sample interposed) were amplified by a wideband, low noise, isolating pre-amplifier and gated with a non-additive gate (contained in the model UTA-2 ultrasonic transducer analyzer manufactured by Aerotech Laboratories, see Fig. 4.2). The power spectra of the gated pulses were measured on an HP model 8553B-8552B spectrum analyzer and were recorded

on either polaroid film or graphically using an XY recorder. The results were generally reproducible to within ±0.5 dB.

The above technique is similar to the method of power spectrum analysis referred to earlier for the backscatter (see Chapter 3 and Appendix B). The main difference lies in the fact that in the case of the absorption technique single pulses from a known target are analyzed, while in the case of the tissue backscatter a train of pulses is analyzed (and compared to the original incident pulse). Generally, the backscatter power spectrum must be averaged to eliminate the effects of interference due to the backscatter fine structure.

4.5 Histological Examinations

Cubes of tissue 5 to 7 mm in size were frozen with a blast of CO_2, or alternatively, they were frozen on a piece of aluminum foil dropped into isopentane held at -40°C (still lower temperatures tended to shatter the samples; moreover, this would also have required much better freeze-drying facilities). The samples were then freeze-dried at a temperature of -40°C and a vacuum of 2 microns (mercury). After freeze-drying for a period of 5 to 10 hours at -40°C, the sample's temperature was allowed to gradually rise to room temperature over a period of about 12 hours. The dried samples were trimmed and embedded in paraffin. Sections 8 to 24 μm thick were cut from the sample blocks. The sections were examined under low to medium magnification with a polarizing microscope and an interference contrast microscope. (Staining was avoided as this gives rise to additional distortion of the samples.) Larger samples for the purpose of measuring air bubble densities and other

inhomogeneities were cut by hand with a sharp scalpel and were examined under a low power stereo-microscope.

4.6 Chemical Analysis

The chemical analyses performed were for total fat, moisture and protein content of the white muscle tissues.

4.6.1 Extraction of Lipids from Muscle

The method of Bligh and Dyer (1959) was used to determine the total lipid content of a white muscle sample. In this method a chloroform-methanol-water mixture is employed to extract the lipids from the muscle. A correction based on moisture content is made in the final determination. In general, a better than 95% extraction of the total lipid is possible with this method.

4.6.2 Moisture Content

The moisture contents of the samples were determined by drying the samples under vacuum. The accuracy of the determinations was about 0.2%.

4.6.3 Determination of Total Protein Content

Total protein contents of the fish muscle samples were obtained by the standard micro-Kjeldahl nitrogen determination method corrected for non-protein nitrogen, the total protein being obtained by multiplying the nitrogen content by the factor 6.25. Duplicate extractions were made for each muscle sample; the samples were normally taken from the epaxial region near the head.

CHAPTER 5

EXPERIMENTAL RESULTS

To acquaint the reader with the nature of the scattering problem and to delineate the mixed body presented by the fish myomere, a number of experimental results and observations relating to the individual scatterers were introduced in Chapter 2. The backscatter cross-sections of the different inhomogeneities encountered were derived and discussed in some detail. In this chapter the emphasis will be on the overall volume scattering process, although some results of scattering measurements from the individual scatterers will also be given and compared with theory.

Using the experimental techniques described in Chapter 4, the volume backscatter from myomere are measured as a function of composition and condition. The experimental values are compared with histological data and measurements on model media of oil and air bubble suspensions. They are then interpreted with the aid of theoretical calculations based on a first order statistical scattering process model of the myomere. The significance of the results towards certain potential applications is briefly discussed.

Initially, to test the validity of the approach and verify the calibrations, the backscatter from gelatin suspensions of air bubbles (Section 5.1) and also oil bubbles (Section 5.2) are measured and compared with theoretical predictions.

5.1 Backscattering from Air Bubbles in a Fluid Medium

The model media were prepared in the following manner. Air bubbles were introduced and evenly dispersed in partially jelled gelatin consisting of two parts gelatin in nine parts of water (by weight). The mixture was then refrigerated for forty-eight hours after which additional air bubbles were introduced with a few millilitres of cold water added to improve the dispersal of the bubbles. This was repeated until no further absorption occurred. Samples of different air bubble concentrations were prepared.

5.1.1 Media Statistical Parameters

Determinations of the bubble diameter distributions were made for three of the media (G3, G4 and G5). The majority of the bubbles in all of the samples were spherical in shape. Interestingly, however, the surfaces of the bubbles, particularly the larger ones, were not smooth; rather they had a slightly corrugated appearance with a roughness estimated from photographs of the order of 1 to 10 μm. The diameter distribution for the G3 sample having the second largest concentration is shown in Fig. 5.1. The distribution of the G4 medium was qualitatively similar to that of the G3 medium. On the other hand, the bubbles of the G5 medium were more uniform in size and this is apparent from the bubble statistical parameters.

The statistical parameters of the media are summarized in Table 5.1. The concentration V_c refers to the fractional volume occupied by the bubbles and is given by

$$V_c = \langle n \rangle \frac{4\pi}{3} \langle a^3 \rangle \qquad (5.1.1)$$

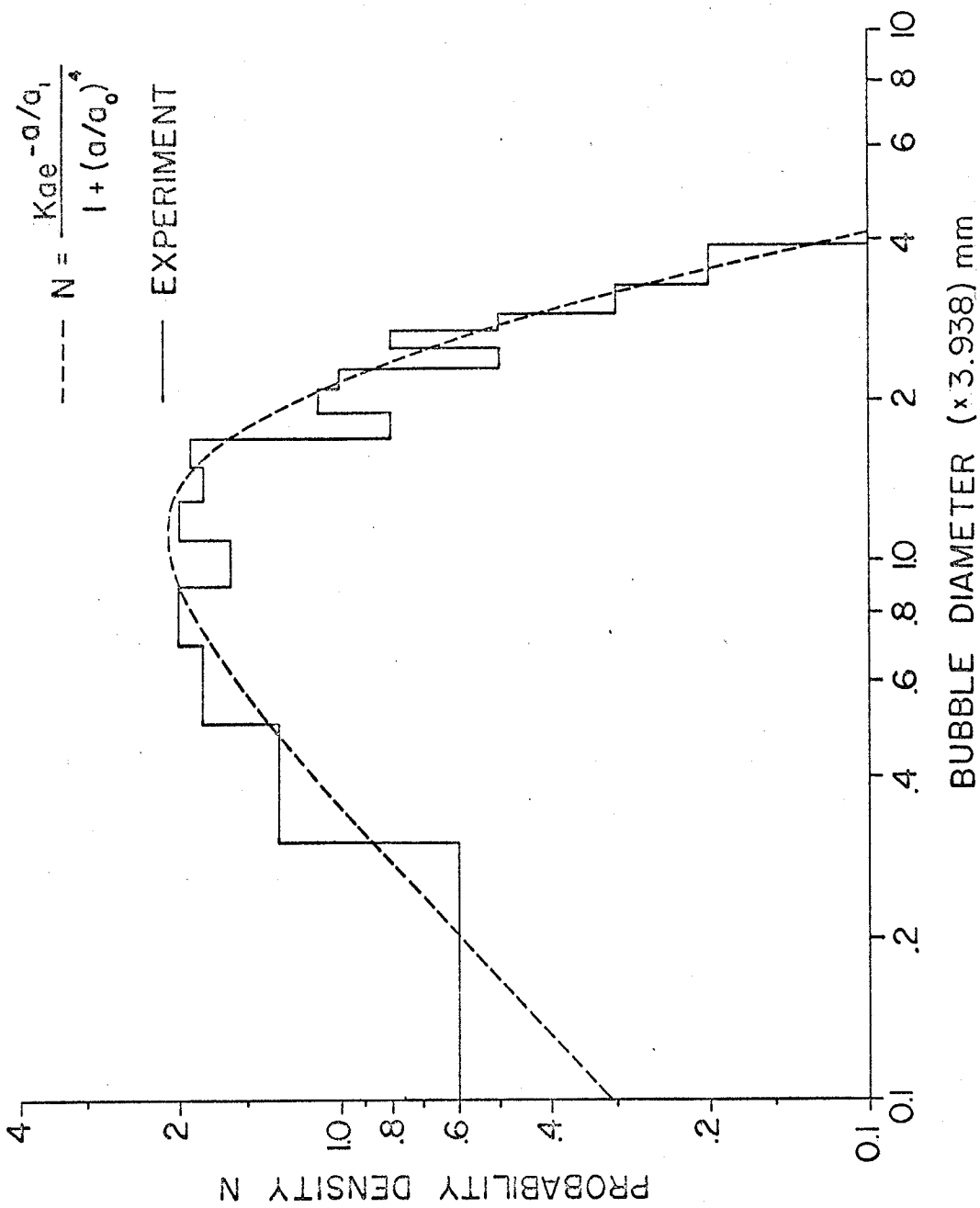

Fig. 5.1 Bubble diameter distribution histogram.

where $\langle n \rangle$ is the average number of bubbles per unit volume and $\frac{4\pi}{3} \langle a^3 \rangle$ is the average volume per bubble.

TABLE 5.1

BUBBLE STATISTICAL PARAMETERS

Sample	$\langle n \rangle$ bubbles/cm^3	$\langle a \rangle$ mm	$\langle a^2 \rangle$ mm^2	$V_c \times 10^3$
G3	330 ± 80	0.20	0.056	26
G4	42 ± 6	0.16	0.041	2
G5	550 ± 150*	0.19	0.043	27

* Small sample

Both the backscatter and the absorption are proportional to the scatterer density n to first order. The absorption should thus furnish an additional measure of the scatterer density. Since the absorption is also required for stationarization of the backscatter, the absorptions were determined simultaneously with the backscatter.

5.1.2 Absorption of the Gelatin Media

Assuming that the various absorption components are additive, the absorption constant of the bubbly medium α_{mgb} may be expressed approximately as

$$\alpha_{mgb} = \alpha_w + \alpha_g + \alpha_b \qquad (5.1.2)$$

where α_w - water absorption

α_g - gelatin absorption

α_b - attenuation due to absorption, viscous drag and scattering by the air bubbles.

α_b is given in terms of the average extinction or total cross-section $\langle Q_e \rangle$ of the bubbles by [Foldy (1945)]

$$\alpha_b = \frac{\langle n \rangle \langle Q_e \rangle}{2} \tag{5.1.3}$$

where $\langle n \rangle$ is the average number of scatterers per unit volume. With the help of the extinction theorem [Stratton (1941); Foldy (1945); Waterman and Truell (1961)]

$$Q_e = \frac{4\pi}{k} \text{ Im } A_s(0)$$

$$= Q_a + Q_s \tag{5.1.4}$$

where $A_s(0)$ is the forward scattered wave amplitude, Q_a is the absorption cross-section and Q_s is the total scattering cross-section. The latter is defined in terms of the bistatic scattering cross-section (σ_{bi}) as

$$Q_s = \frac{1}{4\pi} \int_0^{\pi} \int_0^{2\pi} \sigma_{bi}(\theta', \phi') \, d\theta' \, d\phi' \tag{5.1.5}$$

where $\theta' = \theta_s - \theta_i$, $\phi' = \phi_s - \phi_i$ and the integral is evaluated with the incidence angles θ_i, ϕ_i fixed.

Neglecting absorption by the air bubbles, i.e. $Q_a = 0$, and assuming that the bubbles will behave essentially as Dirichlet scatterers, which implies that the effects of the partial wave resonances may be neglected, we obtain using (2.2.4) and the short wavelength asymptotic solution for the sphere [Morse and Ingard (1968)]

$$Q_s \simeq \frac{4\pi a^2}{1 + (ka)^2} \quad , \quad \text{for } (ka)^2 >> \frac{3\rho_2 c_2^2}{\rho_1 c_1^2} \quad , \quad ka \leq 1 \qquad (5.1.6.a)$$

$$\simeq 2\pi a^2 \quad , \qquad ka > 1 \qquad (5.1.6.b)$$

Eq. (5.1.6.b) differs only by the well-known factor of two from the geometric BCS.[1]

The absorption component α_g of the gelatin was obtained using the pulse spectroscopic technique (Section 4.3.3) and a clear gelatin sample. Over the range 1 to 10 MHz, the absorption per wavelength was linear, measuring 5×10^{-3} cm^{-1}MHz^{-1} at 20°C. The water absorption component α_w was determined by the comparison method described in Section 4.4.2. The value of α_w/f^2 obtained was 2.9×10^{-4} cm^{-1}MHz^{-2}. The determinations of α_{mgb} were made from measurements of the backscatter decay rate and also the spectroscopic method. For the decay rate measurements, a two-way path length of 5.35 cm was employed. In each case the slopes of the resultant logarithmic graphs after correction for beam divergence were constant over the first 4.6 cm.

Experimental and theoretical values of absorption computed using (5.1.6) and (5.1.2) are given in Table 5.2 for the G3 and G5 samples.

---

[1] This problem has received much attention in the past. Basically the problem is that, as the distance separating the scatterers and the receiver is reduced, it becomes increasingly difficult in practice to distinguish the forward scattered field from the incident primary field. However, for ka >> 1, the forward scattered field accounts for half of the scattered power and, as it acts in concert with the primary field, it must be taken into consideration. The net result is that, if the forward scattered component is intercepted by the receiver, the extinction cross-section scattering component will be effectively only half as great. In our case $\delta = (\lambda/4\langle a \rangle) >> (\lambda/4a_T)$, where δ is the forward-scatter beamwidth and a_T is the transducer radius and therefore Q_s is given by (5.1.6).

TABLE 5.2

ABSORPTION OF GELATIN MEDIA CONTAINING AIR BUBBLES

Sample	Freq.	Average Bubble Separation	Experimental (a) α_{mgb}	Experimental (b) α_{mgb}	Experimental α_w	Experimental α_g	Experimental (a) α_b	Experimental (b) α_b	Theoretical α_b
	MHz	λ	cm^{-1}	cm^{-1}	$cm^{-1} \times 10^4$	$cm^{-1} \times 10^3$	cm^{-1}	cm^{-1}	cm^{-1}
G3	1.1	1.3	0.182		4	5.4	0.176		0.610
	2.3	2.7	0.197		15	11.1	0.184		0.586
	3.5	4.1	0.172		35	16.9	0.152		0.578
	4.8	5.7	0.304		67	23.5	0.274		0.574
G5	1.1	1.1	0.218	0.128	4	5.4	0.212	0.122	0.821
	2.3	2.3		0.165	15	11.1		0.152	0.763
	3.5	3.5	0.260	0.194	35	16.9	0.240	0.170	0.752
	4.8	4.8	0.285	0.236	67	23.5	0.255	0.206	0.747

(a) Backscatter decay rate method

(b) Backscatter pulse spectrum method

On the average the decay rate measurement values of α_b are slightly less than 30% of the theoretical values.[1] The reason for this discrepancy is not clear. Waterman and Truell (1961) derive the following criterion for the validity of (5.1.3)

$$\frac{\langle n \rangle Q_e}{k} << 1 \qquad (5.1.7)$$

Substituting the appropriate values from Tables 5.1 and 5.2, we obtain for the worst case $\alpha\lambda/\pi = 0.036$ which is certainly substantially less than unity. Nonetheless, although it would not seem to be in accord with theory, the most likely causes for the discrepancy would appear to be the breakdown of (5.1.3) due to the onset of significant secondary scattering, i.e. higher order multiple scattering, coupled perhaps with the interception of some of the multiple scattered but initially forward scattered intensity (so that for $ka > 1$, we have $Q_s < 2\pi a^2$, see footnote on previous page). Unfortunately, in spite of the fact that scattering and absorption by air bubbles has been extensively studied [e.g. Fox et al. (1955); Kol'tsova and Mikhailov (1969)], absorption data for bubbles in the range of $ka = 1$ to 5 and V_c near 3% appears to be lacking so that we were unable to compare our results with previous work. Finally, we note that if α_b includes a component α_v proportional to frequency as is indicated by the measurements, the high-frequency asymptotic values of

---

[1] An experimental error, probably in the spectroscopic attenuation measurements, is indicated at the lower frequencies by the difference in the values of α_{mgb} obtained by the two methods (Table 5.2). This error may have been caused by some degree of pulse overlap due to reverberation from the air bubbles in the spectroscopic determination.

$(\alpha_b - \alpha_v)$ for G3 and G5 become 0.16 and 0.2, respectively. These values correspond to total scattering cross-sections approximately equal to the geometric cross-sections.

5.1.3 Backscatter Results

The backscatter measurements on samples G3, G4 and G5 were performed with the samples placed in the transition region. For the purpose of ascertaining the effects on the measurements of the transition region positioning, the measurements for G4 were then repeated with the sample placed at s = 3.9 in what is essentially the far field. The measured values for G3, having the highest concentration, were averaged over two measurements each, while G4 and G5 were averaged over three measurements each. In all cases a 15 μsec gatewidth was employed to sample the backscatter while the experimental decay rate values of the absorptions were employed for the TVG. Using the values of $V_\ell^{(2)}$ at s = 1.0 and s = 3.9 given in Tables 4.3 and 4.4, the experimental values of $\langle\Omega\rangle$ were then calculated according to the definition given in Section 2.4.

For the theoretical BCS values we again assume Dirichlet scattering. The cross-section for a spherical bubble can then be approximated as

$$\sigma \simeq \frac{4\pi a^2}{1 + (ka)^2}, \quad (ka)^2 >> \frac{3\rho_2 c_2^2}{\rho_1 c_1^2} \quad \text{and} \quad ka \leq 1$$

$$\simeq \pi a^2, \quad ka > 1 \qquad (5.1.8)$$

At ka = 1 the value of $\sigma/(\pi a^2)$ lies roughly midway of the discontinuity in (5.1.8) as may be seen from Fig. 2.5. The scatterer distribution thus

effectively averages over the discontinuity. Moreover, except at 1.1 MHz where ka = 1 for a = 0.2 mm, relatively few scatterers with ka < 1 are found at the higher frequencies as may be inferred from Fig. 5.1 and Table 5.1.

The theoretical and experimental values of $\langle\Omega\rangle$ are plotted in Fig. 5.2. Despite the relatively large probable errors in Ω and the inherent statistical fluctuations, the experimental and theoretical results are in comparatively good agreement over the range from 1.1 to 3.5 MHz. Only the 4.8 MHz results show any appreciable discrepancy. Whether this error, on the average 2 dB, is due to calibration and TVG setting errors or to changes in the scattering is not certain. However, the results for the gelatin-oil media (Fig. 5.10) suggest that the increase is real. The decreases in the values of $\langle\Omega\rangle$ between 1.1 and 3.5 MHz are approximately by the predicted amount and the experimental and theoretical results agree on the average within 1 dB over this range. Although the theoretical and experimental results differ increasingly with increasing concentration, the increase is within the range of experimental error. In contrast to the absorption results, the relatively good agreement would seem to indicate that the first order scattering model, by taking into account multiple scattering effects by way of the effective absorption constant,[1] still predicts the backscatter adequately for V_c nearly 3%.

---

[1] Strictly speaking, the model is then no longer a first order model.

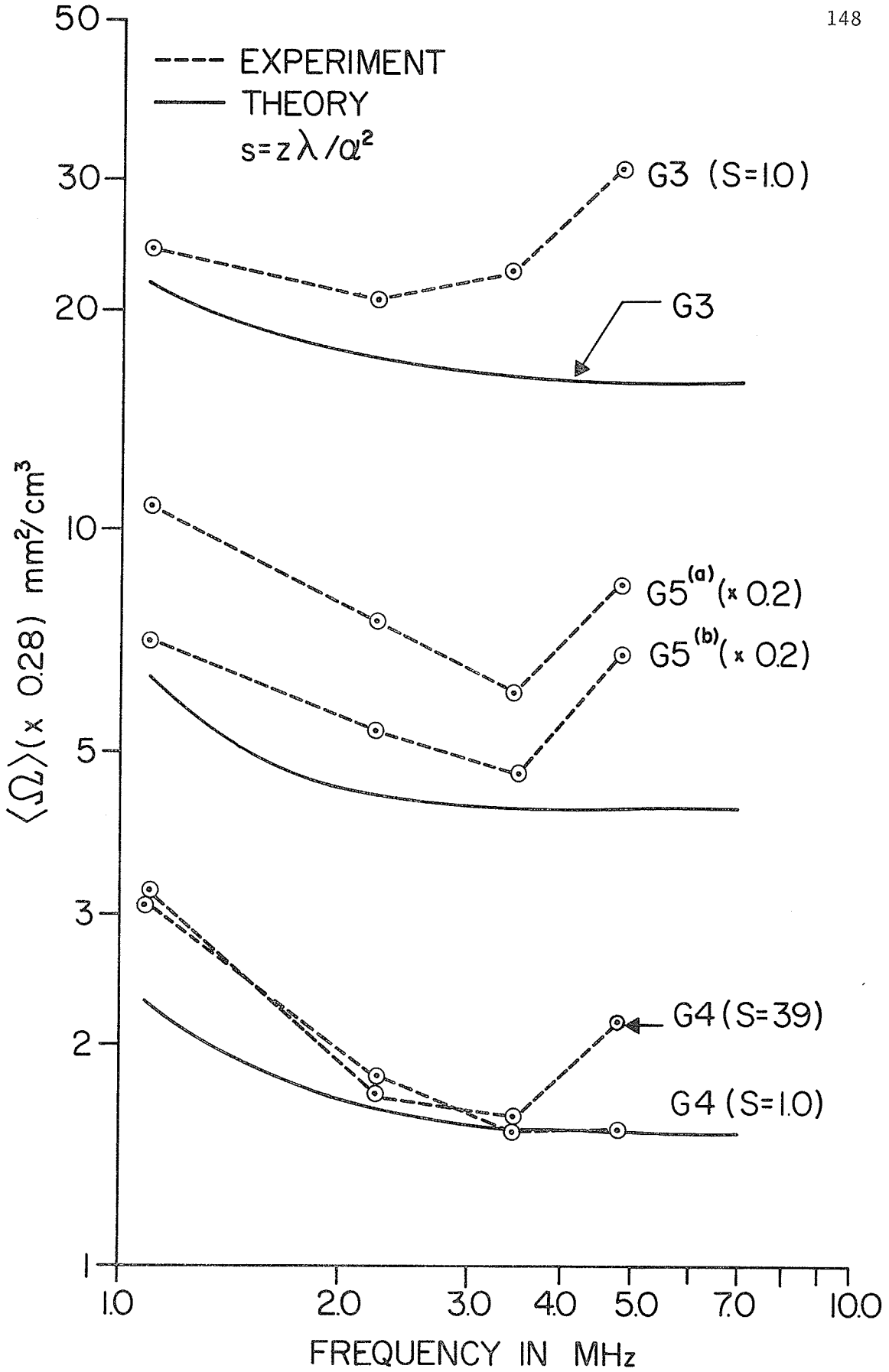

Fig. 5.2 Backscatter coefficients for air bubble media.

Except at 4.8 MHz, the results of the determinations on the G4 sample in the transition and in the far field are seen to be in good agreement. The 4.8 MHz far-field value appears to follow the trend of the measurements for the other two samples.

5.1.4 Coefficient of Variation and Probability Distribution of the Backscatter

The coefficient of variation γ_v is defined by (3.3.16.d); in the limit of the Rayleigh distribution its value becomes 0.5227. The experimental values of γ_v as a function of frequency are shown in Table 5.3.

TABLE 5.3

COEFFICIENT OF VARIATION γ_v OF BACKSCATTER ENVELOPES

Freq. MHz	G3 s = 1.0	G4 s = 1.0	G4 s = 3.9	G5 s = 1.0
1.1	.55	.60	.50	.55
2.3	.62	.64	.52	.65
3.5	.60	.70	.58	.62
4.8	.59	.86	--	.73

The critical parameter determining the rate at which the actual distribution approaches the Rayleigh distribution is the process density defined by (3.3.8) as the number of insonified scatterers times the pulse duration. In the case of the G4 medium, the γ_v's at s = 1.0 are greater on the average than the corresponding G3 and G5 values.

Similarly the G4 values at s = 1.0 are greater than at s = 3.9. This is to be expected since the insonified volumes, and therefore the number of scatterers, differ by a factor nine. As a function of frequency, γ_v is also seen to increase and this is attributable to the shorter pulse lengths with increasing frequency (Table 4.1). The results are thus in good agreement with the theoretical predictions.

The probability P{ } that the normalized envelope magnitude (E/E_{rms}) will exceed the level b may be expressed as

$$P\{(E/E_{rms}) > b\} = 1 - \int_0^{bE_{rms}} g(E)\, dE \qquad (5.1.9)$$

where $E_{rms} = \langle E^2 \rangle^{\frac{1}{2}}$, and $g(E)$ is the probability density distribution of the envelope.

Some examples of the envelope probabilities plotted on Rayleigh distribution graph paper are shown in Fig. 5.3(a-c). The points for G4 at s = 3.9 and G5 at s = 1.0 follow a straight line quite closely, while the points for G4 at s = 1.0 show significantly greater scatter with the lower levels having a greater probability than the higher levels. This is characteristic of low density impulse type processes where the probability of zero signal amplitude is often finite in contrast to the Rayleigh distribution which has zero density at zero envelope amplitude [Middleton (1960), Chapter 11]. This also accounts for the fact that the γ_v's in Table 5.3 are generally greater than 0.52. If a deterministic component were present in the backscatter either when ensemble averaging or time averaging in the presence of a dominant echo (see Chapter 3), γ_v would be less than 0.52 but it would tend towards this limit as $(\langle E \rangle^2 / \langle E^2 \rangle)$ approaches zero.

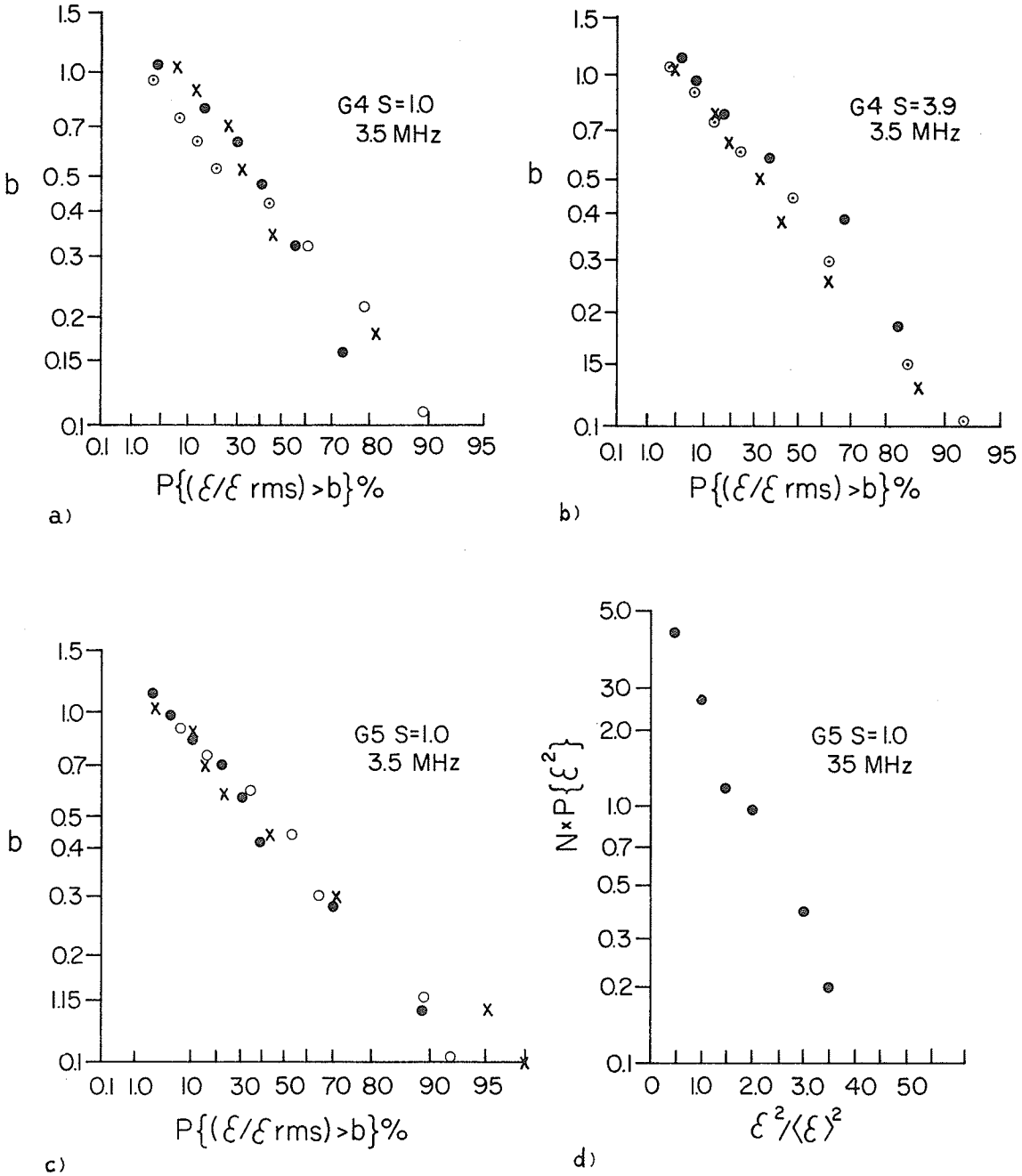

Fig. 5.3 Gelatin media backscatter probability distributions: (a - c) envelope probability; (d) intensity probability density.

Finally, in Fig. 5.3(d) an example of the relative probability density distribution of the intensity $J = E^2$ is given. The points closely approximate a straight line corresponding to an exponential distribution as implied by the Rayleigh distribution of the envelope in Fig. 5.3(c).

5.2 Backscattering from Fish Tissues

Measurements were performed on approximately 150 fresh whitefish and 35 pickerel (Stizostedion vitreum vitreum). The whitefish were obtained dressed (guts removed) and the pickerel in round form through the agency of the Freshwater Fish Marketing Corporation which operates across central and northern Canada. The pickerel were from two to three days old while the whitefish varied in age from two to five days and up to a maximum of ten to twelve days on rare occasions. Thus, in most cases the fish had passed through the rigor stage prior to the measurements. Whitefish were obtained throughout the summer and winter fishing seasons from about thirty lakes in all. Although Lake Winnipeg, which produces a particularly fatty fish and is one of the principal producers of whitefish, was underrepresented, the sample otherwise represents a good cross-section. This is important as whitefish is a highly variable species [Scott and Crossman (1973)]. The pickerel were obtained mostly from the Lake of the Woods area in north-western Ontario.

Prior to performing the measurements, the whitefish were scaled in the epaxial region and clamped as shown in Fig. 4.2. In the case of pickerel, the skin was entirely removed because of the difficulty of scaling pickerel without bruising the flesh. The reason for this was

to reduce the transmission losses and the reverberation which would otherwise result.[1]

5.2.1 Fresh Whitefish and Pickerel Lateral Myomere Backscatter

The whitefish were grouped according to the total lipid content as shown in Table 2.1. The pickerel were much leaner and formed only one group. Fixed TVG's were employed for all of the measurements in this section. The TVG values were obtained from absorption data for whitefish published earlier [Freese and Makow (1968.b)] and from absorption measurements using the non-contact reflector substitution method described in Section 4.4.2. The values of TVG employed, equal to two times the attenuation, are listed in Table 5.4.

The measurements were performed with the sample volume placed in the transition region. For the 1.1 MHz measurements a smaller window (8 to 13 μsec) and a greater delay (15 μsec compared to 7.5 μsec for the other measurements) were employed. This was done in order to gate out radial mode transducer echoes and surface reverberation which tend to become significant at this frequency because of the normally low backscatter level and the greater pulse length.

In addition to the average backscatter coefficient $\langle \Omega \rangle$ we will introduce an average envelope backscatter coefficient $\langle \Gamma_E \rangle$ which will be defined as

---

[1] The two-way transmission loss across the scales on the average was 3.0 ± 1.5 dB at 4.4 MHz for medium-sized (two pound) whitefish and 4.5 ± 1.7 dB at 4.8 MHz for medium-sized pickerel. The average losses decreased with frequency but the standard deviation increased. The transmission losses across the scales varied with the size of the fish, the measurement position, the condition of the fish (e.g. if drying of the scales had occurred) and the origin.

$$\langle \Gamma_E \rangle = \frac{\langle E \rangle}{[\Lambda^{(2)} \int_0^{\Delta t} |s_r(t)|^2 \, dt]^{\frac{1}{2}}} \tag{5.2.1}$$

where $\Lambda^{(2)}$ is defined as the effective beam cross-section of the insonified volume $V_\ell^{(2)}$, see (3.3.5), and $s_r(t)$ is the reference pulse of width Δt. $\langle \Gamma_E \rangle$ may be compared to $\langle \Omega \rangle$ which was defined in Section 2.4 and can be expressed as

$$\langle \Omega \rangle = \frac{\langle E^2 \rangle}{\Lambda^{(2)} \int_0^{\Delta t} |s_r(t)|^2 \, dt} \tag{5.2.2}$$

The choice of (5.2.1) is made for ease of comparison but is to some extent arbitrary as can be seen from (3.2.7). If E^2 contains contributions from coherent scatterers, the coherent component will be proportional to $[\Lambda^{(1)}]^2$ rather than $\Lambda^{(2)}$.

TABLE 5.4

TIME VARIED GAIN (TVG) VALUES

Freq. MHz	Whitefish Fat (×2) dB/cm	Whitefish Lean - Med.-fat (×2) dB/cm	Pickerel (×2) dB/cm	Beef Muscle Tissue (×2) dB/cm
1.1	1.3	1.3	0.65	1.65
2.3	3.0	2.6	1.5	3.5
3.5	4.5	4.0	2.3	5.3
4.8	6.0	5.4	2.8	7.5
7.0	8.0	7.6	--	--

The experimental values of $\langle \Omega \rangle$ and $\langle \Gamma_E \rangle$ as a function of frequency are plotted in Fig. 5.4 and 5.5, respectively. The much lower values of $<\Omega>$ and $\langle \Gamma_E \rangle$ of pickerel compared to whitefish are evident. On the average they are 9 dB lower than the corresponding values for the medium-fat whitefish. The greater irregularity of the pickerel values is due to statistical sampling fluctuations. The pickerel measurement values, with the exception of the 4.8 MHz value, are based on 5 specimens each, 15 specimens in all. The 4.8 MHz value is based on 11 specimens. In the case of the medium-fat and lean groups of whitefish, the 1.1 and 3.5 MHz results are based on the average of 20 specimens each, averaged over three independent measurements. The 2.3 and 4.8 MHz values are based on 7 and 15 specimens, respectively, while the values for the fat group are based on 3 specimens. Due to problems encountered with the transducer, the 7.0 MHz values are based on 2 specimens. For reasons to be explained, the data for specimens exhibiting values of Ω greater than three times the corresponding average values were excluded. Subject to this qualification, the vertical bars in Figs. 5.4 and 5.5 represent the lower and upper bound standard deviations (s.d.) of the lean and fatty whitefish groups. The s.d.'s of the pickerel values are indicated by arrowheads. The logarithmic s.d.'s as a function of frequency are essentially constant for the whitefish groups.

The possible error in the values of $<\Omega>$ increases with frequency and decreases with the number of samples averaged. Since for small TVG errors the corresponding error in the value of $\log<\Omega>$ is almost proportional, see Fig. 4.5, ensemble averaging will average out the errors in Ω due to the random TVG error. In the case of whitefish,

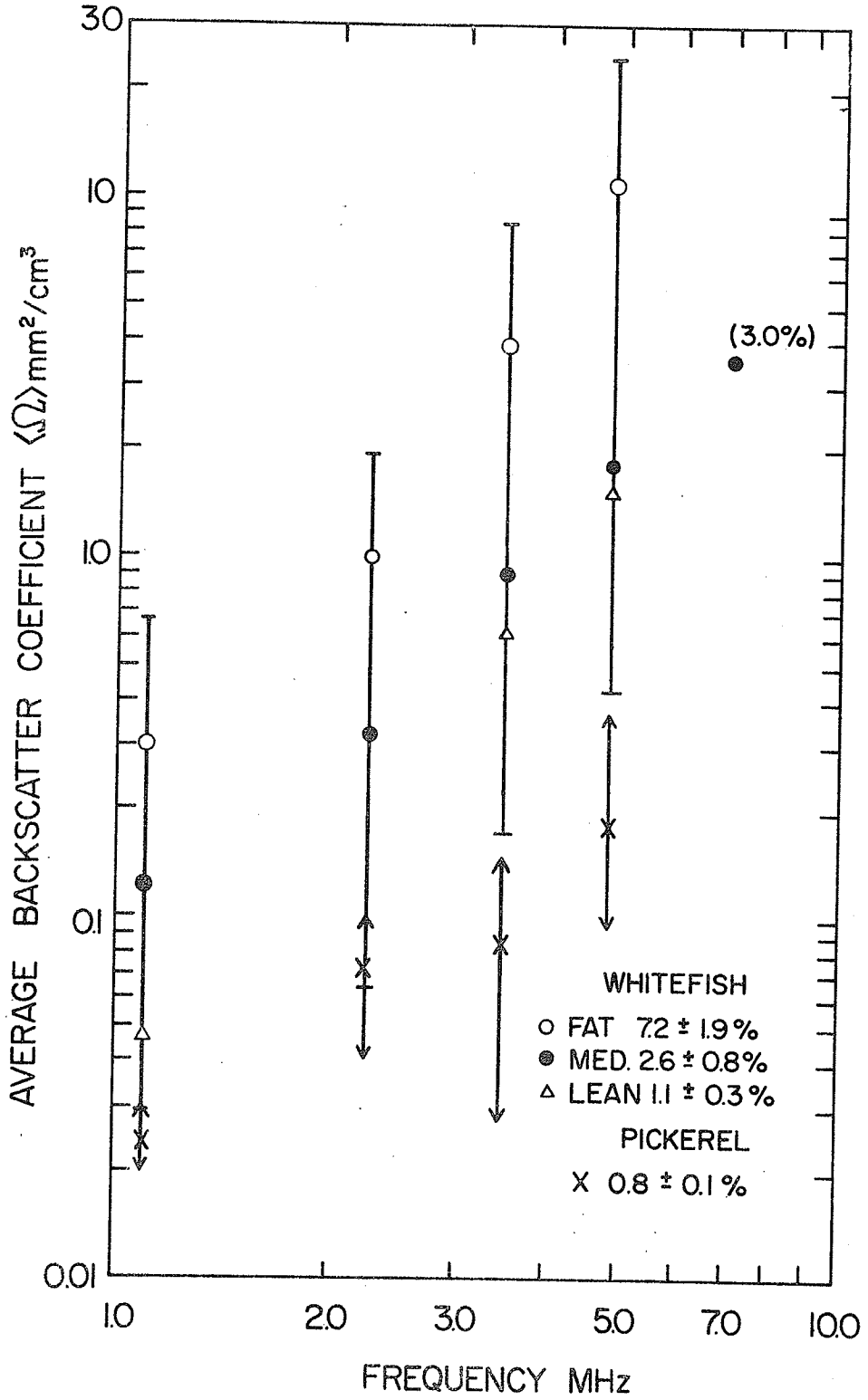

Fig. 5.4 Backscatter coefficients for whitefish and pickerel myomere grouped according to lipid content.

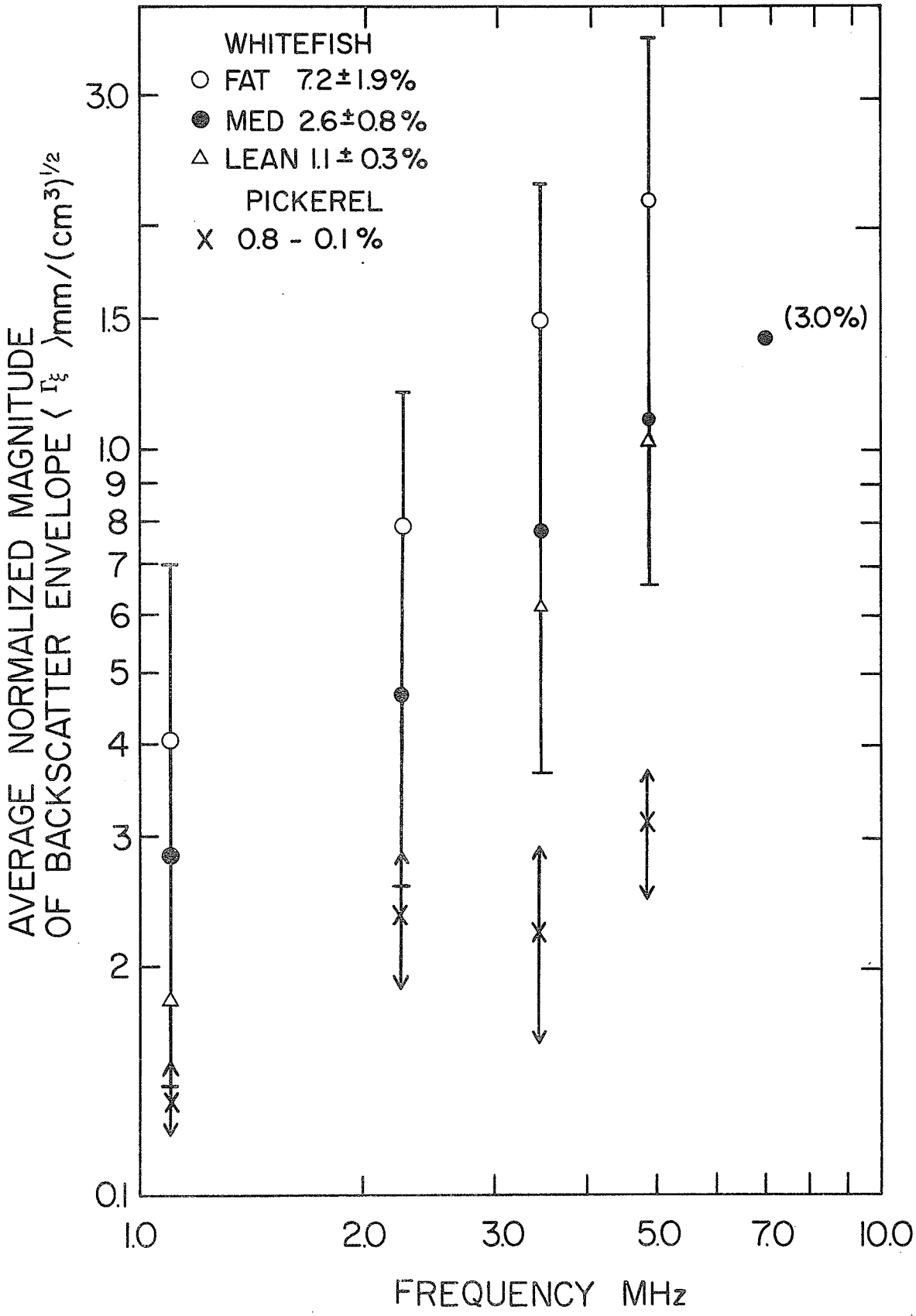

Fig. 5.5 Average normalized magnitude of backscatter envelope for whitefish and pickerel myomere grouped according to lipid content.

the remaining possible systematic TVG error is approximately ±0.5 dB/cm at 4.8 MHz and 0.3 dB/cm at 2.3 MHz with corresponding residual errors in $\langle\Omega\rangle$ of 0.55 dB and 0.33 dB. The only way the residual error in the TVG can be reduced further is by performing simultaneous absorption measurements for each specimen as was done for the gelatin media. However, the above residual errors are of the same order as the maximum standard error in $\langle\Omega\rangle$ (0.3 dB at 4.8 MHz excluding systematic TVG error), and each of these errors is much smaller than the intrinsic s.d. in $\langle\Omega\rangle$ of approximately 5 dB for a given group of whitefish, see Fig. 5.4.

The values of $\langle\Omega\rangle$ can be fairly accurately approximated in the 2.3 to 4.8 MHz range by $\langle\Omega\rangle \doteq \langle\Omega_o\rangle (f/f_o)^x$. For the lean and medium-fat whitefish the slope of $\log\langle\Omega\rangle$ measures 2.3, i.e. the average wavelength dependence is given by $\lambda^{-2.3}$. The 7.0 MHz values were obtained using a focussed transducer and are rather sensitive to TVG error. The result is therefore significant only insofar as it shows there to be no precipitous change in slope between 4.8 and 7.0 MHz. The slopes of all three groups are smaller in the 1.1 to 2.3 MHz range. This is attributable to gas bubble scattering and, to a lesser extent, to scattering from pinbones and the midline structures of the fish. The average dependence for pickerel over the range from 1.1 to 4.8 MHz is found to be $\lambda^{-1.25}$.

As in the case of $\langle\Omega\rangle$, the slope error increases with frequency. However, the residual TVG error is partly cancelled when calculating the slopes. The standard errors of the slope values for the lean and medium-fat whitefish groups are ±0.28 between 3.5 and 4.8 MHz and ±0.23 between 2.3 and 3.5 MHz. The average value over the 1.1 to 4.8 MHz range is ±0.26.

Except in the case of pickerel and fat whitefish, the slopes of the log $\langle \Gamma_E \rangle$ graphs (Fig. 5.5) are within ±0.5% of one-half the slope values of the corresponding log$\langle \Omega \rangle$ graphs. The slope for pickerel averages 0.52, i.e. slightly less than one-half. Comparing Fig. 5.4 and Fig. 5.5, the cause is seen to be the 3.5 MHz $\langle \Gamma_E \rangle$ value which is smaller than the 2.3 MHz $\langle \Gamma_E \rangle$ value in contrast to the corresponding $\langle \Omega \rangle$ values. This indicates a lack of statistical sample homogeneity. If the samples were statistically homogeneous, the slope of log $\langle \Gamma_E \rangle$ would be one-half the slope of log$\langle \Omega \rangle$. The inhomogeneity is due to the fact that the 2.3 MHz and 3.5 MHz measurements were made on two different lots (or populations) of fish containing too few specimens. The lower relative value of $\langle \Gamma_E \rangle$ at 3.5 MHz implies a larger value of $\langle \gamma_v \rangle$. We find that $\langle \gamma_v \rangle$ at 3.5 MHz equals 0.7 compared to 0.58 at 2.3 MHz which indicates that the 3.5 MHz backscatter contained a few large relatively distinct echoes.

In the case of the fat whitefish group, the slope of log $\langle \Gamma_E \rangle$ over the range 2.3 to 4.8 MHz measures 1.35 which is significantly less than one-half the corresponding log$\langle \Omega \rangle$ slope. Here again the problem is one of sample statistical inhomogeneity but in this case caused by one specimen becoming dominant at high frequencies.

Although the graphs are useful for signal processing design, e.g. for parasite detection, they fall short in that they do not indicate the relative probability of the values. For this the probability distribution of the Ω values is required. (The s.d. bars in Figs. 5.4 and 5.5 mark the s.d.'s of the lean and fatty groups; they are not the s.d. of the combined three groups.)

In order to avoid confusion, we will denote the ensemble and time averaged values for a given specimen by the subscript m, and define the average of the given population, e.g. $\langle\Omega\rangle$, by using no subscript.

The relative frequency distribution of $\langle\Omega\rangle_m$ at 3.5 MHz is shown in Fig. 5.6. Except at 1.1 MHz, similar distributions are observed at the other frequencies. The scatter in the values of $\langle\Omega\rangle_m$ is extremely large. Although the two highest values (7.6 and 9.1 mm^2/cm^3) are missing from the figure, unlike in Figs. 5.4 and 5.5 no values have been excluded in calculating $\langle\Omega\rangle$. Based on 60 specimens, the average backscatter coefficient $\langle\Omega\rangle$ = 1.27 mm^2/cm^3 and the median value $(\langle\Omega\rangle_m)_{50}$ = 0.92 mm^2/cm^3. The two largest values therefore significantly weight the average, which is why we excluded them earlier. The median value is given because for detection systems it is of greater significance than the average value. Excluding the two highest values results in average and median values of 1.03 and 0.86 mm^2/cm^3, respectively, while the s.d. of $\langle\Omega\rangle$ is reduced to 0.75 from 1.52 mm^2/cm^3. The above results show that the probability of occurrence of whitefish exhibiting very large $\langle\Omega\rangle_m$ may be slightly greater than was thought earlier [Freese (1973)], although perhaps still only 3 to 4% of the total.

Summarizing, the graphs of Figs. 5.4 and 5.5 show the average backscatter levels (excluding anomalous values) and their dependence on frequency (wavelength). The average dependence of the composite backscatter is clearly not λ^{-4} in the 1 to 7 MHz range. The graphs point to a dependence on the fat content and also confirm to some extent the presence of gas bubbles in the whitefish tissues. The average backscatter coefficient at 3.5 MHz is about 1.3 mm^2/cm^3 and, if we exclude the

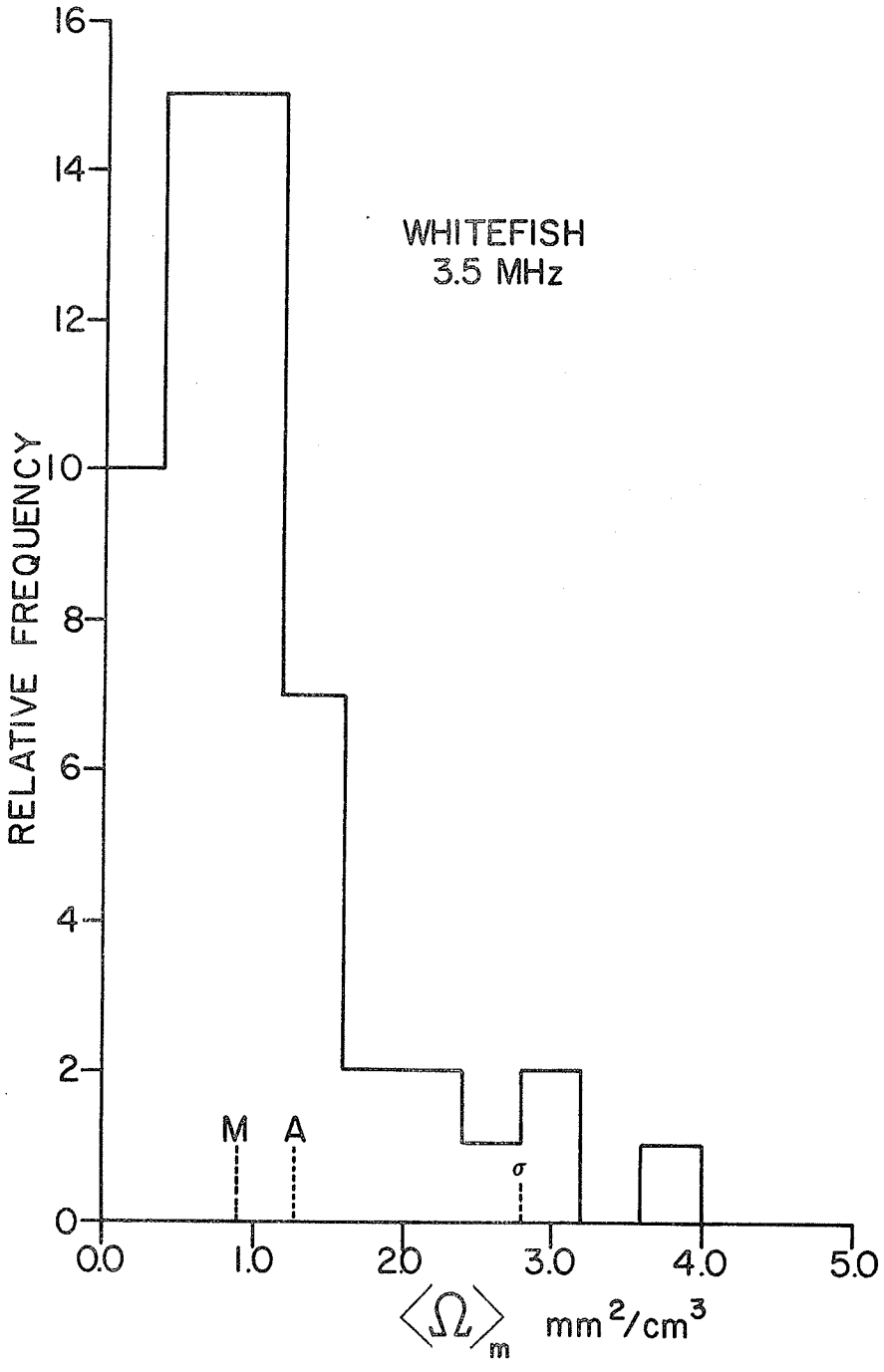

Fig. 5.6 Frequency distribution of the backscatter coefficient at 3.5 MHz for whitefish myomere; not shown in the figure are two samples having values of 7.6 and 9.1 mm^2/cm^3.

anomalously high values, 1.0 mm^2/cm^3. Values at other frequencies in the range from 2 to 5 MHz may be approximately calculated using a value of 2.3 for the logarithmic slope.

5.2.2 Effect of Gas Bubbles

The existence of gas bubbles in the flesh of virtually all of the whitefish specimens (but in few of the pickerel) was confirmed experimentally. An example of moderately high saturation of the flesh is shown in Fig. 2.4 (the scale in this photograph is 9:1). The effect of the gas bubbles is brought to the fore vividly in Fig. 5.7 in which the $\langle\Omega\rangle_m$ values at 1.1 and 3.5 MHz are plotted as a function of the percent total lipid (weight). Although the dependence on lipid content is evident from the fact that only three or four points fall below the diagonals drawn in the figures, the presence of air bubbles is primarily responsible for the very large scatter of the values. [Fig. 5.6 showed the frequency distribution of the $\langle\Omega\rangle_m$ values plotted in Fig. 5.7(b).]

Microscopic examination of the tissues of post rigor whitefish showed a wide distribution of bubble diameters, with the average diameter ranging between 160 and 440 μm. Interestingly, the average diameters of the bubbles showed little increase with increasing concentration. However, as the examination sites were mainly in the regions lying next to the myosepta, we cannot be certain that the measured distributions are entirely representative. In many specimens the bubbles showed a tendency to form clusters.

Numerical values of the backscatter cross-sections at short and long wavelengths for bubbles of different shapes are tabulated in Table 5.5

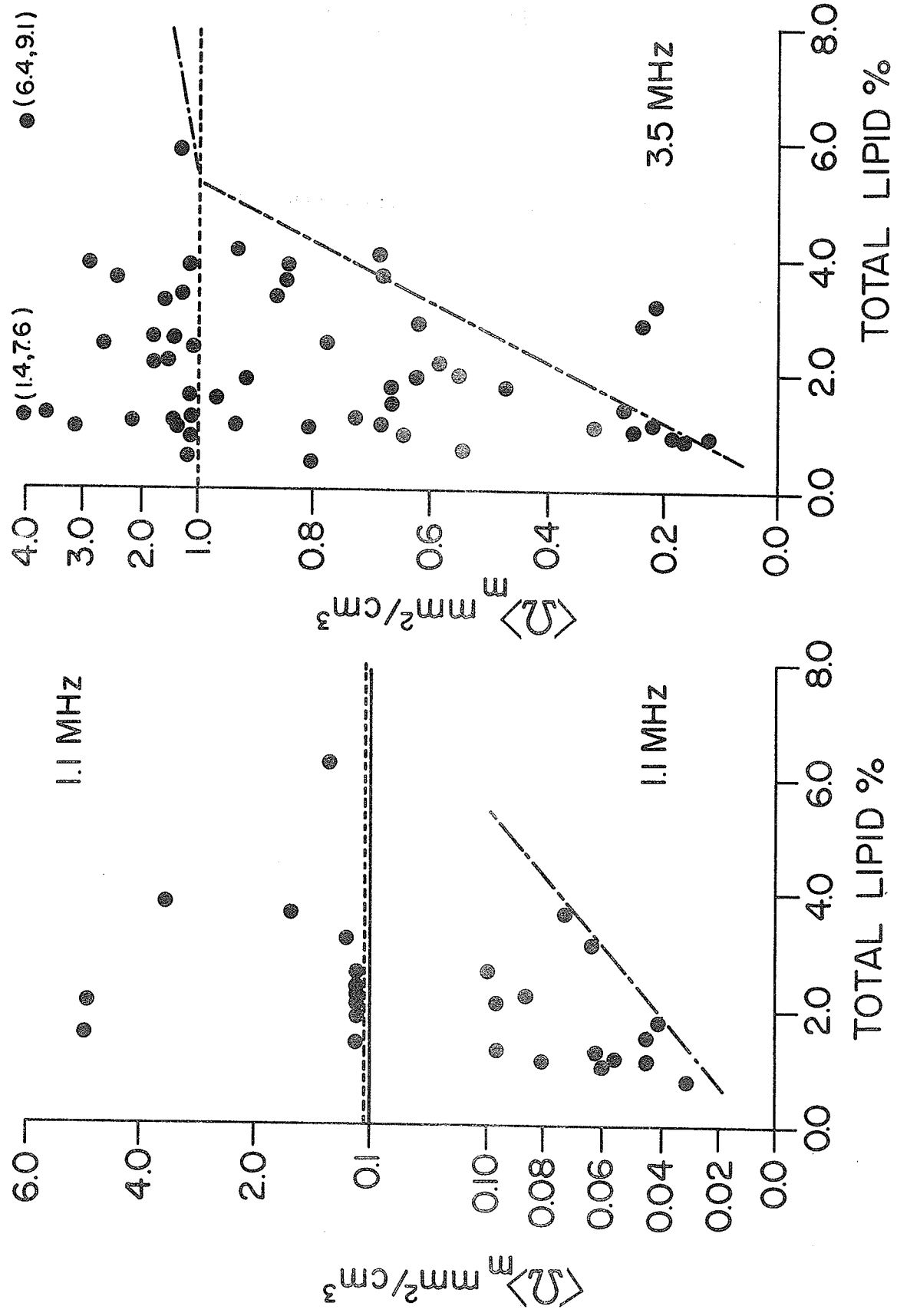

Fig. 5.7 Backscatter coefficients of individual whitefish specimens as a function of myomere total lipid content.

TABLE 5.5

APPROXIMATE BACKSCATTER CROSS-SECTIONS OF GAS BUBBLES

Shape	Monostatic BCS	Radius (a) μm	f MHz	ka	(e)†	σ mm^2	$\frac{\sigma}{\langle\sigma_g\rangle}$
Resonant Sphere δ=ka	λ^2/π	3.2	1.1	0.014	0	0.62	1.9×10^4
δ = 0.1	$4\pi a^2/\delta^2$	3.2	1.1	0.014	0	0.013	4.0×10^2
Sphere $k >> k_{res}$	$\frac{4\pi a^2}{1+(ka)^2}$	100	1.1	0.446	0	0.11	3.3
		100	2.3	0.933	0	0.07	2.1
	πa^2	100	3.5	1.4	0	0.03	1.0
		200	4.8	3.9	0	0.13	1.0
Oblate Spheroid	$\pi a^4/c^2$ (end on, θ=0)	200	4.8	3.9	0.6	0.2	1.6
					0.87	0.5	4.0
(Disc)	$\pi a^2(ka)^2$ (θ=0)				1.00	1.9	15.2
Oblate Spheroid	$\langle\sigma_g\rangle$ Eq. (2.2.13)				0.6	0.12	1.0
					0.87	0.10	1.0
					1.00	0.06	1.0
Truncated Cylinder $L >> \lambda$	Eq. (2.2.2) (θ=90°)	50	1.1	0.223		$0.09\ L^2$	0.89 L
		100	1.1	0.446		$0.17\ L^2$	0.83 L
	kaL^2 (θ=90°)	100	4.8	1.95		$1.95\ L^2$	9.75 L

†Eccentricity

for some representative diameters. For purposes of comparison, the BCS gains are also included. It is apparent that in the case of the spherical bubbles with diameters in the range from 150 to 400 μm, the backscatter level will decrease by several decibels as the frequency is increased. A decrease of this order provides a good indicator of the presence of air bubbles, as well as a rough measure of their average diameter, as was seen for the gelatin media in Section 5.1. However, attempts to estimate directly the contribution of the bubbles to Ω were unsuccessful as the following example illustrates. In the case of specimen #408 with a lipid content of 2.6%, the mean equivalent diameter of the bubbles was 380 μm with a s.d. of 140 μm; a sample of myoseptum surface taken from #408 is shown in Fig. 2.4. The bubble density was estimated roughly at 250/cm^3. Calculating Ω as in Section 5.1, a value of 28 mm^2/cm^3 is obtained which is about ten times greater than the observed value of 2.66 mm^2/cm^3 (the maximum error due to TVG error is 2 dB). Whether the disagreement was caused by poor statistics due to using too small a sample, unrepresentative sampling, or departure from sphericity of the bubbles is not clear. However, in all of the cases examined the measured values of Ω were at least qualitatively proportional to the relative number of bubbles estimated, making due allowance for the lipid content.

Using the results of microscopic examinations together with the data from Fig. 5.7, the measurements were grouped according to the lipid content and the estimated gas bubble concentrations: low (L) - less than 15 bubbles/cm^3; moderate to moderately high (M) - 15 to 150 bubbles/cm^3; high (H) - more than 150 bubbles/cm^3. The resultant values plotted as a function of frequency and the corresponding slopes are shown in Fig. 5.8(a-c).

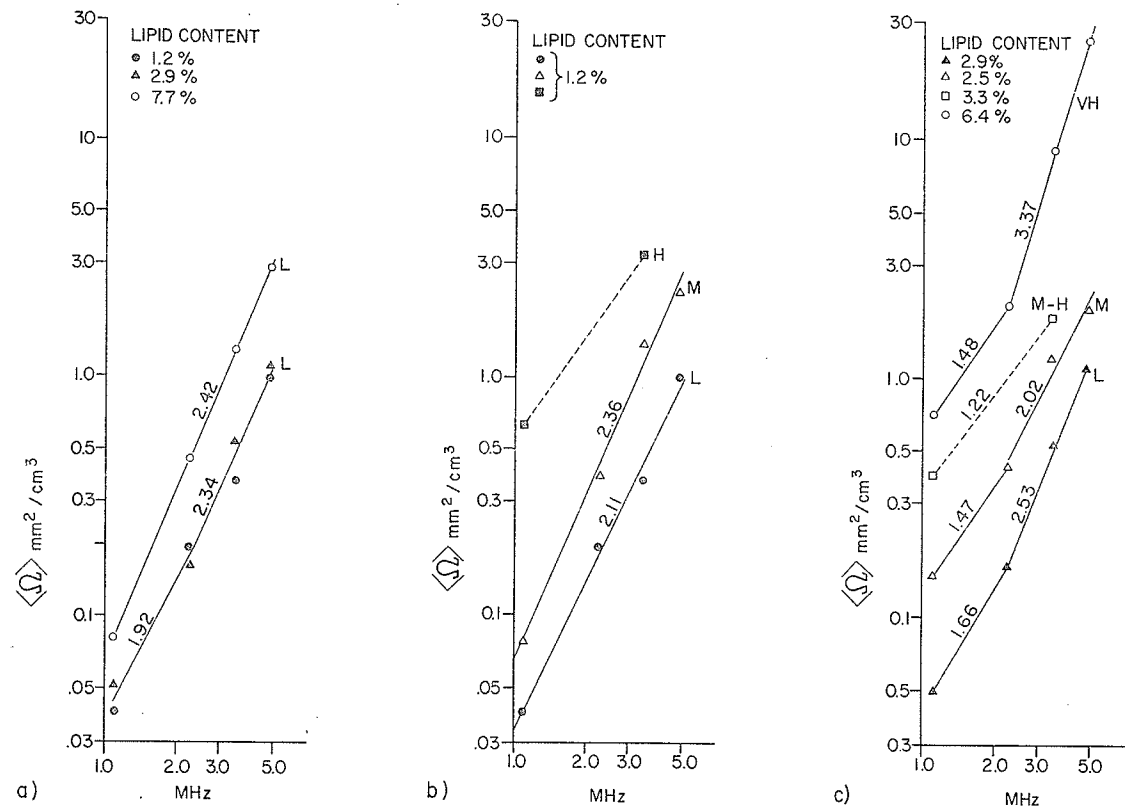

Fig. 5.8 Backscatter coefficients for whitefish grouped according to lipid content and estimated gas bubble concentrations: L < 15/cm^3; M - 15 to 150/cm^3; H > 150/cm^3 (a) Isolated bubbles only (b) Low lipid content; bubble concentrations low to high (c) Lipid content medium to fat; bubble concentrations low to high

In the case of the lean and medium fat specimens containing few bubbles [Fig. 5.8(a)], the two groups were combined for the purpose of determining the slope.

Comparing Fig. 5.8(a) with Fig. 5.4, the slopes of the lean and medium fat group show only slight changes in the 2.3 to 4.8 MHz range, although the $<\Omega>$ values are, of course, much lower. Thus, the slope of the lean group plotted in Fig. 5.8(b) shows a slight decrease from 2.30 to 2.11 over the 1.1 to 4.8 MHz range. In contrast, the medium fat group shows a slight increase from 2.30 to 2.53, while the fat group shows a substantial decline from 3.14 to 2.42 attesting to the effect of the one fat and highly saturated specimen [marked VH in Fig. 5.8(c)] referred to in the previous section.

In the 1.1 to 2.3 MHz range only the medium fat group of the three groups supposedly containing few bubbles shows a distinct change in slope. This would still seem to be primarily due to residual gas bubbles, although, as pointed out earlier, scattering from pinbones and interference from surface scattering could be factors. We note that as the gas bubble concentrations increase, the slopes in the 1.1 to 2.3 MHz range generally decrease, see Fig. 5.8(c), indicating an increasingly larger contribution by the gas bubbles to the overall scattering process. The apparent increase in slope in the range from 2.3 to 4.8 MHz at very high concentrations is an artifact stemming from the use of fixed TVG's (due to the gas bubble scattering losses, the absorption no longer varies as λ^{-1}). However, this is not where the problem lies.

If we subtract the responses for similar lipid contents to obtain the response of the gas bubble process, we obtain in the case of medium

bubble concentrations an average slope of 2.1 ± 0.5 in the 2.3 to 4.8 MHz range, which is nearly the same as for the basic tissue scattering process. This is most unfortunate for it implies that we cannot obtain a correction for the gas bubble contribution to the scattering process (in order to determine the lipid) by simply measuring the backscatter at two frequencies such as 1.1 MHz and 3.5 MHz or frequencies close to these.

Comparing the frequency responses in Fig. 5.8(a-c) with the responses for a single spherical bubble in Table 5.5 and for multiple bubbles (to first order) in Fig. 5.2, as well as the indicated quantitative disagreement, suggests that at these concentrations our first order composite process description which approximates the bubbles in the tissues as a cloud of spherical scatterers is invalid.

Referring to Table 5.5, none of the scatterers exhibits a λ^{-2} response with the exception of the disc. However, if there is a greater tendency for the bubbles to form at the sites of the myosepta, the resultant coherent scattering (Sections 2.3 and 2.4) would cause a decrease in the backscatter with increasing frequency as the beam is not perpendicularly incident. It is clear from Table 5.5 that at shorter wavelengths a slight eccentricity of the bubbles can result in a significant increase in Ω if the axes of rotation are aligned along the incident beam axis.[1]

---

[1] The BCS values for the oblate spheroid in Table 5.5 are only approximate since the ka value is actually too small even for the more complex physical optics solution [Crispin and Maffet, Chapter 4 of Crispin and Siegel (1968)] which should be used in evaluating end-on scattering ($\theta = 0^{o}$). However, for multiple scatterers, the effect of averaging over a distribution of ka values significantly reduces the contribution of higher order terms of the form sin(2kc)/(kc) as has been pointed out in Chapter 2. For the exact solution in terms of spheroidal functions see Chapter 22 of Skudrzyk (1971).

Although this would appear unlikely, the possibility of the gas bubbles assuming prolate shapes as a result of the constraining influence of the muscle fibers cannot be ruled out. However, in the limiting case of a thin rod, the maximum wavelength dependence for Dirichlet conditions is only of the order of λ^{-1} for long wavelengths and λ at short wavelengths. Thus, the disagreement does not seem to be caused by the bubbles not being spherical.

Stability of Gas Bubble Backscatter

In general, it was observed that in fish containing moderate to high bubble concentrations the backscatter was unstable if the fish were still in rigor immediately prior to the measurements being taken. In the case of those specimens exhibiting extremely high backscatter levels of up to 20 mm^2/cm^3 at 1.1 MHz, the largest change tended to occur at this frequency. As much as a five-fold decrease was observed over a period of twenty-four hours. This behaviour is consistent with the explanation offered in Chapter 2 that in some cases the tissues become supersaturated as a result of decompression when the fish is brought to the surface and a very broad bubble spectrum is formed. Afterwards, since the excess pressure of the smaller bubbles is greater, the larger bubbles will tend to grow at the expense of the smaller bubbles either by coalescing with them or by gas diffusion. The smallest bubbles of the order of a few microns would thus tend to disappear. The fact that rigor mortis is gradually resolved probably accelerates this process.

The backscatter coefficient for a group of four whitefish (common origin) still in rigor at the time of measurements is shown in Fig. 5.9(a). The abrupt decrease in Ω by nearly 7 dB in the range from

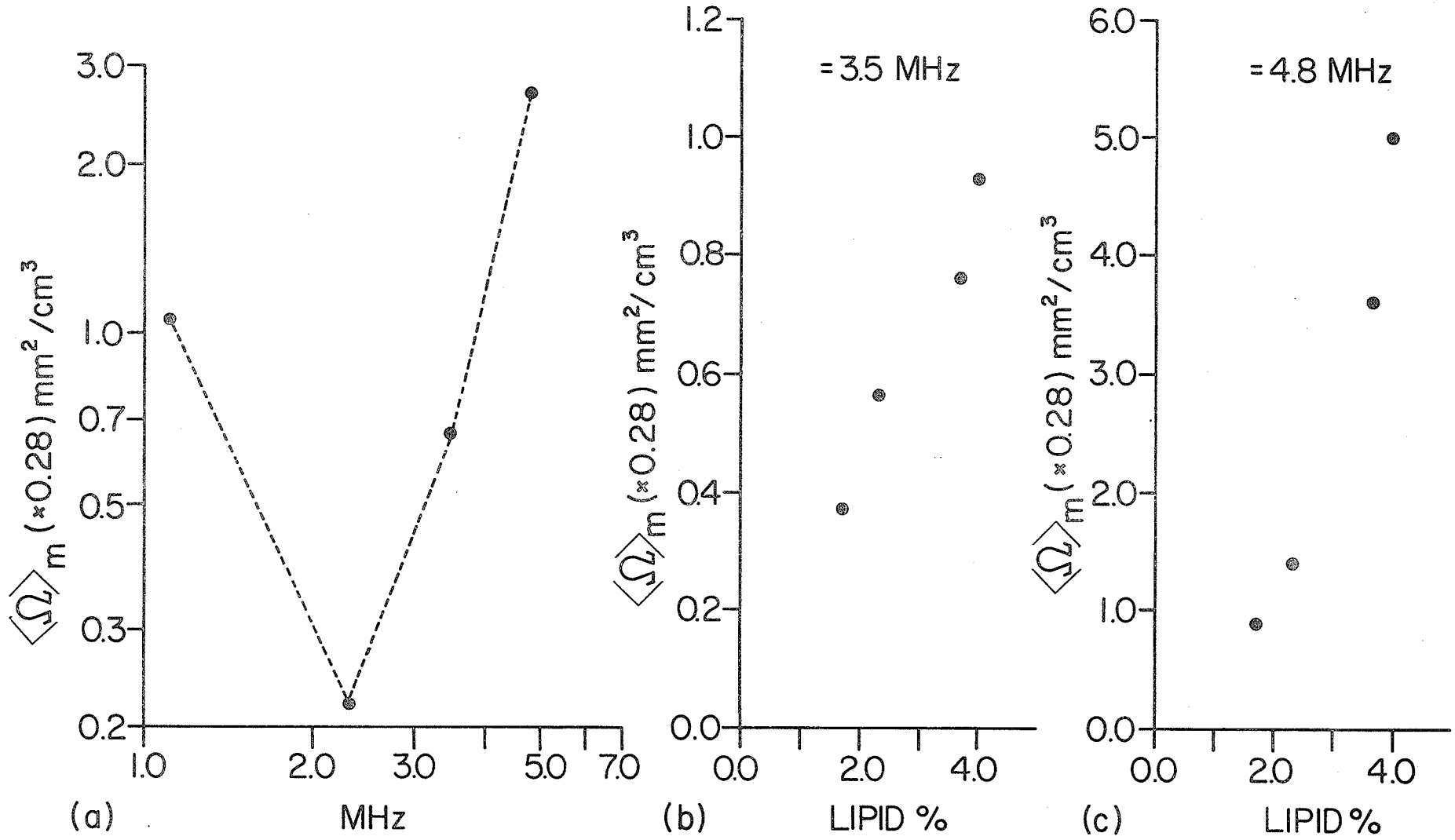

Fig. 5.9 (a) Average backscatter coefficients for four whitefish specimens of common origin containing large gas bubble concentrations.

(b) $\langle\Omega\rangle_m$ at 3.5 MHz vs. lipid content.

(c) $\langle\Omega\rangle_m$ at 4.8 MHz vs. lipid content.

1.1 to 2.3 MHz may indicate resonance scattering. Similarly, specimen #491, which was from a different lake, initially had an $\langle \Omega \rangle_m$ value of 2.8 mm^2/cm^3 at 1.1 MHz. The value had decreased to 0.57 mm^2/cm^3 by the following day when rigor had essentially disappeared. This would seem to indicate that the resonant gas bubbles, if there are any, are largely eliminated by the time rigor mortis is resolved. Once this initial equilibrium has been reached, the backscatter tends to remain stable over a period of a week or more of chilled storage. Changes in the chill temperature appear to have little effect, with changes from 0.5°C to 20°C seldom increasing the backscatter by more than 1.5 dB.

5.2.3 Backscattering by Lipid Inclusions

The dependence of the backscatter on lipid content was already pointed out in the last section and is quite apparent in Fig. 5.4, 5.5, 5.7, 5.8 and 5.9(b-c). The percent total lipid refers to the total lipid content of the white muscle as determined by the Bligh and Dyer (1959) method described in Section 4.6.1. To determine the lipid, the tissues in the epaxial region located just in front of the dorsal fin were excised after the ultrasonic measurements and any superficial adipose tissue was removed before homogenization of the flesh. Usually at least two replicates were performed. Significant variations in fat content and moisture were observed when samples were taken from other parts of the body, particularly the tail region. Although the differences in the replicates on the average were less than 10% of their mean values for low and medium-fat fish, the error in the case of the fatty fish could range as high as 20% in a few instances due to differences in preparing of the samples.

Based on Fig. 5.7, the dependence of the backscatter intensity on the lipid content appears to be approximately linear for lipid contents up to at least 4%. If we assume that the diagonals in Fig. 5.7(b) mark the lower limit of the backscatter variation in whitefish, we obtain a value of 0.20 $mm^2/cm^3/\%$ lipid at 3.5 MHz. Although it may have been a mere coincidence, it is interesting to note that even in whitefish specimens containing large concentrations of gas bubbles the backscatter still shows a high correlation to the lipid content, see Figs. 5.9(b-c).

In view of the above dependence of Ω on the lipid content, it is clear that in the absence of gas bubbles lipid inclusions will usually be the dominant scatterers in whitefish at frequencies above 2.3 MHz. The average background contribution from other scatterers and intracellular liposomes appears to be less than 0.15 mm^2/cm^3 at 3.5 MHz, see Fig. 5.7(b).

If we consider fat whitefish muscle with a total lipid content of 5.9% by weight, 1.2% might be found in the myosepta adipose tissue, 4.0% in the intramuscular-intercellular connective and adipose tissue and the remainder (consisting predominantly of phospholipids) intracellularly. Taking the average equivalent diameter of the globules in excess of 20 μm (which contain perhaps two-thirds of the total intercellular lipid) as 40 μm, the average BCS of the oil globules (Fig. 2.5) becomes $6 \times 10^{-4}(\pi a^2) = 7.5 \times 10^{-7}$ mm^2 at 3.5 MHz. This is based on values of $\rho = 0.91$ gm/cm^3 and $c = 1465$ m/sec for the lipid [Gouw and Vlugter (1967)]. The number of scatterers n obtained from V_c via (5.1.1) comes to 1.15×10^6 $bubbles/cm^3$. The resultant backscatter coefficient equals 0.86 mm^2/cm^3. The contribution of the remainder of the small oil globules (< 20 μm in diameter) is hardly significant and increases Ω to 0.9 mm^2/cm^3.

We have assumed here simple Rayleigh (λ^{-4}) scattering from randomly distributed globules. However, the latter is decidedly not the case. Experimentally it is observed, particularly in fat fish, that the globules are arranged more like beads on a string due to the constraining forces of the adjacent muscle fibers. Such an arrangement was also noted by Greene (1913) when sectioning salmon lateral muscle. However, considering that we have broadside incidence (transverse to the fibers), the maximum possible effect this could have is a dependence somewhere between λ^{-3} and λ^{-4} for diameters of $ka << 1$, and a possible λ^{-1} dependence for $ka \geq 1$. It should be noted that the latter is consistent with scattering by the cells themselves in terms of the background observed in pickerel ($\lambda^{-1.25}$).

The possible scattering contribution by some of the larger oil bubbles presents more of a problem both in terms of their range of diameters and their actual number. It is primarily the presence of these larger globules that accounts for the dependence of Ω on λ being less than λ^{-4} in the case of fat fish. This is illustrated rather well by the results of backscatter measurements performed on suspensions of oil ($\rho = 0.916$ gm/cm^3, $v = 1465$ m/sec) in gelatin.

Media of different oil concentrations were prepared from gelatin with care being taken to exclude all air bubbles. The measurements results are shown in Fig. 5.10. In the case of the LG3 medium, the average bubble diameter was approximately 25 μm with few bubbles exceeding 50 μm. As a result the scattering is almost strictly Rayleigh with the scattering varying in the 2.3 to 4.8 MHz range as $\lambda^{-3.5}$. The difference from an exact λ^{-4} dependence is attributable to the presence of a few larger

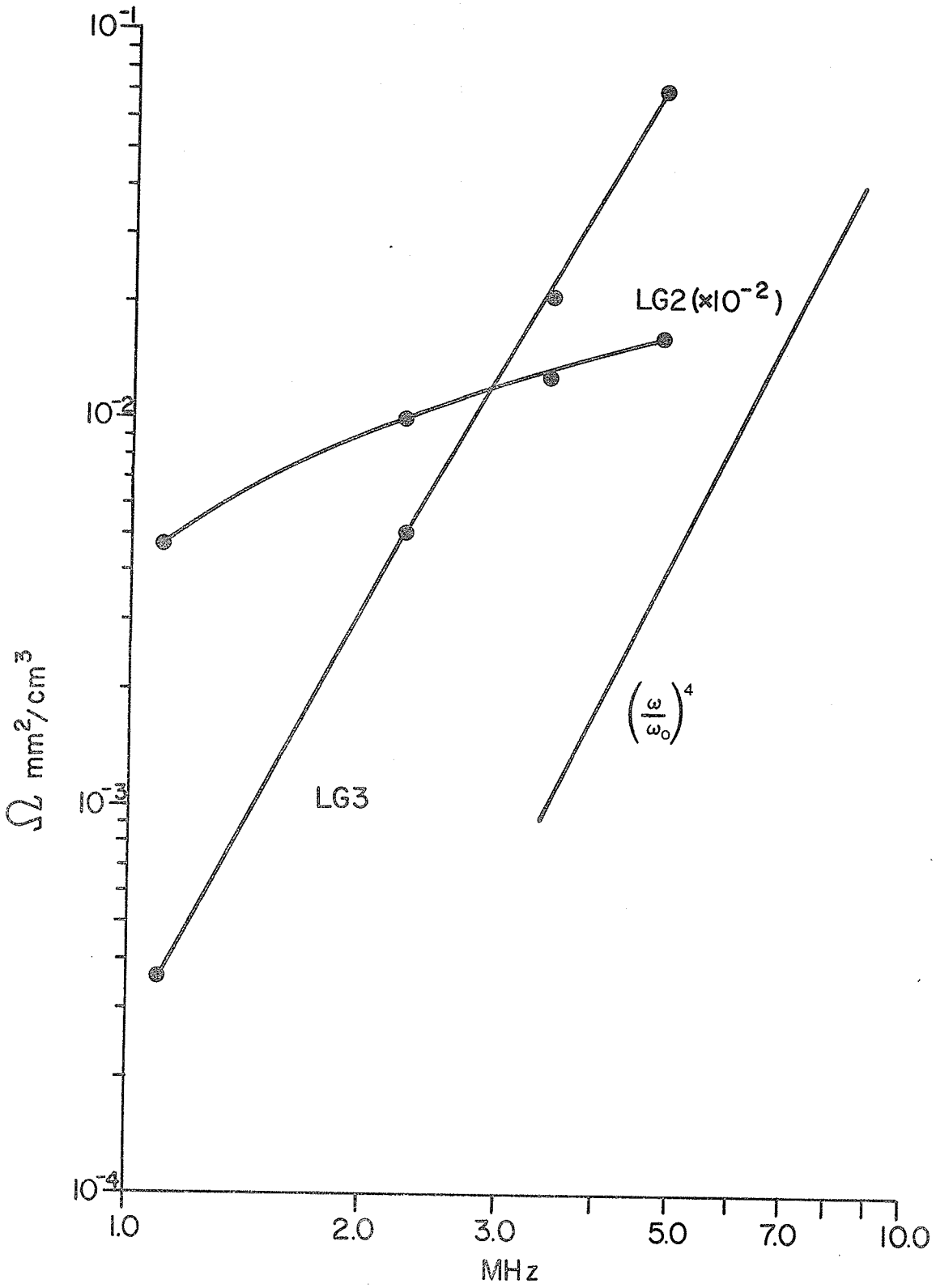

Fig. 5.10 Backscatter coefficients for oil bubble gelatin suspensions
Estimated average bubble diameters: LG2 - 200 μm; LG3 - 25 μm.

bubbles and experimental error due to the fact that all the backscatter levels were near the sensitivity limits of the analyzer. The 1.1 MHz measurement particularly was subject to considerable experimental error at this level because of interference from the 'main bang' reverberation. In contrast to the LG3 medium, the average oil bubble diameter of the LG2 medium was estimated at nearly 200 μm. Moreover, the distribution of the bubble diameters was quite wide, varying from 50 μm to as much as 400 μm. We find that the backscatter varies only as $\lambda^{-0.63}$ in the 2.3 to 4.8 MHz range, increasing to $\lambda^{-1.1}$ at 1.1 MHz. The LG2 backscatter level is also comparable to the level exhibited by fat whitefish free of gas bubbles.

Returning to the calculation of the lipid backscatter, the approximate geometric BCS of an individual globule is obtained by multiplying the BCS of the perfectly reflecting scatterer by the square of the Fresnel reflection coefficient (2.2.4) at normal incidence. Furthermore, if $|R^2| \ll 1$ and the refractive index $(c_1/c_2) \approx 1$, the average backscattered power will be roughly doubled since the rear-axial specular reflection will be only slightly smaller in amplitude than the front-axial specular reflection. Using the above values of $\rho_2 c_2$, $R \simeq 0.10$ at normal incidence so that the backscattered power from a lipid globule at short wavelengths is about 17 to 18 dB lower than from an air bubble of the same size (Table 5.5).

Based on observations of thick sections from specimen #435 containing 5.9% lipid, the average equivalent diameter of the large globules (> 75 μm) was estimated to have been at most 200 μm (some of the largest cells measured 150 × 300 μm^2) with perhaps 100 to 300 of these

large globules per cm^3. Assuming 200 globules/cm^3 and a total geometrical contribution Ω_{geom} of 0.3 mm^2 (equal to the measured value of 1.32 mm^2 less the total Rayleigh contribution of 0.9 mm^2 and the background of 0.1 mm^2) yields an equivalent $V_{c(geom)}$ of approximately .002. This indicates that these large globules contain less than 5% of the nearly 6% total lipid present in the tissues.

Using these values and utilizing the gelatin-oil media results, we now compute Ω at intermediate frequencies. Assuming that Ω_{geom} decreases by 35% (LG2 in Fig. 5.10), the calculated value of Ω at 2.3 MHz becomes 0.43 mm^2/cm^3 compared to a measured value of 0.45 mm^2/cm^3. Similarly, assuming that Ω_{geom} declines to 0.05 mm^2/cm^3 at 1.1 MHz ($\lambda^{-1.5}$ dependence) and the background (varying as $\lambda^{-1.25}$ using pickerel as the model) declines to 0.025 mm^2/cm^3, the calculated value becomes .085 mm^2/cm^3 compared to a measured value of .082 mm^2/cm^3. Although the model is obviously crude, the globules having a very wide roughly exponential distribution, the model does predict the values of Ω at the lower frequencies rather well.

5.2.4 Backscattering from Pinbones

The position of the pinbones in whitefish may be seen in Fig. 2.3. Roughly speaking, the bones project at an angle of 45° in the cross-sectional plane, backwards at about 30° with respect to the median plane and at approximately 25° in the vertical plane. In practice, the incidence angle with respect to the pinbones will be in the neighborhood of 72° (beam incident about 1 cm above the median plane perpendicular to the body surface, see Fig. 4.2). The cross-section area of the bones is roughly halfway between rectangular and elliptical in shape. Towards the outer

ends the pinbones grow finer, tapering from an average of 0.38 × 0.5 mm^2 to about 0.2 × 0.35 mm^2. Assuming that the pinbone specific acoustic impedance resembles that of scales [Freese and Makow (1968.b)], one obtains using (2.2.2) and (2.2.3) the results shown in Table 5.6.

TABLE 5.6

PINBONE BACKSCATTER CROSS-SECTIONS

f MHz	λ mm	ka Radians	θ_1 Degrees	L_{eff} mm	σ mm^2
1.1	1.41	0.60	90	5.1	1.6
			79		7.7×10^{-2}
			72		2.5×10^{-2}
			59		6.2×10^{-3}
3.5	0.45	2.51	90	4.7	1.8
			85		7.1×10^{-2}
			72		3.2×10^{-3}
			61		8.0×10^{-4}

$a = 0.18$ mm
$b = 0.10$ mm
$\rho_2 = 1.41$ g/cm^3
$\rho_1 = 1.055$ g/cm^3
$c_2 = 1.87 \times 10^5$ cm/sec
$c_1 = 1.55 \times 10^5$ cm/sec
$R_c = 50$ mm
$\theta = \pi/4$

The calculated values show that the backscatter for an angle of incidence near 72^o is nearly an order of magnitude greater at 1.1 MHz than at 3.5 MHz. Moreover, comparing these values with the BCS values for gas bubbles of the sizes most frequently encountered (75 to 300 μm) in Table 5.5, we see that the gas bubble BCS values are of the order of

10 dB greater than the pinbone BCS at 1.1 MHz. Experimental measurements on excised pinbones at 3.5 and 5.0 MHz for broadside incidence yielded an average value of 1.1 mm^2 which is in good agreement with the calculated value. Thus, apart from an occasional large echo from a pinbone that is near normal incidence, scattering from pinbones in comparison to other sources will be negligible above 2.3 MHz and this is confirmed experimentally.

5.2.5 Backscattering by the Myosepta

Except in very lean fish and possibly in large fish (> 2 Kgm), it is clear from the earlier results that backscattering by the myosepta, although they constitute a very distinctive feature of the myomere, is not a major factor. Nonetheless, it is of interest to estimate their contribution to the total background to see whether we can explain the differences in the wavelength dependence observed for pickerel and whitefish. Before calculating the backscatter we will describe the myosepta in somewhat greater detail and analyze their surface characteristics.

Physical Structure of the Myosepta

The myosepta separating the individual myomere are composed chiefly of connective tissue, which in fat fish are often crowded with adipose tissue. In whitefish the myosepta are clad with a very thin opaque membrane as shown schematically in Fig. 2.8(d) giving the myosepta a milky appearance (Fig. 2.4). Near the body surface they are often thicker due to agglomerations of lipid cells as can be seen in the whitefish cross-section shown in Fig. 2.3. Viewed edge-on the myoseptum in whitefish resembles a curved rough layer of large and small scale roughness.

The pickerel myosepta are translucent and considerably smoother in appearance than the whitefish myosepta. They are two to three times as thick and are very much tougher than the relatively fragile whitefish myosepta. Sections of whitefish and pickerel muscle cut at approximately right angles to the myosepta are shown in Figs. 5.12 and 5.13.

The specific admittance of the myosepta connective tissue is probably constant. The density of whitefish myosepta samples consistently averaged about 1.07 ± 0.005 gm/cm^3. The velocity is estimated at $(1.58 \pm 0.02) \times 10^5$ cm/sec yielding a normalized specific admittance of 0.964 ± 0.013.

The principal surface parameters of whitefish and pickerel myosepta were determined from enlargements of lean sample sections. For the l.s. roughness the sections were sampled at intervals of 150 μm over 3 to 5.7 mm lengths of the myosepta, while for the s.s. roughness a sampling interval of 74 μm was used. In determining the l.s. roughness a value of unity was assumed for the cross-correlation coefficient K_{cc} (see Section 2.3.3), although perhaps 0.9 is a more realistic value.

The correlation functions of the roughnesses C(d) were determined for myosepta cross-sections lying parallel to a vertical line in the median plane of the body of the fish. The correlation functions in the case of the l.s. roughness approximated a Gaussian distribution rather well near the origin, see Fig. 5.11. For values of $d > T_{\xi\ell}$ (l.s. correlation constant) it was difficult to evaluate C(d) due to the distortion and curvature of the samples. However, there did not appear to be any periodicity.

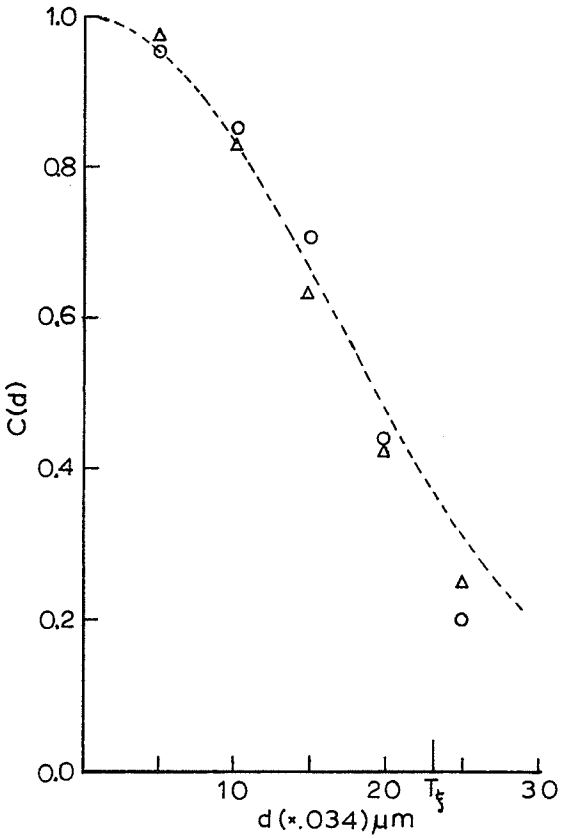

Fig. 5.11 Experimental roughness autocorrelation of whitefish myoseptum surface; specimen #430; myomere lipid content 1.5%.

Fig. 5.12 Edge-on view of myosepta in medium whitefish; myomere lipid content approx. 3%.

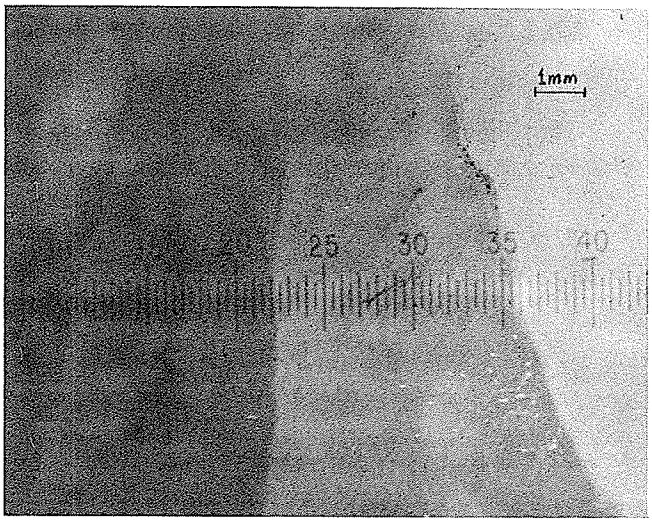

Fig. 5.13 Edge-on view of myosepta in a large pickerel (1.8 Kg).

The correlation lengths and the r.m.s. roughnesses for whitefish are given in Table 5.7. Some correlation of the magnitudes of the h_ℓ, h_s and ℓ_o values was apparent. The s.s. roughness correlation distance is very much smaller than the shortest wavelength utilized and hence will not give rise to coherent scattering. Any contribution by the s.s. roughness to the diffuse backscatter will be insignificant in comparison to the diffuse scatter resulting from the l.s. roughness if the cross-correlation constant for the two sides of the layer is slightly less than unity as is indicated.

TABLE 5.7

STATISTICAL PARAMETERS OF WHITEFISH MYOSEPTA

Parameter		Average Dimension μm	Normalized[1] Value at 3.5 MHz ($\times \lambda^{-1}$)	Comments
Thickness	(ℓ_o)	50	0.11	ranges between 20 - 130 μm
Large Scale Roughness r.m.s. elev.	(h_ℓ)	50 ± 25	0.11 ± 0.055	values given are for lean-medium whitefish weighing 0.5 - 1.0 Kgm
Correlation Distance	($T_{\xi\ell}$)	630 ± 230	1.4 ± 0.5	
Small Scale Roughness r.m.s. elev.	(h_s)	~7	0.016	radius of curvature of myosepta in insonified region 2 - 4 cm
Correlation Distance	($T_{\xi s}$)	<80	<0.18	

(1) λ = 450 μm

The l.s. roughness of the pickerel is similar to the l.s. roughness of whitefish given in Table 5.7, while the s.s. roughness appears to be still smaller. No adipose tissue was noted within the myosepta of any of the pickerel samples examined.

Finally, it should be mentioned that in pickerel weighing about 1 Kgm the myotome thickness ranges from 5 to 6 mm (fiber length is 6 to 9 mm) compared to 3 to 4 mm in whitefish of the same weight. Therefore, pickerel muscle contains 35 to 50% less myosepta area than whitefish muscle.

Comparison of Backscattering by the Myosepta as a Function of the Angle of Incidence

Considering the surface roughness parameters in Table 5.7, we observe that at 3.5 MHz the value of $T_{\xi\ell}/\lambda$ is only 1.4. Ideally we should have $T_\xi >> \lambda$ for the Kirchoff approximation to be valid. However, comparisons of the Kirchoff values for a variety of periodic rough surfaces with the more accurate values obtained using the Rayleigh method[1] suggest that in many cases the Kirchoff method still yields an acceptable estimate of $\langle\Gamma\rangle$ for T_p/λ approaching unity; T_p is the surface periodicity and has a role similar to the surface correlation distance T_ξ. [Beckmann and Spizzichino (1963) give a number of comparisons in their monograph.] Although the above is encouraging, because we are essentially exceeding the limits of validity of the physical optics theory, we should not expect the theory to yield more than a qualitative estimate.

---

[1]The Rayleigh method is basically the inverse of the Kirchoff procedure but is also applicable when edges are present on the surface (see Chapter 4, loc. cit.).

Values of the pulse intensity scattering coefficient $\langle \Gamma\Gamma^* \rangle_m \equiv \langle \Gamma\Gamma^* \rangle_{\text{fbp layer}}$, where the subscripts f, b and p denote the finite reflectivity, beamwidth and pulse, respectively, were computed for different membrane thicknesses. For the lower range of surface roughness, $h_\ell = 25$ μm, the maximum value (normal incidence) of the Rayleigh parameter (2.3.53) at 3.5 MHz is 0.4866. Therefore, we employ (2.4.22) together with (2.3.73). In the case of the specular component, we used either (2.3.11) or (2.3.12) for the layer reflectivity depending on the layer thickness. To effect the change to the exact expression for the layer reflectivity, we replace $4|R_i|^2 \sin^2 \alpha_2 \ell$ by the square of the absolute value of R_ℓ given by (2.3.11). [We note that for $\alpha_2 \ell = n\pi \pm \pi/2$, where $n = 1,2\ldots$, $R_\ell = R_i$. In contrast, the value based on (2.3.12) would be in error by +6 dB.] Values of $[\langle \Gamma\Gamma^* \rangle_{\text{fbp layer}} (ka)^2 \cos^2 \delta_i]$ for the upper range of surface roughness were calculated at 4.8 MHz, where $g = 8.52$, $\delta_i = 0$. In this case we use (2.4.18) and (2.3.73). A further modification was the substitution of the asymptotic evaluation (2.3.66) due to Fung and Leovaris (1969) in place of Beckmann's evaluation (2.3.62) for $g >> 1$.

The admittance of the myoseptum membranes was determined by excising a number of membranes and comparing the specular reflection at normal incidence with the specular pulse from a rigid planar reflector. In calculating the theoretical values of $\langle \Gamma\Gamma^* \rangle_{\text{fbp layer}}$ care was taken to employ the appropriate equivalent radii. For the coherent component, i.e. for the beam pattern $\left[\frac{2J_1(x)}{x}\right]^2$ and the gain $(ka)^2$, $r_{eq}^{(1)}$ applies, see Table 4.3. As discussed in Section 3.6, the gain is then reduced by 3.9 dB measured at 3.5 MHz. For the diffuse component, $r_{eq}^{(2)}$ is applicable for the equivalent insonified area.

The calculated values of $[\langle \Gamma\Gamma^* \rangle_m k^2 a^2 \cos^2 \delta_i]$ for different membrane thicknesses are plotted in Fig. 5.14(a), while the backscatter strengths at 3.45 MHz are plotted in Fig. 5.14(b). A number of experimental values are also shown in Fig. 5.14(b). Considering the degree of approximation introduced to the problem, the experimental and theoretical angular dependences of the backscatter are in surprisingly good agreement, at least for angles up to 10^o. Moreover, the values appear to be roughly in quantitative agreement as well. The different membrane thicknesses are seen to have very little effect on the diffuse backscatter, the backscattering being essentially all diffuse for $\delta_i > 3^o$. However, at 3.5 MHz the diffuse backscatter for angles of $\delta_i \approx 40^o$ and g = .286 is clearly negligible.

The situation is quite different at 4.8 MHz for g = 8.52. Although the backscatter strengths at 4.8 MHz (given by $\langle \Gamma\Gamma^* \rangle_m (ka)^2 \pi a^2 \cos^2 \delta_i$, where $\pi a^2 = 22.9$ mm^2) and at 3.45 MHz are approximately equal in magnitude at $\delta_i = 15^o$, unlike for the latter, the decrease of the 4.8 MHz backscatter with angle is much more gradual. Some ripple is also introduced into the angular response as the membrane thickness becomes greater. However, even for this roughness (h_ℓ = 75 μm), the backscatter strength at $\delta_i = 40^o$ is still only 2×10^{-3} mm^2. The fact that the membrane thickness has little effect on the magnitude of the diffuse scatter in part explains the lower backscatter level of pickerel compared to whitefish.

Assuming that in the case of whitefish the insonified volume will be intercepted on the average by three myosepta, the total contribution by the myosepta to the tissue scattering process at 4.8 MHz would be at most of the order of .02 mm^2/cm^3 or approximately 20% of the observed background.

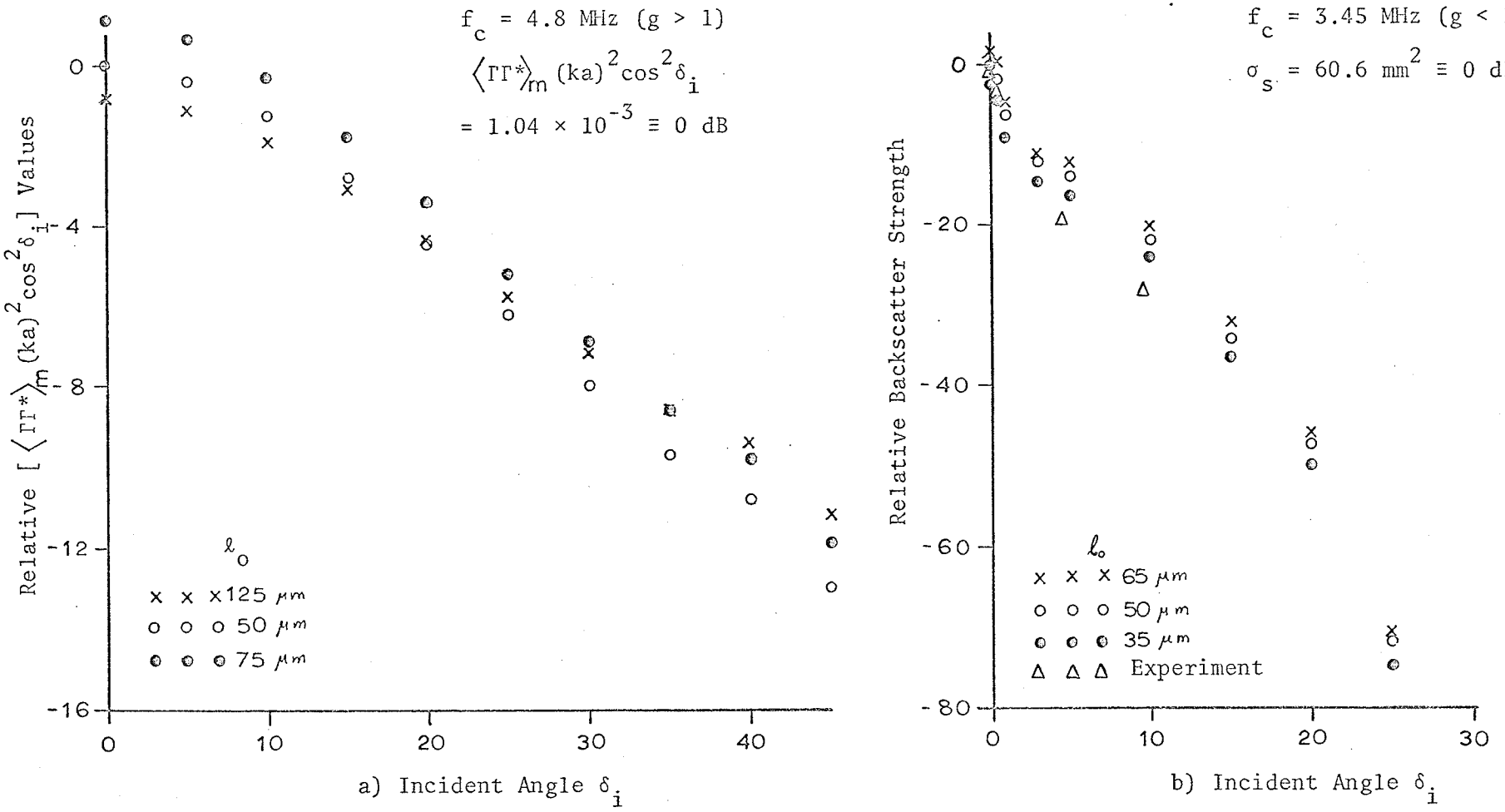

Fig. 5.14(a) Estimated myosepta pulse intensity scattering coefficient as a function of incidence angle and average membrane thickness.

(b) Backscatter level as a function of incidence angle for a whitefish myoseptum sample 'in situ'.

5.2.6 Effect of Other Tissue and Measurement Parameters on the Myomere Backscatter

Comparisons of the backscatter coefficient for whitefish with the total protein content usually showed a very slight negative correlation, which can probably be ascribed to the slightly negative correlation of the lipid and protein content (Table 2.1).

In contrast to the relatively low correlation with protein, the correlation of Ω with the moisture content was actually higher than for the lipid content. For homogeneous groups of whitefish, the correlation coefficient of Ω versus percentage total lipid was typically of the order of 0.80 at a level of significance of 0.5% or better, while for Ω versus percentage moisture it would range as high as 0.95. The dependence, of course, is spurious since the moisture and lipid content are highly negatively correlated (Table 2.1). Typically the correlation of lipid with moisture observed for whitefish was in the range of -0.8 to -0.9 at a level of significance of 0.1% or better.

The higher correlation of Ω with moisture than with the lipid content would seem to be mainly attributable to the significantly greater overall accuracy of the moisture determinations.

In this connection it should be pointed out that the correlation of the lipid content with $\langle \Gamma_E \rangle^2$ [see (5.2.1)] was usually also somewhat higher than for $<\Omega>$. The reason for this would seem to be the smaller relative contribution of the occasional large interfering echoes from other scatterers to $\langle \Gamma_E \rangle$ compared to $<\Omega>$. For practical applications, e.g. determining the lipid content using backscatter, it is therefore preferable to time average (integrate) the gated stationarized backscatter

envelope before squaring. From the point of view of the circuit designer this has obvious advantages in that it requires only a fraction of the multiplier bandwidth that is needed for squaring the signal envelope.

The effects on the backscatter of various other factors including temperature at the time of measurement, storage time on ice, pre-rigor or post rigor condition, mechanical damage of the tissues (bruising) and the effect of probe positioning were briefly investigated. The first three factors were considered in Section 5.2 in connection with the stability of the gas bubble backscatter. The temperature and storage time in the post rigor stage were of secondary importance. Similarly the effect of mechanical damage on the backscatter in post mortem fish unless quite severe, that is resulting in major lesions or open gashes of the flesh, was also a relatively minor factor.

The effect of the probe positioning on the backscatter appears to be significant. For low backscatter levels the backscatter from the upper epaxial region seems to be slightly greater than from the lower epaxial region, Fig. 5.15. On the other hand the backscatter from the lower epaxial region along the lateral muscle roughly between the nape and a position halfway between the dorsal and anal fin did not differ significantly on the average.

Seasonal variations although not specifically investigated presumably would be mirrored in the nutritional state of the fish (usually poorer, i.e. lower lipid content, at the end of winter or at spawning time) and also by movements of the fish from warmer to cooler water so that the probability of fish with higher gas bubble concentrations in the tissues is likely to be greater in the summer.

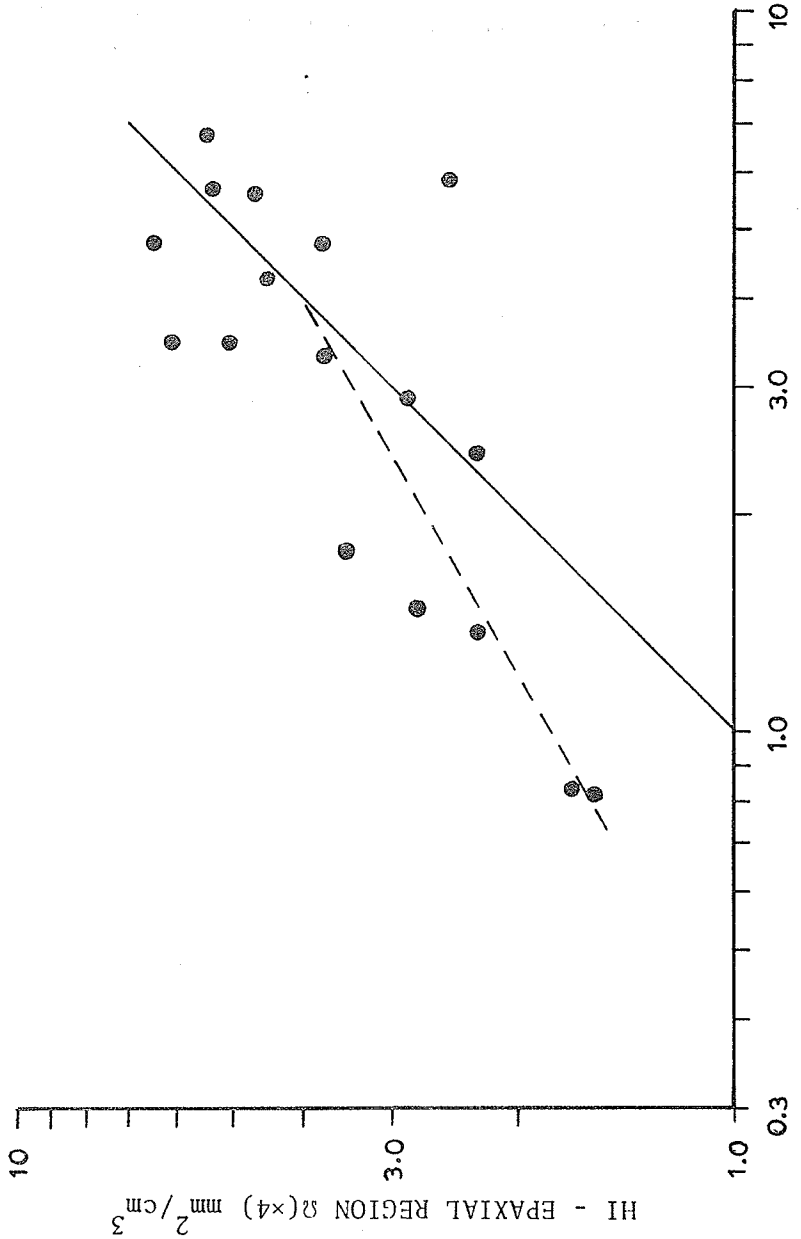

Fig. 5.15 Comparison of backscatter coefficients for the upper (HI) and lower (LO) epaxial region of the whitefish lateral muscle; the solid line marks equal values of Ω.

This concludes our consideration of backscattering by fish myomere. In the next section we very briefly consider the results of some preliminary backscatter measurements on two samples of bovine myomere.

5.3 Backscattering by a Sample of Bovine Skeletal Muscle

The beef samples (sirloin) were obtained from a local butcher. As a result little was known about the samples other than that the meat was fresh and graded A 2. The meat was well-marbled with fat and relatively free of any thick tendinous connective tissue sheaths. The absorption was similar to the absorption values obtained previously by Freese and Makow (1968,b) for beef muscle, see Table 5.4.

The values of the backscatter coefficient based on averages of two independent measurements per sample are plotted in Fig. 5.16. The low values of Ω at 3.5 MHz relative to the values at the other frequencies are probably the result of a measurement error. Assuming this to be the case, the average dependence on wavelength over the range from 1.1 to 4.8 MHz is found to be $\lambda^{-2.4}$, rising from λ^{-2} in the 1.1 - 2.3 MHz range to λ^{-3} in the 2.3 - 4.8 MHz range. The experimental accuracy of the wavelength dependence is approximately ± 0.5. Although the present backscatter results give at best only a qualitative indication of the backscatter coefficient, the average value of Ω appears to be significantly greater than for fish myomere free of gas bubbles which would seem to be in accord with the histological picture of the bovine myomere.

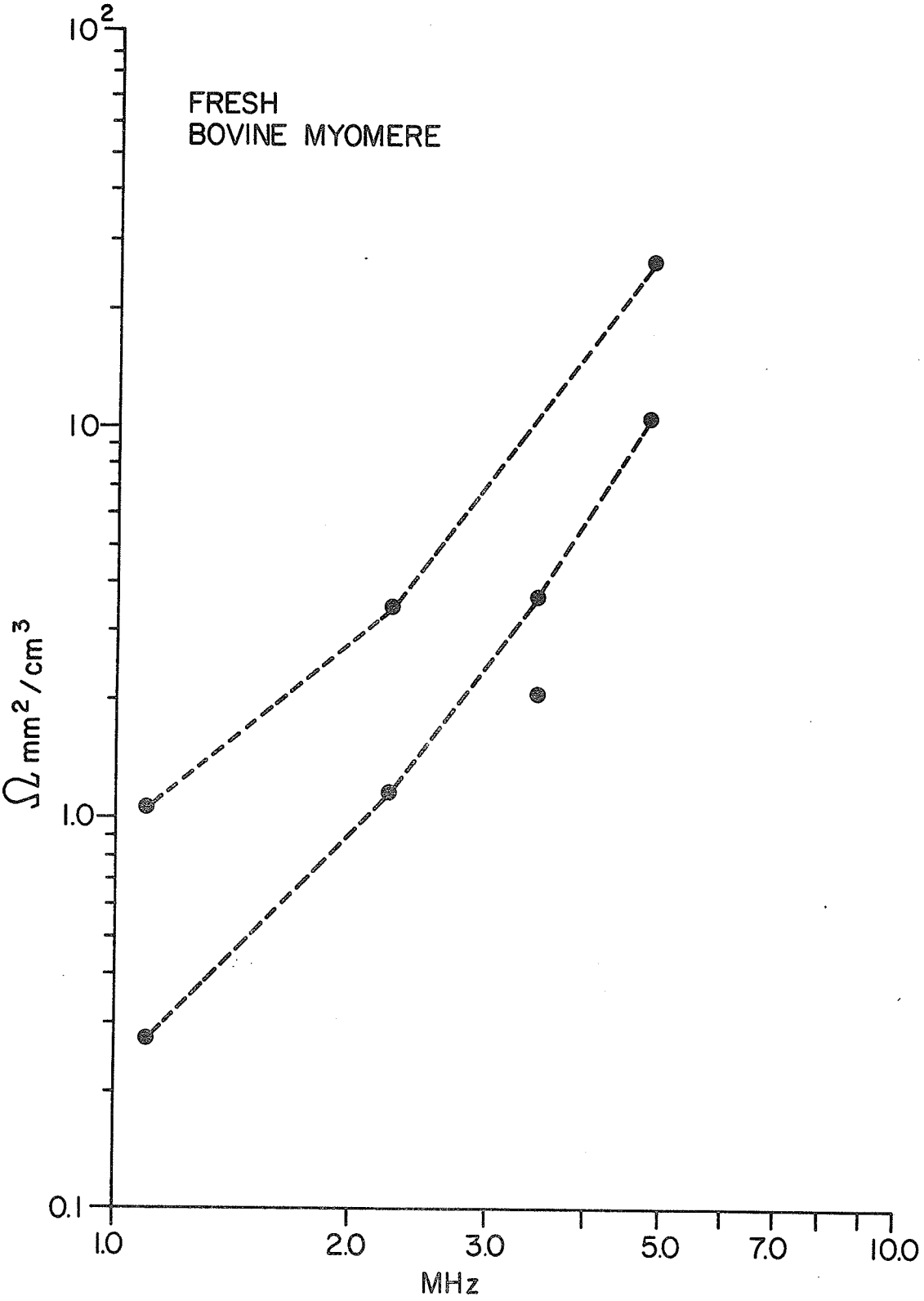

Fig. 5.16 Backscatter coefficient for a sample of beef muscle.

CHAPTER 6

CONCLUSIONS

The results of this investigation would appear to confirm the validity of the measurement technique for the determination of volume scattering by tissues, subject to the qualification that there are no large coherent scatterers, i.e. large with respect to the beam diameter, dominating the scattering. The significant scatterers in the fish myomere were isolated and their contribution to the overall scattering process, as well as their dependence on wavelength, was determined. The results also demonstrate the value of the Middleton-Ol'shevskii phenomenological approach for analyzing complex scattering situations such as the muscle tissue scattering process.

6.1 Summary

The comparison of the backscatter measurements on the gelatin model media with first order theory yielded substantial quantitative agreement in the 1.1 to 3.5 MHz frequency range, provided that the experimentally determined absorption values for the media were employed. The experiment represents a test of the validity of the first order scattering theory, the statistical model, the scattering coefficient definition (2.4.23), the stationarization (3.3.5), the backscatter characteristics of the suspended gas bubbles, the equivalent insonified volume determinations, the reference cross-section calibration and the instrument calibration. Implicit is the restriction on the pulse

bandwidth, which should not exceed the limits set as determined by the absorption of the medium and the maximum path length used for the backscatter measurements (Section 3.5).

The decrease in $\langle\Omega\rangle$ in the 1.1 to 2.3 MHz range (Fig. 5.2) and the quantitative agreement indicate that, as far as the backscatter is concerned, the gas bubbles behave approximately as spherical Dirichlet scatterers for $0.7 < ka < 4$. On the other hand, the experimental absorption coefficient at high volume concentrations was significantly lower than the calculated value based on first order theory. The values differed on the average by more than 3:1. The disagreement was greatest at 1.1 MHz where, theoretically, the total cross-section of the bubbles is also greatest. This suggests a breakdown of the single scattering assumption and needs to be further investigated.

The far-field and near-field measurements in the transition region were in agreement (Fig. 5.2), with the exception of one value at 4.8 MHz. However, this value was in agreement with the trend established by the other transition-field measurements.

It was found that the dependence of the backscatter from the myomere (transverse incidence) in the frequency range of 2.3 to 4.8 MHz can be approximately described by a power law of the form $\Omega = \Omega_o(\lambda_o/\lambda)^x$, where λ is the wavelength. In the case of whitefish, Ω generally varies as $\lambda^{-2.3}$ compared to roughly $\lambda^{-1.3}$ for pickerel and $\lambda^{-2.4}$ for a sample of bovine muscle. The $\lambda^{-1.3}$ dependence in pickerel is due primarily to scattering by the muscle fibers and the myosepta.

The scattering measurements on whitefish reveal a strong dependence of the backscatter on the total lipid content and, if the

tissues are free of gas bubbles, lipid inclusions are likely to be the dominant scatterers. However, it is also shown that, as a result of decompression, gas bubbles are almost invariably present in whitefish, in which case these tend to be the predominant scatterers. The fact that gas bubbles were much more common in whitefish than in pickerel is probably explained by the preference of whitefish for deeper, colder water with the attendant increase in pressure.

The average backscatter coefficient Ω of whitefish myomere free of gas bubbles and containing 3% total lipid is approximately 0.5 mm^2/cm^3 at 3.5 MHz. For total lipid contents of up to 6%, a roughly linear relationship between the backscatter intensity and the lipid content is observed, with Ω varying at a rate of roughly 0.2 $mm^2/cm^3/\%$ lipid.

The dependence of Ω on moisture, which actually shows a slightly higher correlation, is thought to be spurious since the moisture and lipid content tend to be highly negatively correlated (Table 2.1). The higher correlation is probably mainly attributable to the greater overall accuracy of the moisture determinations.

Only a very slight correlation of backscatter and protein content was evident in the case of whitefish.

The residual backscattering or background level in the case of whitefish free of gas bubbles and having negligible lipid content (< 1%) appears to be of the order of 0.1 mm^2/cm^3 at 3.5 MHz (Fig. 5.7). The greater number of myosepta and scattering by pinbones at the lowest frequencies would appear to account for the slightly higher background in whitefish compared to pickerel (Fig. 5.4). Under normal circumstances, however, scattering by the myosepta in whitefish does not appear to be a significant factor (Fig. 5.14).

It was found that the backscatter level does not differ significantly with position along the lateral muscle in the region of the dorsal fin. However, for low backscatter levels, the backscatter from the upper epaxial region may be slightly greater than from the lower epaxial region (Fig. 5.15).

The major obstacle encountered in determining lipid content from the backscatter is the presence of gas bubbles in the tissues as a result of decompression. In over two thirds of the whitefish specimens measured the gas bubbles were the dominant scatterers. The significance of this, for example, in the measurement of the absorption in fish tissues, does not appear to have been fully appreciated in the past. The effect of the bubbles increases the backscatter level an average of 3 to 4 dB at 3.5 MHz. Taking scattering by the gas bubbles into account, the average backscatter level in whitefish is thus 10 to 11 dB higher than in pickerel (Figs. 5.4 and 5.5).

In general, it was found that the wavelength dependence of the scattering by the gas bubbles in the myomere was not compatible with first order scattering by a cloud of spherical bubbles. In selected whitefish free of gas bubbles the dependence on wavelength did not differ significantly (increasing on the average to $\lambda^{-2.4}$) from whitefish containing moderate concentrations of gas bubbles (Fig. 5.8). This appears to rule out a simple differential measurement technique using two frequencies for determining the lipid content for whitefish.

On a few occasions anomalously high backscatter was observed. These fish were invariably very fresh and still in rigor. The backscatter in these cases was unstable, with the level decreasing over a

period of one day by 3 dB or more at 1.1 MHz (less at higher frequencies). This may be attributed to a shift in the mean diameter of the bubble spectrum as a result of the absorption and aggregation of the smaller bubbles. Once this initial period had passed the backscatter tended to remain at a stable level.

6.2 Suggestions for Further Work

The investigation of the backscatter properties could be extended to other types of tissues. Volume backscatter by human tissues, both healthy and diseased (e.g. tumors, oedema), is of obvious interest. However, there are also a number of potential applications involving livestock such as cattle, swine and poultry.

Backscatter properties from other commercially important fatty fish species likely to be reasonably free of gas bubbles could be determined,with a view towards implementation of non-destructive lipid content measurement for which there is presently a need. The most likely candidate in both of these regards appears to be inshore caught salmon. Other commercially important species worth examining are herring and sardines.

The lack of experimental scattering and extinction data at high scatterer concentrations reported in the open literature is most apparent. It is suggested that multiple scattering and secondary interaction be systematically studied using media whose first order scattering characteristics are well understood. The most useful dependent parameter is probably the extinction cross-section. Suspensions of gas bubbles of increasing concentrations with bubble diameters in the range $0.1 < ka < 0.7$ might be suitable for this purpose.

The theoretical results reported in this thesis for a surface of finite reflectivity should be checked experimentally. Two aspects to be considered are the use of $\langle R \rangle$ or R_1 as defined in the text and the validity of (2.3.45) and (2.3.54), more specifically (2.3.58), (2.3.60) and (2.3.61) for monostatic scattering. A surface interface having a small Brewster angle and no critical angle, i.e. $1 < c_1/c_2 < \rho_2/\rho_1$, would be the preferred choice for the latter. Unfortunately, such a system is physically difficult to realize as there should be no mode conversion at the interface, nor should the second medium be lossy. A rough surface of soft rubber in a medium of alcohol might be satisfactory, although the resultant Brewster angle (66°) is hardly small.

REFERENCES

I. Acoustic and Electromagnetic Scattering Theory and Measurements

Baker, B. B. and E. T. Copson. 1950. The Mathematical Theory of Huygens' Principle. 2nd ed. The Clarendon Press, Oxford

Barrick, D. E. 1968. "Relationship between slope probability density function and the physical optics integral in rough surface scattering," Proc. IEEE 56(10): 1728-1729

Beckmann, P. and A. Spizzichino. 1963. The Scattering of Electromagnetic Waves from Rough Surfaces. Pergamon Press, New York

Born, M. and E. Wolf. 1964. Principles of Optics. 2nd ed. rev. Macmillan Co., New York

Brekhovskikh, L. M. 1960. Waves in Layered Media. (Trans.) Academic Press, New York

Clay, C. S. and H. Medwin. 1964. "High-frequency acoustical reverberation from a rough-sea surface," J. Acoust. Soc. Am. 36(11): 2131-2134

Crispin, J. W., Jr. and A. L. Maffett. 1968. "RCS calculation of simple shapes--monostatic," Ch. 4, p.83-153. In J. W. Crispin, Jr. and K. M. Siegel (eds.). Methods of Radar Cross-section Analysis. Academic Press, New York

Crispin, J. W., Jr. and K. M. Siegel (eds.). 1968. Methods of Radar Cross-section Analysis. Academic Press, New York

Eckart, C. 1953. "The scattering of sound from the sea surface," J. Acoust. Soc. Am. 25(3): 566-570

Foldy, L. L. 1945. "The multiple scattering of waves--I. General theory of isotropic scattering by randomly distributed scatterers," Phys. Rev. 67(3-4): 107-119

Fox, F. E., S. R. Curley and G. S. Larson. 1955. "Phase velocity and absorption measurements in water containing air bubbles," J. Acoust. Soc. Am. 27(3): 534-539

Freese, M. MS, 1973. "The automatic detection of parasites by the ultrasonic echo method," Fish. Res. Bd. Canada Tech. Rep. No. 346

Fung, A. K. and A. Leovaris. 1969. "Experimental verification of the proper Kirchoff Theory of wave scattering from known randomly rough surfaces," J. Acoust. Soc. Am. 46(5) Pt. 1: 1057-1061

Heaps, H. S. 1956. "Reflection of a plane acoustic wave from a surface of nonuniform impedance," J. Acoust. Soc. Am. 28(4): 666-671

Hickling, R. 1962. "Analysis of echoes from a solid elastic sphere in water," J. Acoust. Soc. Am. 34(10): 1582-1592

Horton, C. W., Sr., S. K. Mitchell and G. R. Barnard. 1967. "Model studies on the scattering of acoustic waves from a rough surface," J. Acoust. Soc. Am. 41(3): 635-643

Horton, C. W., Sr., and T. G. Muir. 1967. "Theoretical studies on the scattering of acoustic waves from a rough surface," J. Acoust. Soc. Am. 41(3): 627-634

Ishimaru, A. 1969. "Fluctuations of a focussed beam wave for atmospheric turbulence probing," Proc. IEEE 57(4): 407-414

Keller, J. B. 1953. "A geometrical theory of diffraction," Proc. Symp. Microwave Optics, Eaton Electronics Res. Lab., McGill Univ., Montreal

Kerker, M. 1969. The Scattering of Light and Other Electromagnetic Radiation. Academic Press, New York

Khimunin, A. S. 1972. "Numerical calculation of the diffraction corrections for the precise measurement of ultrasound absorption," Acustica 27(4): 173-181

Kol'tsova, I. S. and I. G. Mikhailov. 1969. "Scattering of ultrasonic waves in heterogeneous systems," Akust. Zh. 15(3): 453-455 [Sov. Phys.-Acoust. 15(3): 390-392 (1970)]

Kuo, E. Y. T. 1964. "Wave scattering and transmission at irregular surfaces," J. Acoust. Soc. Am. 36(11): 2135-2142

Leovaris, A. and A. K. Fung. 1973. "Backscatter measurements of acoustic layers from a known irregular layer," J. Acoust. Soc. Am. 53(3): 950-952

Lommel, E. 1885. "Die Beugungserscheinungen einer kreisrunden Öffnung,..." Abh. d. Königl. Bayer. Akad. d. Wissensch XV, Pt. 2, 233
[Cf. Born and Wolf (1964)]

Melton, D. R. and C. W. Horton. 1970. "Importance of the Fresnel correction in scattering from a rough surface--1. Phase and amplitude fluctuations," J. Acoust. Soc. Am. 47(1) Pt. 2: 290-298

Mohammed, A. 1967. "Calculation of an average backscattering coefficient of a scattering layer in a frequency band," J. Acoust. Soc. Am. 41(1): 177-181

Morse, P. M. and H. Feshback. 1953. Methods of Theoretical Physics. McGraw-Hill, New York

Morse, P. M. and K. U. Ingard. 1968. Theoretical Acoustics. McGraw-Hill, New York

Papadakis, E. P. and K. A. Fowler. 1971. "Broad-band transducers: radiation field and selected applications," J. Acoust. Soc. Am. 50(3) Pt. 1: 729-745

Parkins, B. E. 1967. "Omnidirectional scattering of acoustic waves by rough imperfectly reflecting surfaces," J. Acoust. Soc. Am. 41(1): 126-134

Rayleigh, Lord. 1896. The Theory of Sound. Vol. II. 2nd ed. Reprinted by Dover Publishing, New York

Rheinstein, J. 1968. "Backscatter from spheres: a short pulse view," IEEE Trans. AP-16(1): 89-97

Schoch, A. 1950. "Schallreflexion, Schallbrechung und Schallbeugung," Ergeb. der exakten Naturw. 23: 127-134

Seki, H., A. Granato and R. Truell. 1956. "Diffraction effects in the ultrasonic field of a piston source and their importance in the accurate measurement of attenuation," J. Acoust. Soc. Am. 28(2): 230-238

Skudrzyk, E. 1971. The Foundations of Acoustics. Springer-Verlag, New York - Wien

Stenzel, H. 1938. "Über die von einer starren Kugel hervorgerufene Störung des Schall-feldes," Elektr. Nachr. Techn. 15: 71-78

Twersky, V. 1950. "On the non-specular reflection of plane waves of sound," J. Acoust. Soc. Am. 22(5): 539-546

_____ 1951. "On the non-specular reflection of sound from planes with absorbent bosses," J. Acoust. Soc. Am. 23(3): 336-338

_____ 1962. "On scattering of waves by random distributions--I. Free-space scatterer formalism," J. Math. Phys. 3: 700-715

Van De Hulst, H. C. 1957. Light Scattering by Small Particles. John Wiley & Sons, New York

Waterman, P. C. and R. Truell. 1961. "Multiple scattering of waves," J. Math. Phys. 2(4): 512-537

Wheelon, A. D. 1959. "Radio-wave scattering by tropospheric irregularities," J. Res. N.B.S. 63D(2): 205-233

Zemanek, J. 1971. "Beam behaviour within the nearfield of a vibrating piston," J. Acoust. Soc. Am. 49(1) Pt. 2: 181-191

II. Statistics of Reverberation Processes, Communications Theory, Signal Processing and Instrumentation

Abramowitz, M. and T. Stegun (eds.). 1964. Handbook of Mathematical Functions with Formulas, Graphs and Mathematical Tables. AMS 55, N.B.S., U.S. Dept. of Com., Washington

De Groot, A. W. MS, 1970. "An electronic ultrasound backscatter analyzer," M.Sc. Thesis. University of Manitoba, Winnipeg

Faure, P. 1964. "Theoretical model of reverberation noise," J. Acoust. Soc. Am. 36(2): 259-266

Marcum, J. 1948. "A statistical theory of target detection by pulsed radar," Mathematical Appendix. Rand. Corp. Res. Memo. RM-753, July
[Cf. IRE Trans. IT-6: 145-267 (April, 1960)]

Middleton, D. 1960. An Introduction to Statistical Communications Theory. McGraw-Hill, New York

_____ 1967. "A statistical theory of reverberation and similar first-order scattered fields--Part I. Waveforms and the general process; Part II. Moments, spectra and special distributions," IEEE Trans. IT-13(3): 372-414

_____ 1969. Errata. IEEE Trans. IT-15(1): 111-112

_____ 1972. "A statistical theory of reverberation and similar first-order scattered fields--Part III. Waveforms and fields; Part IV. Statistical models," IEEE Trans. IT-18(1): 35-90

Mullen, J. A. and D. Middleton. 1958. "The rectification of non-Gaussian noise," Quart. Rev. Math. 15: 395-419

Ol'shevskii, V. V. 1967. Characteristics of Sea Reverberation. (Trans.) Consultants Bureau, New York

Parzen, E. 1960. Modern Probability Theory and Its Applications. John Wiley & Sons, New York

Rice, S. O. 1945. "Mathematical analysis of random noise," Bell System Tech. J. 24, Pt. III: 52-114

Twersky, V. 1963. "Signals, scatterers and statistics," IEEE Trans. AP-11: 668-680

_____ 1964. Errata. IEEE Trans. AP-12: 363-364

III. Ultrasonic Absorption, Velocity and Scattering in Biological Media; Applications

Aldridge, E. E. and H. G. Tattersall. 1971. "Utilization of ultrasonic scatter," Ultrasonics Conference, London, England, Sept. 1971. Abstract in Ultrasonics 9 (Supplement): p.7

Dunn, F. and W. J. Fry. 1961. "Ultrasonic absorption and reflection by lung tissue," Physics in Medicine and Biology 5: 401-410

Dunn, F., P. D. Edmonds and W. J. Fry. 1969. "Absorption and dispersion of ultrasound in biological media," Ch. 3, p.205-332, in H. P. Schwan (ed.), Biological Engineering. McGraw-Hill, New York

El'piner, I. E. 1964. Ultrasound: Physical, Chemical and Biological Effects. Consultants Bureau, New York

Freese, M. 1969. "Ultrasonic inspection of parasitized whole fish," FAO Technical Conference on Fish Inspection and Quality Control, FIC/69/0/12, Halifax, Canada, July 1969, 13p. Also in R. Kreuzer (ed.) Fish Inspection and Quality Control. Fishing News (Books) Ltd., London, England

_____ MS, 1973. "The automatic detection of parasites by the ultrasonic echo method," Fish. Res. Bd. Canada Tech. Rep. No. 346

Freese, M. and D. Makow. 1968(a). "Ultrasound backscatter in fresh and thawed animal tissue," J. Fish. Res. Bd. Canada 25(3): 605-606

_____ 1968(b). "High frequency ultrasonic properties of freshwater fish tissue," J. Acoust. Soc. Am. 44(5): 1282-1289

Gitis, M. B. and A. S. Khimunin. 1968. "Diffraction effects in ultrasonic measurements (review)," Akust. Zh. 14(4): 489-513 [Sov. Phys.-Acoustics 14(4): 413-431]

Gorshkov, N. F. 1957. "The propagation of pulses in an elastic absorptive medium," Sov. Phys.-Acoustics 3: 163-172

Gouw, T. H. and J. C. Vlugter. 1967. "Physical properties of triglycerides--III. Ultrasonic sound velocity," Fette-Seifen-Anstrichmittel 69(3): 159-164

Haslett, R. W. G. 1962. "The backscattering of acoustic waves in water by an obstacle--II. Determination of the reflectivities of solids using small specimens," Proc. Phys. Soc. 79: 559-571

Hill, C. R. 1972. "Session 5:7, Seattle Workshop on Ultrasound and Biological Tissues--New uses and developments (diagnosis)," p. 251-252, in J. M. Reid and M. R. Sikov (eds.), Proceedings of a Workshop on Interaction of Ultrasound and Biological Tissues. Battelle Seattle Research Center. DHEW Publ. (FDA) 73-8008

Kononenko, V. S. and V. F. Yakovlev. 1969. "Precision method for measuring the velocity of ultrasound in a liquid at 0.7 - 30 MHz," Akust. Zh. 15(1): 78-82
[Sov. Phys.-Acoustics 15(1): 65-68]

MacDonald, J. S. and M. K. Brachman. 1956. "Linear-system integral transform relations," Rev. of Modern Phys. 28(4): 393-422

Matsui, T. and K. Shibata. 1971. "Acoustic properties of high frequencies in fish tissue," Bull. of the Faculty of Fisheries, Nagasaki Univ., No. 32: 83-101

Pauly, H. and H. P. Schwan. 1971. "Mechanism of absorption of ultrasound in liver tissue," J. Acoust. Soc. Am. 50(2) Pt. 2: 692-699

Reid, J. M. and M. R. Sikov (eds.). 1972. Proceedings of a Workshop on the Interaction of Ultrasound and Biological Tissues. Batelle Seattle Research Center, Seattle, Washington. DHEW Publ. (FDA) 73-8008

Senapati, N., P. P. Lele and A. Woodin. 1972. "A study of the scattering of sub-millimeter ultrasound from tissues and organs," IEEE Ultrasonics Symposium, Boston, Mass.

Szilard, J. and G. Scruton. 1973. "Revealing the grain structure of metals by ultrasonics," Ultrasonics 11(3): 114-120

Waag, R. C. and R. M. Lerner. 1973. "Tissue macrostructure determination with swept-frequency ultrasound," IEEE Ultrasonics Symposium, Monterey, Calif.

Wild, J. J. and J. M. Reid. 1953. "The effects of biological tissues on 15 Mc pulsed ultrasound," J. Acoust. Soc. Am. 25: 270-283

IV. Fish Biology and Biochemistry, Tissue Histology

Awad, A. A. MS, 1967. "Chemical and physical alterations of frozen whitefish and bovine skeletal muscles," Ph.D. Thesis, Univ. of Wisconsin

Borgstrom, G. (ed.). 1961. Fish as Food. Vol. 1. Academic Press, New York

Greene, C. W. 1913. "The storage of fat in the muscular tissue of the King Salmon and its resorption during the fast of the spawning migration," Bull. U.S. Bur. Fish. 33: 69-138

Greene, C. W. and C. H. Greene. 1913. "The skeletal musculature of the King Salmon," Bull. U.S. Bur. Fish. 33: 21-60

Harder, W. 1964. "Anatomie des Fische," p.56, in R. Demoll, H. N. Maier and H. H. Wunsch (eds.), Handbuch des Binnenfischerei Mitteleuropas. Vol. IIA. E. Schweizerbart'sche Verlagsbuchhandlung (Nagele u. Obermiller), Stuttgart, West Germany

Jacquot, R. 1961. "Organic constituents of fish and other aquatic animal foods," Ch. 6, p.145-209, in G. Borgstrom (ed.), Fish as Food. Vol. 1. Academic Press, New York

Scott, W. B. and E. J. Crossman. 1973. Freshwater Fishes of Canada. Bull. Fish. Res. Bd. Canada No. 184. Information Canada, Ottawa

V. Analytical (Chemistry) Procedures

Bligh, E. G. and W. J. Dyer. 1959. "A rapid method of total lipid extraction and purification," Can. J. Biochem. Physiol. 37: 911-917

Dyer, W. J. and J. R. Dingle. 1961. "Fish proteins with special reference to freezing," Ch. 9, p.275-327, in G. Borgstrom (ed.), Fish as Food. Vol. 1. Academic Press, New York

Food and Agriculture Organization of the United Nations. 1969. Technical Conference on Fish Inspection and Quality Control, Halifax, Canada [Cf. R. Kreuzer (ed.), Fish Inspection and Quality Control. Fishing News (Books), Ltd., London, England (1971)]

McIvor, G. H. 1965. Report of the Commission of Inquiry into Freshwater Fish Marketing. Queen's Printer, Ottawa

Stevenson & Kellogg, Ltd. 1970. "Marketing fish in Canada-- Vol. 1- Strategies to increase fish consumption," a report prepared for the Fisheries Council of Canada, Ottawa

APPENDIX A

POINT-SCATTERER MODEL STATISTICAL FRAMEWORK

The equivalent point-scatterers are assumed to be randomly and independently distributed in the insonified tissue volume. Specifically, it is assumed that in any sufficiently small subdivision ΔV_ℓ of the volume V_ℓ the following conditions prevail:

(i) the scatterers are statistically independent or if $P\{N_i\}$ is the probability of N_i scatterers in a volume element dV_i in ΔV_ℓ then $P\{N_i, N_j\} = P\{N_i\}P\{N_j\}$ where dV_i and dV_j are non-overlapping regions;

(ii) if dV_i is sufficiently small

$$P\{N_i > 1\} << P\{1_i\} \text{ or } P\{0_i\}$$

or the probability of finding more than one scatterer in dV_i is negligible compared to the probability of finding one (or none);

(iii) the probability of finding one point-scatterer in the volume element dV_i is $P\{1_i\} = n_i dV_i$ where n_i is the volume density of scatterers (N per unit volume) and n_i is entirely non-random.

These conditions suffice to specify the Poisson distribution of the scatterers in the volume element ΔV_ℓ given by [Parzen (1960)]

$$P\{N\} = \frac{(n_\ell \Delta V_\ell)^N}{\lfloor N} \exp(-n_\ell \Delta V_\ell) \qquad (A.1.1)$$

An elemental volume has been specified because, in general, n_ℓ is not constant throughout the bounded volume V_ℓ. Rather, n_ℓ may be a function of position in V_ℓ. Criteria for minimum volumes are derived by Ol'shevskii (1967).

If an independent elementary event $U(t, \vec{r}, \vec{q})$ is associated with each point, a resultant process $X(t)$ may be defined as the superposition of M independent random events

$$X(t) = \sum_{m=1}^{M} U_m(t, \vec{r}_m, \vec{q}_m) \qquad (A.1.2)$$

where $\vec{r}_m$ is the spatial coordinate of the m^{th} point and $\vec{q}_m$ denotes its other associated stochastic properties.

The moments of $X(t)$ may be obtained directly from the hierarchy of probability density distributions W_n of the process or, alternatively, via the characteristic function. One may thus write for a process dependent function $E(X)$

$$\left\langle E[X(t)] \right\rangle = \int_{-\infty}^{\infty} W_1(t, \vec{a})\, E[X(\vec{a}, t)]\, d\vec{a} \qquad (A.1.3)$$

where $\vec{a}$ is the configuration vector.[1] This direct method has perhaps the advantage of providing more direct physical insight into the

---

[1] The notation $\vec{q}$, $\vec{r}$, where $\vec{q}$ refers to the random properties of the scatterer and $\vec{r}$ to its random spatial coordinates, are often combined into a single configuration vector. The integration is performed over the configuration space.

averaging process but in order to evaluate (A.1.3) the probability density distribution $W_1(t, \vec{a})$ must be determined. However, the moments can also be determined by differentiation of the characteristic function which is normally considerably simpler than integration of the probability density.

The derivation of the n^{th} order characteristic function $F_n(j\vec{\xi}|\Delta V_\ell)$ is given by Middleton (1960, 1967). For the Poisson distribution, $F_n(j\vec{\xi}|\Delta V_\ell)$ turns out to be

$$F_n(j\vec{\xi}|\Delta V_\ell) = \exp[n_\ell V_\ell(\langle \exp j \sum_{p=1}^{n} \xi_p U(t_p - t_m, \vec{q}, \vec{r})\rangle_{\vec{q},\vec{r}} - 1)] \tag{A.1.4}$$

where $j = \sqrt{-1}$, the $\langle\ \rangle$ indicate ensemble averaging over $\vec{q}$, $\vec{r}$ of the scatterers in the volume element ΔV_ℓ and m indicates the m^{th} scatterer.

It should be remembered that $\vec{r}_m$ and t_m will be dependent through the relation $t_m = 2|\vec{r}_m|/c$ when operating monostatically; $F_n(j\vec{\xi}|\Delta V_\ell)$ is defined for a time $t = t'$ at which the process is jointly considered. The key to deriving F_n explicitly is that, although the component states of the process $X = \sum_m^N U_m(t_m, \vec{q}_m, \vec{r}_m)$ are in general <u>not</u> independent, each component state X_w (a member of the set t_N) is the result of exactly N random variables over the identical configuration space. Ensemble averaging of the X_w must therefore yield the same result as averaging the underlying random variables (on which the X_w are dependent) according to the theorem on the transformation of probabilities [Parzen (1960)]. The important difference is that by our earlier assumption the N events are now independent. The condition of statistical independence of the events results in considerable simplification.

In (A.1.1) we indicated that the point-scatterer density n_ℓ might be a function of the coordinates of ΔV_ℓ. Integrating with respect to $\Delta V_\ell \to dV$ over the volume V_ℓ, (A.1.3) may be generalized to the non-homogeneous Poisson process where now

$$P\{N\} = \frac{\left(\int^{V_\ell} n_\ell(v)\, dv\right)^N}{\underline{\lfloor N}} \exp\left[-\int^{V_\ell} n_\ell(v)\, dv\right] \qquad (A.1.5)$$

It is clear that with n_ℓ constant throughout the volume V_ℓ we require also a constant volume cross-section as a function of $t = 2r/c$ if the process is to be homogeneous. Subject to certain restrictions this can be arranged in the experiments.

Making use of the fact that

$$F_n(j\vec{\xi}|V_\ell) = \prod_{\ell=1} F_n(j\vec{\xi}|\Delta V_\ell) \qquad (A.1.6)$$

(the ΔV_ℓ are non-overlapping and independent), one obtains

$$F_n(j\vec{\xi}|V_\ell) = \exp \int_{V_\ell} n_\ell(\vec{r}) \left\langle \exp\, j \left[\sum_{p=1}^{n} \xi_p\, U[(t_m - t_p), \vec{q}, \vec{r}]\right] - 1 \right\rangle_{\vec{q}} dv \qquad (A.1.7)$$

which for a constant scatterer density n_ℓ reduces to (A.1.4) with ΔV_ℓ replaced by V_ℓ. Note that n refers to the order, while n_ℓ denotes the scatterer density.

Following Middleton (1960), the L^{th} order moment of X is given by

$$\mu'^{(L)}_{m_1,\ldots m_n} = (-j)^L \frac{\partial^L}{\partial\xi_1^{m_1}\, \partial\xi_2^{m_2} \ldots \partial\xi_n^{m_n}} F_n(j\vec{\xi}|\Delta V_\ell)\Big|_{\vec{\xi}=\vec{0}} \qquad (A.1.8)$$

where $L = \sum_{i=1}^{n} m_i$.

Because of the form of (A.1.4) it is advantageous to employ the semi-invariants or cumulants of the process. The cumulant function $K_n(j\vec{\xi}|\Delta V_\ell) = \ell n\ F_n(j\vec{\xi}|\Delta V_\ell)$. The semi-invariants $\lambda^{(L)}$ are given by

$$\lambda^{(L)}_{m_1 m_2 \ldots m_n} = (-j)^L \frac{\partial^L}{\partial \xi_1^{m_1}\ \partial \xi_2^{m_2} \ldots \partial \xi_n^{m_n}} [K_n(j\vec{\xi}|\Delta V_\ell)]\Big|_{\vec{\xi}=\vec{0}} \qquad (A.1.9)$$

The semi-invariants may be expressed in terms of the moments or, more conveniently, in terms of the central moments, defined in the case of the one-dimensional distribution $W_1(X)$ as the moment about the mean of the distribution. The first moment $\langle X(t_1)\rangle$ becomes

$$\langle X(t_1)\rangle = (-j) \frac{\partial F_n}{\partial \xi_1}\Big|_{\xi=0} = \int_{V_\ell} n_\ell(\vec{r})\ \langle U[(t_1 - t_m), \vec{q}, \vec{r}]\rangle \underset{q}{\rightarrow} dv \qquad (A.1.10)$$

since $F_1(j\xi_1|V_\ell)\Big|_{\xi_1=0} = 1$. Similarly the second moment may be obtained

$$\langle X(t_1)\ X(t_2)\rangle = (-) \frac{\partial^2 F_n}{\partial \xi_1\ \partial \xi_2}\Big|_{\xi_1, \xi_2 = 0}$$

$$= \int_{V_\ell} n_\ell(\vec{r}) \langle U(t_1 - t_m, \vec{q}, \vec{r}) U(t_2 - t_m, \vec{q}, \vec{r})\rangle \underset{q}{\rightarrow} dv + \langle X(t_1)\rangle\ \langle X(t_2)\rangle \qquad (A.1.11)$$

The integral of (A.1.11) is referred to as the covariance of the process. By setting $t_1 = t_2$ the total (coherent and incoherent) intensity is obtained.

APPENDIX B

CORRELATION COEFFICIENTS AND POWER SPECTRA

Instantaneous Process

The correlation coefficient $K(t_1,t_2)$ furnishes an important and convenient tool for ascertaining broad stationarity of the reverberation process and also investigating, for example, the effects of near-field operation and scatterer coherence. For finite signal pulses $s(t) = s_o(t)e^{-j\omega_o t}$, a non-dispersive medium, and impulse (δ-function) scatterers, the correlation coefficient $K_x(\tau_r)$ of the instantaneous process X(t) becomes

$$K_x(\tau_r) = \frac{2\cos\omega_c\tau_r}{T_{ef}} \int_o^{T-|\tau_r|/2} s_o(u - \frac{\tau_r}{2})\, s_o(u + \frac{\tau_r}{2})\, du \qquad (B.1.1)$$

where $\tau_r = t_2 - t_1$ and T_{ef} is defined by (3.3.9). For $s_o(t)$ real, $K_x(\tau_r)$ is real and symmetrical about $\tau_r = 0$. If $K_o(\tau_r)$ is the envelope of the correlation coefficient $K_x(\tau_r)$, it follows from (B.1.1) that

$$K_x(\tau_r) = K_o(\tau_r)\cos\omega_c\tau_r \qquad (B.1.2)$$

As an example, for the cosine pulse

$$s(t) = \cos^2\left[\frac{\pi(t-T)}{2T}\right]e^{-j\omega_c(t-T)} \quad , \quad |t - T| \le T$$

$$= 0 \quad , \quad |t - T| > T \qquad (B.1.3)$$

and one obtains using (B.1.1) and (B.1.2)

$$K_o(\tau_r) = \frac{1}{2T_{ef}} \left\{ \left[T - \frac{|\tau_r|}{2} \right] \left[1 + \tfrac{1}{2}\cos \frac{\pi|\tau_r|}{T} \right] + \frac{T}{\pi} \sin \frac{\pi|\tau_r|}{T} \right.$$

$$\left. - \frac{T}{4\pi} \sin \frac{\pi|\tau_r|}{T} \right\} \quad , \quad |\tau_r| \leq 2T \qquad \text{(B.1.4)}$$

The correlation coefficient if the medium is dispersive is much more complex and in contrast to (B.1.1) is time dependent. Expressing the zero and first order terms of the variance [Re Z(t)] defined by (3.3.5) as

$$G_v(t)^{\frac{1}{2}} e^{-j\omega_c t} \sum_{i=1}^{3} a_i(t)\, s_{oi}(t) \qquad \text{(B.1.5)}$$

where

$$G_v(t_1) = \tfrac{1}{4} \frac{T_c^2 c_2}{(4\pi)} \langle n(t_1) \rangle \Lambda^{(2)}(t_1) \langle \sigma \rangle_{\vec{q}}$$

and

$$\sum_{i=1}^{3} a_i(t)\, s_{oi}(t) = a_1 s_o(t) + a_2 \dot{s}_o(t) + a_3(t)\, \dot{s}_o(t)$$

and employing the definition [see (A.1.11)]

$$K_z(t_1, \tau_r) = \frac{\left\langle Z^*(t_1)\, Z(t_1+\tau_r) \right\rangle - \left\langle Z^*(t_1) \right\rangle \left\langle Z(t_1+\tau_r) \right\rangle}{\left\langle Z^*(t_1)\, Z(t_1) \right\rangle - \left\langle Z^*(t_1) \right\rangle \left\langle Z(t_1) \right\rangle} \qquad \text{(B.1.6)}$$

the term $\left\langle Z^*(t_1)\, Z(t_1+\tau_r) \right\rangle$ of (B.1.6) has the form

$$\left\langle Z^*(t_1)Z(t_1+\tau_r)\right\rangle = G_v(t_1)\cos\omega_c\tau_r \left\{ \sum_{i=1}^{3} \int \left\langle a_i^*(t_1)a_i(t_1+\tau_r)s_{oi}(t_1)s_{oi}(t_1+\tau_r)\right\rangle_{\vec{q}} dt \right.$$

$$\left. + \sum_{i\neq j}^{3} \int \left\langle a_i^*(t_1)a_j(t_1+\tau_r)s_{oi}(t_1)s_{oj}(t_1+\tau_r)\right\rangle_{\vec{q}} dt \right\} \quad \text{(B.1.7)}$$

Referring to (3.3.4) and (3.3.5), $a_1 = 1$ and only a_3 is time dependent.

Envelope Fluctuations

Subject to the assumptions of Gaussian quasi-harmonic reverberation stationary in an interval much greater than the correlation interval τ_{or}, it may be shown [Ol'shevskii (1967)] that the correlation coefficient $K_E(\tau_r)$ of the reverberation envelope fluctuations is approximately equal to the square of the correlation coefficient envelope $K_o(\tau_r)$. Retaining only the first two terms of the series derived for $K_E(\tau_r)$, Ol'shevskii gives the following expression

$$K_E(\tau_r) \simeq 0.91\ K_o^2(\tau_r) + 0.058\ K_o^4(\tau_r) + \ldots$$

$$\simeq 0.91\ K_o^2(\tau_r) + 0.09\ K_o^4(\tau_r) \quad \text{(B.1.8)}$$

which indicates that $K_E(\tau_r)$ falls off somewhat more rapidly than $K_o^2(\tau_r)$.

The reverberation statistical power spectrum for a non-stationary process may be defined via a Wiener-Khintchine-like relationship

$$W_r(\omega,t_1) = \sigma_x^2 \int_{-\infty}^{\infty} K_x(t_1,\ t_1+\tau_r)\ e^{j\omega\tau_r}\ d\tau_r$$

$$= G_v(t_1)\ |S(\omega,t_1)|^2 \quad \text{(B.1.9)}$$

where $\sigma_x^2 \simeq G_v(t_1)T_{ef}$ is the process variance; $G_v(t_1)$ is defined as before. If there is any 'DC power', i.e. $\langle Z(t) \rangle \neq 0$, it must be added to the spectrum at the origin $\omega = 0$ as a δ-function scaled proportionally to $|\langle Z(t) \rangle^2|$.

For the real signal, i.e. Re s(t), the signal pulse amplitude spectrum is separated into two parts

$$S(\omega,t_1)_{real} = \tfrac{1}{2}\,[S(\omega,t_1) + S^*(\omega,t_1)]$$

$$= \tfrac{1}{2}\,[S_o(\omega-\omega_c,t_1) + S_o(\omega+\omega_c,t_1)] \qquad \text{(B.1.10)}$$

and the real power spectrum is hence

$$|S(\omega,t_1)_{real}|^2 = |S_o(\omega-\omega_c,t_1)|^2 \quad , \quad (\omega-\omega_c) \geq 0 \qquad \text{(B.1.11)}$$

while for the complex signal the power spectrum is simply $|S_o(\omega-\omega_c,t_1)|^2$. The power spectrum of the reverberation may similarly be rewritten as

$$W_{or}(\omega_d,t_1) = \sigma_x^2 \int_{-\infty}^{\infty} K_o(t_1,t_1+\tau_r)\, e^{j\omega_d\tau_r}\, d\tau_r$$

$$= G_v(t_1)\, |S_o(\omega_d)|^2 \quad , \quad \omega_d = \omega-\omega_c \qquad \text{(B.1.12)}$$

For the real signal we multiply $W_{or}(\omega_d,t_1)$ by the factor one-half, or alternately, we restrict ω_d to positive frequencies only.

The envelope fluctuation spectrum $W_{Ef}(\omega)$ may be expressed as the auto-convolution of the power spectrum of the envelope of the reverberation correlation coefficient $K_o(\tau_r)$. If the second term

of (B.1.8) is neglected

$$W_{Ef}(\omega, t_1) \simeq \sigma_E^2 \int_{-\infty}^{\infty} K_o^2 (t_1, \tau_r) e^{j\omega\tau_r} d\tau_r \qquad (B.1.13)$$

therefore by (B.1.12) and the convolution theorem

$$W_{Ef}(\omega, t_1) \simeq \frac{\sigma_E^2}{2\pi T_{ef}^2} \int_{-\infty}^{\infty} |S_o(\nu, t_1)|^2 |S_o(\omega-\nu, t_1)|^2 d\nu \qquad (B.1.14)$$

The fact that $K_E(\tau_r)$ falls off slightly faster than $K_o^2(\tau_r)$ implies that the actual spectrum of the envelope fluctuations is slightly wider then $W_{Ef}(\omega, t_1)$.

APPENDIX C

SCATTERING OF RECTANGULAR- AND COSINE-SHAPED PULSES FROM A ROUGH SURFACE

For quasi-narrowband Gaussian beam incidence, the expression derived in Section 2.4.2 for the ensemble averaged scattered pulse was

$$\left\langle p_s(\vec{r},t)\right\rangle = \frac{-F(\delta_i,\delta_s)R_i P_{io} A}{c}\int_{-\infty}^{\infty} j\omega\, S(\omega)\, e^{-\gamma_1^2\omega^2 - j\omega t_{ro}}\, d\omega \quad \text{(C.1.1)}$$

For the cosine pulse given by (B.1.3) with $\Delta T \equiv T$, we define $\omega_o = \pi/\Delta T$, $\omega_2 = \omega_c + \omega_o$ and $\omega_1 = \omega_c - \omega_o$. Hence, using the transform relation

$$\frac{1}{2\pi}\int_{-\infty}^{\infty} e^{-\gamma^2\omega^2 - j\omega t}\, d\omega = \frac{1}{2\gamma\sqrt{\pi}}\, e^{-t^2/4\gamma^2} \quad \text{(C.1.2)}$$

we obtain

$$\begin{aligned}\left\langle p_s(\vec{r},t)\right\rangle = {} & j\tfrac{1}{4}\mu_{zc} R_i P_{io} A \\ & \times \Bigg\{ e^{-\omega_c^2\gamma_1^2 - j\omega_c t_{ro}}\left[\operatorname{erf}\left(\frac{t_{ro}-\Delta T}{2\gamma_1} + j\omega_c\gamma_1\right) - \operatorname{erf}\left(\frac{t_{ro}+\Delta T}{2\gamma_1} + j\omega_c\gamma_1\right)\right] \\ & + \tfrac{1}{2} e^{-\omega_2^2\gamma_1^2 - j\omega_2 t_{ro}}\left[\operatorname{erf}\left(\frac{t_{ro}-\Delta T}{2\gamma_1} + j\omega_2\gamma_1\right) - \operatorname{erf}\left(\frac{t_{ro}+\Delta T}{2\gamma_1} + j\omega_2\gamma_1\right)\right] \\ & + \tfrac{1}{2} e^{-\omega_1^2\gamma_1^2 - j\omega_1 t_{ro}}\left[\operatorname{erf}\left(\frac{t_{ro}-\Delta T}{2\gamma_1} + j\omega_1\gamma_1\right) - \operatorname{erf}\left(\frac{t_{ro}+\Delta T}{2\gamma_1} + j\omega_1\gamma_1\right)\right]\Bigg\}\end{aligned} \quad \text{(C.1.3)}$$

In contrast to the incident pulse, the averaged scattered pulse appears smeared out and exhibits no discontinuities in its derivatives unless $\gamma_1 = 0$ [i.e., g = 0 (smooth surface) and $\vec{\mu}_{xy} = [0,0]$ or the incident beam is homogeneous]. A still clearer picture of the distorting effect may be obtained by considering the simple rectangular pulse defined by

$$\begin{aligned} s(t) &= e^{-j\omega_c t_{ro}} && |t_{ro}| \leq \Delta T \\ &= 0 && |t_{ro}| > \Delta T \end{aligned} \qquad \text{(C.1.4)}$$

Since we may write $\cos^2\left(\frac{\pi t}{2\Delta T}\right) = (1 + \cos \pi t/\Delta T)$, the amplitude for the rectangular pulse is contained in the first square brackets of the cosine pulse solution (C.1.3), i.e.

$$\left\langle p_s(\vec{r},t)\right\rangle = j\tfrac{1}{2}\mu_{zc} R_i P_{io} A\, e^{-\omega_c^2\gamma_1^2} \times \left[\operatorname{erf}\left(\frac{t_{ro}-\Delta T}{2\gamma_1} + j\omega_c\gamma_1\right) - \operatorname{erf}\left(\frac{t_{ro}+\Delta T}{2\gamma_1} + j\omega_c\gamma_1\right)\right] e^{-j\omega_c t_{ro}} \qquad \text{(C.1.5)}$$

where $\operatorname{erf}(x) = \frac{2}{\sqrt{\pi}} \int_0^x e^{-u^2}\, du$.

The derivative of (C.1.5) is referred to in Chapter 3; it is given by

$$\frac{\partial}{\partial t_{ro}} \left\langle p_s(\vec{r},t)\right\rangle = \frac{\mu_{zc} R_i P_{io} A}{\gamma_1\sqrt{\pi}} \exp\left[\frac{-t_{ro}^2 - \Delta T^2}{4\gamma_1^2}\right] \sinh\left[\frac{t_{ro}\Delta T}{2\gamma_1^2} + j\omega_c\Delta T\right]$$

$$\exp\left[-j\omega_c t_{ro}\right] - j\omega_c \left\langle p_s(\vec{r},t)\right\rangle \qquad \text{(C.1.6)}$$

As can be seen, the coherently scattered pulse becomes increasingly smeared out near the edges as γ_1 increases. Although this behaviour

only applies to the ensemble averaged pulse, the effect is exactly the same as if the pulses had passed through a square-law absorbing medium.

Scattered Pulse Energy or Process Intensity

The ensemble averaged autocorrelation function $\langle E(\tau) \rangle$ is given by

$$\langle E(\tau_r) \rangle = \int_{-\infty}^{\infty} \langle p_s^*(\vec{r},t)\ p_s(\vec{r},t+\tau_r) \rangle\ dt$$

or, using the Wiener-Khintchine theorem, by

$$\langle E(\tau_r) \rangle = \frac{1}{2\pi} \int_{-\infty}^{\infty} \langle p_s^*(\vec{r},\omega)\ p_s(\vec{r},\omega) \rangle\ e^{-j\omega\tau_r}\ d\omega \qquad (C.1.7)$$

where $p_s^*(\vec{r},\omega) = F[p_s(\vec{r},t)]$.

Employing rectangular coordinates with $x_2 = x_1 + \zeta$, and $y_2 = y_1 + \eta$, $\langle E(\tau_r) \rangle$ becomes for the Gaussian beam defined by (2.4.4) and for a stationary surface (in the broad sense)

$$\langle E(\tau_r) \rangle = \frac{E_{on}}{2\pi} \int_{-\infty}^{\infty} d\omega \iint_{A_1} \exp\left[-\frac{2x_1^2}{a^2} - \frac{2x_1\zeta}{a^2} - \frac{2y_1^2}{b^2} - \frac{2y_1\eta}{b^2} \right] dx_1 dy_1\ k^2 |S(\omega)|^2$$

$$\times \iint_{A_2} \exp\left[-\frac{\zeta^2}{a^2} - \frac{\eta^2}{b^2} \right]\ e^{-g[1-C(\zeta,\eta)]}\ e^{j\mu_x\zeta + j\mu_y\eta}\ d\zeta d\eta \qquad (C.1.8)$$

where $E_{on} = F(\delta_i,\delta_s)^2 |R_i|^2 |P_{io}|^2$. If the rough surface is sufficiently large so that the beam amplitude is small near the edges, the limits of the integral over A_1 may be extended to $\pm\infty$ yielding

$$\langle E(\tau_r) \rangle = \frac{E_{on}}{2\pi} \int_{-\infty}^{\infty} \frac{\pi ab}{2} \iint_{-\infty}^{\infty} \exp\left[-\frac{\zeta^2}{a^2} - \frac{\eta^2}{b^2} \right] \operatorname{erfc}\left(\frac{\zeta}{\sqrt{2}a} \right) \operatorname{erfc}\left(\frac{\eta}{\sqrt{2}b} \right) e^{-g[1-C(\zeta,\eta)]}$$

$$\times\ e^{j\mu_x\zeta + j\mu_y\eta}\ d\zeta d\eta\ k^2 |S(\omega)|^2\ d\omega \qquad (C.1.9)$$

where

$$\text{erfc}(x) = 1 - \frac{2}{\sqrt{\pi}} \int_o^x e^{-u^2}\, du \quad .$$

For the Gaussian surface considered in Chapter 2, (C.1.9) may be evaluated asymptotically for the case of $g >> 1$ and $a > T_x$, $b > T_y$. Under these conditions the coefficient $\exp\left[-g/2\ (\zeta^2/T_x^2 + \eta^2/T_y^2)\right]$ diminishes rapidly away from the origin so that we may set $\text{erfc}(\zeta)\text{erfc}(\eta) \simeq 1$. Similarly for $g << 1$, (C.1.9) may be evaluated in the same manner provided $a >> T_x$ and $b >> T_y$. However, if T_x and T_y are of the same order as a and b or greater, it will be necessary to evaluate the integrals term by term. Normally, however, a and b will be substantially greater than the correlation lengths. We shall evaluate (C.1.9) for this latter case and $g << 1$.

Setting $\text{erfc}(\zeta)\text{erfc}(\eta) \simeq 1$, we have for a pulse of duration $2\Delta T$

$$\left\langle E(\tau_r) \right\rangle \simeq \frac{E_o k_c^2 \pi ab T_{ef}}{2\gamma_1 \sqrt{2\pi}} \int_{-\tau_r+2\Delta T}^{\tau_r-2\Delta T} e^{-u^2/8\gamma_2^2}\, K_o(\tau_r-u)\, \cos\omega_c(\tau_r-u)\, du$$

$$+ \frac{E_o k_c^2 g_c \pi mn T_{ef}}{2\gamma_2 \sqrt{2\pi}} \int_{-\tau_r+2\Delta T}^{\tau_r-2\Delta T} e^{-u^2/8\gamma_2^2}\, K_o(\tau_r-u)\, \cos\omega_c(\tau_r-u)\, du \quad ,$$

$$g_c << 1 \qquad \text{(C.1.10)}$$

For the rectangular pulse defined by (C.1.4) the autocovariance function is easily derived

$$T_{ef}\, K_o(u) = 2\Delta T - |u| \qquad |u| \leq 2\Delta T$$

$$= 0 \qquad |u| > 2\Delta T \qquad \text{(C.1.11)}$$

Substituting (C.1.11) into (C.1.10) and setting $\tau_r = 0$, the pulse energy becomes

$$\langle E(0) \rangle = \frac{2k_c^2 E_o \Delta T \pi ab}{\gamma_1 \sqrt{2\pi}} \int_o^{2\Delta T} e^{-u^2/8\gamma_1^2} (1 - u/2\Delta T) \cos(\omega_c u)\, du$$

$$+ \frac{2k_c^2 g_c E_o \Delta T \pi mn}{\gamma_2 \sqrt{2\pi}} \int_o^{2\Delta T} e^{-u^2/8\gamma_2^2} (1 - u/2\Delta T) \cos(\omega_c u)\, du \quad ,$$

$$g_c << 1 \qquad \text{(C.1.12)}$$

The integrals of (C.1.12) may be expressed in series form as

$$\int_o^{2\Delta T} e^{-u^2/4\gamma^2} (1 - u/2\Delta T) \cos\omega_c u\, du = 2\Delta T \sum_{m=0}^{\infty} \frac{H_{2m}(j\gamma\omega_c)(\Delta T/\gamma)^{2m}}{\lfloor 2(m+1)}$$

$$= \gamma \sum_{p=0}^{\infty} \sum_{q=0}^{\infty} \frac{(-1)^{p+q}(2\omega_c \Delta T)^{2p}(\Delta T/\gamma)^{2q+1}}{(2p+2q+1)(p+q+1)\lfloor q \lfloor 2p} \qquad \text{(C.1.13)}$$

The $H_{2m}(jX)$ are Hermite polynomials of complex argument.

The form of the complete solution is not all that illuminating for, although necessarily $\Delta T\omega_c >> 1$, $\Delta T/\sqrt{2\pi}$ may be larger or smaller than unity. For simplicity let us assume $\phi_i = 0$, then by our previous assumption ($a >> T_x$) γ_2^2 in the backscatter direction reduces to

$$\gamma_2^2 = \frac{T_x^2 \sin^2\delta_i}{c^2} + \frac{g_o}{2} \quad , \qquad \delta_s = \delta_i$$

and hence for $\delta_i >> 0$

$$\frac{\Delta T}{\gamma_2} \simeq \frac{c\Delta T}{T_x |\sin\delta_i|} \quad , \qquad T_x \sin\delta_i >> \sqrt{2}\, h \cos\delta_i \quad .$$

In other words $\Delta T/\gamma_2 > \sqrt{2}$ signifies that the spatial pulse length along the surface plane exceeds $\sqrt{2}$ times the correlation length. This condition

is less restrictive than the condition $2\gamma^2\omega_c$ BW $<< 1$ which must be met if (2.4.22) is to be valid. Normally the criterion $\Delta T/\gamma_2 > \sqrt{2}$ will apply for the myosepta and accordingly we may extend the limit $2\Delta T$ in (C.1.12) to ∞. For the rectangular pulse this results in

$$\left\langle E(0)\right\rangle_{\substack{\delta_s=\delta_i \\ \phi_s=\pi}} \simeq k_c^2\, g_c\, \pi mn\, E_o\, 2\Delta T\, e^{-2\gamma_2^2\omega_c^2} \times \left\{1 - \frac{\sqrt{2}\,\gamma_2\, e^{2\gamma_2^2\omega_c^2}}{\Delta T\,\sqrt{\pi}}\left[1 - 2D(\sqrt{2}\,\gamma_2\omega_c)\right]\right\}, \quad g_c << 1 \tag{C.1.14}$$

where

$$D(x) = x\, e^{-x^2}\int_o^x e^{t^2}\, dt$$

is Dawson's integral which is tabulated [ASM55, ed. by Abramowitz and Stegun (1964)]. Clearly as ΔT increases, the average intensity $\langle E(0)\rangle/(2\Delta T)$ approaches the CW result (2.4.5).

For the cosine pulse of duration $2\Delta T$, see (B.1.3), $T_{ef} = 3/4\Delta T$ and

$$T_{ef}K_o(\tau_r) = \frac{\Delta T}{2}\left\{\left[1 - \frac{|u|}{2\Delta T}\right]\left[1 + \tfrac{1}{2}\cos\frac{\pi|u|}{\Delta T}\right] + \frac{3}{4\pi}\sin\frac{\pi|u|}{\Delta T}\right\}, \quad |u| \le 2\Delta T, \quad |u| > 2\Delta T \tag{C.1.15}$$

The first part of (C.1.15) is simply the rectangular pulse component for which the solution has been obtained above, and the remaining components may be evaluated by letting $\omega_o = \pi/\Delta T$ and setting $\omega_1 = \omega_c - \omega_o$ and $\omega_2 = \omega_c + \omega_o$ as for the pulse amplitude (C.1.3) and then using the trigonometric identities. For the 'exact' solution in terms of Hermite polynomials we require the additional relation

$$\int_o^{2\Delta T} e^{-u^2/4\gamma^2}\sin(\omega u)\, du = -j2\Delta T\sum_{m=0}^{\infty}\frac{H_{2m+1}(j\gamma\omega)(\Delta T/\gamma)^{2m+1}}{\lfloor 2(m+1)}$$

If $\Delta T/\gamma_2 > \sqrt{2}$ a result comparable to (C.1.14) may be obtained for the cosine pulse, i.e.

$$\left\langle E(0)\right\rangle_{\substack{\delta_s=\delta_i \\ \phi_s=\pi}} \simeq k_c^2 g_c\, \pi mn\, E_o\, \Delta T$$

$$\times \left\{ \frac{e^{-2\gamma_2^2\omega_c^2}}{2} \left(1 - \frac{\sqrt{2}\,\gamma_2\, e^{2\gamma_2^2\omega_c^2}}{\Delta T\,\sqrt{\pi}} \left[1 - 2D(\sqrt{2}\,\gamma_2\omega_c) \right] \right) \right.$$

$$+ \frac{e^{-2\gamma_2^2\omega_1^2}}{8} \left(1 - \frac{\sqrt{2}\,\gamma_2\, e^{2\gamma_2^2\omega_1^2}}{\Delta T\,\sqrt{\pi}} \left[1 - 2D(\sqrt{2}\,\gamma_2\omega_1) \right] \right)$$

$$+ \frac{e^{-2\gamma_2^2\omega_2^2}}{8} \left(1 - \frac{\sqrt{2}\,\gamma_2\, e^{2\gamma_2^2\omega_2^2}}{\Delta T\,\sqrt{\pi}} \left[1 - 2D(\sqrt{2}\,\gamma_2\omega_2) \right] \right)$$

$$\left. + \frac{3}{8\pi\sqrt{\pi}} \left(\frac{D(\sqrt{2}\,\gamma_2\omega_2)}{\sqrt{2}\,\gamma_2\omega_2} - \frac{D(\sqrt{2}\,\gamma_2\omega_1)}{\sqrt{2}\,\gamma_2\omega_1} \right) \right\} \qquad \text{(C.1.16)}$$